2011

Bio-implantable microdevices and structures for functional electrical stimulation applications

Naga Srinivas Korivi
Louisiana State University and Agricultural and Mechanical College, nkoriv1@tigers.lsu.edu

BIO-IMPLANTABLE MICRODEVICES AND STRUCTURES FOR FUNCTIONAL ELECTRICAL STIMULATION APPLICATIONS

A Dissertation

Submitted to the Graduate Faculty of the
Louisiana State University and
Agricultural and Mechanical College
in partial fulfillment of the
requirements for the degree of
Doctor of Philosophy

in

The Department of Electrical and Computer Engineering

by
Naga Srinivas Korivi
B.Eng., University of Madras, 1998
M.S., Louisiana Tech University, 2002
May, 2011

ACKNOWLEDGMENTS

I wish to express my profound gratitude to Dr. Pratul Ajmera, my graduate advisor. My association with Dr. Ajmera truly began at the lowest point of my academic life. His guidance, patience and trust encouraged me to overcome my biggest challenges. His guidance is based on giving freedom to the student, while at the same time imbibing in the student a sense for attention to detail. As a consequence, one cannot help but set high standards of excellence for oneself, and constantly try to meet those standards. On a personal level, I learnt from his high integrity and unwavering dedication to work. I would like to express my gratitude to Dr. Martin Feldman, and Dr. Theda Daniels-Race, members of my graduate committee. Dr. Feldman's trust, support and advice over the years have helped me immensely. Dr. Daniels-Race showed belief in me in difficult times. I will never forget her various kind gestures. In my opinion, Professors Ajmera, Feldman, and Daniels-Race are the embodiment of everything that is right in the present day university environment. I am truly privileged to be associated with them.

I am thankful to Dr. Frank Greenway and Dr. Hwang Lee for being on my graduate committee, and for feedback on my research. Dr. Greenway introduced me to the problem of obesity, and provided a basis for the problem statement in this research.

I am thankful to Mr. Golden Hwaung, and Mr. James Breedlove for the years of help, technical and otherwise, guidance and friendship. I thank Dr. Jolene Zheng for performing rodent surgeries to implant some of the devices developed in this research. I thank Microprobes for Lifescience, Inc., for evaluating some of the cuff electrodes developed in this research.

My family has been the greatest source of strength during my academic endeavors. For their infinite love, patience and support, I will be indebted the rest of my life.

TABLE OF CONTENTS

ABSTRACT

This dissertation describes the development of microstructures and devices for applications in functional electrical stimulation. A nerve cuff electrode design has been developed for applications in neural electrical stimulation and recording, which addresses limitations with existing cuff electrodes. The developed clip-on micro-cuff electrode design consists of a naturally closed cuff with inner diameter in the micro-scale or above. A novel pinch-hinge feature allows a user to easily open the cuff and place it on target nerve tissue for stimulation or recording purposes. Upon release of the pinch-hinge, the cuff assumes its normally closed nature. The device conducts and reads electrical signals in the amplitude and frequency range of typical neural signals. A typical clip-on cuff device with 800 μm inner diameter is opened to its maximum extent by a relatively low force of less than 0.8 N, offering an alternative to other designs requiring application of a force for cuff closure.

For applications involving gastric muscle stimulation, a novel gastric pacing electrode is fabricated in biocompatible silicone elastomer. In response to physiological temperature of about 37 ˚C, polyethylene glycol embedded inside the device body melts due to which the structure changes from a more rigid state initially to a more flexible state. This is expected to reduce tissue penetration during and after electrode implantation.

A comprehensive piece-wise discrete element equivalent circuit model has been developed to represent an electrode-neural tissue interface. This model addresses internal aspects of both the tissue and the electrode surface and is an improvement over previous models. The equivalent circuit is employed in conjunction with electronic circuit simulation software to study the electrical response of an axon to external stimulus. Simulation results broadly correlate with practical observations reported by others.

Lastly, a new percutaneous access device functioning as an interface between implants and the external world is reported here. The device made of silicone elastomer incorporates stress concentration features and shows promise for improved robustness and reliability. The device also incorporates micro-scale porous structures to allow for tissue in-growth to facilitate anchoring of the device.

CHAPTER 1: BRIEF DESCRIPTION OF CHAPTER CONTENT

A brief description of the following chapters is given below.

Chapter 2: Introduction, Literature Review and Problem Statement

Functional electrical stimulation (FES) is one of the important medical innovations of the current time. FES is based on periodic or constant electrical stimulation of specific nerves, nerve fibers and muscles by a single or multiple set of electrodes, for control and treatment of numerous pathological conditions. While the underlying physiological aspects form the basis for a particular FES technique, its development and implementation largely depend on the successful engineering of bio-implantable electrodes for electrical stimulation of biological tissue, recording of bio-potentials from said tissue, and devices capable of providing effective routing of electrical connections from the implanted electrodes to other external devices. Chapter 2 reviews the present state-of-the-art in the major technologies pertaining to FES, namely (1) electrodes for nerve stimulation; (2) electrodes for gastric stimulation; (3) equivalent electric circuits for the interface formed by an electrode with tissue; and (4) devices to route electrical wires from an implanted electrode to equipment external to the body. The review describes the challenges and drawbacks with existing technology in these four major areas, and lists specific needs/innovations necessary to address them. Chapter 2 also provides information leading to the contents of succeeding chapters.

Chapter 3: Research Goals

Based on the specific innovations required to address the present challenges in FES technology, Chapter 3 lists the innovations made in the present dissertation research. These innovations are listed under four major topics, namely (1) electrodes for nerve stimulation; (2)

electrodes for gastric stimulation; (3) equivalent electric circuits for the interface formed by an electrode with tissue; and (4) devices to route electrical wires from an implanted electrode to equipment external to the body.

Chapter 4: Electrode Technology Development

Chapter 4 describes the development of technology for nerve stimulation electrodes. For applications involving FES of nerves and nerve fibers, one of the most commonly employed electrode design is the cylindrical cuff electrode. This design offers several advantages. However, there are some problems involved with the current design technology. The currently available cuff electrodes need to be manually opened, placed on the target nerve and then closed during surgery. The cuff opening is typically secured by epoxy, wax or small piece of silicone rubber, in an intra-operative procedure immediately after implantation. This procedure becomes significantly more complicated when the cuff electrodes are small in dimension. Therefore, there is a need for an electrode design that can preserve the advantages of a cuff structure, while overcoming the cuff closure or securing problem.

A problem with several existing cuff electrode designs is that they are made by the assembly of discrete components including cylindrical tubing serving as the cuff, and metal wires serving as electrode leads. The electrode wires are inserted into the cuff and secured by means of epoxy. This reduces the robustness of the device, as the interface between the electrode wire and cuff wall is vulnerable to pulling forces acting on the wire. A cuff electrode design that provides for a robust electrode wire-cuff interface is very essential. A major problem with commercially available cuff electrodes is that they are not suitable for small anatomies, i.e. smaller nerves and nerve fibers, often with diameters in the sub-mm or micro-scale. It is difficult to open and close regular cuff structures as they get smaller. Therefore, there is a need for a cuff

electrode design that can effectively address the stimulation of small diameter nerves and nerve fibers.

Considering the above stated problem areas in the present nerve stimulation electrode technology, Chapter 4 describes the development of a novel electrode design to address the following:

1. Problem of securing the cuff opening after implantation on a target nerve tissue.
2. Develop cuff electrodes for sub-mm or micro-scale diameter nerve tissues.
3. Improving robustness of the cuff-electrode wire interface.

Chapter 4 also describes technology development for gastric stimulation electrodes. Gastric pacing or the electrical stimulation of the gastric wall and muscles is of interest in the treatment of obesity and obesity related conditions. Pacing electrodes are implanted in the muscular layer of the stomach wall, to incite the required response from the stomach muscle. However, this type of lead placement often results in the stomach wall being penetrated, causing experimental failure and possible patient trauma. This poses a bigger challenge in the case of intestinal electrical stimulation for obesity treatment where a similar placement of leads is required. The intestinal wall is thinner than the stomach wall, making it more susceptible to penetrations by the electrode leads. It has been suggested that smaller electrode leads are more appropriate for intestinal stimulation. Another major problem encountered with electrodes implanted in the stomach or intestinal wall is the displacement of the leads from the desired position, which has been attributed as a major reason for weight loss failure in gastric stimulation studies. Another problem is the device failure from lead fracture, due to rigid nature of the electrode implanted in an environment involving flexing muscle tissues.

Given the requirements for gastric pacing electrodes, Chapter 4 describes the development of electrode technology to address the following:

1. Development of a miniaturized gastric stimulation electrode based on incorporating metal leads on flexible polymeric substrates, aimed at alleviating the lead penetration problem during implantation. The structural flexibility is expected to reduce lead fracture problems. The electrode incorporates a structure whose flexibility can be changed from a more rigid state initially to a more flexible state at physiological temperature. The structural flexibility is expected to reduce tissue penetration and lead fracture problems during and after implantation.
2. Development of features that enable direct anchoring of the pacing electrode to gastric tissue at more than one electrode location.

Chapter 5: Equivalent Circuit Model for Tissue-Electrode Interface for Nerve Stimulation

The passage of an electrical stimulus signal through biological tissue may inflict injury by several possible mechanisms, the major of those being electrical in nature. For a specific stimulation electrode design, it is pertinent to understand the electrical effects at the tissue-electrode interface during the stimulation process. This is important because it is essential to ensure that charge flow into the target tissue does not exceed acceptable levels during the electrical stimulation. Towards this, designing an equivalent circuit model of the tissue-electrode interface and studying its response to typical stimulation signals will help researchers in designing a safe and successful stimulation protocol. Previous reports have represented the electrode-tissue interface as an electrode immersed in an electrolyte and have neglected any representation of the internal components of the tissue being stimulated. Other reports have focused solely on representing the tissue being stimulated in terms of electrical circuit

equivalents, while neglecting to include any components or modules to represent the metal surface and the interface formed by it with the tissue. In this context, Chapter 5 describes development of an integrated equivalent circuit model with components to address both aspects of tissue being stimulated by a metal surface. This circuit behavior is analyzed using PSPICE electronic circuit simulation software.

Chapter 6: Routing Technology for FES Applications

An essential part of a typical FES research activity is the physical routing of electrode lead wires from the implanted electrode to equipment that supplies the electrical stimulation signal. This equipment may be implanted or situated externally i.e. outside the body. In many situations, it is difficult to implant the signal generator and electric power equipment. In such cases, it is more practical to supply the signal and electric power through a physical interconnection or wiring traversing between the implanted electrode and external signal/power source. Special devices, known as percutaneous access devices (PADs), are used to support electrical wiring as it exits the test animal's or human's skin and protect the wire from mechanical forces exerted by body motion and other causes.

A typical PAD consists of a base or flange structure that is implanted and a conduit structure that allows an interconnection between the in-vivo and the external devices. The conduit structure is typically a skin piercing element, partially protruding out of the skin while being placed under it. The base or flange structure functions mainly as an anchor for the device. The skin piercing nature of PADs poses great challenges in the design and integration of these devices for FES applications. Some of the existing PAD designs are highly application specific, thereby restricting their general usage. Another drawback is that most of the currently available PADs rely on the use of specialized and expensive equipment for the device fabrication.

Additionally, device design changes may be difficult to implement on the fly. A major problem with existing PADs is the incidence of infection, leading to device failure caused mainly by relative movement of the base/flange structure due to external forces arising from routine motion of the body. There have been very few reports on PADs incorporating components that aid in relieving the forces acting on the base. Another area of concern is the incorporation of micro-scale pores and microstructures, in the implanted part of the design in order to encourage connective tissue in-growth. Until now, most PADs having such porous structures are based on the attachment of commercially available discrete porous fabric or polymeric layers onto the main device. The attachment is typically done by an adhesive. Other PADs, with tailor-made porous structures, employ complicated methods and equipment to make such structures. It is beneficial to develop simple methods to form micro-scale pores and structures in biocompatible materials to facilitate growth of connective tissue.

Chapter 6 describes several useful innovations in PAD technology being made in this dissertation research. This chapter specifically describes the following:

1. Development of fabrication technology for PADs, based on convenient and easy-to-implement processes involving proven bio-implantable materials.
2. Novel PAD design with features aimed at reducing the forces transferred to the implanted portion of a typical PAD.
3. Development of methodologies to create micro-porous and micro-patterned layers of highly biocompatible materials like medical grade silicone for applications in connective tissue growth. The developed processes enable pore dimensions from the sub-micron range to several hundred microns. The resulting porous layers may be inbuilt into PADs during their fabrication or may be free-standing to function as add-on structures.

Chapter 7: Summary, Conclusions and Recommendations for Further Research

Chapter 7 summarizes the results of the present research work. It lists the conclusions drawn from various aspects of this dissertation and recommends areas for further research.

CHAPTER 2: INTRODUCTION, LITERATURE REVIEW AND PROBLEM STATEMENT

2.1. Introduction

Functional electrical stimulation (FES) is among the important medical innovations of the modern era. FES is based on a periodic or constant electrical stimulation of specific nerves, nerve fibers or muscles by a single or multiple set of electrodes, for the control and treatment of numerous physiological conditions [1, 2]. One of the first and the most widely known examples of a FES application is cardiac pacing, which involves the application of electrical pulses to the heart for the purpose of regulating the heart beat [3]. Ever since the advent of cardiac pacemakers some decades ago, the field of FES has evolved substantially and numerous FES devices have been developed for different medical applications. Some of the FES applications developed till date include control of paralyzed limbs, suppression of chronic pain, partial restoration of eye sight, bladder control, speech restoration and other types of organ function restoration [4-11].

In recent years, there has been significant global interest in FES techniques for the treatment of obesity. The obesity epidemic has become one of the bigger challenges facing the well-being of humans worldwide [12]. The prevalence of obesity in children and young adults in almost every country is a cause for grave concern. In the U.S, one out of every three individuals is characterized as obese and 5% of the population is in the morbidly obese category [13, 14]. The effects of obesity and morbid obesity are manifested in a myriad of health conditions such as type-2 diabetes, high blood pressure/heart disease, osteoarthritis or rapid wear and tear of weight-bearing joints, sleep/respiratory problems, gastroesophageal reflux disease, infertility, urinary stress and menstrual irregularities [15-20]. Some of the common methods employed to

counter obesity such as pharmaceutical drugs and traditional weight loss programs are effective only for a small percentage of people. Weight loss programs have modest long-term results with participants typically known to recover their weight in a short time [21-23]. It has been shown in several studies that weight recovery will occur upon the withdrawal of pharmaceutical drug-based therapy [24].

Due to the long-term ineffectiveness of traditional treatment options, bariatric[1] surgery (e.g. Roux-en-Y gastric bypass surgery for stomach reduction and rerouting the digestive tract) has been employed to avoid adverse effects resulting from morbid obesity for patients with body mass index greater than 40 or even 35, if the patient suffers from other serious medical conditions [25, 26]. The number of overall bariatric surgeries has grown by 900% in a span of just six years between 1998 and 2004 with a 20 fold increase in adults between ages 55 and 64 during the same period [27]. According to a recent study, approximately 1% of eligible individuals with morbid obesity receive bariatric surgery [28]. That is more than 150,000 individuals, by current population figures. Even though direct in-patient death rate during bariatric (gastric bypass) surgery has declined in recent years, its value of approximately 0.2% is still significant.

In recent years, FES has become one of the important techniques being researched for the treatment and control of obesity [29]. FES of specific nerves and muscles has been shown to be useful in treating obesity and obesity-related physiological disorders [30-32]. In comparison to bariatric surgery, which is highly invasive and irreversible, a typical FES based method requires minor surgery with a much lower risk to the patients and hence is an extremely attractive alternative.

[1] Bariatrics: branch of medicine dealing with the causes, prevention, and treatment of obesity.

It is clear that FES technology has a very significant role to play in the future healthcare endeavors of mankind. With its multitude of applications, FES is one of the more important medical technologies in existence currently. The persisting global interest in FES research indicates the potential for substantial growth in the FES field in future years. While the underlying physiological aspects form the basis for a particular FES technique, its development and implementation largely depend on (1) successful engineering of bio-implantable electrodes for the electrical stimulation of biological tissue, (2) recording of bio-potentials from the tissue, and (3) devices capable of providing effective routing of electrical connections or transmission of power and signals to and from the implanted electrodes to other in-vivo[2] or external devices. Successful engineering of such electrodes and devices is closely linked to development of methodologies to employ and structure proven biocompatible materials so they may be utilized for long-term in-vivo applications.

It is the objective of this dissertation to address the development of novel electrode technology and routing and feed-through solutions for electrode wires. The research results reported in this dissertation may be applied to a variety of situations though the current work was initiated with a focus on obesity treatment applications.

2.2. Electrode Technology for Nerve Stimulation

For applications involving FES of nerves and nerve fibers, numerous stimulation electrode designs have been developed till date [33]. The reported devices include those based on assembly of discrete components, wire strands, thin film technology, and micro-fabrication [34-39]. One of the most commonly employed electrode design is the cylindrical cuff electrode [40-

[2] In-vivo: inside the body; a term generally used in this document while referring to an implanted or internal condition.

44]. This design is characterized by its simplicity and relative ease of usage. Figure 2.1 shows an example of a cuff electrode.

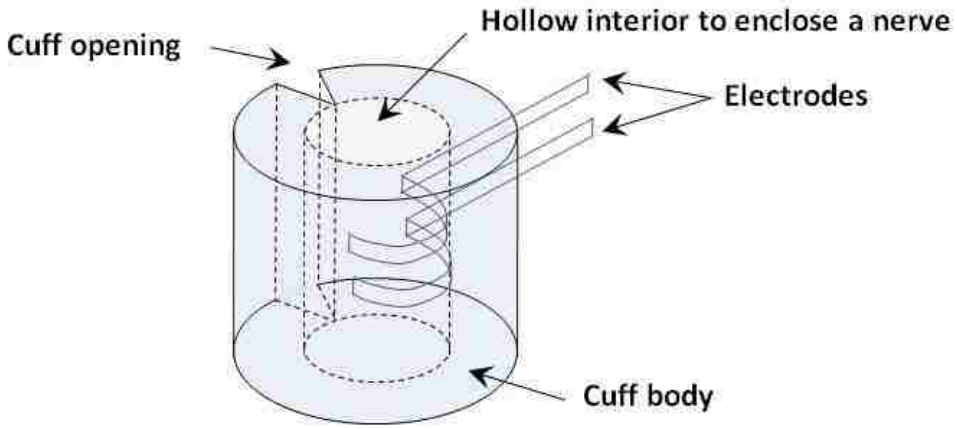

Figure 2.1: Schematic of a cuff electrode. The cuff body is typically made of a flexible material like silicone rubber or another polymer.

2.2.1. Cuff Electrode Design

One of the major reasons for a general preference for the cuff type electrode design is its suitability for long term nerve stimulation or recording, and for situations where the subject undergoes motion, a situation common in most practical cases [45].

Cuff electrodes offer several advantages compared to other commonly used electrodes including reduction in stimulus intensity required for nerve activation, minimization of mechanical damage to nerves, reduced probability of lead failure, and selective stimulation of a target tissue[3] [46-48]. However, there are some problems involved in the use of the cuff type design that need further consideration.

[3] Target tissue: a term generally used in this document to refer to the specific physiological organ or tissue being electrically stimulated.

2.2.1.1. Nerve Cuffs for Micro-scale Nerves and Nerve Fibers

One of the major drawbacks of the present nerve cuff technology is the paucity of cuff electrode designs for the stimulation of nerves and nerve fibers with effective diameters in the micro-scale, which is of interest for human and animal subjects and offers advantages in some applications [49]. For example, it is possible to achieve better bladder emptying while employing a FES-based approach by activating small nerve fibers innervating the bladder compared to when large and small fibers are simultaneously activated [50].

For any new FES technique involving nerve stimulation, it is the prevalent practice to first develop animal-based test protocols. While canine, feline, and porcine test platforms are routinely employed, rodent-based test platforms are preferred in numerous applications because of the smaller size of the animal and the corresponding reduction in the costs incurred. However, the development of FES-based rodent models has numerous challenges, primarily due to small diameters of rat nerves and fibers. To illustrate, the effective diameters of feline nerves and fibers are in the millimeter range depending on a particular nerve tissue, while values for similar nerve tissue in rats are in the millimeter and micrometer range [46, 51]. The electrodes employed for stimulating nerves in canine, porcine and feline test animals are generally not suitable for smaller test animals like rats. The smallest cuff electrodes commercially available in the United States are made for large nerve diameters and are generally not suitable for nerves and fibers with diameters in the micro-scale. For example, the smallest cuff electrode from Microprobes for Lifescience, Inc. has internal diameter of 500 μm, which may be too large for smaller diameter nerves [52]. Many cuff electrode designs reported are suitable for relatively large nerves, but are difficult to scale down for use with smaller nerves in the 0.5-1 mm diameter range [42]. Thus, there is a need for specific cuff electrode designs that cater to small dimensions of nerve tissues.

2.2.1.2. Cuff Electrode Closure Technology

A typical cuff electrode has a lengthwise opening (Figure 2.1) that has to be closed after bio-implantation on the target nerve. The closure of the cuff is required in order to ensure that the cuff electrode stays secured on the target nerve. In applications involving bio-potential recording by nerve cuff electrodes, a closed cuff reduces unwanted electrical noise from surrounding physiological ambient [53]. A completely closed cuff ensures that there is usually a fixed amount of extracellular[4] fluid trapped around the nerve by the cuff. Extracellular fluid can conduct electricity. A varying amount of extracellular fluid may surround the nerve in the case of a partially open cuff, causing undesirable electrical noise. The currently available cuff electrodes need to be manually opened, placed on the target nerve and then closed, prior to their operation. The cuff opening is typically secured by epoxy, wax, small pieces of silicone rubber, or suture thread [54-59]. This involves the use of intra-operative procedures during surgery to secure or seal the cuff opening immediately after its placement on a nerve. To illustrate, Jellema *et al.* fabricated a length-wise split cuff made of Impregnum, a polyether elastomer commonly used in dental impression applications [60]. The target nerve was placed in the cuff and sealed by freshly mixed Impregnum during surgery. This design attempted to solve the cuff sealing problem. However, there are some drawbacks with this type of approach. The cuff sealing procedure is intra-operative and has to be done with great care. The freshly mixed Impregnum may flow into the cuff and cover the electrode leads partially or even completely. Another drawback with Jellema *et al.*'s design is that once the cuff is sealed, it may be difficult to remove from the nerve, with the removal procedures potentially damaging the nerve. This cuff closure method provides a permanent seal that may require sharp cutting tools to open.

[4] Extracellular: refers to the space outside a cell, occupied by fluid consisting of metabolites, ions, proteins and other substances that may affect cellular function.

Among other designs, Loeb *et al.* reported a cuff electrode design based on a silicone rubber cuff with a length-wise slit opening [42]. Stainless steel wire strands inlaid in the cuff functioned as electrodes. During implantation surgery, the cuff was placed on the target nerve and a silicone rubber flap was used to seal the cuff opening. Silicone epoxy was used to attach the flap over the cuff and seal it. While the use of the silicone flap allows the cuff to stay closed and secured on the target nerve, this method of intra-operatively sealing the cuff is not convenient.

Among other examples of cuff electrodes with cuff closure schemes, Banzett developed a design which consisted of a block of Teflon machined to include a groove or channel [61]. Silver wire electrodes were set within the channel and the target nerve was laid in it. Another plate of Teflon or alternately, a flexible piece of insulating material was sutured over the bottom plate containing the channel, to prevent the nerve from slipping out. The main drawback of this type of design is that the cuff is relatively bulky and stiff. The use of silver wires as electrodes is another drawback because silver is not considered a bio-compatible material [62]. Similar cuff electrode designs were reported by others [63, 64].

There are several cuff designs that are based on securing the cuff opening by suture thread [55]. The use of sutures to secure a cuff is prevalent in current state of the art commercially available cuff electrodes [52, 65]. Among the drawbacks of this method includes difficulty in tying suture threads around a cuff in regions of limited anatomical space. Additionally, there is a possibility of compressive nerve damage due to sutures being tied too tight. In some other electrode designs, suture threads have been used to tie electrodes directly to target tissue [66]. This is potentially hazardous due to a possibility of abrasive tissue damage from the relative motion of the cuff.

The intra-operative procedures to seal the opening of cuff electrodes may translate to additional time on the surgical table for the patient. The use of intra-operative procedures becomes significantly more complicated when the cuffs are small in dimensions, required for the smaller diameter nerves and nerve fibers [67]. Therefore, there is a need for an electrode design that can preserve the advantages of a cuff structure, while overcoming or reducing the cuff securing problem.

Crampon *et al.* reported a nerve cuff electrode based on the use of a shape memory alloy (SMA) armature [68]. Nickel titanium SMA wires were used to form an armature, which was integrated into silicone rubber cuffs. The shape recovery temperature was set at slightly under 37 ^{0}C. At room temperature, the electrode was in an initial closed position. By cooling the electrode to 10 ^{0}C, the cuff could be easily opened by the surgeon and placed around the target nerve. After implantation, the physiological temperature of about 37 ^{0}C caused the SMA armature to reach its shape recovery temperature, and thereby regain its original closed shape. The armature rigidity has to be chosen carefully, which can be a drawback in the use of this device. Experiments showed that a low rigidity SMA caused the electrode to function improperly, while a more rigid armature tore the silicone cuff during closing.

Durand *et al.* reported a nerve cuff electrode which could be closed by means of a snap closure feature with male and female mating structures [69]. The mating structures were engaged to close the cuff. The snap closure feature and the cuff body were made of silicone polymer. The main drawback of this cuff electrode is that its implantation requires a high degree of dexterity to avoid tissue damage during placement on a nerve and subsequent cuff closure. The authors reported that a force of about 2 N was required for cuff closure. This magnitude of force can

harm the nerve if the cuff is improperly closed using the snap closure structures. It may be difficult to implement this cuff electrode design for smaller diameter nerves and nerve fibers.

A similar design was reported by Maschino *et al.* whose cuff electrode could be placed on a nerve and subsequently closed by means of interlocking structures [70]. The cuff electrode was made by incorporating metallic layers in a polymeric cuff body made by injection molding. This type of cuff electrode may not be easy to install on delicate nerves and nerve fibers, particularly those with smaller diameters. There is a possibility of tissue damage when pressure is applied on the cuff structure to engage the interlocking features. Additionally, the usage of this type of device may be challenging at smaller dimensions.

Other approaches to address the cuff closure or cuff securing problem have been based on highly specific designs. For example, Dubkin *et al.* reported a cuff electrode design based on winding wire electrodes around a segment of rigid tubing which was secured to a target nerve by means of a segment of flexible tubing with a longitudinal slit [71]. The flexible tubing segment was secured in place by its own natural tension. A similar design was proposed by Barone *et al.* with a variation in that the flexible tubing segment was held in place by nylon suture threads tied around its exterior [45]. The main disadvantages with these designs include the possibility of nerve damage caused by placing a rigid tubing segment adjacent to the nerve. With Barone *et al.*'s design, there is the additional possibility of nerve compression injury due to strapping the cuff to the nerve. Both these designs also limit the electrode surface area that can be in contact with the enclosed nerve.

Similarly, McCarty *et al.* developed a cuff consisting of electrodes set within the core of a stiff insulating cylindrical segment in which the nerve could lie [72, 73]. A zig-zag channel cut into the cylindrical segment allowed its implantation on a nerve while preventing the device from

slipping off the nerve. The main drawbacks of this design are the stiffness or rigidity of the cuff and the relatively delicate implantation procedure required to avoid nerve damage by the zig-zag ends of the cuff opening. There is a need to overcome the inherent drawbacks of cuff designs that are based on the natural rigidity of a cylindrical segment or cuff.

A type of cuff electrode design that addresses the cuff closure and securing problems is the spiral cuff. There have been many reports on the development and use of cuff electrodes based on the spiral cuff design. Naples *et al.* reported one of the first spiral cuff electrodes [74]. In its most common configuration, the spiral cuff electrode is of the self-curling type, typically including a self-curling sheet of non-conductive material biased to curl into a tight spiral. The biasing is typically done by bonding a pre-stretched polymer layer to an un-stretched polymer layer [75]. Due to tensile stress of the pre-stretched layer, the structure curls, thus becoming a spiral. The inner diameter of the spiral can be pre-set by the fabrication process. The electrodes are typically metal wires or strips located peripherally around the inner diameter of the cuff. Alternately, the electrodes may be placed between the two polymeric layers and active electrode surfaces created by manually opening windows in the pre-stretched polymer layer.

Spiral cuffs electrodes have several inherent drawbacks. A major drawback is the lack of applicability to small nerves. Existing spiral cuff electrodes do not reliably interface to small nerves [76]. Another major problem is the difficulty in implanting such electrodes on nerves that are located in regions with limited space. For example, the greater splanchnic nerve segment located just under the diaphragm in rodents is not easy to access [77]. This particular nerve segment is of interest in the treatment of obesity. The tissue access problem is exacerbated in cases where the target nerve fiber or bundle, due to its position in the body, is not easily encircled by spiral cuffs without complicated surgery or without inflicting damage to the

surrounding tissue. Additionally, there may be a need for special applicator tools to implant spiral cuffs on a nerve [76].

A variation of the self-curling spiral cuff is the self-sizing spiral cuff [78]. Rather than curl into a spiral with a pre-set inner diameter, the self-sizing spiral cuff curls closely around the nerve. One of the drawbacks of the self-sizing spiral cuff electrode is that such electrodes tend to interfere with normal swelling and movement of the nerve. Damage to the nerve fibers can result when the self-sizing spiral cuff curls too tight around the nerve preventing the flow of nutrients, blood and other critical fluids [79]. Several self-sizing cuff electrode designs have been reported to be fragile and difficult to install [80]. Other self-sizing cuff designs have not produced long-term satisfactory results because of difficulties related to their self sizing nature [81]. In contrast, conventional cuff electrodes have shown satisfactory results over continuous periods of 15 years and more [44]. Hence, though the spiral cuff design addresses the cuff securing and closure problem, the conventional cuff electrode design with the lengthwise slit cylinder is preferable.

2.2.1.3. Robustness of Nerve Cuff Electrodes

Several cuff electrode designs reported so far have been based on the assembly of discrete components including cylindrical tubing serving as the cuff, and metal wires serving as electrode leads [54, 56, 57, 59, 82]. The electrode wires are inserted into the cuff and secured by means of epoxy [83].

An example is an electrode design by Sauter *et al.* whose cuff was a rigid tube of silicone rubber with a wedge-shaped longitudinal slit [83]. Platinum wire electrodes were inserted into the cuff and attached to the outer cuff wall by epoxy. Implantation involved sliding the cuff back and forth on a nerve till the nerve slipped through the slit into the cuff. The tube's rigidity caused it to spring close to prevent it from slipping off the nerve. In principle, by selecting tubing with

appropriate inner diameter, the cuff electrode can be made with micro-scale inner diameters. Implantation of this type of cuff electrode can be traumatic to the nerve. This type of cuff electrode employs the natural rigidity of a cylindrical tubing to enclose a nerve and stay secured to it. The rigidity of the tubing may cause nerve injury.

Another example of a cuff electrode made by assembly of various components is a device by Fenik *et al.* who used commercially available polyethylene tubing for the cuff body [54]. The inner diameter of the cuff was defined by choosing appropriate inner diameter commercial tubing. The device included two silver wire electrodes, one of which formed a hook around the nerve. The other electrode was placed near the nerve inside the cuff, in the extracellular fluid surrounding the nerve. The electrodes were held in place by applying molten dental wax to one end of the cuff after implantation and curing it at room temperature. The cured wax also secured the cuff to the nerve.

In principle, this cuff electrode can be made with micro-scale inner diameter by selecting tubing with appropriate inner diameter. A drawback of this cuff electrode design is that one of the cuff ends is closed. Therefore, it is suitable for capping cut nerves only because the design does not allow the cuff to be used with normal, continuous nerves. The sealing of one end of the cuff by dental wax has to be done with utmost care to avoid covering the electrodes. The use of silver as electrode material is not optimal in terms of biocompatibility.

In both the aforementioned examples, only a limited amount of epoxy or wax secures the electrode wire-cuff interface. This reduces the robustness of the device, as the electrode wire and cuff wall interface is vulnerable to pulling forces that may act on the wire mostly due to play or relative motion of the internal organs. Detachment of the electrode wire from the cuff results in device failure, requiring surgical re-implantation of the cuff electrode device. In some cases, the

electrode leads are connected to insulated wire cables by soldering and the junction is sutured to tissue adjacent to the target nerve in order to relieve the stress at the junction [42]. This may result in tethering damage to the nerve and electrode leads. Therefore, it is advantageous to have a cuff electrode design that overcomes these problems and provides for a robust electrode wire-cuff.

2.2.2. Summary of Problems in Cuff Electrode Technology

The problem areas in the present cuff electrode technology for the electrical stimulation of nerves and nerve fibers are summarized below:

1. There is a paucity of cuff electrode designs suitable for nerves and nerve fibers in the sub-mm or micro-scale diameters. There is a need to develop a cuff electrode for micro-scale diameter nerve tissue.
2. The present methods of securing the opening of cuff electrodes after placement on a nerve include the use of epoxy or equivalent, or a piece of silicone to close the opening. Other methods involve the use of sutures to close the cuff opening, while others involve the use of a rigid cuff that tries to retain a closed condition. These methods have numerous drawbacks, making it imperative to solve the cuff closure problem by design innovations.
3. In several existing cuff electrode designs, the electrodes are inserted into a cuff, and secured in place by means of epoxy or wax. This does not provide for a robust interface between the electrodes and cuff wall, making the overall device susceptible to failure. Therefore, there is a need to improve the robustness of nerve cuff electrodes, especially at the cuff-electrode wire interface.

2.3. Electrode Technology for Gastric Muscle Stimulation

There are two fundamental FES approaches for the treatment of obesity and obesity related conditions. One approach involves the stimulation of nerves and nerve fibers specific to the digestive system, hunger, and satiety among others [84-86]. The other approach generally referred to as gastric pacing, involves the electrical stimulation of stomach muscles to modulate the frequency of the stomach's smooth muscle wave. This type of procedure has been found to be useful in the treatment of obesity and obesity related health problems [87-90]. However, there are several challenges being faced in gastric pacing applications due to the limitations of the currently available pacing electrode technology.

2.3.1. Gastric Electrode Technology Review

Gastric electrical stimulus may be applied at any location which allows the electrical stimulus to produce a local contraction at the desired section of the stomach or other organs in the gastro-intestinal tract [91]. To apply a gastric electrical stimulus, the pacing electrodes may be implanted on the inner or outer surface of the stomach or other organs in the gastro-intestinal tract [92]. It is pertinent to briefly review the structure of the stomach wall cross-section. The stomach wall has seven layers of tissues (Figure 2.2). The seven tissue layers include the oblique, circular, and longitudinal muscle layers of the muscularis externa that contract and expand, interposed between the interior stomach mucosa[5] and the external serosa. The outermost layer is the serosa[6] or a serous membrane. Gastric stimulation electrodes may be placed either on the serosa, or the mucosa or alternately placed between two layers such as the longitudinal and circular layers [93, 94].

[5] Mucosa: mucus membrane lining various organs.
[6] Serosa: a serous membrane or serosa is a smooth membrane made of a thin layer of cells which excrete fluid.

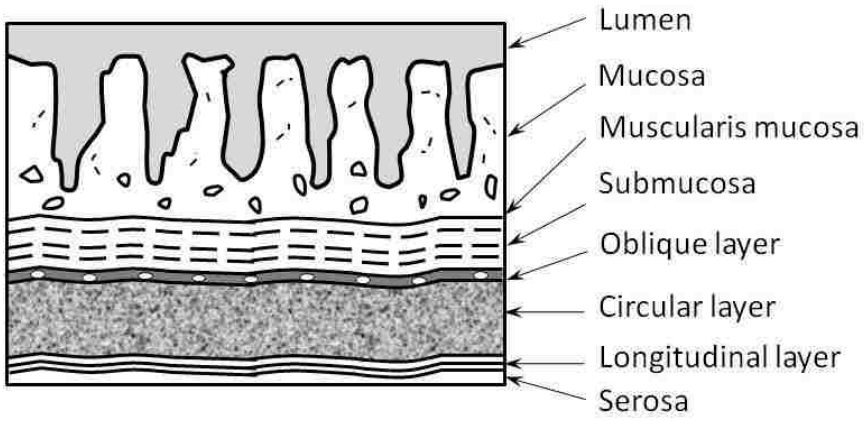

Figure 2.2: Schematic of cross-section of the stomach wall showing its different layers [Adapted from reference 94].

2.3.1.1. Gastric Electrode Designs

Most of the gastric pacing reports till date have involved the use of commercially available pacing electrodes from Medtronic Inc., Metacure (USA) Inc., and A&E Medical Corp. Among these, the most commonly used electrode is the model 4300/4301 series made by Medtronic Inc [95, 96]. There have been several reports based on the use of this electrode for gastric pacing applications [32, 95, 97-99]. The model 4300/4301 pacing electrode consists of three sections, namely a connector section, body section and an anchoring section. The connector section includes a connector pin to electrically couple the electrode lead into a pulse generator. The body section includes an electrical conductor surrounded by an insulating material, terminating with the main electrode lead. The anchoring section consists of a curved needle coupled to the main electrode body by a suture thread, and a separate anchoring sleeve. The use of this type of electrode is based on partially piercing the stomach wall tissue at one location by the curved needle and its exit from another location on the stomach wall. The needle is used to

pull the suture thread through the tissue in order to implant the main electrode lead in an intramuscular position.

Generally, the lead (e.g. in model 4300) is sewn through the gastric serosa laterally into the muscularis externa to locate the stimulation electrode within. A large incision is necessary to access the implant location. With this type of device, there is a possibility of tissue damage during electrode implantation.

Most of the commercially available electrodes employ relatively rigid structural features [100]. Such structurally rigid electrodes have several drawbacks [101]. For functional electrical stimulation applications, the electrode size should be maximized because this minimizes the current density and thereby, minimizes tissue damage [102]. However, it is not feasible to increase the surface area of a rigid electrode as it would increase its overall size and increase the possibility of tissue damage on penetration by the electrode. Additionally, the normal flexing of surrounding tissue may be hampered or even prevented by rigid electrodes. If the target tissue or the surrounding tissue is sufficiently muscular, its flexing may result in tissue irritation or damage, especially at the electrode ends where tissue may be pinched against the rigid electrode. In contrast, a flexible electrode structure may allow for the maximization of electrode surface area in contact with the target tissue. Flexibility in an electrode enables it to adapt to the natural configuration and position of the tissue being stimulated. A flexible electrode has enough flexure itself and therefore does not constrain the tissue to the extent by a rigid electrode.

Gastric pacing electrodes are typically implanted in the muscular layer of the stomach wall, generally in the serosa i.e. the membrane that encloses the stomach [103]. This placement of the stimulation electrodes in the wall is required to incite the required response from the stomach muscle. However, the downside of this type of electrode lead placement is that it often

results in the stomach wall being penetrated due to the rigidity of the electrode, causing experimental failure and possible patient trauma [104]. The stomach wall penetration primarily occurs during implantation of the electrodes [105]. In the use of commercial gastric pacing electrodes, perforation of the gastric wall during implantation is so frequent that endoscopic or gastroscopic assessment of the lead placement is performed during the implantation procedure [104, 105]. A bigger challenge is faced in the case of intestinal electrical stimulation for obesity treatment, an extension of the gastric pacing technique where a similar placement of electrode leads is required [106]. The intestinal wall is thinner than the stomach wall, making it more susceptible to penetrations by the electrode leads. It has been suggested that electrode miniaturization can help reduce this problem [106]. So far, there have been no reports on miniaturized electrodes for gastric and intestinal pacing.

Another problem with present gastric electrode technology is the device failure from electrode lead fracture, due to the rigid nature of the electrode implanted in an environment involving flexing muscle tissue [107]. Stress concentrations may be induced in the rigid electrodes due to surrounding tissues during the course of chronic implantation. These stress concentrations may cause fatigue failures in the electrode lead. A significant portion of muscle electrode failures have been attributed to mechanical causes [108, 109]. Some studies have reported electrode failure due to lead fracture in 50% of cases involving gastric electrical stimulation [110]. Fatigue related mechanical failures can be avoided by minimizing stress concentrations along the electrode [111, 112]. An electrode design should address the various types of mechanical stresses and strains which can result in failure. A flexible electrode can minimize the possibility of tissue penetration, and mechanical stress concentrations that may result in fatigue failure [108].

Among the other commercial electrodes, stainless steel wires such as those manufactured by A&E Medical Corp have also been employed as gastric pacing electrodes [91, 113]. While tissue penetration and lead fracture problems may be reduced in the usage of wire electrodes, there are other problems associated with such electrodes. One of the major drawbacks of bipolar wire electrodes is the limited electrode surface area that is in contact with the tissue being stimulated. Gastrointestinal stimulation often requires high energy stimulation, distributed over large electrode surface areas to avoid tissue damage [101]. Due to the limited electrode surface area available in bipolar wire electrodes, only a limited amount of electrical stimulus energy can be transferred to tissue without damaging it.

2.3.1.2. Gastric Electrode Anchoring

A major factor deciding the eventual success of a pacing electrode is the anchoring or securing of the electrode to the tissue being stimulated. The proper anchoring of an electrode is important in order to fix its position at a certain location while improper or inadequate anchoring will result in the displacement of the electrode leads from its initial position. This latter displacement may occur over time and result in failure. Displacement of electrode leads implanted on the stomach or intestinal wall has been described as a major reason for weight loss failure in gastric stimulation studies [114]. In some studies, the partial or complete displacement of electrode leads has resulted in about 50% failure rate of the electrode leads [103]. The present commercial gastric pacing electrode technology has not adequately dealt with the lead displacement problem. In one type of commercial electrode, the anchoring is usually done by suturing the proximal[7] end of the electrode [97-99]. The sutures are applied at an anchoring sleeve. Some other commercially available electrodes are typically fixed to the stomach wall by

[7] Proximal: the beginning of a structure or organ; a term commonly used to refer to the point in the body where an implant joins the body.

means of similar anchoring sleeves or clips [115]. These electrodes require post-operative monitoring to detect electrode displacement. The current high incidence rate in electrode displacement after implantation implies that the present methods of suturing are not sufficient to prevent displacement. For pacing electrodes placed laterally on the stomach wall, suturing at one location of the electrode is not sufficient to anchor the lead body.

Another anchoring method for pacing electrodes involves the use of a metallic barb at the tip of the electrode to engage target tissue by penetrating it to an extent [116-119]. This engagement is expected to secure or anchor the electrode to the tissue at the desired location. This type of anchoring is widely prevalent in present day pacing electrode technology. In this method, the electrode lead and the tissue anchoring mechanism are integrated in the same structure.

When a tissue penetrating anchor is integrated with the electrode lead, it is said to be an active fixation. It is also possible that tissue penetrating anchors may exist separately from the electrode i.e. in a non-active fixation scheme, to solely function as anchors [120, 121]. The use of tissue penetrating anchors has several drawbacks. During insertion of the structure into tissue, the sharpened end of an anchoring corkscrew or helix may damage or even tear the adjacent tissue [100]. Movement of the inserted anchoring helix can result in damage and irritation to the tissue at the site of the attachment. Typical stomach wall motion or body motion, such as movement of limbs, may also cause the electrode to exert forces on the anchoring helix, which may cause irritation or inflammation of the tissue, or perforation of the tissue wall.

A tissue penetrating anchoring helix or metallic barb is screwed into the tissue, typically by rotation of the entire electrode body. Often, a torque is applied when the surgeon attempts to screw-in the electrode anchor mechanism. Due to this applied torque, there is twisting of the

electrode body, which makes it more difficult for the surgeon to implant the electrode [122]. This makes it necessary for additional design features that enable one to screw in the anchor without twisting the device body, increasing the overall complexity of the device and its usage [123-125]. Another problem with screw-in type anchoring mechanisms is the danger of over-rotation of the screw anchor resulting in tissue damage and penetration [125]. This makes it necessary to incorporate features to prevent over-rotation of the anchoring screw, increasing the overall complexity of the device. Another drawback of helical or metallic barb anchored electrodes is the need for features that enable the easy manipulation and general handling of the electrode during implantation. The incorporation of such handling features may make the electrode device bulky [126]. In addition to all the aforementioned drawbacks of tissue penetrating anchors, a major problem is its relative lack of efficacy, with electrode displacement rates reported to be higher than desired [127]. Clearly, the present anchoring technology based on tissue penetrating anchor designs have their limitations and will benefit from further improvements.

2.3.1.3. Non-commercial Gastric Electrodes

The few reported non-commercial gastric pacing electrode designs are based on structurally rigid integrated electrode and anchor structures, and depend on tissue penetrating barb anchors. Therefore, the problems related to rigidity in the electrode body and electrode anchoring have persisted in these non-commercial designs as well.

An example is the gastric pacing electrode design reported by Swoyer *et al.* which employed tissue penetrating helixes and barbed hooks with sharpened tips that perforated the gastric serosa and lodged in the muscularis externa or the submucosa [94, 128]. Another example is a pacing electrode reported by Cigaina, consisting of a pin electrode formed with retention barbs at its tip and pressed into the gastrointestinal wall [129]. The main drawback of these

designs is that the prevention of axial movement and perforation of the gastric wall at the site of attachment cannot be assured by the limited engagement of the necessarily short and minute anchoring barbs with the serosa or sub-serosa tissue. The maximum depth of penetration of a tissue penetrating anchor is typically in the range of 1 mm to 15 mm depending on the exact location of the structure, in order to ensure that its free end does not extend through the stomach wall [94, 130]. Other anchoring methods have been reported, mainly for the anchoring of tissue penetrating gastric pacing electrodes **[**131-134]. An example is a design by Tronnes *et al.* that included an anchor movable along the length of an electrode relative to another anchor so that tissue was captured between the two anchors [135]. The intention was to retain the electrode in position. The method of implantation of the stimulation electrode involved piercing the target tissue and pulling the electrode body through the tissue. Similar anchoring schemes for gastric stimulation electrodes were reported by Imran *et al.* [132, 133].

The anchoring schemes reported by Tronnes *et al.* and Imran *et al.* can be traumatic to the stomach tissue due to the nature of the implantation method. Clearly, there is a need for better anchoring mechanisms to overcome the limitations of present anchoring technology. Specifically, the problems like electrode migration and dislodgment need to be addressed.

2.3.1.4. Flexible Gastric Electrode Technology

In order to solve some of the rigidity related problems with present pacing electrodes, a few researchers have proposed electrode designs incorporating flexible structures and components. Ben-Haim *et al.* recommended the use of flexible and elastic electrode leads for gastric electrical stimulation [136]. In their gastrointestinal stimulation experiments, they employed electrode leads made of a coiled wire, so that if the lead was stretched, the coil extended, rather than break the wire. The authors also included pre-selected weakened points in

the electrode leads, so that if the strain applied on the lead was above a pre-determined value, it would break at one of the preselected points, rather than damage adjacent tissue structures. Further details on the electrode design and materials were not provided.

There have been other reports like those from Foley and Cigaina *et al.*, involving flexible polymeric anchors attached to pacing electrodes [101, 126]. The main drawback of these designs is the need for sharp features at the tip of the device to allow the electrode to penetrate the target tissue prior to anchor deployment. Hess *et al.* reported a method wherein a helical penetrating anchor was provided with a flexible, polymeric coupling bridging the anchor to the rest of the electrode body [118]. The tip of the helical anchor functioned as the stimulation electrode lead. The flexible polymeric coupling was expected to relieve some stress at the anchor-electrode joint. However, the rigidity of the helical anchor itself and that of the actual electrode lead was not addressed. The aforementioned problems can be addressed by design innovations that allow incorporation of enhanced flexibility in gastric pacing electrodes.

There has been inadequate development of flexible electrode technology for gastric pacing applications. The advantages offered by flexible electrodes include reduction of tissue penetration, and reduced incidences of lead fracture and electrode displacement [108, 137]. There are factors to consider while designing electrode flexibility. An electrode lead that is too compliant can be distorted by the surrounding tissue so that its load bearing capabilities are reduced [109]. In other words, an electrode lead that is too flexible may not be able to drive the muscle properly. Another factor to consider is the need for some rigidity in the electrode body, especially to facilitate ease of handling during its surgical implantation. A few reports on muscle pacing electrodes have reported employing features such as a stiffening stylet to stiffen the lead body and forceps to grasp the electrode to facilitate implantation [138]. Ideally, it is preferable to

have some initial rigidity in the pacing electrode to facilitate its handling during implantation surgery, followed by a subsequent increase in structural flexibility to ensure that rigidity related problems are avoided in the implanted condition.

2.3.2. Summary of Problems in Gastric Electrode Technology

The preceding review of the gastric stimulation electrode technology clearly shows some limitations with existing state-of-the-art. To summarize, the major problems include:

1. Damage to the target tissue including tissue penetration and/or electrode lead fractures caused by the rigidity or lack of sufficient structural flexibility in the stimulation electrode structure. Hence, development of novel pacing electrode designs on flexible substrates needs to be investigated to address these problems. The new pacing electrode designs should also consider miniaturization to address requirements of intestinal pacing.
2. Need for electrode designs that incorporate features allowing an electrode to be adequately secured to the tissue being stimulated, without being displaced during or after implantation.

2.4. Equivalent Models for the Tissue-electrode Interface

The ultimate objective of any FES application is to achieve the desired electrical stimulus on the target nerve or muscle, while ensuring that damage to the tissue is minimized or avoided in the process. The passage of an electrical stimulus signal through biological tissue may inflict injury by several possible mechanisms, the major of those being electrical in nature [139]. Therefore, for a specific electrode design, it is pertinent to understand the electrical effects at the tissue-electrode interface during the stimulation process [140-143].

Electric current in the electrodes and wires is carried by electrons, whereas current in the biological tissue is carried by ions. During electrical stimulation, chemical reactions occur at the tissue-electrode interface, which are still not fully understood. The waveforms used to apply the electrical stimulus can significantly affect some factors including stimulation threshold charge, tissue damage by high charge injection, and electrochemical by-products [144-149].

The selection of parameters for the stimulus waveform is an important part of a FES application [150]. Towards this, developing an equivalent circuit model of the tissue-electrode interface and studying its response to typical stimulation signals will make it easier to select appropriate parameters for electrical stimulation. The behavior and response of such an equivalent circuit to different types of stimulus waveforms have to be understood prior to implantation of the actual electrode. This will help in designing a safe and successful stimulation protocol.

2.4.1. Modeling the Nerve Tissue-electrode Interface

The functional electrical stimulation of nerves is more critical than that of muscles because the required stimulation signals are much smaller, due to low stimulation thresholds for nerves. Consequently, there is an increased danger of tissue damage in nerve stimulation. Therefore, the present discussion is focused on developing equivalent circuit models for the interface formed by a nerve fiber with a stimulation electrode surface.

Considering a nerve as the target tissue, it is relevant to review the structure of a nerve. The structural unit of the nervous system is a neuron which is a nerve cell. Neurons are designed to carry information from one location to another. The general structure of a motor neuron is shown in Figure 2.3.

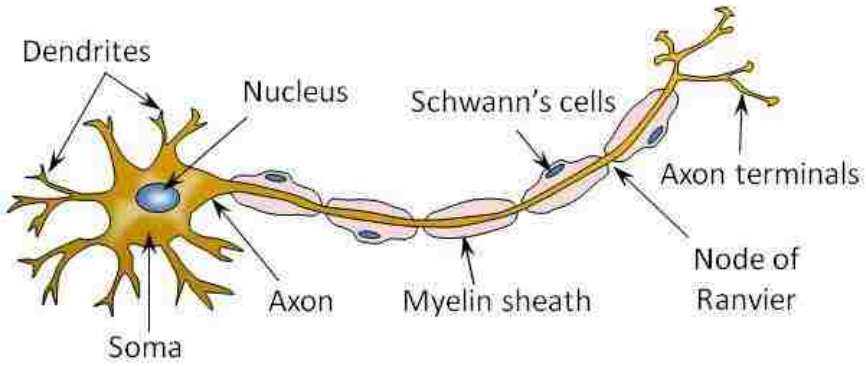

Figure 2.3: Schematic diagram of a neuron or nerve cell.

The dendrites receive input signals and transmit them to the cell soma, which is the main body of the neuron and contains the nucleus. The axon carries the signal from the soma to the target. The maximum length of an axon can extend up to a few feet. Axons may or may not be surrounded by a myelin sheath, which is a segmented, white fatty substance. There are unmyelinated regions between the myelin covered segments on the axon, known as nodes of Ranvier. The transit of signals through a neuron is made possible by flow of ions through the membrane of the neuron. Figure 2.4 shows a segment of a cell with its constituent ions. Neurons make use of different ions and their flow, to create electric currents. The flow of ions is influenced by concentration gradients, and special proteins that move the ions [151, 152]. When there is no current flow across the membrane of a cell or neuron, the potential across the membrane is constant and is called the resting potential. This resting potential is created by the difference in the concentrations of certain ions inside and outside the cell membrane. Under resting potential conditions, the concentration of sodium (Na^+) ions inside the cell is lower than that of the cell exterior, while the reverse is true for potassium (K^+) ions; and the inner surface of the cell membrane has a net negative charge while the outer surface has a net positive charge.

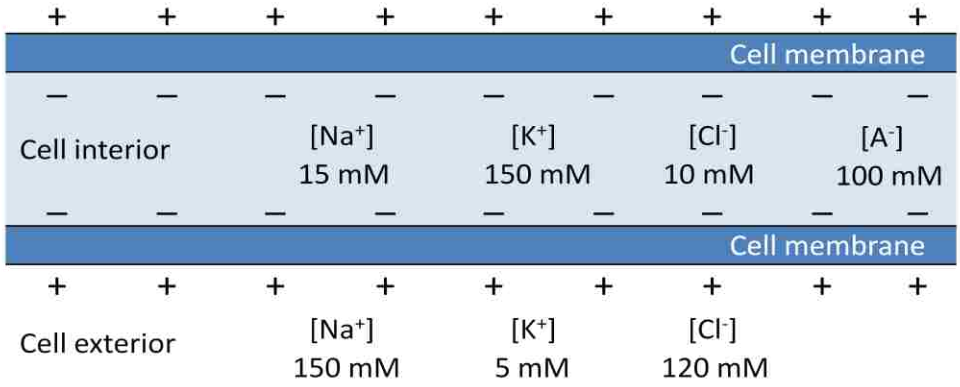

Figure 2.4: Schematic diagram of a cell or neuron segment, with typical constituent ions and their concentrations inside and outside the cell under resting potential condition. [A^-] refers to the protein concentration inside the cell, considered to have a net negative charge. Unit mM refers to milli-molar.

2.4.1.1. Neural Mechanism-based Equivalent Models

The modeling of how an electric field applied on a nerve tissue elicits changes in the excitability of an axon can provide a valuable tool for the design, development and detailed understanding of a FES application protocol [153]. In order to model the behavior of a nerve fiber, some reports have proposed equivalent electrical circuits of an axon, based on the internal processes occurring in a nerve. Most of these equivalent circuits stem from a circuit model originally proposed by McNeal [154]. An equivalent electrical network was proposed to approximate a myelinated axon or a nerve fiber with a myelin sheath by McNeal, as shown in Figure 2.5 [154]. Myelin has a high electrical resistance, and therefore, the McNeal model for myelinated axons considers electrical current to be flowing between the nodes of Ranvier only. In the McNeal model, the membrane of every node consists of a nodal capacitance C_{me}, an ionic voltage source corresponding to the resting potential of the membrane (V_{res}), and a non-linear membrane conductance G_{me}. The axial internodal conductance or the conductance of the axoplasm between two nodes is represented by G_{ax}. The internal potential or the potential inside

the axon at the n^{th} node is given by $V_{in,N}$. The external potential or the potential outside the axon membrane at the n^{th} node is represented by $V_{ex,N}$. The resting potential V_{res} is the membrane potential on the interior side with respect to the exterior side in excitable cells in absence of excitation, and is considered a constant with a typical value of -70 mV [155]. The McNeal or similar models give a reasonable representation of the electrical effects inside an axon and make it possible to simulate currents in an axon.

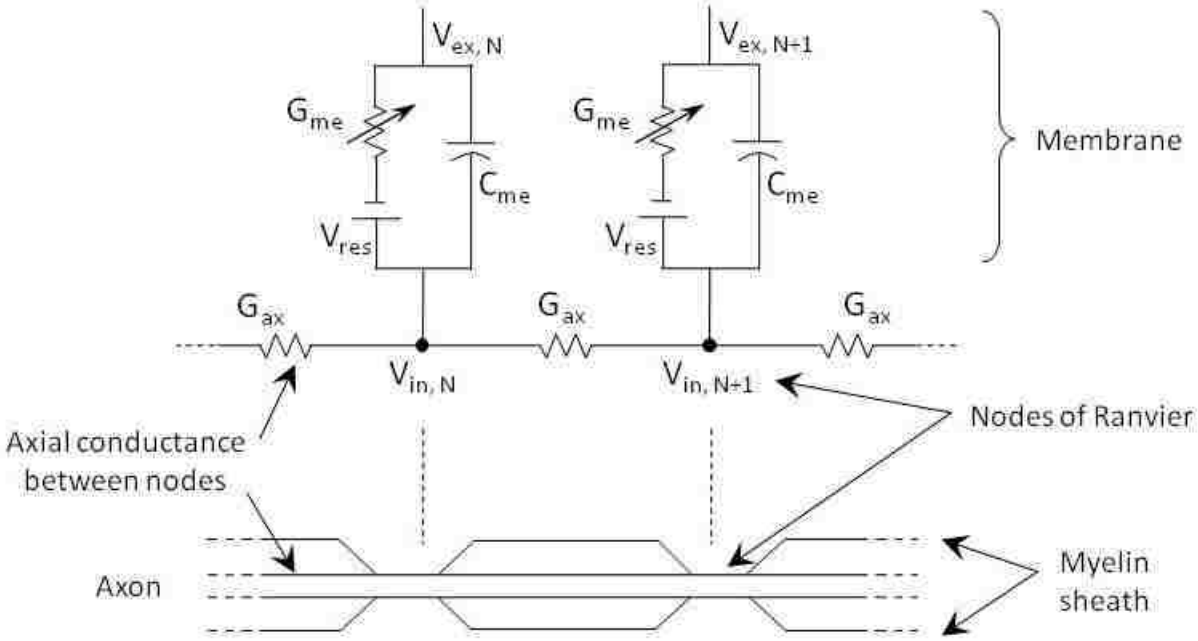

Figure 2.5: Schematic diagram of an electrical network representing a myelinated nerve fiber [Adapted from reference 154].

Several other reported equivalent circuit models to simulate an axon or nerve fiber are either directly based on the McNeal model or are similar to it [49, 156, 157]. All these equivalent circuit models including the McNeal model represent neural mechanisms or the inner mechanisms of an axon, and do not consider the stimulating electrode surface and the interface it forms with the target nerve. Specifically, they do not include any faradaic and resistive elements

representing the interface, thereby not accounting for electrochemical processes occurring at the electrode-tissue interface.

2.4.1.2. Electrochemical Mechanism-based Equivalent Models

Some researchers have proposed equivalent electrical circuits for the tissue-electrode interface from an electrochemical perspective [158-160]. In the simplest form, this interface is considered as an interface formed when an electrode is immersed in an electrolytic solution. When an electrode contacts a solution, there exists a double layer of charge at the interface (Figure 2.6), as proposed by Helmholtz [161]. Such a layer is analogous to a charged capacitor, indicating that any model for the tissue-electrode interface must incorporate capacitance.

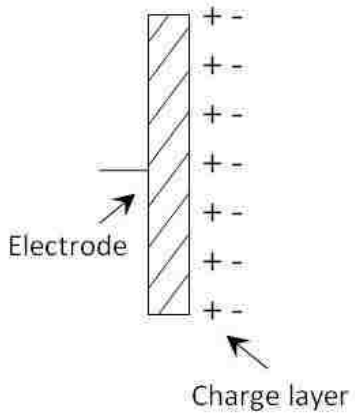

Figure 2.6: Schematic diagram of a double layer of charge formed in the electrolyte near the interface when an electrode surface is immersed in an electrolytic solution [Adapted from reference 161].

The electrochemistry based equivalent circuits developed to represent a tissue-electrode interface have included a double layer capacitance component. An illustration is an equivalent circuit proposed by Vetter [158]. This circuit was made of a combination of resistances and

capacitances (Figure 2.7A). The interfacial impedance was composed of a faradaic impedance in parallel with a double layer capacitance C_d which was in series with the solution resistance R_{sol}. The faradaic impedance was composed of the charge-transfer resistance R_{ct}, the diffusional impedance Z_{diff}, and the reaction impedance, Z_{re}. Similarly, Geddes *et al.* proposed two circuit models for the tissue-electrode interface, shown in Figure 2.7B [162]. Both models contained a half-cell potential ($E_{1/2}$). In the first model, the Warburg capacitance (C_{wa}) was shunted by the faradaic resistance (R_{far}) to account for the direct-current carrying property of the interface. The second model placed the half-cell potential in series with the Warburg components (R_{wa}, C_{wa}), and the Faradaic resistance was placed in parallel with the Warburg components to account for the direct-current property of the interface. Another model described by Sluyters-Rehbach *et al.* incorporated the Warburg components (R_{wa} and C_{wa}) and a resistance (R_{se}) in series with a parallel combination of resistance (R_{par}) and capacitance (C_{par}), as shown in Figure 2.7C. This combination was shunted by a capacitance (C_{sh}) [163]. Similar equivalent circuits with combinations of resistances and capacitances have been reported by others [164].

The tissue-electrode equivalent circuit models represented above have not included the target tissue. The target tissue's components and their properties have to be taken into consideration to understand the net effect of the stimulus signal on the tissue. Therefore, such equivalent circuits may not be adequate to model the behavior of the tissue-electrode interface in a practical scenario.

For the functional electrical stimulation of nerve tissue, a more complete equivalent circuit model for the tissue-electrode interface should include both the electrochemical and neural aspects. Therefore, it is essential to develop an integrated model with both these aspects to model its electrical behavior. To the best of our knowledge, there are no reports on an integrated

equivalent circuit model. A detailed integrated equivalent circuit model is an important scientific tool to develop protocols for specific applications of stimulation electrode devices. A detailed study is required to examine the response/behavior of an integrated equivalent circuit model to different stimulation waveforms and parameters utilizing circuit simulation software such as PSPICE.

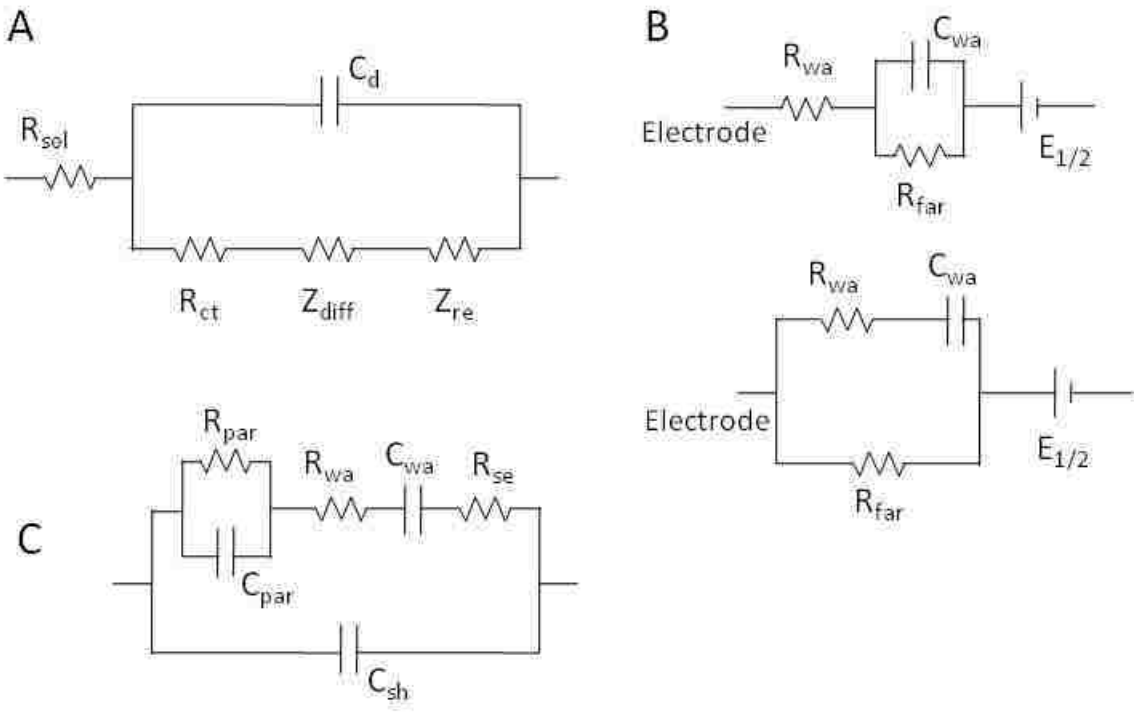

Figure 2.7: Schematic diagrams of equivalent circuits for a tissue-electrode interface, based on physical structure and electrochemical mechanisms, as proposed by (A) Vetter [158]; (B) Geddes *et al.* [162]; (C) Sluyters-Rehbach *et al.* [163].

2.4.2. Conclusions and Summary of Problems in Equivalent Models

In order to avoid potential tissue damage caused by the passage of an electrical signal during stimulation, an understanding of the electrical effects on the nerve tissue is useful. Equivalent circuits representing the tissue-electrode interface help in this aspect and enable the

researcher to establish thresholds for safe and effective stimulation protocols. To summarize the problems pertaining to the development of equivalent circuit models for tissue-electrode interfaces, the following points are listed:

1. Previous reports showing equivalent circuits for tissue-electrode interfaces have been focused disproportionately on one aspect of an interface i.e. either on the processes internally occurring at the target tissue or on the mechanisms/phenomena related to the metal electrode. A complete and reasonably accurate representation of a tissue-electrode interface is possible only when the two aspects are integrated into one model. There is a need for such an integrated equivalent model for studying functional electrical stimulation of nerve tissue.
2. To date, a detailed examination of a tissue-electrode interface by modeling it with circuit simulation software like PSPICE or similar has not been reported. Such a software based study will help in simulating numerous practical scenarios, and provide data on the approximate parameters to be used for effective and safe stimulus of the target nerve.

2.5. Routing Technology for FES Applications

An essential part of a typical FES research activity is the physical routing of electrode lead wires from the implanted electrode to another module that supplies the electrical stimulation signal. This stimulation signal supply module may be implanted or situated externally i.e. outside the body. Implantable stimulation systems include an implanted signal and power source and therefore, preclude any necessity for a physical interconnection for the electrical wiring from the implanted electrode to any external electronic equipment. The stimulation signal and electrical power are supplied from the implanted electronics and battery. Also, bio-potential signals from the target tissue can be recorded and transmitted wirelessly to an external device. However, the

surgical procedure required to implant an electrical stimulation system is often a severe deterrent, particularly for non-clinical and research applications [108]. Additionally, implantable stimulation systems for FES applications are not easy to develop for animals with smaller anatomy like rodents, cats and dogs. The smallest commercial implantable stimulators are expensive and highly application-specific. To the best of our knowledge, there are no commercially available implantable stimulators in the United States for rodent-based FES research. A drawback of implantable stimulation systems is that the implanted batteries are not able to supply power for long duration in applications like gastric muscle pacing, where electrical power requirements are typically high [165]. The implanted batteries can be recharged wirelessly, but such systems are difficult to implement for small animal anatomies. In such cases, it is more practical to supply the stimulation signal information and electric power through a physical interconnection or wiring traversing between the implanted electrode and an external signal/power source. In general, for FES research based on small-animal test platforms, researchers often prefer the physical wiring approach, though it is comparatively rudimentary with respect to the implantable stimulator approach.

It is a challenging task to establish physical routing of wires as it involves electrical wiring to pass through the skin of the test animal. The portion of wiring immediately exiting from the skin of the animal is susceptible to damage due to motion of the animal, often resulting in wire breakages and subsequent stoppage of the experiments [166]. The wire breakage after implantation can occur due to large mechanical stress created in the subcutaneous[8] plane [107]. Another major problem is the maintenance of the skin around implanted wiring and cables exiting the skin in chronic animal implant applications [167]. Skin damage or tearing around the exiting wires and cables can occur easily, causing infections. Therefore, special devices are

[8] Subcutaneous: under the skin

needed for preventing wire breakage and infection at the interface of the skin and the exiting wire [168]. Such devices, known as percutaneous[9] access devices (PADs), function to support the electrical wires as they exit the test animal's skin and protect the wires from mechanical forces exerted by the animal's motion and other causes.

Percutaneous access devices have been employed in several FES studies to facilitate the exit of electrode wires through the skin to external stimulation equipment [55, 169-171]. A typical PAD consists of a base or flange structure that is implanted subcutaneously i.e. under the skin and a conduit structure that allows interconnection between the in-vivo and external devices (Figure 2.8). The conduit structure is typically a skin piercing element, and partially protrudes out of the skin from beneath. The base or flange structure under the skin functions mainly as an anchor for the device. The skin piercing nature of PADs poses great challenges in the design and integration of such devices in FES applications. The existing designs for PAD type devices suffer from one or a combination of reasons that are detailed in the following sections.

2.5.1. PAD Fabrication Technology

Most of the currently available PAD designs rely on the use of specialized equipment like chemical vapor deposition and etching machinery, and plasma sources for the device fabrication [172-174]. To illustrate, Cosentino *et al.* reported a PAD made of titanium and coated with carbon [175]. A vapor deposition process was employed to deposit the coating of carbon on the titanium body. Similarly, Klein *et al.* reported a PAD made primarily of titanium, and coated with vapor deposited carbon [176].

Others have reported PADs either made of pyrolytic/vitreous carbon or coated with layers of carbon [174, 177]. Methods like these require vapor deposition equipment for the device

[9] Percutaneous: through the skin or piercing the skin. This term typically refers to an implanted device or application that exits the skin to permit interaction with the external world.

fabrication. It may be inconvenient for researchers to easily implement such PAD designs due to lack of easy access to the required equipment. Others have reported PADs made by ceramic materials, involving high temperature sintering processes in the device fabrication [178]. The sintering temperatures employed are about 1250 ^{0}C or higher. A major drawback posed by the use of rigid structures made of titanium, carbon or ceramic in a PAD is the limitation on the structural flexibility of the device.

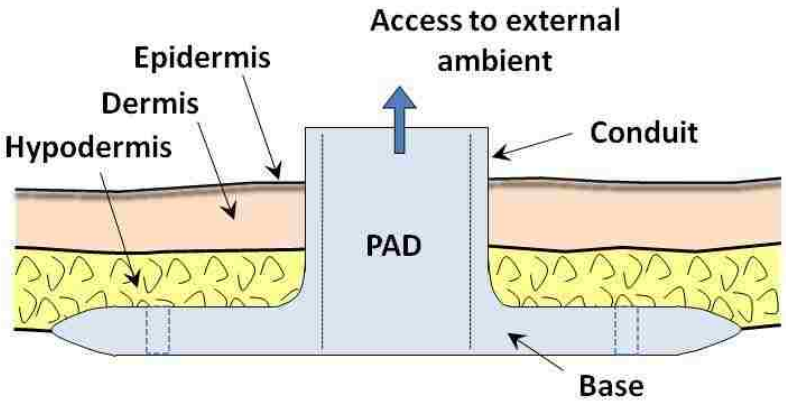

Figure 2.8: Schematic of a typical percutaneous access device (PAD) with an implanted base and a skin-piercing conduit.

There have been reports of some PAD designs based on extensive manual assembly of sub-components or modules. To illustrate, Zimmerman proposed a PAD made by combining several components of different materials like polyester velour, and silicone plastic [179]. Similar PAD designs involving significant assembly of components have been developed by others [180]. In any PAD design, some degree of assembly is acceptable during the fabrication process. However, PADs made by combining or assembling many components are not convenient to realize. There are some PAD designs that require the assembly of some components just prior to implantation in a patient [181]. Such PAD devices are not convenient to

use. If the device fabrication processes are complicated, then design changes may be difficult to implement on the fly. Therefore, PAD designs based on convenient and easy-to-implement fabrication processes will be very useful to researchers.

2.5.2. Bacterial Infection

Infection caused by PADs remains a major problem in the use of such devices [182, 183]. PAD related infections ultimately result in failure of the implant or application [184, 185]. An important cause of infection and device failure is the migration of skin cells. It is the nature of the skin to grow inwards from its opening around the skin-piercing conduit of a PAD. This occurs by the downward migration of the epidermis or epithelial[10] cells from the skin immediately around the conduit, a phenomenon known as epithelial downgrowth. A schematic representation of this phenomenon is shown in Figure 2.9. As a result of this phenomenon, bacteria may be carried into the body from the outside by the migrating skin cells causing infection. The prevention of bacterial infection is one of the most important factors determining the survival of the implanted PAD and by extension, the FES application employing the PAD. The epithelial downgrowth, if unchecked, will continue till the skin cells migrate around the implanted portion of the PAD, encapsulate it and push the PAD out of the body [186]. Therefore, it is essential to restrict the progress of epithelial downgrowth and prevent it from enveloping the device.

For a successful PAD, the skin opening around the percutaneous conduit should be limited to the outer diameter of the conduit, thereby avoiding infection [187-189]. The movement of the PAD due to internal and external forces contributes to the enlargement of the skin opening around the PAD conduit. The enlargement of the skin opening can be prevented by

[10] Epithelial cells: the cells lining the cavities and surfaces of structures throughout the body.

the reduction of relative movement between the implant and skin [190]. This can be achieved by adequately anchoring the implanted base/flange section of the PAD in subcutaneous tissue.

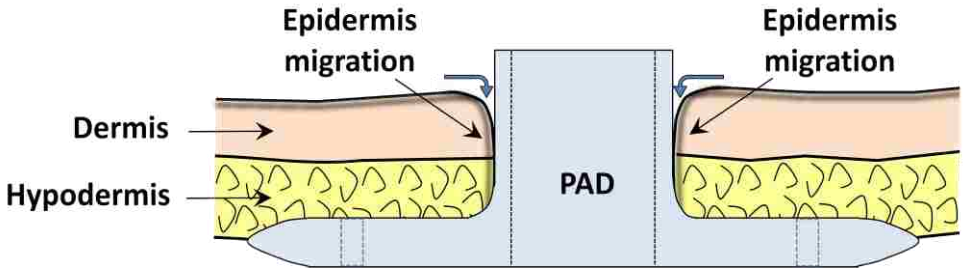

Figure 2.9: Schematic of the downward migration of epidermis or epithelial downgrowth occurring at the skin immediately around the conduit of a PAD.

It is common for PADs to incorporate micro-scale pores and microstructures in the implanted part or the base of the device to encourage connective tissue in-growth to enable stronger anchoring of the implanted base [191]. The anchoring is made possible by the growth of connective tissue into the porous features [192]. Anchoring of the percutaneous access device greatly minimizes or even prevents the motion of the PAD base, caused by external forces acting on the external portion of the device thereby minimizing the risk of bacterial infection. To illustrate, Merritt *et al.* studied infection rates in implants made of porous and dense material in mice [193]. They concluded that the infection rate at the sites with porous implants was less than that with the dense implants, if tissue in-growth occurred in the porous implants prior to exposure to bacteria. Similar results were reported by Kiechel *et al.* [194].

Connective tissue also aids in inhibiting epithelial downgrowth [195]. Winter reported that percutaneous implants made of porous polytetrafluorethylene (PTFE) became invaded by

fibrous tissue which prevented the migration of epidermis[11] alongside the implants and therefore, a stable ring of epidermal tissue was formed near the skin surface [196]. Winter suggested that the epidermal cell movement was halted when they were confronted by healthy collagen bundles incorporated in the pores of the implants. This indicates that the placement of pores need not be limited to the base or flange of the PAD. For example, porosity in the lower conduit structure may help in providing a barrier for the downward migration of epidermal cells. Strategic placement of pores and structures of appropriate dimensions may prevent the downward migration of bacteria-carrying epithelial cells thereby reducing the risk of bacterial infection [196, 197].

2.5.2.1. Porosity

It is essential to ensure that porous materials employed for the growth of connective tissue have proper pore dimensions [198]. There has been some diversity in the reported values of optimal pore dimensions for connective tissue growth in literature. Several studies have reported that for porous meshes and layers, materials with small pore sizes (< 50-80 μm) experience less tissue in-growth than those with larger pore sizes (> 80-100 μm) [199-203]. Other studies have recommended pore sizes of ≥40 μm for connective tissue to be formed on the surface of a percutaneous implant [192]. Others have recommended pore sizes greater than or equal to 80 μm for tissue in-growth [204]. Deviations from these dimensional trends occur when the pore dimensions in the materials are made small enough to compare with cell dimensions in tissue [205, 206]. Winter recommended a 10 μm pore size for PTFE materials [196]. Squier *et al.* recommended a pore size greater than 3 μm in Millipore filter material based on PTFE [207]. In another study by Brauker *et al.*, it was reported that porous mesh membranes of PTFE material,

[11] Epidermis: outermost layer of the skin.

with pore diameters of 0.8 – 8 µm are appropriate for connective tissue growth [208]. Table 2.1 summarizes some porous materials and pore dimensions employed for connective tissue growth in percutaneous access device applications.

Table 2.1: List of some porous materials and optimal pore dimensions for the growth of connective tissue, as recommended in literature.

Reference	Pore size (diameter) recommended, and material used
Hulbert *et al.*, 1972 [200]	100-150 µm, $CaO.Al_2O_3$, $CaO.TiO_2$, $CaO.ZrO_2$
Winter, 1974 [196]	10 µm, Polytetrafluorethylene (PTFE) 40 µm, Hydron sponge
Cestero *et al.*, 1975 [201]	200 µm, Polyethylene 300 µm, Polypropylene
Merritt *et al.*, 1979 [193]	100-200 µm, Vitallium 100 µm, Polyethylene
Kantrowitz *et al.*, 1980 [209]	500 nm, Hytrel polyester elastomer, Copel silicone polycarbonate, Lexan polycarbonate, VITUF polyethylene terephthalate, Mylar
Squier *et al.*, 1981 [207]	≥ 3 µm, Millipore® filter
Bessette *et al.*, 1981 [210]	≥ 3 mm, Silastic silicone elastomer
von Recum, 1984 [192]	≥ 40 µm, Polyester terephthalate (Dacron® velour)
Lundgren *et al.*, 1986 [204]	≥ 80 µm, Titanium coated monofilament polyester fabric
Campbell *et al.*, 1989 [211]	1-3 µm, Versapor® filter (polyvinyl chloride/polyacrylonitrile copolymer)
Poirier *et al.*, 1990 [212]	50-125 µm, Polytetrafluorethylene (PTFE) 400-800 µm, Polyester velour (Dacron velour)
Kantrowitz *et al.*, 1993 [213]	0.5-1 µm, Silicone-polycarbonate Dacron® velour
Brauker *et al.*, 1995 [208]	0.8-8 µm, Polytetrafluorethylene (PTFE)
Sanders *et al.*, 2005 [206]	12-68 µm, Polyurethane (68 µm maximum size tested)

The diversity in pore dimensions may be attributed to the type of material being employed for the percutaneous implant, species of the test animal and other aspects of the application at hand. Therefore, it is impractical to assign the same specific optimal pore dimensions to all material cases for tissue in-growth for a given application. There are several

drawbacks with the technology currently available for the incorporation of micro-scale pores and structures in PAD applications. The following sections describe these drawbacks in detail.

2.5.2.1.1. Commercial Porous Materials

To date, most percutaneous access devices reported with porous structures are based on the attachment of commercially available discrete layers of porous fabric onto the main device [176, 180, 214, 215]. The attachment is usually done by an adhesive [212, 214]. The discrete porous layers are typically not made of the same material as the PAD body. Currently, one of the most commonly used commercially available porous materials is Dacron®, which is a polyester terephthalate material [216].

As seen in Table 2.1, the diversity in the reported values of optimal pore dimension points to a need for tailor-made porosity with specific range of dimensions of pores for a given application. In applications calling for tailor-made porosity in a specific material, it may be inconvenient to employ commercially available porous layers due to possible unavailability of material meeting the desired specifications. For example, in a study by Bessette *et al.*, silicone implants with pores ranging up to 6 mm were implanted in monkeys [210]. To the best of our knowledge, there are no current commercial sources for porous medical grade silicone layers. In general, there is a need for greater control on dimensions of porosity in the materials employed for PAD applications. This can be made feasible if methodologies are developed to create porosity of specific desired dimensions in a given material.

2.5.2.1.2. Tailor-made Porous Materials and Methods

Currently available PAD designs that incorporate tailor-made porous structures employ methods like nuclear bombardment and other complicated processes to make such structures

[181, 217]. Kantrowitz *et al.* reported a PAD design which incorporated porous surfaces where the pores or cavities were formed by nuclear bombardment on a polycarbonate surface by a Californium-252 spontaneous fission source in a vacuum chamber, followed by a chemical etching process in a sodium hydroxide solution [181]. Kojima *et al.* reported the use of microscopic carbon fibers to create porous surfaces, especially on the base of their PAD [174]. The carbon fibers were commercially procured or alternately, made by chemical vapor deposition. Subsequently, the base of the PAD was treated with oxygen plasma to improve the biocompatibility of the carbon coating. Shimotoso *et al.* reported porous ceramic layers made by laminating sheets of perforated ceramic sheets, so that the pores communicated with each other [178]. Subsequently, a sintering process was performed at more than 1300 ^{0}C.

Manual methods are some of the most common techniques employed to date for pore formation in different materials for PADs. Lee *et al.* reported a PAD design which incorporated a polymeric base perforated with holes to facilitate growth of connective tissue [172]. The fabrication of these holes was by a mechanical process requiring a rack and pinion tool. The authors suggested that alternate methods may be employed to makes pores including punching, shear-punching, drilling, piercing and machining. The main drawback of these pore formation methods is that they are labor intensive and may not easily form micro-scale dimension pores. Similar methods reported for making Silastic medical grade silicone rubber layers porous, included employing a leather punch to manually make perforations in silicone layers [210]. This method is tedious and does not easily allow for the formation of micro-scale dimension pores.

In another report, three dimensional porous structures were made by stacking thin sheets of silicone rubber, for PAD applications [217]. Each individual sheet had pores in the desired diameter and was patterned with protrusions, made by molding the silicone rubber over a master

mold template made by photolithography or electron discharge micromachining. The protrusions on the stacked sheets created the effect of interconnected pores. Similar development of three dimensional porous structures by stacking microfabricated layers of polymer have been reported by others [218]. The main drawback of these types of methods is the extensive assembly required after the fabrication of individual patterned silicone rubber sheets. Brown *et al.* reported a porous metal mesh for tissue in-growth [219]. The porous metal mesh was made by subjecting a titanium metal sheet to perforation, contouring and expansion by drawing it in two directions to open pores. The use of metal meshes may place restrictions on the structural flexibility of the device, especially if the device body is polymeric. Metal meshes like these have to be manually attached to a PAD by means of an adhesive. It would be beneficial to develop simple methods to form micro-scale pores and structures with any desired dimensions in biocompatible materials to facilitate the growth of connective tissue.

2.5.2.1.3. Role of Micro-structured Surfaces

There have been reports that micro-machined surfaces may be beneficial in preventing the downward growth of epithelial cells, and for directed cell orientation and migration [220, 221]. Earlier efforts on micro-machined texturing of percutaneous implants involved the usage of micro-machined epoxy substrates. Chehroudi *et al.* placed grooved and smooth epoxy percutaneous implants in the parietal area of rats [222]. They observed that after ten days of implantation, the epidermis migrated downward to the subcutaneous flange in the smooth implants, while in the grooved implants the epithelial migration was inhibited. In another report showing similar results, percutaneous implant surfaces made of micromolded epoxy were sputter-coated with 50 nm of titanium [223]. The implants had micro-scale groove patterns, with the grooves separated by about 20 µm. These reports followed previous studies that showed that

inflammatory cells behaved distinctly different at smooth and rough surfaces [224, 225]. Inflammatory cells play an important role in the response of tissue to implants [226, 227]. The main drawback of micro-machined epoxy substrates is that epoxy resin can offer limited biocompatibility, at best. It is therefore important to explore the micro-machining of other materials that offer high biocompatibility.

While titanium offers high biocompatibility, it is useful to develop micro-machined polymeric materials to provide greater structural flexibility to the device. However, there are several challenges in the micro-scale patterning of proven biocompatible materials. Primary among them is the incompatibility of such biocompatible materials with standard micro-fabrication processes. Conventionally used materials (e.g. silicon, photoresist) offering excellent micro-fabrication ability may be limited in terms of biocompatibility. Material and structural properties of silicon make it unsuitable for many biological applications. There have been no studies conducted on the long-term usage and stability of photoresist materials in physiological ambient. Therefore, there is a need for developing methods to pattern highly biocompatible materials that are proven for implantable applications and for employing them to realize more efficacious PADs.

2.5.3. Action of Mechanical Forces

The action of forces on the PAD structure results in shearing or tearing at the skin-PAD interface [228]. Forces acting externally on the skin-piercing conduit of a typical PAD are translated to the implanted base of the PAD, causing its movement [209]. Any movement of the implanted base prevents the PAD from being adequately anchored to the subcutaneous tissue and may easily translate to infection, and subsequent device failure. Forces on the conduit also create its motion, resulting in tearing of the surrounding skin [209]. The tearing of skin around the PAD

conduit provides an enlarged opening for bacteria to enter the body from the external ambient (Figure 2.10). Therefore, the reduction of the relative movement between the PAD and skin increases the chances of a successful percutaneous device [229, 230].

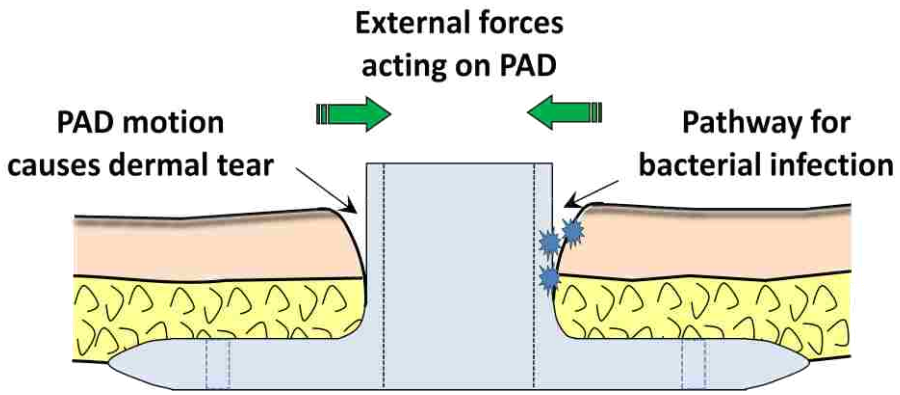

Figure 2.10: Schematic of the action of external forces on a PAD conduit, resulting in skin tearing around the conduit. The enlarged opening in the skin enables bacteria to enter the body from outside.

There is a need to include specific structures and features in a PAD design that can help in reducing the effects of forces incident on the PAD in its normal operational ambient. Several PAD devices reported previously were based on rigid structures, without features to enable the reduction of stress caused by incident forces [231]. There have been only a few reports on devices incorporating features to minimize the mechanical stresses at the PAD-skin interface [232-235]. These reports either deal with highly specific applications or do not adequately address the reduction of stress due to incident forces.

2.5.3.1. Bone Anchoring to Reduce Stresses

Some researchers have reported PADs anchored in the bones of test animals to reduce the effect of incident forces. It was reported that direct and indirect bone-anchoring favored the longevity of percutaneous implants, by minimizing the mechanical stresses at the interface

between the PAD implant and the skin [235-237]. Though the anchoring of a PAD to subcutaneous bone is a simple and effective method to minimize interfacial mechanical stress, it is more appropriate for certain locations of the body like the head, and not generally suitable for areas of the body where the skin moves relative to the underlying organs [238].

In cases where no underlying bone is available for PAD anchoring, the bone-based anchoring methods cannot be used. For example, peritoneal dialysis requires the placement of a percutaneous implant for a catheter in the highly mobile tissue of the abdominal wall. In such situations, PAD devices have to be anchored in soft-tissue.

2.5.3.2. PADs with Features for Stress Reduction

To date, there have been only a few reports on soft-tissue anchored PAD designs with features that can reduce stress [239]. In one report, Kantrowitz *et al.* described a PAD whose skin-piercing conduit was made of a soft, flexible, biocompatible material such as silicone [213]. The authors suggested that the use of a soft, flexible material would allow the conduit structure to absorb the forces acting externally on the PAD. Some others have also advocated the use of a flexible silicone conduit in a PAD as a method for stress relief [240]. The use of a flexible material like silicone for the PAD conduit may not be sufficient to absorb the incident forces. While silicone materials allow a degree of flexibility in a member, there is still a need for additional methods to reduce the effect of forces incident on the PAD conduit.

Grosse-Siestrup *et al.* reported a PAD with an air-filled elastic ring incorporated around the skin piercing conduit, located between the conduit and the neighboring skin [232]. The authors suggested that the air-filled ring may act as a low modulus area and reduce stresses caused by movement of the conduit. A major drawback of this design is that the stress relieving feature (the air-filled ring) is placed at the junction of the PAD conduit and the surrounding skin.

This type of placement may allow for only a limited degree of movement of the conduit without damaging the interface formed by the conduit with the neighboring skin. Therefore, other types of design features may be required for more effective stress relief.

Hastings *et al.* reported a PAD with a design feature aimed at relieving stress [233]. In their design, the skin piercing conduit was attached to and placed in a cylinder at the PAD-skin interface. A gap was incorporated between the conduit and the outer cylinder. It was expected that this gap would serve as a stress reduction area, permitting the axial movement of the conduit and compensating for axial forces. This design is applicable mainly for the reduction of axial forces, and does not address the reduction of stresses from lateral and torsional forces. In this PAD design, the subcutaneous base or flange structure has been omitted. A base structure would have provided additional stability and stress relief.

Among other reports, Becker *et al.* described a PAD design for introducing a catheter into the body [241]. Their device incorporated an external bend in the skin piercing conduit. The authors suggested that the external bend reduced stress on the PAD–skin interface because no bending moment was generated when a dressing was applied to the PAD implant location. A similar PAD design was employed by Holmberg *et al.* in their experiments with total artificial heart implants [186]. Their device consisted of a skin piercing conduit which was bent at an angle to the plane of the skin.

The main drawback with both these designs is that while an external bend in the PAD conduit may serve a very specific purpose, it is not sufficient to address the reduction of forces generally acting on the PAD in its regular operational conditions. For example, the PAD developed by Becker *et al.* deals with a specific purpose i.e. the reduction or prevention of bending moments while applying dressings at the PAD implant location [241]. An improvement

to these designs is one reported by Kojima *et al.,* whose PAD had an elastic spring-like component to aid in stress relief [174]. This feature was located under the skin inside the body in order to address the reduction of in-vivo stresses acting on the PAD. However, there was no feature in the design to address external forces acting on the conduit which are much more severe than typical in-vivo forces.

2.5.4. Conclusions and Summary of Problems with Current PAD Designs

The preceding sections have detailed the problem areas in existing PAD technology and have highlighted the need for innovation to address these problems. Specifically, there is a need to address the following aspects:

1. Development of fabrication technology for PADs based on convenient and easy-to-implement processes involving proven bio-implantable materials.
2. Development of methodologies to create micro-porous and micro-patterned layers of highly biocompatible materials such as medical grade silicone, for applications in connective tissue growth and prevention of epithelial downgrowth, among others.
3. Novel PAD designs with features aimed at reducing forces transferred to the implanted portion of a typical PAD.

CHAPTER 3: RESEARCH GOALS

3.1. Nerve Cuff Electrode Technology

Considering the problem areas detailed in the previous chapter in the sections pertaining to the present cuff electrode technology for stimulating nerves and nerve fibers, the present dissertation describes development of novel electrode design features aimed at addressing the following aspects:

1. Development of a cuff electrode for micro-scale diameter nerve tissues.
2. Solving the problem of securing the opening of a cuff electrode, after its implantation on a target nerve tissue.
3. Improving the robustness of cuff electrodes, especially at the cuff-electrode wire interface.

3.2. Gastric Pacing Electrode Technology

The present dissertation research aims at addressing the following aspects in gastric pacing electrode technology:

1. Development of miniaturized gastric stimulation electrodes based on incorporation of metal leads on flexible substrates, aimed at alleviating the lead penetration problem during implantation.
2. Design feature that allows the electrode to transform from an initial more rigid state to a more flexible state.
3. Features that enable the direct anchoring of the pacing electrode to the gastric tissue, at more than one location of the electrode and preferably employing mechanisms that avoid tissue penetrating anchors.

4. Other features and structures integrated on the electrode, capable of promoting the growth of connective tissue, aimed at minimizing electrode displacement after implantation i.e. enhancing the anchoring of the electrode to the gastric tissue. The features may include microstructures integrated on the electrodes, capable of promoting the growth of connective tissue, aimed at minimizing electrode displacement after implantation.

3.3. Modeling the Tissue-electrode Interface

To avoid potential tissue damage caused by the passage of an electrical signal during stimulation, an understanding of the electrical effects due to the electrode leads is useful. Therefore, a part of the proposed dissertation research aims at addressing:

1. Electrical modeling of a nerve-electrode interface for the micro-cuff electrode being developed in this research. Towards this, an equivalent electrical circuit representing the nerve-electrode interface is developed and modeled using the PSPICE electronic circuit simulation software.
2. The study of the response of the equivalent circuit model to different types of electrical stimulus signal protocols.

3.4. Percutaneous Access Device (PAD) Technology

This dissertation describes several useful innovations in the development of PAD technology for FES applications. Specifically, this dissertation addresses the following aspects:

1. Development of fabrication technology for PADs based on convenient and easy-to-implement processes involving proven bio-implantable materials.

2. Novel PAD design with features aimed at reducing the forces transferred to the implanted portion of a typical PAD.
3. Development of methodologies to create micro-porous and micro-patterned layers of highly biocompatible materials like medical grade silicone for applications in connective tissue growth and prevention of epithelial downgrowth. The developed layers may be free-standing to function as add-on structures or inbuilt into percutaneous access devices during their fabrication. The developed processes should enable pore dimensions from the sub-micron range to several hundred microns.

CHAPTER 4: ELECTRODE TECHNOLOGY DEVELOPMENT

4.1. Nerve Cuff Electrode Development

4.1.1. Introduction

The importance of a cuff electrode design in the functional electrical stimulation (FES) of nerves and nerve fibers has been described in Chapter 2. There are several problems involved in the use of the cuff design that have not been addressed by currently available cuff electrodes. These problems involve the closure of a cuff electrode's opening after implantation on a nerve, and securing of the cuff electrode to a target nerve. Other drawbacks with existing technology include the lack of available designs for micro-scale dimension nerves, and limited robustness of the cuff-electrode wire interface.

A cuff electrode design, called the clip-on micro-cuff electrode (Figure 4.1), is developed here to address the challenges present in currently available cuff electrodes [242, 243]. This developed cuff design can be used for stimulation of nerves and nerve fibers with diameters in the micro-scale or above, in humans and animals. The developed cuff electrode can also be extended to applications involving recording of electrical signals from nerves and nerve fibers. The proposed cuff device involves metal wire or foil electrodes incorporated in a cuff made of Silastic, a commercially available medical grade silicone elastomer (Figure 4.1). The cuff is in a naturally closed position. A pinch-hinge type structure is incorporated in the cuff electrode by which the user can conveniently open and close the cuff to enclose the tissue being stimulated. Once implanted, the cuff will stay on the nerve due to its naturally closed position, till the pinch hinge is used to open it [242, 243]. The clip-on design feature is expected to enhance the general ease of handling such cuff devices. The electrical connection wires leading away from the main

electrodes are enclosed in an insulation that is embedded in the device body. This provides strength to the interface between the electrode wire and cuff body.

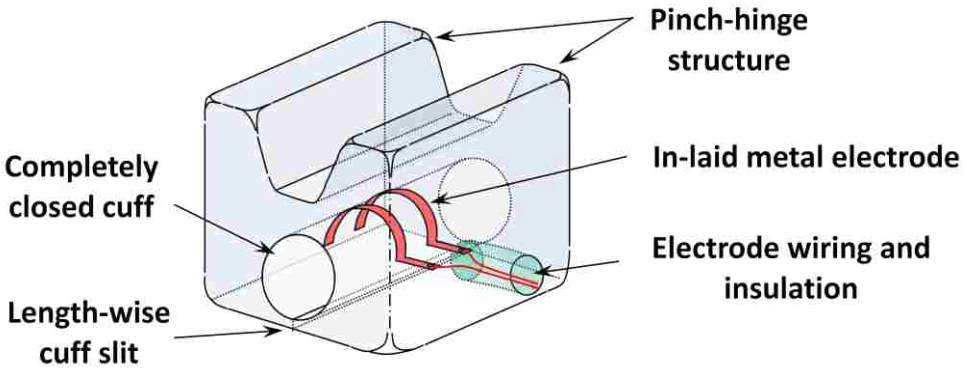

Figure 4.1: Schematic representation of the developed clip-on cuff electrode that ensures complete closure of the cuff in its natural state. A pinch-hinge feature allows for easy opening and closing of the cuff. By means of the pinch-hinge, the device can be 'clipped-on' to a target nerve.

The developed cuff electrode is designed to address the following factors:

1. The problem of securing the cuff opening after implantation on a target nerve tissue.
2. The need for a cuff electrode for micro-scale diameter nerve tissue.
3. Complete closure of the cuff.
4. Improving the robustness of cuff type electrodes, especially at the cuff-electrode wire interface.

The developed clip-on cuff electrode can also be used for larger diameter nerves and nerve fibers. The fabrication of the device is based on processes that include simple processing technology, and molding of silicone elastomer. The details of the fabrication processes and some test results on the developed clip-on micro-cuff electrode are discussed in the following sections.

4.1.2. Materials and Methods

4.1.2.1. Fabrication with a Molding Step

To realize the clip-on micro-cuff device shown in Figure 4.1, the following fabrication procedure was employed. In the first step, a flat sheet of plastic was used as the base substrate and was cleaned with de-ionized (DI) water and air dried (Figure 4.2A). A layer of polyvinyl alcohol (PVA) was spin-coated on the substrate to function as a mold release layer (Figure 4.2B). An aqueous solution of PVA (1:8 ratio by weight of PVA dissolved in DI water) was used for this purpose. After spin-coating, the mold release layer was allowed to solidify at room temperature for 8 hrs.

Subsequently, a thin layer of Silastic (medical grade silicone) was spin-coated on the solid mold release layer (Figure 4.2C). This silicone layer was cured in a convection oven at 60 ^{0}C for 3 hrs. In the next step, a metal wire of a known diameter was coated with a thin layer of the mold release chemical, as shown in Figure 4.2D. This was done by dip-coating the wire in an aqueous solution of PVA (1:8 ratio by weight of PVA to DI water) for two minutes. The wet mold release layer was solidified at room temperature for 8 hrs.

The coated metal wire was placed in conformal contact with the thin silicone layer on the substrate. Two metal foil electrodes were placed in contact with approximately half-the circumference of the metal wire (Figure 4.2E). These metal foils were previously cut to size from commercially available 25 µm thick stainless steel foil and spot-welded to long stainless steel wires, which served as interconnecting wires from the implanted electrode to other electronic equipment. The stainless steel interconnecting wires were insulated from the surroundings by small diameter tubing made of medical grade silicone. In the next step, a thick layer of uncured silicone liquid was poured over the wire-foil assembly and cured at 60 ^{0}C for 3 hrs (Figure 4.2F).

As this thick layer was cured, it bonded permanently with the underlying thin silicone layer. Subsequently, the entire cured silicone structure was released from the substrate by dissolving the mold release layer on the substrate. The free-standing, cured silicone structure with the embedded wire-foil assembly is shown in Figure 4.2G.

In the next step, a plastic material was patterned by machining. The pattern was complementary to the pinch-hinge structure required for the clip-on electrode. This patterned plastic layer served as a master mold template for molding the silicone pinch-hinge structure. The mold was coated with mold release chemical, using the coating process described earlier. Subsequently, uncured silicone liquid was poured over the mold and allowed to settle into the features (Figure 4.3A). Subsequently, the free-standing cured silicone structure with the embedded wire-foil assembly was inverted and placed on the mold coated with uncured silicone, as shown in Figure 4.3B.

The entire set-up was thermally cured, so that the uncured silicone permanently bonded with the cured silicone. The cured structure was then released from the mold to yield a pinch-hinge feature added on to the existing silicone structure with the embedded wire-foil assembly (Figure 4.3C).

At this stage of the fabrication process, the hollow cuff and its opening were still needed to be defined. The cuff opening was defined by manually making a slit/cut on the cured structure, as shown in Figure 4.3D. Subsequently, the structure was placed in an ultrasonic bath of water. The cuff opening allowed water to enter and dissolve the mold release coating on the wire. This allowed the embedded cylindrical wire piece to be removed from the cured silicone, leaving behind a hollow cuff structure with a length-wise slit. The obtained cuff structure was in a naturally closed position. Depressing the pinch-hinge structure allowed the cuff to be opened. To

obtain the final device shown in Figure 4.1, the extra silicone was trimmed from the cured structure.

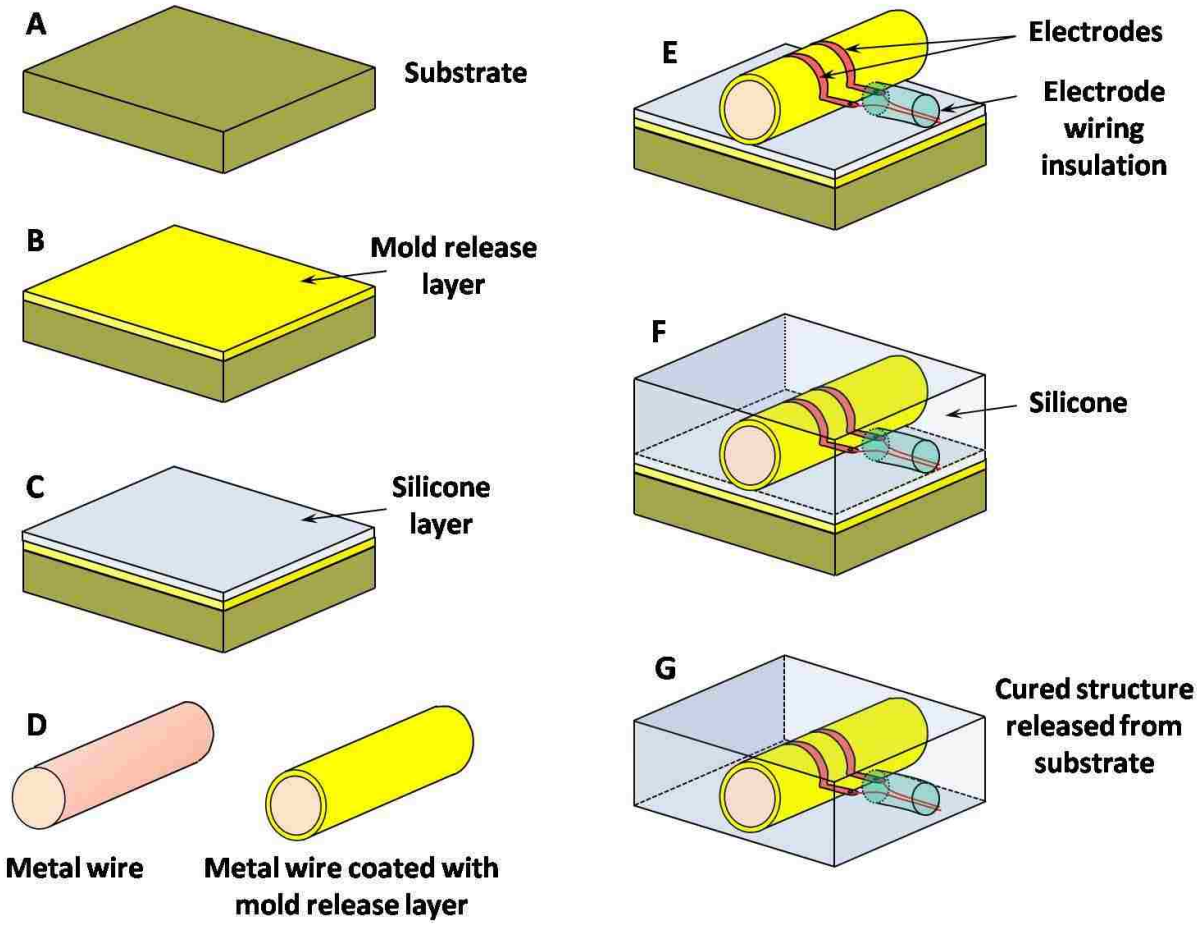

Figure 4.2: Schematic of the initial steps involved in the cuff electrode fabrication process.

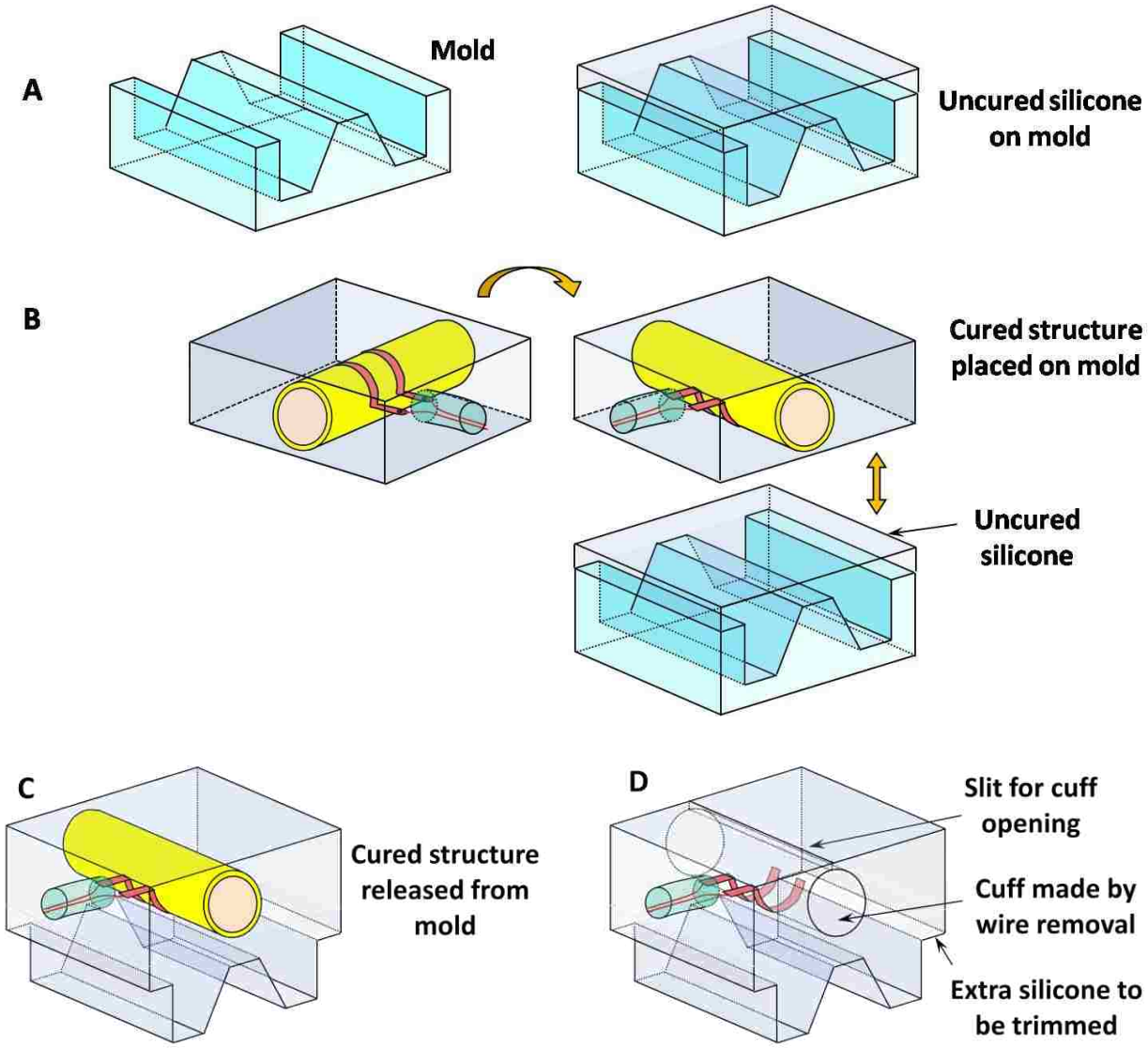

Figure 4.3: Schematic of the remaining steps involved in the cuff electrode fabrication process.

4.1.2.2. Layer-by-layer Fabrication

An alternate fabrication method was investigated based on a layer-by-layer approach. The clip-on cuff electrode design shown in Figure 4.4 was realized by this method.

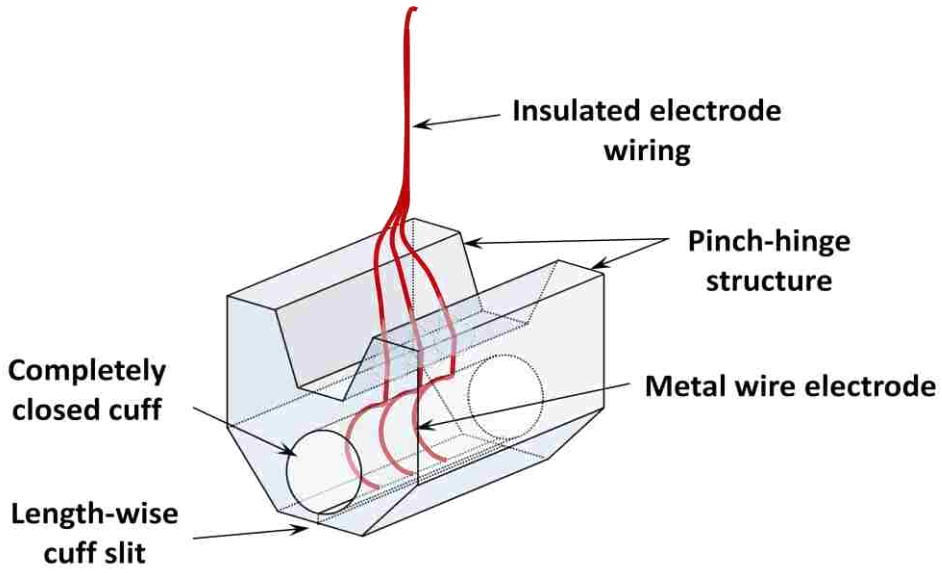

Figure 4.4: Schematic diagram of an embodiment of the clip-on micro-cuff electrode made by a layer-by-layer fabrication process.

In the first step, a flat sheet of plastic to be used as the base substrate was cleaned with DI water and air dried. A layer of PVA was spin-coated on the substrate to function as a mold release layer (Figure 4.5A). An aqueous solution of PVA (1:8 PVA to DI water ratio by weight) was used for this purpose. After spin-coating, the mold release layer was allowed to solidify at room temperature for 8 hrs.

A thin layer of medical grade silicone (Silastic) pre-polymer was spin-coated on the solid mold release layer (Figure 4.5B). This layer was cured in a convection oven at 60 ^{0}C for 3 hrs. In the next step, a metal wire of a known diameter was dip-coated with a thin layer of PVA (Figure 4.5C). The wet PVA layer was solidified at room temperature for 8 hrs. The coated metal wire was placed in conformal contact with the cured Silastic silicone layer on the substrate (Figure 4.5D). In the next step, a thicker layer of uncured silicone liquid was poured over the wire and

cured thermally at 60 ^{0}C for 3 hrs (Figure 4.5E). As this thicker layer was cured, it bonded permanently with the underlying thin silicone layer. Subsequently, the cured silicone structure was released from the substrate by dissolving the mold release coating on the substrate in an ultrasonic bath of water. Further ultrasonic treatment in a bath of water dissolved the mold release coating on the wire, allowing for the wire to be easily pulled out from the silicone (Figure 4.5F).

By means of a blade, the free-standing cured Silastic structure with the hollow cylinder was manually trimmed at the sides to the desired lateral dimensions of the cuff. One side of the structure was manually cut to remove some silicone material, to form a pinch-hinge feature (Figure 4.5G). On the other side of the structure, the edges were trimmed (Figure 4.5H). This served to reduce the overall size and mass of the device. In the next step, the cuff opening was defined by manually making a slit on the cured structure, as shown in Figure 4.5I.

At this stage of the fabrication process, the main body of the device was obtained with the cuff structure in a naturally closed position. Depressing the pinch-hinge structure allowed the cuff to be opened. To complete the cuff electrode device, electrodes needed to be incorporated in the cuff. A 12 inch segment of electrode wire (multi-strand stainless steel, with Teflon insulation) was stripped of its Teflon coating at one end to expose a length of bare wire. The purpose of this particular length of wire (50 µm diameter) was to function as an electrode lead inside the cylindrical space of the cuff. The cuff body (Figure 4.6A) resulting from the earlier fabrication steps was slightly opened by holding the arms of the pinch-hinge and applying a squeezing force (Figure 4.6B). A syringe needle (26½ gauge) was employed to pierce the cuff body from the pinch-hinge side (Figure 4.6C). The needle was allowed to exit from the cuff side, through the open cuff. The insulated end of the electrode wire was inserted into the needle from

the cuff side (Figure 4.6D). When the wire appeared at the other side of the needle, it was held by tweezers and gently pulled through till a few cm of the wire came out (Figure 4.6E).

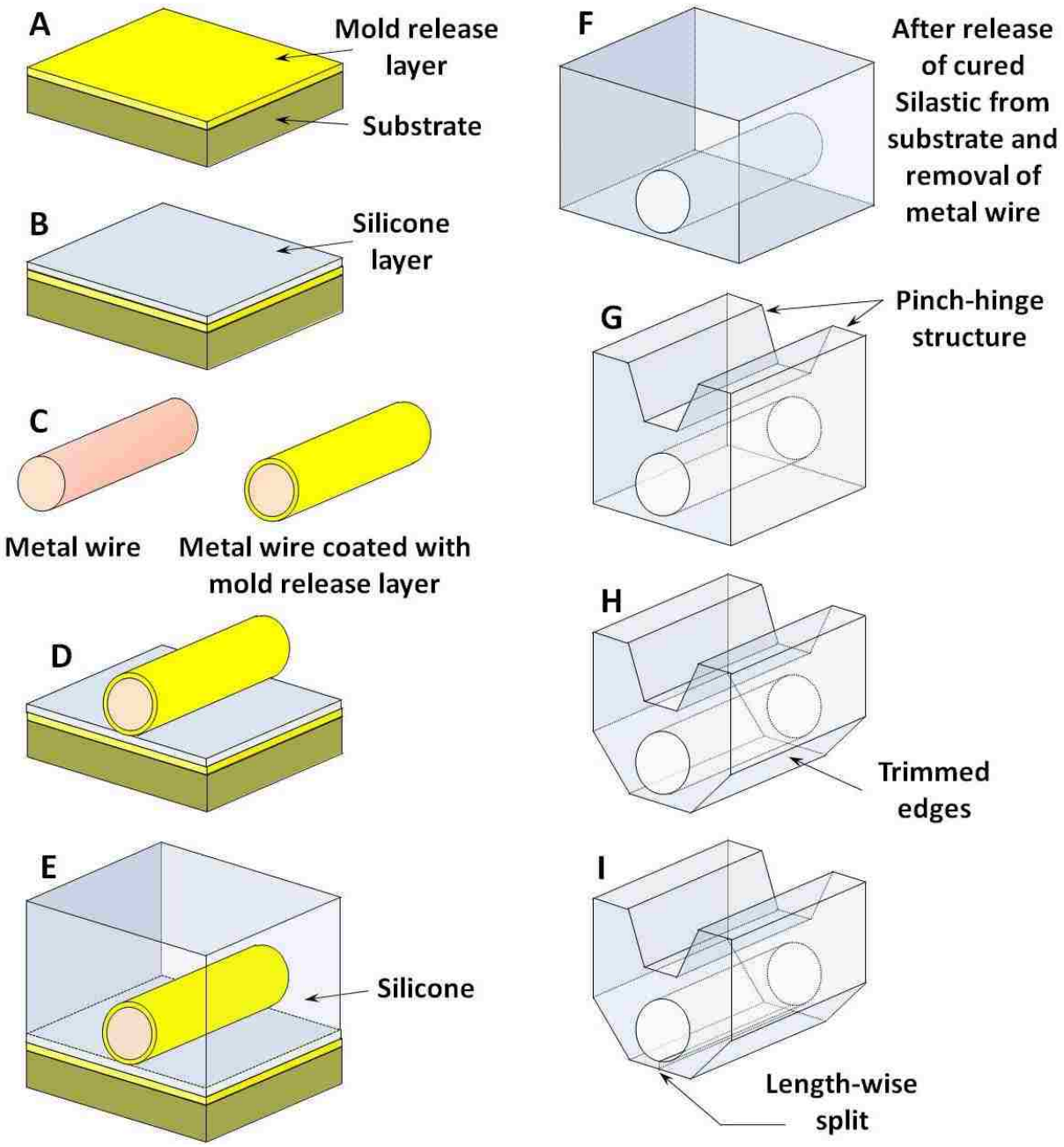

Figure 4.5: Schematic of the initial steps involved in the cuff fabrication process.

At this juncture, the syringe needle was disengaged from the cuff body leaving the wire inside the cuff body. This was done by holding the electrode wire at the cuff opening side and the cuff body with one hand, and gently pulling out the needle with a twisting motion (Figure 4.6F). As the needle was pulled out, the cuff body material collapsed around the wire, holding it tightly. In the next step, the wire was pulled further from the pinch-hinge side till only the un-insulated part of wire was inside the cylindrical opening (Figure 4.6G).

The entire process was repeated to introduce two more electrode leads (Figure 4.6H). At this juncture, there were three electrode leads in the open space of the cuff cylinder (Figure 4.6H). These electrode leads need to be bent against the cuff inner walls, so that they lie along part of the cuff cylinder's circumference. Therefore, the next step involved opening the cuff to enclose a pin and rotating the pin to bend the electrode leads (Figure 4.6I). This operation shaped the electrode leads, so that they lay against the cuff inner wall (Figure 4.6I). Subsequently, the electrode wire-cuff body interface or the point of exit of each electrode wire was reinforced by some silicone (Figure 4.6J).

4.1.2.3. Conventional Cuff Electrode Fabrication

To obtain a perspective on the advantages of the clip-on micro-cuff electrodes, it was pertinent to compare them to conventional cuff electrodes. Towards this, conventional cuff electrodes based on cylindrical tubing were fabricated along the lines of fabrication processes reported for such cuff devices [83].

A commercially available silicone rubber cylindrical tubing of appropriate inner diameter was chosen. With a razor blade, a segment of desired length of the silicone tubing was slit open along its full length. Two holes were defined on the cylinder by means of a hypodermic syringe needle, and metal wires were inserted into the cuff (Figure 4.7A).

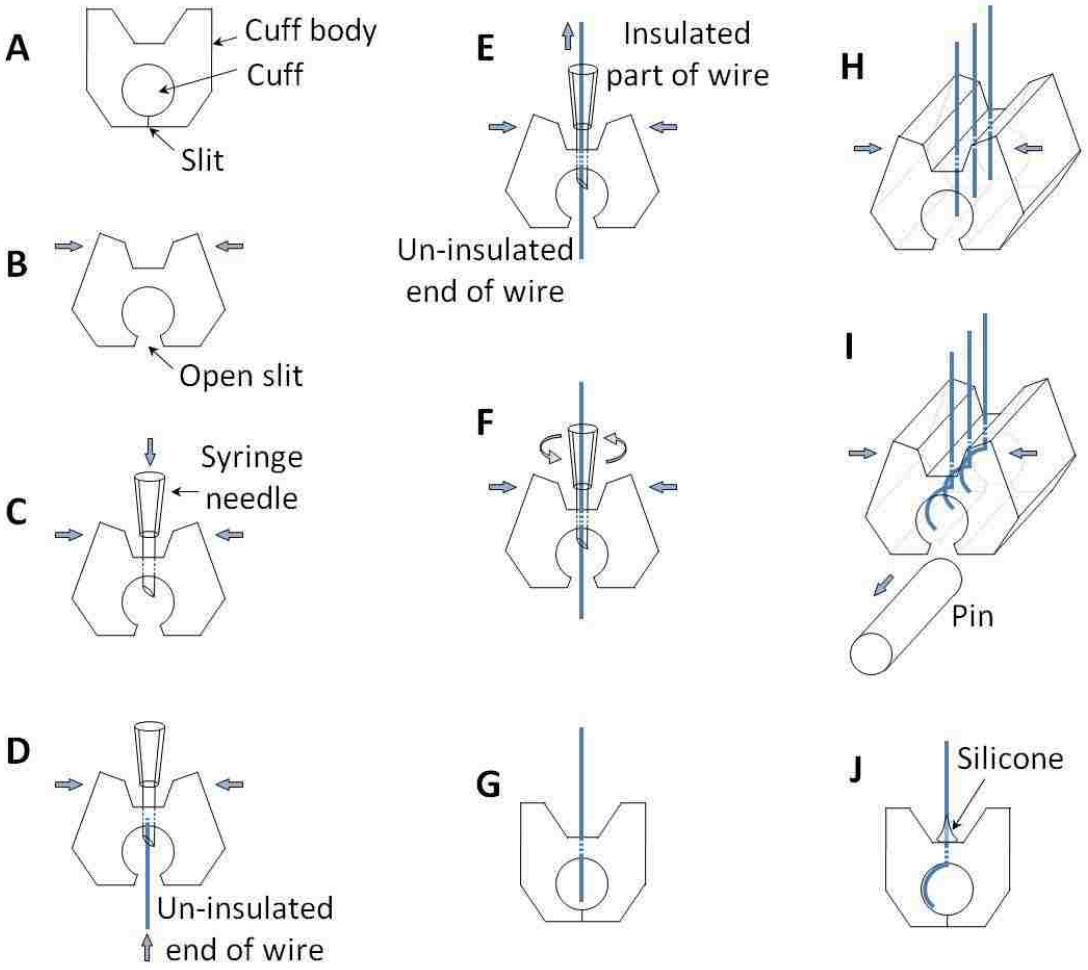

Figure 4.6: Schematic of the remaining steps in the cuff fabrication process. The figures are not drawn to scale.

The wire sections inserted into the cuff were un-insulated, whereas the sections of the wires exiting the cuff were insulated. Using a pin, the wire sections inside the cuff were shaped to form hooks or lie against part of the inner circumference of the cuff (Figure 4.7A). The exit point of the wires from the cuff wall was reinforced by applying epoxy at the interface of the wires and the cuff exterior (Figures 4.7A and 4.7B).

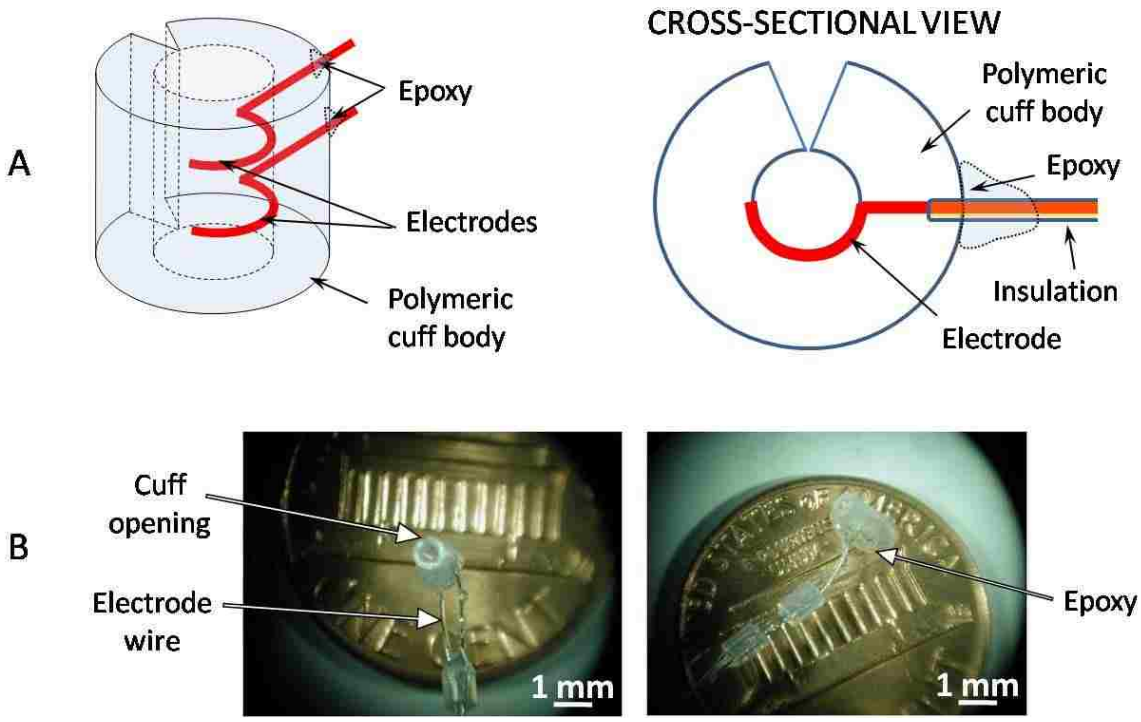

Figure 4.7: (A) Schematic diagrams of a conventional cuff electrode based on a cylindrical tubing segment; (B) Stereo microscope images of a conventional cuff electrode resulting from the described fabrication process.

4.1.3. Results and Discussion

4.1.3.1. Device Fabrication

A version of the clip-on micro-cuff electrode, shown in Figure 4.1, was successfully fabricated using the process detailed in section 4.1.2.1. Figure 4.8A shows stereo microscope images of the fabricated device. The micro-cuff electrode shown in Figure 4.8B has cuff dimensions of ~300 µm inner diameter and a cuff length of 2 mm as seen in Figure 4.8C. This device can be used for nerves with diameters in the range 200-250 µm and lengths of 3-4 mm, like the celiac ganglia nerve branches in rodents (Appendix B). Metal foils were incorporated inside the cuff to function as electrode leads (Figure 4.8C). The spot-welded joint between the

metal foils and the electrical wires was embedded in the silicone material of the body. Additionally, the electrical wires were enclosed in medical grade silicone tubing which was partially embedded in the silicone body of the cuff (Figure 4.8D). This was designed to provide for a robust interface between the cuff and the electrical wiring. This fabrication process can be used to make cuffs with any specific inner diameter in the range 100 µm to >1mm. The dimensions of the pinch hinge and the overall device can be reduced. The total weight of the micro-cuff device including the electrode wires for the version made by this method was in the range of 0.2-0.3 gm.

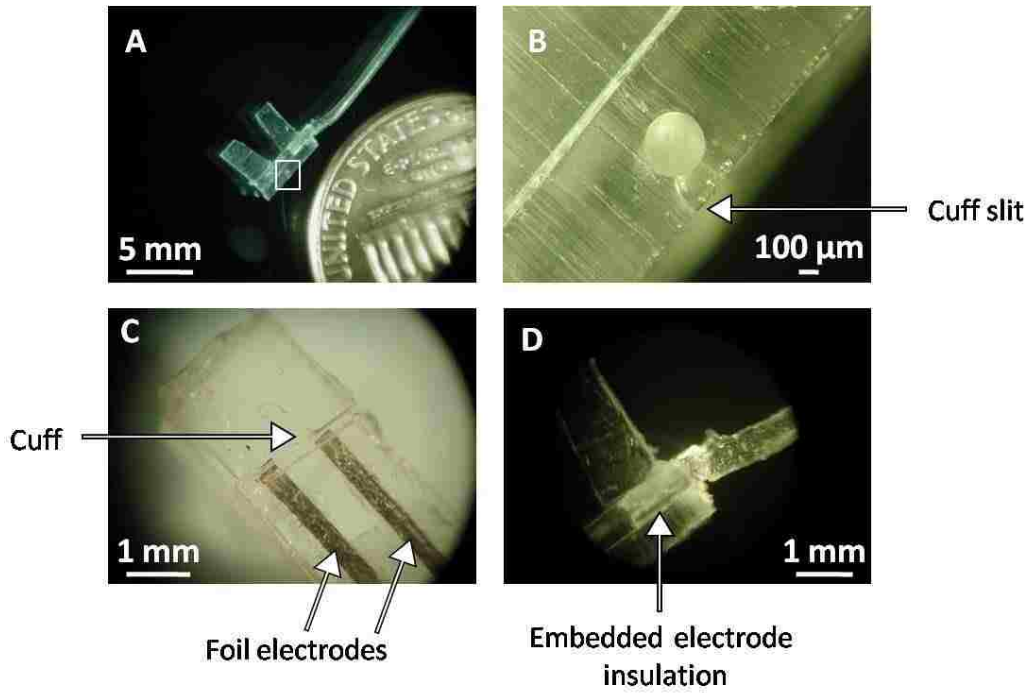

Figure 4.8: Stereo microscope images showing a version of the clip-on micro-cuff electrode made by the fabrication process with a molding step, showing, (A) the cuff edges in a naturally closed position; (B) close-up view of the cuff cross-section showing the naturally closed cuff edges, highlighted in the previous image; (C) a perspective of the cuff showing the incorporated metal foil electrodes; (D) electrode insulation embedded into the main body of device.

Another version of the clip-on micro-cuff electrode device was made by the layer-by-layer fabrication method described in section 4.1.2.2. Devices with cuff inner diameters of approximately 400 μm and 800 μm were made (Figure 4.9). Bare metal wires were incorporated inside the cuff and insulated portions of wires exited from the cuff body. The exit point of the wires was reinforced by applying liquid silicone pre-polymer and curing it thermally (Figure 4.9B). This provided the effect of embedding these wires in the cuff body.

The use of the same type of silicone material for the device body and the wire reinforcement is designed to provide for a robust interface between the cuff body and electrical wiring. A maximum of three electrode wires were incorporated in the present devices. More number of electrodes can be installed, if required. The total weight of the micro-cuff device including the electrode wires for the version made by the layer by layer method was in the range of 0.2-0.3 gm.

Silastic silicone elastomer has been considered an appropriate material for human implantation primarily because of its relative immunological inertness [244-246]. For applications such as the developed clip-on micro-cuff electrode, the choice of Silastic as the body material offers advantages such as molding ability, and relative ease of fabrication. For both versions of the clip-on micro-cuff device, efforts are on-going to reduce the overall mass of the device. However, it must be pointed out that there is a limitation on how much mass can be reduced. Due to the presence of the clip-on feature, it is not feasible to expect a mass comparable to conventional cuff electrodes that are built on light-weight silicone rubber tubing. The pinch-hinge feature contributes to the mass of the device.

In addition to the two fabrication methods described here, a molding method, described in Appendix C, was investigated to fabricate a version of the developed clip-on micro-cuff

electrode design. In summary, our experimental observations indicate the feasibility of realizing the clip-on micro-cuff device by a molding process.

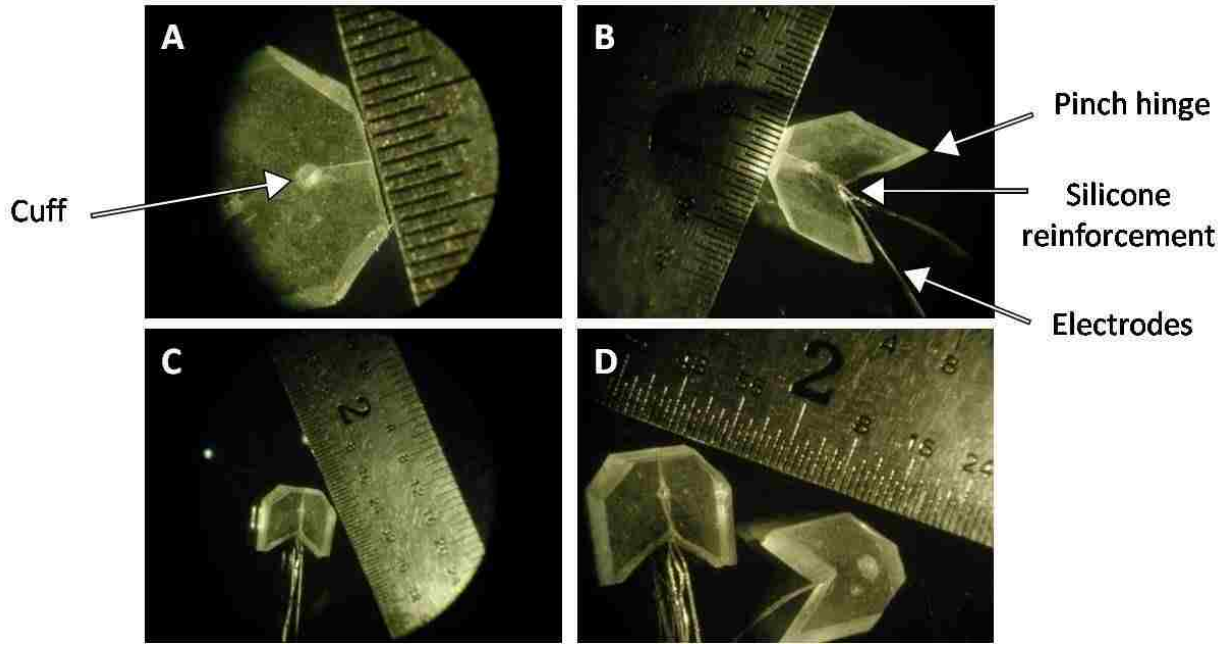

Figure 4.9: Stereo microscope images of a version of the clip-on micro-cuff electrode made by the layer-by-layer process. The device is placed adjacent to a 1/64 inch scale ruler.

4.1.3.2. Device Characterization

The clip-on micro-cuff electrodes resulting from the fabrication method in section 4.1.2.1 and the layer-by-layer process were tested for the electrical connectivity of electrode leads, the efficacy of the closed cuff, and the general durability of the cuff-electrode wire interface. The results are discussed in the ensuing sections. The devices fabricated with a molding step in section 4.1.2.1 having effective electrode foil areas in the range 0.3–0.4 mm^2 and weighing between 0.2-0.3 gm were tested. The layer-by-layer devices tested had effective electrode wire areas in the range 0.2-0.3 mm^2 and weighed in the range 0.2-0.3 gm. The total surface area of the

former devices was in the range 45-60 mm^2. The total surface area of the layer-by-layer devices was in the range 55-70 mm^2.

4.1.3.2.1. Electrical Testing

To check for electrical connectivity, the electrical impedance between the electrode leads of the developed micro-cuff devices was measured in air ambient and in potassium chloride (KCl) solution at room temperature. The impedance measurement in solution was done by immersing the cuff electrode into a glass beaker with 100 ml of 2M KCl solution and measuring impedance between the electrode leads (Figure 4.10) with an impedance meter (Tenma® dual display LCR meter, model 72-960). For a two-electrode device, impedance was measured between the two electrode leads. For a three-electrode device, two electrode leads were tied together and impedance was read between the tied leads and a third electrode lead. The process was repeated with other combinations of electrode leads. This type of impedance measurement on cuff electrodes has been employed by others [247].

The measured electrical impedance readings are listed in Table 4.1. In air ambient, the impedance between the electrode leads was very high, i.e. it was over the limit of measurement (10^7 Ω) for the impedance meter used. This indicated that the electrode leads were separated from each other. The impedance values of the devices in solution were found to be inside a range from 300 Ω to 3 kΩ. This is close to the range of values reported for other cuff devices in literature [9, 248]. The impedance readings indicated that the electrode leads inside the cuff functioned properly i.e. they were sufficiently exposed inside the cuff. The electrical connectivity test is required to ensure that the fabrication processes did not affect the electrode leads inside the cuff. For the cuff devices made by the process involving a molding step, it is important to ensure that the electrode leads inside the cuff are not inadvertently covered by

silicone pre-polymer during fabrication. For the devices made by the layer-by-layer method, it is necessary to ensure that sufficient lengths of electrode leads are available inside the cuff, since some electrode leads may be pulled out during the electrode wire incorporation process.

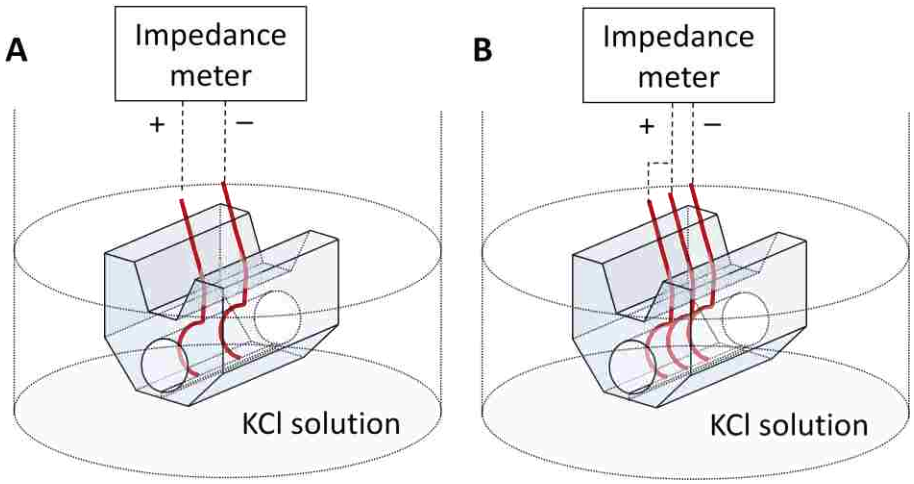

Figure 4.10: Schematic diagrams of electrical connectivity tests on the developed clip-on micro-cuff electrode devices in (A) two-electrode configuration; (C) three-electrode configuration.

Table 4.1: Electrical impedance readings for the clip-on micro-cuff electrode, measured between its electrode leads.

Fabrication method of micro-cuff	**Average impedance**			
	In air ambient		**In 2M KCl solution at room temperature**	
	120 Hz	1 KHz	120 Hz	1 KHz
Involving a molding step (section 4.1.2.1)	$> 10^7$ Ω	$> 10^7$ Ω	2.11 kΩ	310 Ω
Layer-by-layer (section 4.1.2.2)	$> 10^7$ Ω	$> 10^7$ Ω	2.83 kΩ	372 Ω

The clip-on micro-cuff electrodes were evaluated for their applicability in bio-potential recording. The device was immersed in KCl solution and the electrical impedance between its electrode leads was measured. The KCl solution was then agitated by a magnetic stir bar, to simulate the effects of physiological ambient in motion. The impedance readings showed considerable, random fluctuations in the readings, ranging between 2.5 kΩ -14 kΩ for a 120 Hz measurement. In the next step, the two circular openings at the lateral ends of the micro-cuff were closed by attaching pieces of silicone. The cuff electrode was introduced into the KCl solution again. The KCl solution entered the cuff gradually and filled the cuff interior. Subsequently, electrical impedance readings were obtained and found to be in the range of those measured in stationary KCl solution, with the cuff ends open. The solution was then agitated by magnetic stirring. It was observed that the impedance readings did not show appreciable changes due to the moving solution, ranging between 2.2 kΩ - 3 kΩ for a 120 Hz measurement. Subsequently, the cuff endings were opened by removing the silicone pieces and electrical impedance was measured in agitated KCl solution. The impedance values were found to fluctuate considerably. These results indicate that the normally closed position of the cuff in the developed device more or less fixes the volume inside the cuff, when its lateral openings are closed.

When a cuff electrode encloses a nerve, the lateral openings of the cuff can be considered closed for practical purposes. For the developed micro-cuff electrode, this implies that there is negligible electrical noise from the ambient, when the cuff encloses a nerve. Therefore, the clip-on micro-cuff electrode can be used for the recording of electrical signals from the enclosed tissue, without the risk of reading tangible electrical noise from the ambient.

In another test, electrical signals in the micro-volt range and at a given frequency were fed to the electrodes of the clip-on cuff by means of an experimental test set-up (Figure 4.11) in air ambient. A resistor R_2 was connected between electrodes E1 and E2 to simulate an enclosed nerve. The electrical resistance of a nerve trunk of 1.06 mm diameter is approximately 28.75 kΩ/cm [249]. Due to a spacing of 2 mm between the electrodes, the value of R_2 was chosen to be 5.6 kΩ, to simulate a 2 mm long nerve trunk enclosed between the electrodes. The signals read by the electrodes were recorded after amplification.

A recorded sinusoidal wave voltage signal at 1 kHz with amplitude of approximately 150 µV, amplified by a gain of 91, is shown in Figure 4.11. Signals with amplitude as low as 75 µV and frequency in the range 100 Hz – 5 kHz were successfully read by the self-closing cuff. These signals are in the range of typical electroneurogram (ENG) signals in terms of magnitude and frequency [250].

4.1.3.2.2. Mechanical Testing

An objective of the developed cuff electrode design was to provide a robust interface between the cuff body and the electrode wiring. The developed micro-cuff electrode was subjected to a mechanical pull test to study robustness of the electrode wire-cuff interface. The force test involved opening the cuff to enclose a metal pin and allowing the cuff to return to its normally closed state. The metal pin had an outer diameter slightly smaller than the cuff inner diameter and its length was significantly greater than the cuff length. Subsequently, the longitudinal slit opening of the micro-cuff device was sealed by epoxy. The enclosed metal pin was clamped at its two ends (Figure 4.12). The electrical wires exiting the cuff were attached to the hook of a force gauge (Chatillon, NY, USA, Gauge-R, Model 516-1000). A pulling force was applied to the electrical wires and progressively increased till the removal of one or all the wires

from the cuff body. The force values at which the wire removal occurred were noted and are shown in Table 4.2.

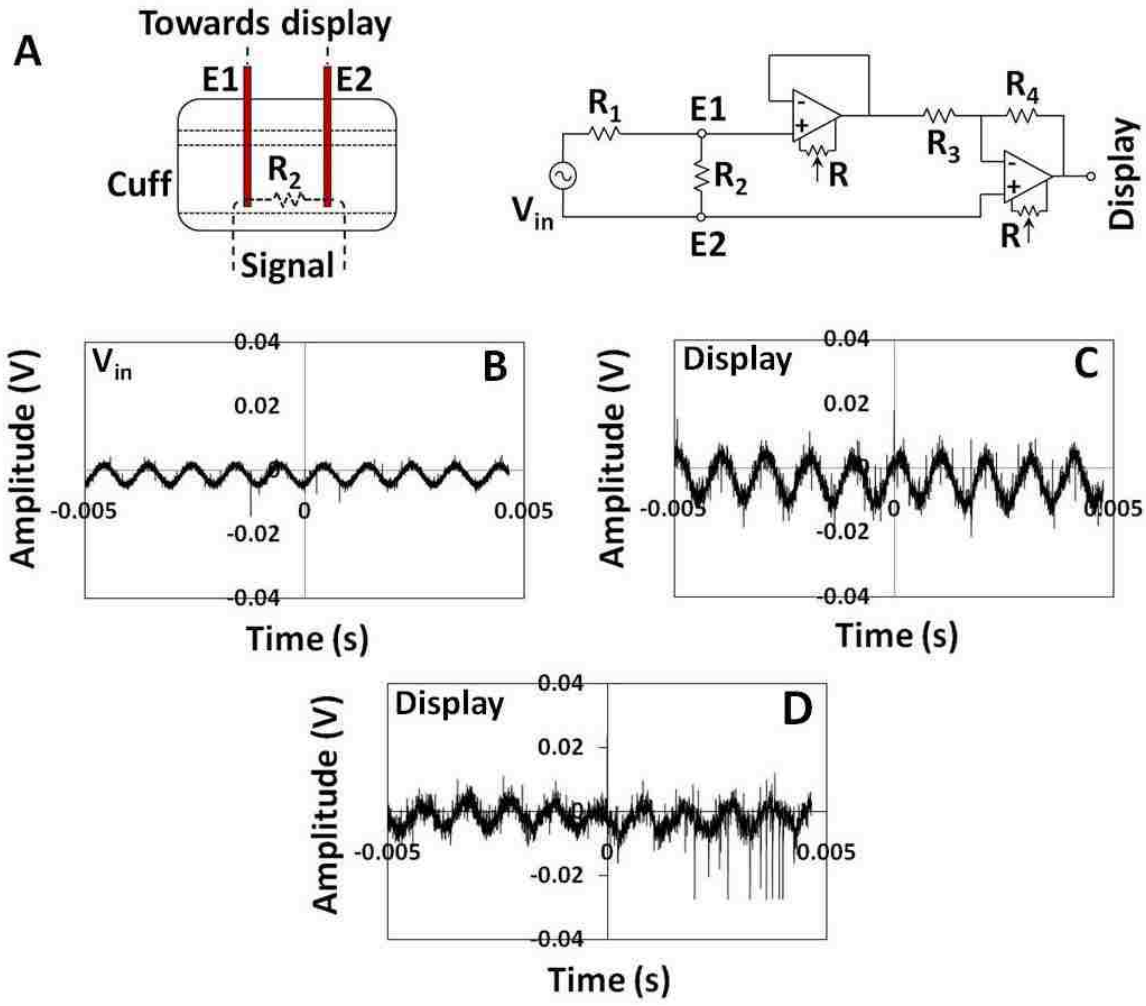

Figure 4.11: (A) Schematic of external testing of versions of the developed cuff electrode to study their applicability in stimulation or recording. Digital oscilloscope data of real-time recording of (B) an artificially generated voltage signal V_{in} given to the electrodes of the cuff device through a $R_2/(R_1 + R_2)$ voltage divider; (C) an amplified signal read by the electrodes of the layer-by-layer cuff, with R_1= 220 kΩ; (D) an amplified signal read by the electrodes of the micro-cuff, with R_1= 440 kΩ. The signal inversion is due to the use of an amplifier in the final stage of the test set-up. No filtering component or equipment was employed for removal of electrical noise.

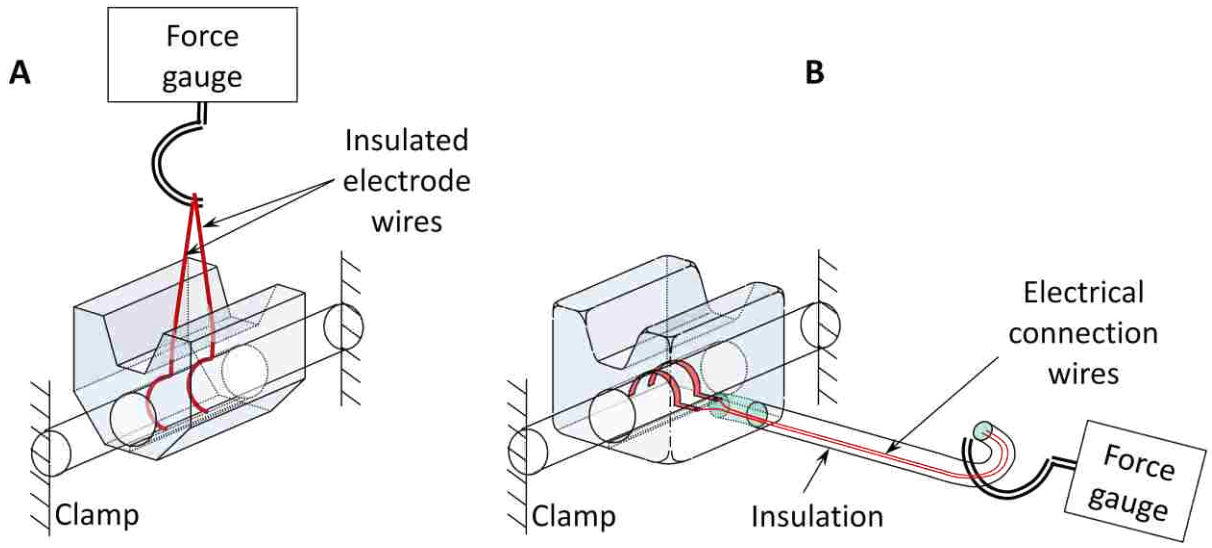

Figure 4.12: Schematic diagrams of force test set-up for the clip-on micro-cuff electrode devices made by (A) layer-by-layer process; and (B) process involving a molding step.

The force tests were conducted for the two versions of the micro-cuff electrode, i.e. the versions of the devices made by the layer-by-layer method and by the method involving a molding step. For comparison, force tests were also conducted in the same manner on conventional-type cylindrical cuff electrodes. During the course of all the force test experiments, the metal pin enclosed in the cuff did not bend from the force applied on the wires. The force tests on all three types of cuff electrodes were conducted in two stages – as the devices were manufactured and after their immersion in Ringer's solution for 1 month. The force tests on the clip-on micro-cuff devices showed that the electrode wires could withstand significant values of pulling force, without getting displaced from the main cuff body. In contrast, the force tests on the conventional-type cuff electrodes showed that the wires were removed from the cuffs at a

much lower pulling force value (Table 4.2). In the case of the clip-on cuff device made by the process involving a molding step, the strength of the electrode wire - cuff body interface can be attributed to embedding of the electrode wire insulation in the cuff body. Another factor is the use of the same material for the device body and the embedded insulation of the electrode lead wires, which provides for a robust interface. In the case of the clip-on cuff made by the layer-by-layer process, the strength of the interface between electrode wire and silicone cuff body can be attributed to the use of silicone elastomer for reinforcing the interface. Both versions of the micro-cuff devices retained the strength of the cuff-wire interface after 1 month immersion in Ringer's solution (Table 4.2). This indicated the applicability of the micro-cuff devices for long term implantations. In contrast, the conventional cuff showed a small decrease in robustness of the cuff-wire interface.

Table 4.2: Data from force testing of the cuff-wire insulation interface.

Device type	**Average force for cuff-insulation failure**	
	As manufactured	**1 month immersion in Ringer's solution @ room temperature**
Layer-by-layer micro-cuff	3.2 N	3.2 N
Micro-cuff involving a molding step	3.3 N	3.3 N
Conventional cylindrical cuff	1.2 N	1.1 N

A major goal of the present research is to address securing of a cuff electrode to a target tissue. Force tests performed on the clip-on micro-cuff device indicated the efficacy of its normally closed cuff design in addressing the securing problem. A metal pin was enclosed in the micro-cuff and the cuff was returned to its normally closed state. The enclosed metal pin was clamped at both its ends. The electrical wires exiting the cuff were attached to the hook of a force gauge and a pulling force was applied to the wires. During the course of the testing, the

enclosed metal pin did not bend from the force applied. The force was progressively increased till the cuff was removed from the enclosed wire. The force value at which the cuff removal occurred was noted. Table 4.3 shows the force data collected in this manner. It can be seen that the naturally closed cuff stays on the wire up to an applied pulling force of 1.9 N. While reference data is not available on the magnitudes of typical forces acting on a cuff electrode in an implanted condition, it has been reported that muscle electrodes with tissue penetrating anchors can be pulled free from the muscle tissue at forces in the range 0.5 N – 2.3 N [251, 252].

Table 4.3: Data from force testing of the closed cuff enclosing a metal pin.

Device type	Average force for cuff removal
Layer-by-layer micro-cuff	1.9 N
Micro-cuff involving a molding step	1.9 N
Conventional cylindrical tube cuff	0.2 N

The pinch hinge feature in the developed micro-cuff electrode was subjected to durability testing by pressing the arms of the pinch-hinge structure till they contacted each other, thereby opening the cuff to its maximum extent. The pinch-hinge was released to return the cuff to its normally closed condition. This procedure was repeated continuously several times. The pinch-hinge did not fail during the testing process nor did it sustain any visible damage during the testing process. The tests indicated that the cuff can withstand more than 50 open-close operations, which is significantly more than needed during a typical lifetime of such a device.

4.1.3.2.3. Boiling Water Test

In order to test for the durability of the cuff body material, the clip-on micro-cuff electrodes were immersed in boiling water for 5 min. The boiling water test is typically

employed to test polymeric structures and layers for the extent of cross-linking. As proof of cross-linking, the polymeric structures are expected to remain insoluble in water at 100 ^{0}C for 5 min [253]. The cuff electrodes survived the boiling water test, indicative of adequate cross-linking of the Silastic silicone used for the device body. Optical microscopic inspection of the devices indicated no disintegration of the polymeric body. Raman spectral analysis of different parts of the Silastic body after the boiling water test showed all the frequency assignments characteristic to Silastic. It can be concluded that the material properties of the cuff were not appreciably affected by the boiling water test. The cuff electrodes were subjected to a mechanical pull test after the boiling water test. The results showed that the electrode wire-cuff wall interface failed at force levels similar to those of unboiled cuff electrodes. This indicated that there was no weakening or degradation of the electrode wire-cuff wall interface. The overall integrity of the cuff body and the pinch hinge did not appear to be affected by the boiling water test. The choice of Silastic silicone elastomer as the device material and the present fabrication processes are appropriate for the developed micro-cuff electrode.

4.1.4. Discussion

Two versions of the clip-on micro-cuff electrodes proposed here have been developed. The pinch-hinge structure incorporated in the electrode is a useful innovation by which the user can easily open the cuff and place it on the tissue being stimulated. When the pinch hinge is released by the user, the cuff assumes its normally closed nature. The pinch hinge feature negates the need for securing the cuff electrode to the target nerve by suture threads or some other intra-operative procedure. The clip-on cuff electrode offers researchers an easy means to stimulate nerves and nerves fibers with effective diameters in the micro-scale and higher. In addition to general applications involving electrical stimulation of nerves, the developed clip-on micro-cuff

electrode design may be useful for the recording of electrical signals from nerve tissue [254]. For recording applications, it is important for the nerve or nerve fiber to be enclosed or confined in a nearly finite space with non-conductive walls. It is important to ensure that stray signals are not recorded from the ambient and neighboring organs. It is also beneficial to have a nearly constant amount of extracellular fluid around the nerve tissue at the region where recordings are being made. These criteria are met by the developed clip-on cuff electrode design. The impedance measurements from the sealed micro-cuff electrode indicate that the cuff can hold an approximately constant volume inside, in solution ambient. This indicates that the electrode leads inside the cuff will not read signals from outside the cuff when a nerve is enclosed by the cuff.

The cuff fabrication processes are relatively simple and can be extended either directly or with slight modifications to other biocompatible polymer materials such as polyimides, and polyethylene, among others. All the fabrication processes investigated here allow for the number of metal electrodes in the device to be increased or decreased, depending on the application. For the purpose of technology demonstration, stainless steel foils and wires have been used as electrode material in the present research. The choice of this material for electrodes is by no means an endorsement of its properties for implantable applications. Alternately, platinum or platinum-iridium or any other appropriate metal can be used as electrode material with the fabrication processes described here.

Initial commercial feedback received on the present embodiments of the clip-on cuff electrode indicated that the devices may be slightly bulkier than desired [255]. The feedback recommended that it is beneficial to reduce the overall dimensions and mass of the device. Therefore, this research has attempted to decrease the overall dimensions of the cuff electrode. There may be a limitation on the extent to which the pinch-hinge feature can be dimensionally

reduced. If the pinch-hinge feature is made too small, then it may not allow for easy operation by the user. More importantly, if the pinch-hinge is too small, then depressing it may not allow the cuff to be opened sufficiently, as indicated by our mechanical modeling study. Therefore, other parts of the cuff have to be dimensionally reduced. Our mechanical modeling study, detailed in the following section, suggests that reduction of the cuff wall thickness may be beneficial.

4.1.5. Modeling

4.1.5.1. Cuff

A mechanical modeling study was conducted to understand the effects of some of the cuff dimensions. Assumptions made in the modeling study are as follows:

1. The cuff is modeled as a thick-walled hollow cylinder with open ends (Figure 4.13).
2. Since the clip-on cuff electrode has a closed cuff in the normal position, the presence of the length-wise cuff opening is neglected.
3. The nerve enclosed by the cuff is considered as an incompressible fluid. This is a worst case assumption, because actual nerves may be compressible and there may be changes in volume.
4. Any possible effects from the metal electrode leads are not considered.
5. The Young's modulus of the cuff material, i.e. Silastic silicone elastomer, is considered constant, for the stress range in a closed cuff.
6. It is assumed that there are no temperature changes.
7. It is assumed that there is no external pressure acting on the cuff.
8. A uniform internal pressure of 20 mm of Hg is assumed to be acting on the inner walls of the cuff. The selection of this particular value of internal pressure is based on the correlation of tissue pressure and blood flow. Nerve tissue enclosed in a cuff device may

experience swelling. When this occurs inside a closed cuff, there is a pressure applied on the enclosed nerve tissue. If the pressure applied on a nerve is about 20 mm of Hg, the intra-neural blood flow is initially impaired [256]. By about 80 mm of Hg, neural blood flow stops completely [257]. Since there is only a minimal interference with neural blood flow at 20 mm of Hg, the present modeling study assumes an internal pressure of 20 mm of Hg acting on the inner walls of the cuff.

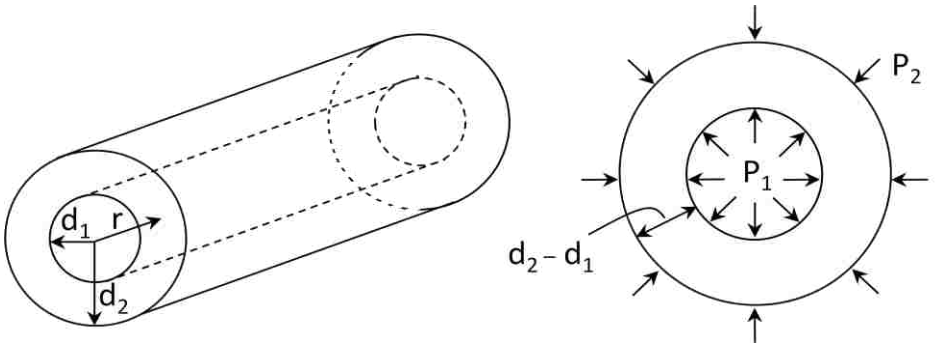

Figure 4.13: The clip-on micro-cuff is modeled as an open-ended, thick-walled cylinder, with an internal cuff radius = d_1, outer cuff radius = d_2, and an internal force P_1 and an external force P_2.

Since the cuff is considered as a hollow cylinder in this modeling study, the change in the inner radius of a thick-walled cylinder due to uniform internal and external pressures is given by [258]:

$$\Delta r = \frac{r}{E(d_2^2 - d_1^2)}\left[(1 - \upsilon)(P_1 d_1^2 - P_2 d_2^2) + \frac{(1+\upsilon) d_1^2 d_2^2}{r^2}(P_1 - P_2)\right], \qquad (4.1)$$

where Δr = change in cuff internal radius, P_1 = uniform internal pressure, P_2 = uniform external pressure, r = radial coordinate, E = modulus of elasticity (Young's modulus) of the cylinder

material, v = Poisson's ratio of the cylinder material, d_1 = cuff internal radius, and d_2 = cuff external radius.

Under an internal pressure, the cuff undergoes expansion to an extent, i.e. an internal pressure changes the cuff inner radius. Since it is assumed that there is no external pressure acting on the cuff, $P_2 = 0$. The internal pressure is considered to act on the inner surface, i.e. $r = d_1$. Therefore, equation 4.1 becomes,

$$\Delta r = \frac{d_1 P_1}{E(d_2^2 - d_1^2)}[(1 - \upsilon)d_1^2 + (1 + \upsilon)d_2^2]. \quad (4.2)$$

The Young's modulus E for Silastic is set at 2.5 N/mm^2. The Poisson's ratio υ for Silastic is set at 0.5. These values are obtained from literature [259, 260]. Employing equation 4.2, the change in internal radius of the cuff was plotted as a function of the cuff inner radius (Figure 4.14).

Figure 4.14 shows the variation in cuff inner radius when the internal pressure P_1 of the cuff changes to 20 mm of Hg from zero. Different values of cuff inner radius were used to calculate the corresponding change in internal radius. As expected, Δr is also a function of the cuff wall thickness.

The results indicate that the effect of cuff wall thickness on Δr does not appear to be significant in cuffs with smaller inner radius d_1 for somewhat thicker wall thickness values. However, the cuff wall thickness has a greater role to play in cuffs with larger inner radius. For cuffs with larger d_1, the thinner the cuff wall, the larger is the change in Δr. These results imply that the cuff wall thickness is not a critical factor for cuffs with smaller inner radius. For cuffs with larger inner radius, it is beneficial to keep the cuff wall thickness to a smaller value, in order to accommodate internal pressure changes. The modeling also considered the effect of the elastic properties of the cuff body. For a cuff wall thickness of 2 mm, the Δr values have been

plotted as function of the cuff inner radius d_1, for different values of Young's modulus of Silastic silicone (Figure 4.15).

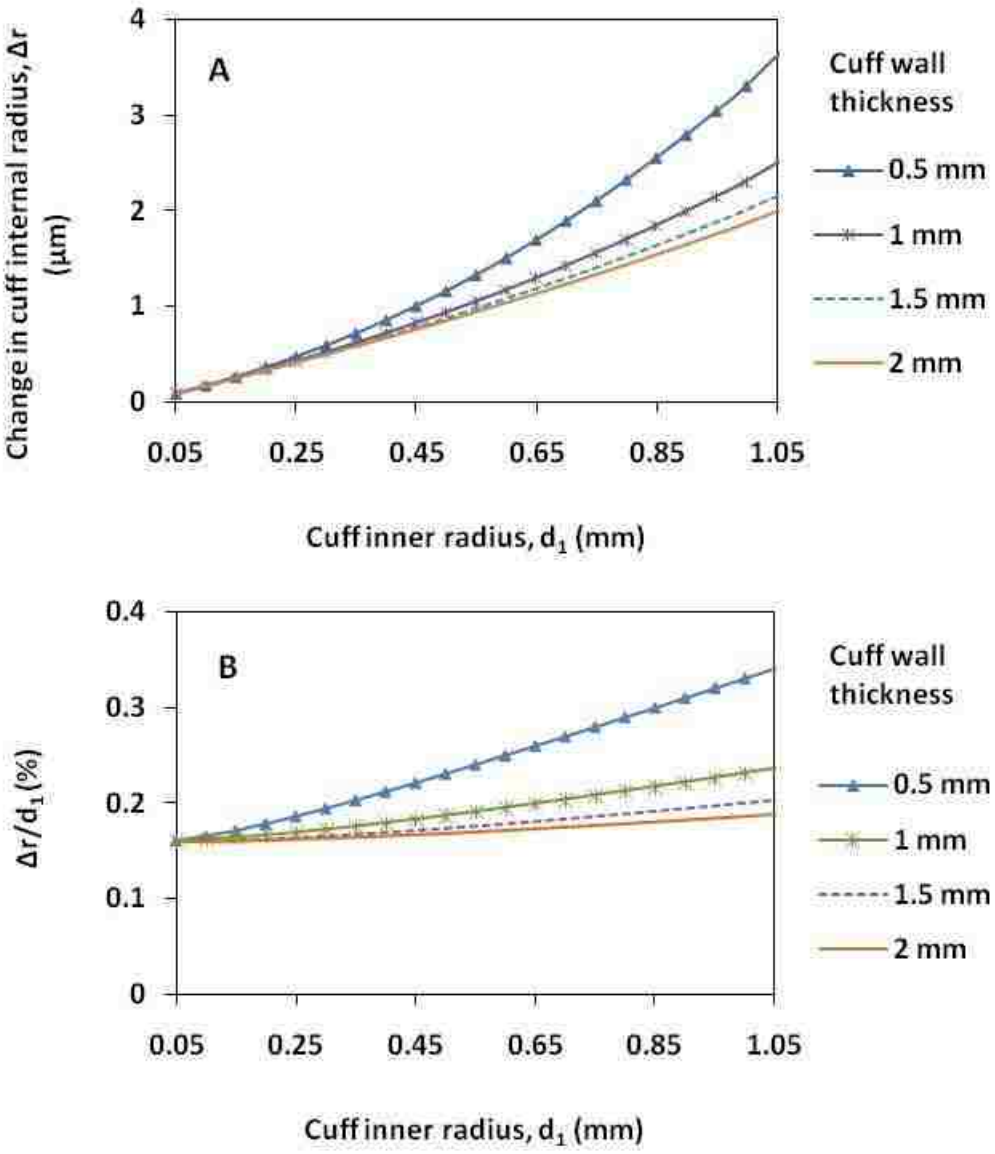

Figure 4.14: (A) Change in the inner radius of a cuff Δr as a function of its original internal radius d_1 for different values of wall thickness, when an uniform internal pressure of 20 mm of Hg is applied on the inner walls of the cuff and outer wall pressure is zero; E = 2.5 N/mm^2. (B) Percentage change in the ratio of $\Delta r/d_1$ with d_1.

The results indicate that in general, a lower Young's modulus allows for a larger Δr, and is therefore desirable for the cuff body material. The influence of the Young's modulus is not significant for cuffs with smaller d_1. As the d_1 value increases, the Young's modulus of the cuff material plays an increasing role in determining Δr, i.e. the extent of cuff expansion. These results hold true for other values of cuff wall thickness and higher values of cuff inner radius.

The Young's modulus based modeling results show the need for modulation of elasticity in the cuffs. In general, it may be beneficial to make the cuff with a more elastic material. Previous reports on polydimethylsiloxane (PDMS) silicone elastomer have indicated that the curing process of PDMS pre-polymer influences the mechanical properties of the cured PDMS [261-263]. Other reports have indicated the effect of heat treatment during curing on the mechanical properties of PDMS [264].

In summary, the following conclusions can be drawn on the influence of some dimensions and material properties of the cuff:

1. For larger inner radii, it is beneficial to keep the cuff wall thickness to a smaller value to provide flexibility.
2. The influence of the Young's modulus is not significant in cuffs with smaller inner radius. As the cuff inner radius increases, a lower Young's modulus allows for a larger Δr, and is therefore desirable in cases where increase in pressure P_1 is accompanied by increase in nerve volume.

4.1.5.2. Pinch-hinge

A mechanical modeling study was conducted to understand the effects of the pinch-hinge dimensions. Assumptions made in the modeling study are as follows:

1. The developed cuff electrode has a pinch hinge feature that is akin to a partially v-shaped filleted hinge structure (Figure 4.16A). Therefore, the pinch-hinge is modeled as a partially v-shaped filleted hinge.
2. The opening force acting on the pinch-hinge is assumed to act on one of the arms of the pinch-hinge (Figure 4.16B). The other arm is assumed to be in a stationary, fixed position. This is a reasonable assumption considering the symmetry of the pinch-hinge structure [265].

The width of the pinch-hinge arms h_w is small in our devices. Hence, this dimension is considered zero where applicable.

The pinch-hinge subjected to a bending moment M_z will rotate about the z-axis, and the angular displacement is β_z. Extending the compliance equations for v-shaped flexure hinges, the torsional stiffness k of the pinch-hinge structure is given by [266]:

$$\frac{1}{k} = \frac{\beta_z}{M_z} =$$

$$\frac{3}{2Ew_c{l_c}^2}\left\{\frac{1}{\left(2X_1+{X_1}^2\right)}\left[\frac{(1+X_1 sin\alpha)}{(1-X_1-cos\alpha)^2}+\frac{\left(3+2X_1+{X_1}^2\right)sin\alpha}{\left(2X_1+{X_1}^2\right)(1+X_1-cos\alpha)}+\right.\right.$$

$$\left.\left.\frac{6(1+X_1)}{\left(2X_1+{X_1}^2\right)^{3/2}}arctan\left(\sqrt{\frac{2+X_1}{X_1}}tan\frac{\alpha}{2}\right)\right]-\frac{{X_2}^2 cot\alpha}{{X_1}^2(1+X_2)^2}+\frac{cot\alpha}{(1+X_1-cos\alpha)^2}\right\}, \quad (4.3)$$

where k = torsional stiffness of the pinch-hinge, α = angle of the pinch-hinge arm from the horizontal axis, E = Young's modulus of the cuff material i.e. silicone. E = 2.5 N/mm^2, w_c = width of the pinch-hinge, l_c = radius of the pinch-hinge joint,

$$X_1 = \frac{t_c}{2l_c}, \text{ and} \quad (4.4)$$

$$X_2 = \frac{t_c}{2f_c}. \quad (4.5)$$

Here, t_c = minimum thickness of the hinge or distance between the hinge joint to the cuff, and

f_c = height of the pinch-hinge arms.

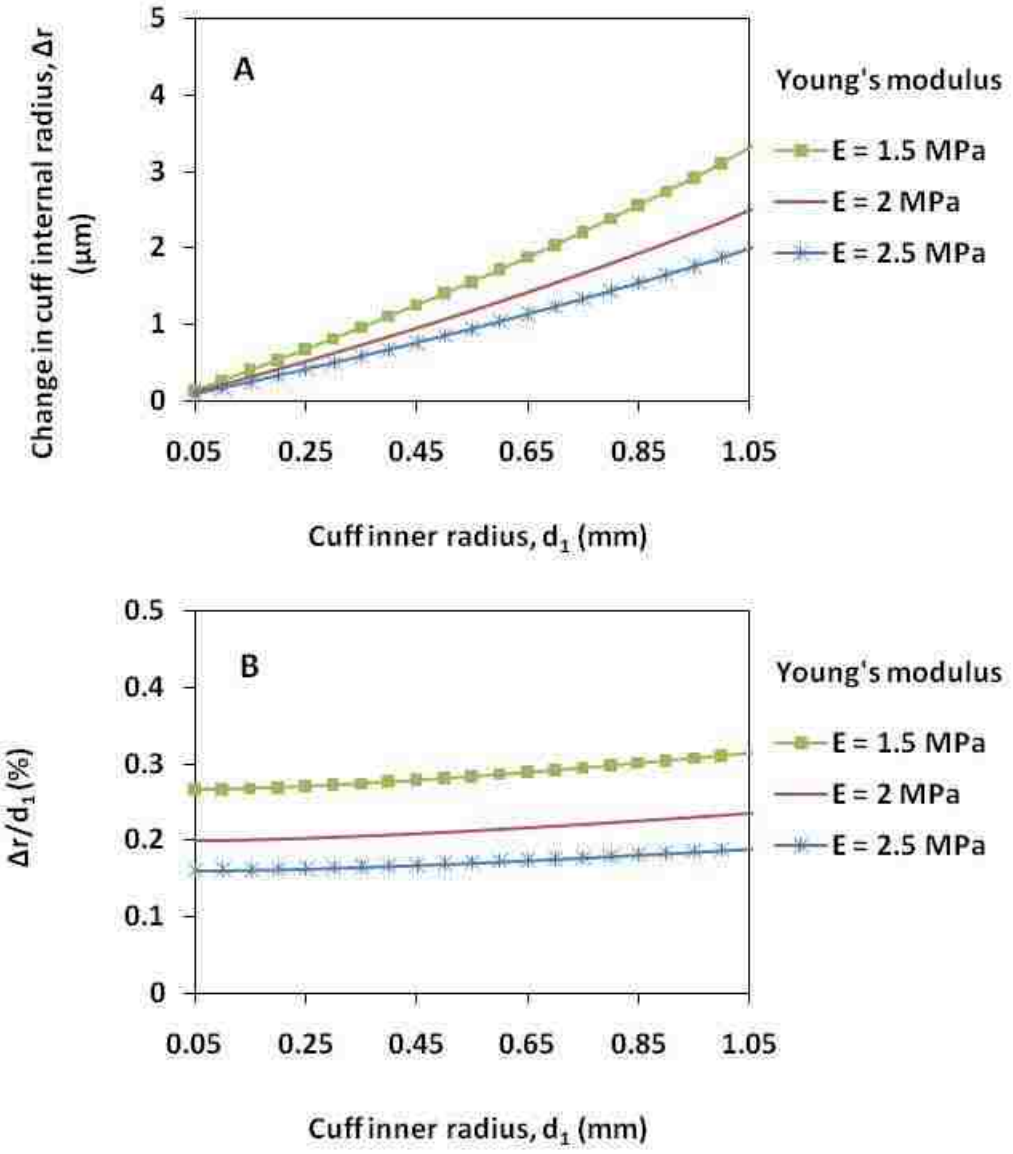

Figure 4.15: (A) Change in the inner radius of a cuff under uniform internal pressure of 20 mm of Hg and zero external pressure, as a function of its original internal radius at zero internal pressure for different values of Young's modulus. The cuff wall thickness is set at 2 mm. (B) Percentage change in the ratio of $\Delta r/d_1$ with d_1.

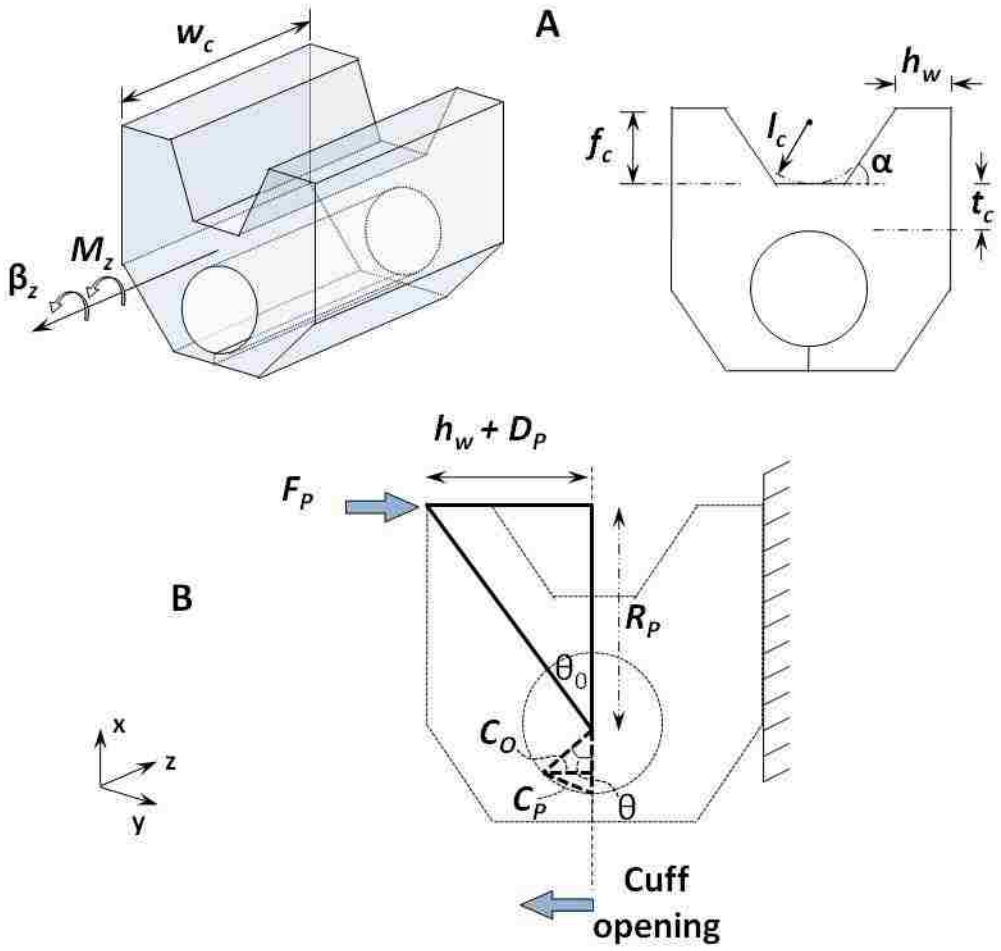

Figure 4.16: (A) Schematic of the pinch-hinge structure of a clip-on cuff without electrodes inside. The various geometric parameters are marked. (B) A two-dimensional rendering of the cuff with a force F_P acting on an arm of the pinch-hinge, with the other arm fixed.

In equation (4.3), parameters such as E, w_c, have a linear relationship to torsional stiffness k and are therefore not the focus of attention here. The other parameters such as t_c, f_c, α are studied for their effect on k. The nominal dimensions of the pinch-hinge include t_c = 1 mm, w_c = 4 mm, l_c = 5 mm, and f_c = 4 mm.

Using equation (4.3), the torsional stiffness k is calculated as a function of f_c, the height of the pinch-hinge arms. The plot shown in Figure 4.17 indicates a negligible influence of f_c on stiffness k. However, at low values of f_c (< 2 mm), there is some minor variation in k. Also, decreasing α decreases stiffness k for a given value of f_c. The calculations were done using MATLAB software. An example program to calculate torsion stiffness of the pinch-hinge is provided in Appendix D.

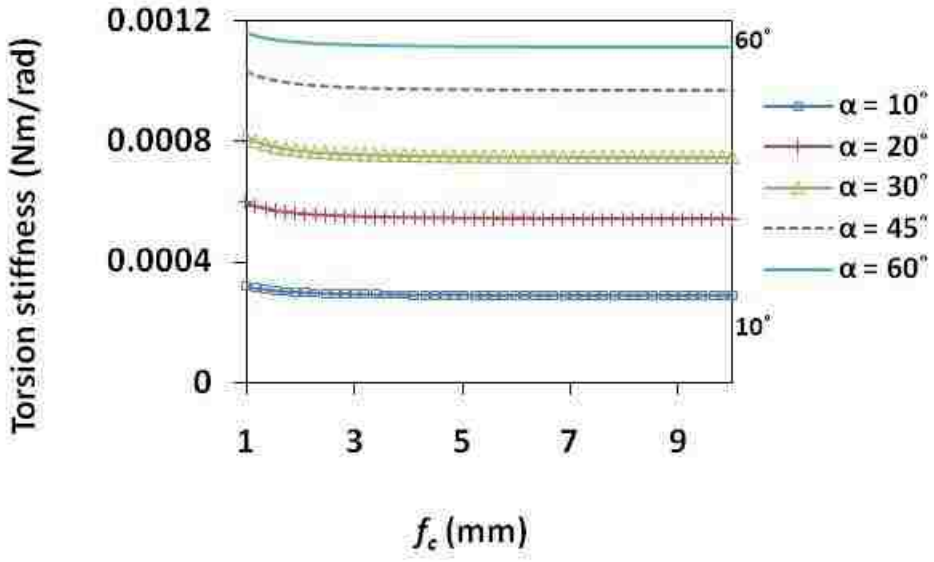

Figure 4.17: Torsional stiffness k of the pinch-hinge as a function of f_c, the height of the pinch-hinge arms, plotted for different values of α. Here, E = 2.5 N/mm^2, t_c = 1 mm, w_c = 4 mm, and l_c = 5 mm.

Equation (4.3) is used to determine torsional stiffness k as a function of t_c, the distance between the hinge joint to the cuff (Figure 4.18). In general, the value of k increases as t_c increases. This indicates the benefit of having a low t_c value. Another aspect is the correlation with α. For larger values of α, an increase in t_c results in a more significant increase in stiffness. This indicates that it is beneficial to employ a lower angle of the pinch-hinge arm.

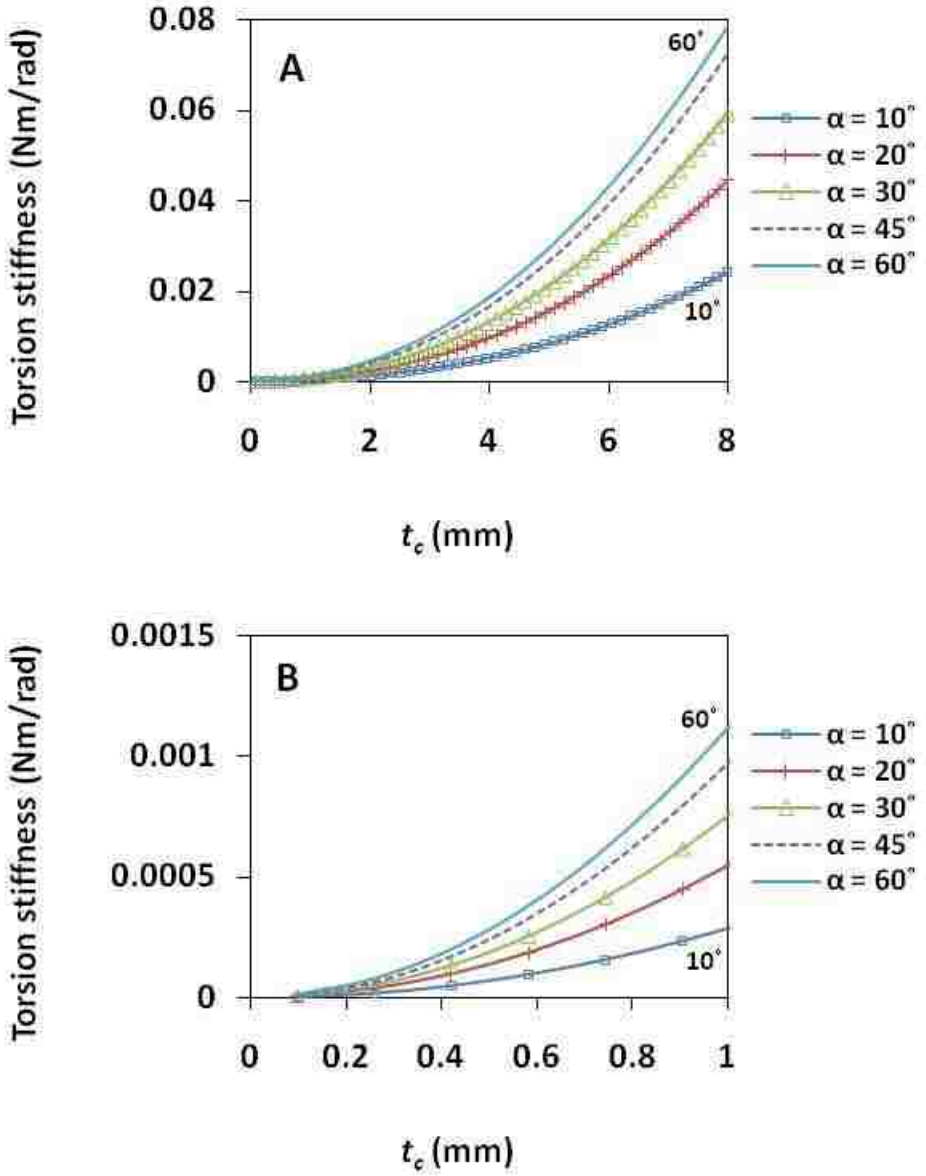

Figure 4.18: (A) Torsional stiffness k of the pinch-hinge as a function of t_c, the vertical distance from the pinch-hinge joint to the cuff, plotted for different values of α. Here, w_c = 4 mm, l_c = 5 mm, and f_c = 4 mm. (B) An expanded view showing the torsion stiffness values for lower range of t_c.

Equation (4.3) was used to determine k for different values of α (Figure 4.19). In general, the value of k increases with an increase in α. The increase in k is not significant for low values

of the ratio X_1. For higher values of ratio X_1, the stiffness increases considerably. Though the plot does not show data for $X_1 > 1$, the behavior is applicable for $X_1 > 1$. Since $X_1 = t_c/2l_c$, it is beneficial to employ t_c smaller than l_c. For devices fabricated in this work, X_1 is typically lower than 1.

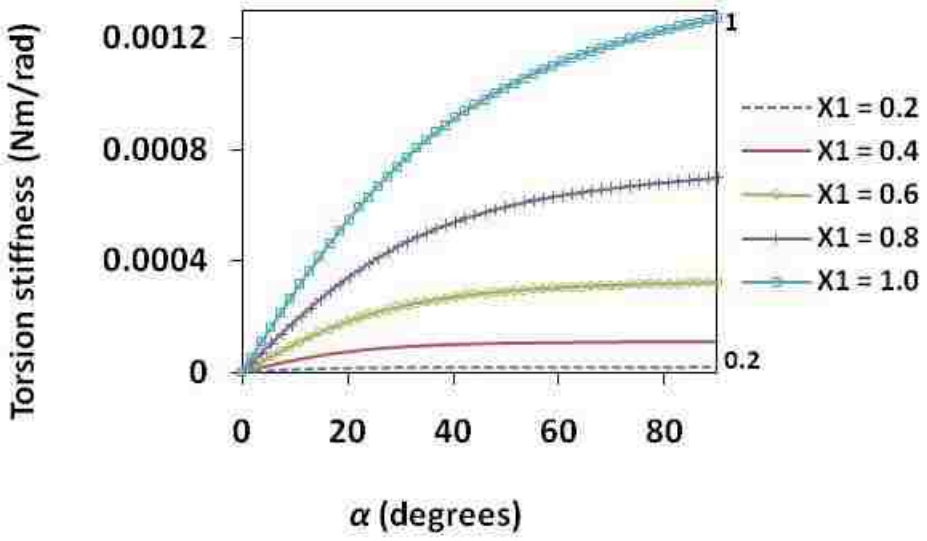

Figure 4.19: Torsional stiffness k of the pinch-hinge as a function of α. Here, $X_1 = \frac{t_c}{2l_c}$, w_c = 4 mm, l_c = 5 mm, and f_c = 4 mm.

Extending the theory for typical pinch-hinge type gripper clips to the present pinch-hinge structure, the cuff opening force F_P can be expressed by [265]:

$$F_P . R_P = k . \theta, \tag{4.6}$$

where F_P = opening force, R_P = distance of force application on the pinch-hinge arms, k = torsional stiffness of the pinch-hinge, calculated by equation (4.3), and θ = rotational angle, in radians.

For sake of simplicity, in discussing the results of the present modeling study, θ values are converted to degrees and expressed as such, in the following text.

From Figure 4.16, we have,

$$tan(\theta_0 - \theta) = \frac{D_P(\theta)}{R_P}, \tag{4.7}$$

where θ_0 is the angle when the pinch-hinge arm is at the rest position to the central axis, as shown in Figure 4.16B; and $D_P(\theta)$ is the distance between the pinch-hinge arm and the central axis for a rotational angle of θ. Therefore, equation (4.6) becomes:

$$F_P = \frac{k}{R_P}\left[\theta_0 - tan^{-1}\left(\frac{D_P(\theta)}{R_P}\right)\right]. \tag{4.8}$$

In the rest position, i.e. for $\theta = 0$, $D_P(\theta) = D_P$; where D_P is half the distance between the pinch-hinge arms. For $\theta = \theta_0$, $D_P(\theta) = 0$. The force needed to move the pinch-hinge arm from rest position to the center, i.e. the case where $\theta = \theta_0$ is given by:

$$F_P = \frac{k}{R_P}[\theta_0] = \frac{k}{R_P} tan^{-1}\left(\frac{D_P}{R_P}\right). \tag{4.9}$$

The rotation angle (θ) can be related to the cuff opening C_P by a chord length equation, given by:

$$C_P = 2r_c sin\frac{\theta}{2}, \tag{4.10}$$

where r_c is the cuff inner radius.

The cuff horizontal opening C_O due to motion of one arm of hinge is given by:

$$C_O = r_c sin\theta\ . \tag{4.11}$$

The total cuff opening from symmetry if equal amount of force F_P is applied in opposite directions on each hinge is $2r_c\sin\theta$.

Equations (4.6) and (4.11) allow the calculation of the opening force to be exerted on the pinch-hinge to open the cuff by a certain extent. Here, the equations (4.6) and (4.11) are used to plot the cuff opening as a function of the opening force (Figure 4.20). Here, as the force is increased, the value for rotational angle θ increases till it reaches the maximum value of θ_0 at the extreme point shown on the graph. It can be seen that a larger force allows for a larger cuff

opening. The correlation of force F_P with the cuff opening Co is influenced by the torsional stiffness (k) of the pinch-hinge (Figure 4.20). For a specific cuff opening, the opening force increases with an increase in torsion stiffness.

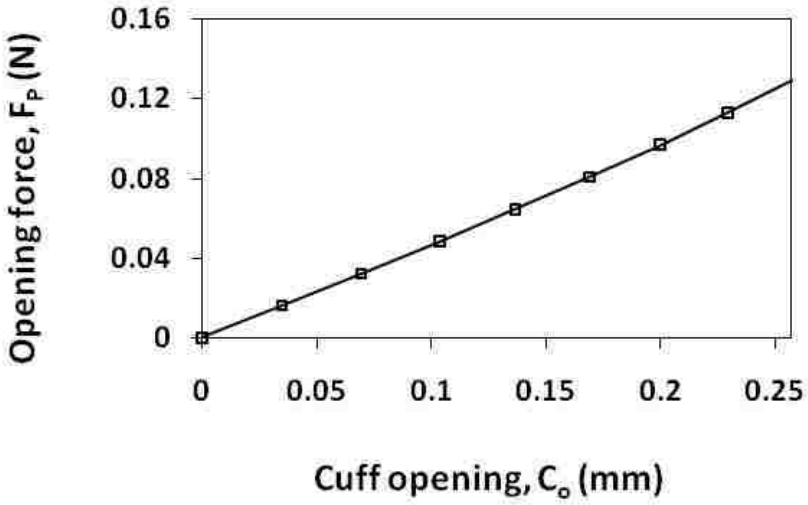

Figure 4.20: The cuff opening force F_P on one arm as a function of the cuff opening C_O. The distance of force application (R_P) was 3 mm, and D_P = 4.5 mm which corresponds to a $\theta_0 = 40^\circ$. The dimensions of the structure were t_c = 1 mm, w_c = 4 mm, l_c = 5 mm, f_c = 4 mm, and r_c = 0.4 mm.

The correlation of applied force with the cuff opening is influenced by the distance R_P. For a specific cuff opening, as expected, the opening force decreases with an increase in distance R_P. This is validated by experimental readings of opening force F_P shown in Table 4.4. The experimental data shown in Figure 4.21 were obtained from a clip-on cuff with the same dimensional parameters as the modeled case. In theoretical calculations of F_P, the value of k is 0.001 Nm/rad based on nearest match to data obtained in Figure 4.17 for $\alpha = 50^\circ$.

The maximum cuff opening values shown in Figure 4.21 result from the motion of one pinch-hinge arm when $\theta = \theta_0 = tan^{-1}(D_P/R_P)$, and the pinch-hinge arm moves from its rest position by a distance D_P. From symmetry consideration, the total cuff opening will be twice this

amount when both arms are pinched with the magnitude of force F_P acting on opposite directions.

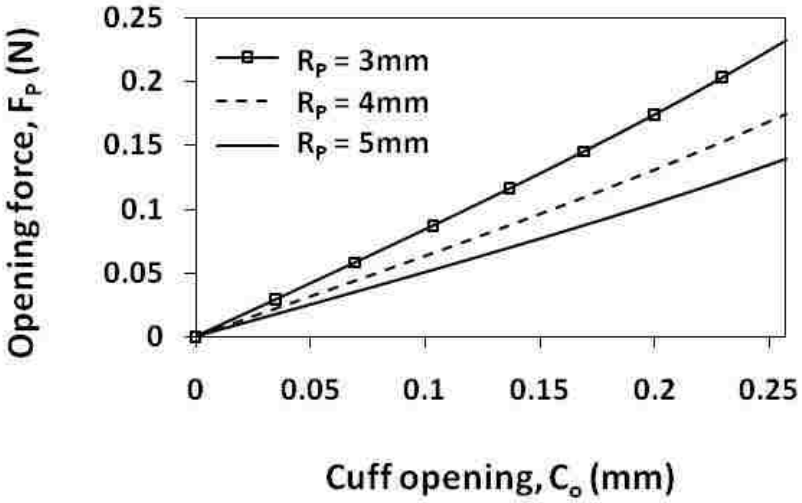

Figure 4.21: The cuff opening force F_P as a function of the cuff opening C_O due to a single arm of the pinch-hinge, calculated using equation (4.6). The torsional stiffness k for this case is 0.001 Nm/rad. The dimensions of the structure include t_c = 1 mm, w_c = 4 mm, l_c = 5 mm, f_c = 4 mm, D_P = 4.5 mm, and r_c = 0.4 mm.

Table 4.4: Force data obtained by opening a cuff to its maximum extent, with one pinch-hinge arm contacting the other, and $2\theta = 2\theta_0 \approx 80^\circ$. Dimensions of the cuff are t_c = 1 mm, w_c = 4 mm, l_c = 5 mm, f_c = 4 mm, r_c = 0.4 mm, and $2D_P$ = 9 mm. Value of k is 0.001 Nm/rad in theoretical calculation of F_P.

R_P (mm)	F_P (Experimental)	F_P (Theoretical)
3	0.72 ± 5% N	0.465 N
4	0.51 ± 5% N	0.349 N
5	0.42 ± 5% N	0.279 N

The experimental measurements of opening force F_P were obtained by applying force on one arm of the pinch-hinge by means of a force gauge. The other arm was kept fixed and

stationary by means of a clamp. For maximum cuff opening, the pinch-hinge arms were made to contact each other. There is some variation between experimental and theoretical values of F_P. This can be attributed to factors such as experimental procedure, among others. Due to manual placement of the force gauge on the pinch-hinge arm, there may be some deviation in intended values of R_P. Another factor is the size of the force gauge component that makes contact with the pinch-hinge arm. The relatively large dimension of this component creates some error in measuring R_P exactly. Another aspect to consider is the torsional stiffness value used in the theoretical calculations. This value is calculated by considering Young's modulus (E) as 2.5 N/mm^2. The value of E depends partially on the curing temperature of the silicone elastomer and the amount of curing agent employed. Variations in these factors will lead to a variation in E value, and therefore torsional stiffness.

In the present case, the clip-on cuff has θ_0 value of approximately 40˚. Using equation (4.11), the maximum cuff opening $2C_O$ can be obtained for a given cuff inner diameter. Table 4.5 lists the maximum opening theoretically possible for clip-on cuffs with inner diameter 400 µm and 800 µm respectively. It also lists the target nerve diameters based on recommendations that the cuff inner cross-section area be 2.5-3 times that of the target nerve ideally [267]. It can be seen that for a rotational angle of θ = 40˚, the clip-on cuffs can accommodate the nerve diameters recommended for a specific cuff inner diameter.

Table 4.5: Maximum possible cuff opening, $2C_O$, calculated for a rotational angle of θ = 40˚.

Cuff inner diameter, $2r_c$ (µm)	**Maximum cuff opening possible, $2C_O$ (µm)**	**Nerve diameter recommended (µm) [267]**
400	257	231-253
800	514	462-506

The gap between the pinch-hinge arms plays a role in the interaction of the opening force with the distance of force application (Figure 4.22). A smaller gap between the arms implies a lower force requirement to open the cuff. As the distance of force application (R_P) increases, the gap between the arms does not significantly influence the opening force. Figure 4.22 refers to the force needed for the maximum opening of the cuff for $\theta = \theta_0$.

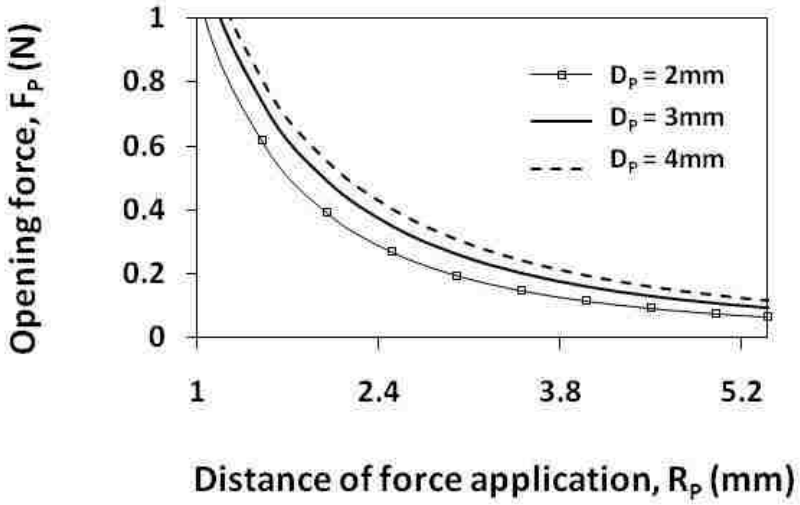

Figure 4.22: The cuff opening force as a function of R_P, the distance of force application, calculated using equation (4.9). The torsional stiffness k for this case is 0.001 Nm/rad. The dimensions of the structure were t_c = 1 mm, w_c = 4 mm, l_c = 5 mm, f_c = 4 mm, and r_c = 0.4 mm.

In summary, these results have the following implications on design and usage of clip-on cuff electrode devices:

1. For a larger cuff opening C_O, it is beneficial to increase the rotational angle θ.
2. For a given set of cuff dimensions, a larger distance of force application (R_P) is beneficial. In other words, it is beneficial to apply force at the ends of the pinch-hinge arms, for maximum leverage to open to the cuff.

3. It is beneficial to have a low value of torsional stiffness, as this would decrease the force needed to open the cuff. This can be achieved by incorporating (a) a lower Young's modulus (generally caused by a higher curing temperature for silicone elastomer); (b) a smaller angle α of the pinch-hinge arms; (c) a smaller distance (t_c) between the joint of the pinch-hinge arms and the cuff.

4.2. Gastric Pacing Electrode Technology Development

4.2.1. Introduction

There is significant interest in the treatment of obesity and obesity related physiological conditions using gastric electrical stimulation or gastric pacing. In this regard, technology development for applications in gastric pacing electrodes is of great importance. The problems faced with present gastric pacing electrodes have been detailed in Chapter 2. These include electrode lead fracture, tissue penetration and electrode displacement, all occurring during and/or after implantation. These problems are mainly related to the structural rigidity of the pacing electrode.

To address this, a new pacing electrode with a flexible body is developed here [268]. It is expected that the flexibility of the developed pacing electrode may minimize or even eliminate electrode lead fractures during chronic implantation. The flexibility of the developed electrode may also reduce or eliminate tissue penetration and electrode displacement.

Use of flexible electrodes may face certain potential limitations. Deformations during implantation may hamper proper placement of a flexible electrode on a tissue. A few reports on muscle pacing electrodes have reported features such as a stiffening stylet employed during implantation to stiffen the lead body and forceps to grasp the electrode to facilitate implantation [138]. Therefore, it appears that initially some rigidity may be required in the electrode body to

facilitate ease of handling and implantation, followed by a subsequent increase in structural flexibility.

The embodiments of the new gastric pacing electrode design developed here incorporate the following innovations/features [268]:

1. A flexible gastric pacing electrode made of bio-implantable polymer, aimed at alleviating the lead penetration problem during implantation.
2. Incorporation of a design feature that transforms the electrode structure from a more rigid initial state to a more flexible state later [269].
3. Suture holes at different locations along the periphery of the electrode structure to enable its direct anchoring to the gastric tissue by means of sutures. The peripheral anchoring of the electrode structure is expected to reduce its displacement after implantation.
4. Micro-scale porosity optionally built into the electrode structure, and aimed at promoting the growth of connective tissue. This is expected to help minimize electrode displacement after implantation by enhancing anchoring of the electrode to the gastric tissue.

4.2.2. Developed Design for Gastric Pacing Electrode

The developed gastric pacing electrode consists of a silicone elastomer body incorporating metal foil electrodes (Figure 4.23). Windows in the surface of the silicone body expose underlying metal foil electrodes, which are otherwise embedded in the silicone body. A medical grade silicone elastomer such as Silastic is used as the material for the body. Through holes are provided peripherally on the silicone body of the electrode. These holes are used to apply sutures and secure the device to target tissue (e.g. the gastric wall), so that the electrode foils lie flush against the tissue, in contact with it. Optionally, micro-scale porosity is provided in the silicone body where it comes in contact with the target tissue [268]. The micro-scale porosity

is expected to encourage the growth of connective tissue into the silicone material, with the objective of enhancing the device anchoring.

In another embodiment of the developed pacing electrode design, additional rigidity is provided to the device structure by means of a sealed trough provided at the back of the electrode body. This trough contains a thermo-responsive polymer polyethylene glycol (PEG). Polyethylene glycol is a highly biocompatible material that has been employed in a variety of biomedical applications [270-273]. Ideally, the PEG contained in the trough is in solid form at room temperature, imparting some rigidity to the electrode body. After implantation, at physiological temperature (~37 ^{0}C), the PEG melts to liquid form, causing the electrode body to lose some rigidity. A grade of PEG known as PEG-1000 melts at about 37 ^{0}C. This embodiment of the developed electrode is useful if the flexibility of the original embodiment poses handling problems during implantation. Alternately, a sealed channel network filled with PEG can be employed for additional rigidity [269].

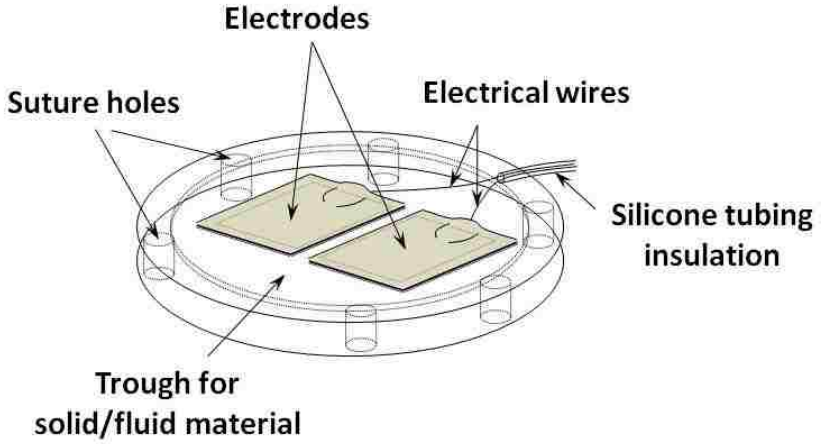

Figure 4.23: Schematic of the developed gastric pacing electrode.

4.2.3. Device Fabrication

The fabrication of the developed gastric pacing electrode is a layer-by-layer process starting from the uppermost layer of the device. In the first step, a porous silicone elastomer layer is fabricated in the form of a circular ring (Figure 4.24A) by molding uncured silicone or silicone pre-polymer doped with a foreign material. The doped pre-polymer is poured on an appropriate master mold, followed by thermal curing. The cured layer is made porous by extracting the foreign material in a suitable solvent. The pore formation processes are described in greater detail in Chapter 6. In the next step, silicone is molded on a suitable complementary master mold to obtain a solid silicone layer with two windows in it (Figure 4.24A). The window dimensions are slightly smaller than the total surface area of the metal electrodes. The windows allow the metal electrode surfaces to make contact with the target muscle tissue, while holding the electrodes in place. The silicone layer with the windows is bonded to the porous silicone ring-shaped layer (Figure 4.24B) by a simple process described below in section 4.2.3.2.

In the next step, electrodes in the form of metal foils of suitable size are spot-welded to electrical contact wires and placed on top of the solid silicone layer with the windows (Figure 4.24C). Subsequently, uncured silicone is cast over the electrode foil assembly and allowed to cure. This results in the electrode foils being embedded in the silicone body, except for the areas where the foils are partially exposed by the windows on the other side. A portion of connecting wires spot-welded to the electrode foils are also partially embedded in the silicone body (Figure 4.24D). In the next step, a solid silicone layer separately molded with a sealed trough is placed in conformal contact with the layer containing the electrode foils. Both layers are bonded to yield a single layer, with the empty trough embedded in between. The bonding process is described below in section 4.2.3.2.

In the next step, the trough is incorporated with heated liquid polyethylene glycol from one end by injecting with a hypodermic syringe needle. Prior to injection, the trough is perforated with one or more outlet holes. The injection is continued till appearance of PEG solution droplets at the outlet holes. The PEG is then allowed to solidify at the room temperature or lower. This typically occurs in few minutes. Subsequently, all the perforations in the trough are closed by applying silicone and curing it at room temperature for 18-20 hrs. There is a very small increase in volume when PEG changes from solid to liquid state. So, to accommodate for the volume change, the volume of PEG injected into the trough is slightly lower than the total inner volume of the trough.

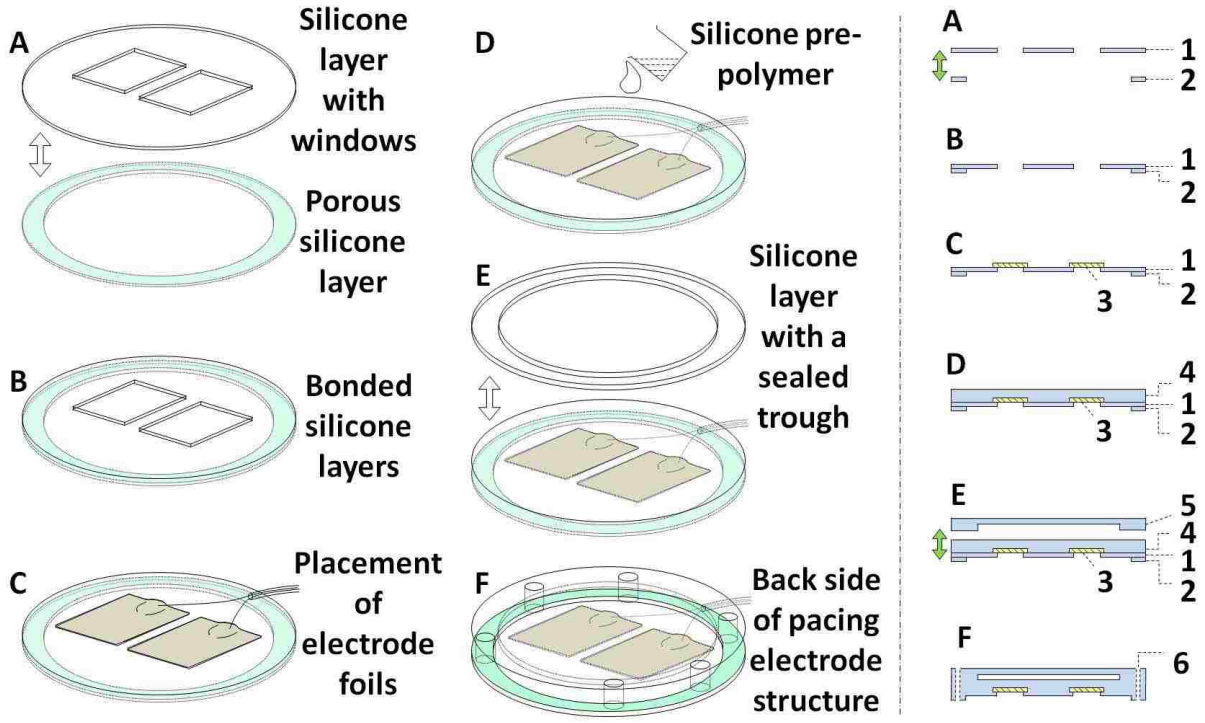

Figure 4.24: Schematic of the fabrication process of the developed gastric pacing electrode. A cross-sectional representation of the fabrication process steps is also shown.

4.2.3.1. Method of Coring Silicone to Form Suture Holes

The peripheral suture holes on the pacing electrode body can be made by coring the final silicone body of the electrode with a modified syringe needle as shown in Figure 4.25. A hypodermic syringe needle of a specific gauge is cut by means of a diamond saw to obtain a flat edge (Figures 4.25A-C). The cut end with the flat edge is then filed to impart an angle to the needle walls at the cut end (Figures 4.25D, E).

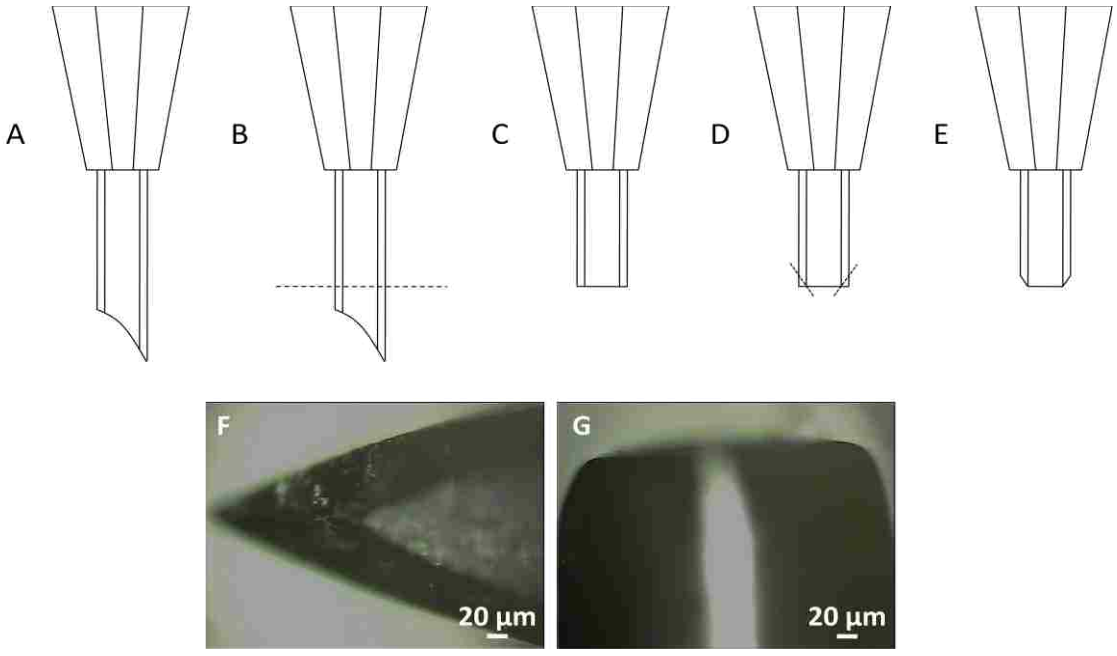

Figure 4.25: Schematic of (A) a hypodermic syringe needle; (B) cutting the curved tip of the needle by a diamond saw; (C) the resulting cut end of the needle with a flat edge; (D) filing of the cut end to impart an angle to the needle walls at the tip; (E) the final modified needle with angled sidewalls at its tip. Microscope images of the tip of (F) an unmodified syringe needle; (G) a modified needle with a flat tip formed by the sawing operation, and angled sidewalls at the flat tip.

In the next step, a solid silicone layer is placed on a flat hard surface. The modified needle tip is then held perpendicular to the plane of the solid silicone layer and pushed into it manually till it fully penetrates through the silicone layer (Figure 4.26). Subsequently, the needle is slowly pulled out of the silicone layer. A plug of the silicone material is removed from the layer by the exiting needle.

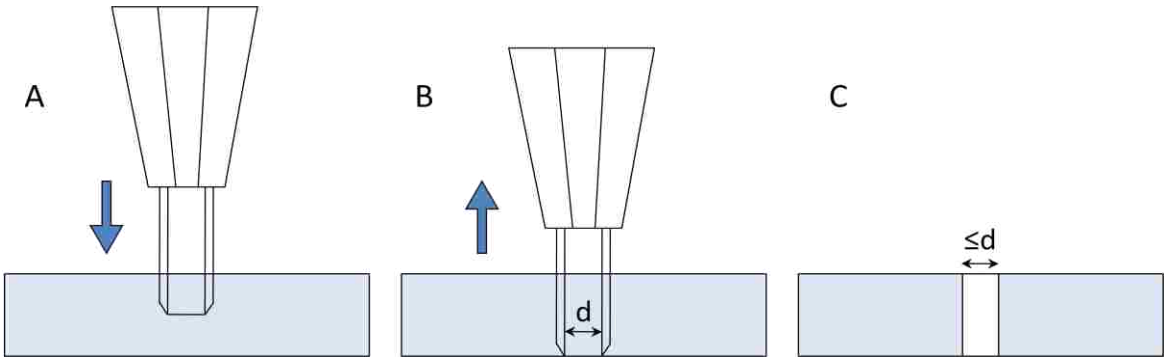

Figure 4.26: Schematic of the coring of a solid silicone layer by a modified hypodermic syringe needle, showing; (A) the placement and insertion of the needle perpendicular to the plane of the layer; (B) pulling out of the needle after it has penetrated through the silicone layer; (C) a hole with diameter less than or equal to the inner diameter of the needle is formed in the layer.

Ideally, the angled walls of the cut end of the needle allow the needle to enter the silicone layer and displace silicone material in the form of a cylindrical mass. The diameter of the displaced cylinder is approximately equal to the inner diameter of the needle. The length of the displaced cylinder is equal to the silicone layer's thickness. A typical cylindrical hole formed in a silicone layer by a modified syringe needle is shown in Figure 4.27. Though this method of making holes is a serial process, it is suitable for the present fabrication process of the gastric pacing electrode. Alternately, holes can be formed on the electrode body by a molding process.

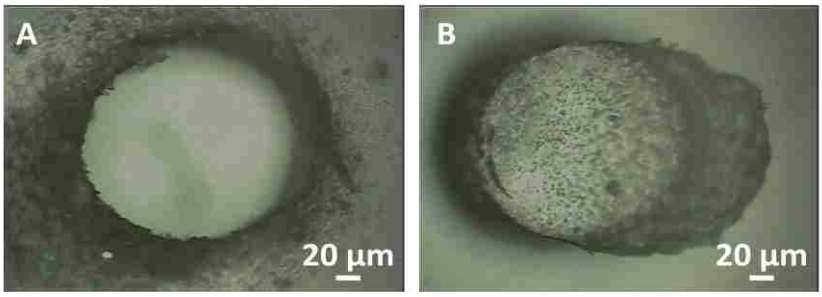

Figure 4.27: Optical microscope images of (A) a hole cored by a modified syringe needle in a silicone layer of thickness 500 µm; (B) the silicone material removed in the hole formation, in the form of a cylinder.

4.2.3.2. Method of Bonding Two or More Silicone Layers

The fabrication of the developed gastric pacing electrode involves the bonding two or more layers of solid or cured silicone. The method of bonding cured silicone layers is shown in Figure 4.28. A thin layer of uncured silicone is coated on one of the solid or cured layers (Figure 4.28A). The second cured layer is gently placed in contact with the uncured silicone coating (Figure 4.28B). The curing of the silicone coating sandwiched between the solid layers results in the formation of a single silicone structure (Figure 4.28C).

Thermal or room temperature curing can be used to solidify the sandwiched uncured silicone coating. The uncured silicone layer is typically made by spin-coating silicone pre-polymer on one of the cured silicone layers. Alternately, the uncured silicone layer can be made by spread-casting silicone pre-polymer on one of the cured silicone layers. This method can be extended to bond multiple layers of solid silicone. If there are molded features or structures on one or more of the cured layers, then the uncured layer must have a thickness less than the cured layers being bonded.

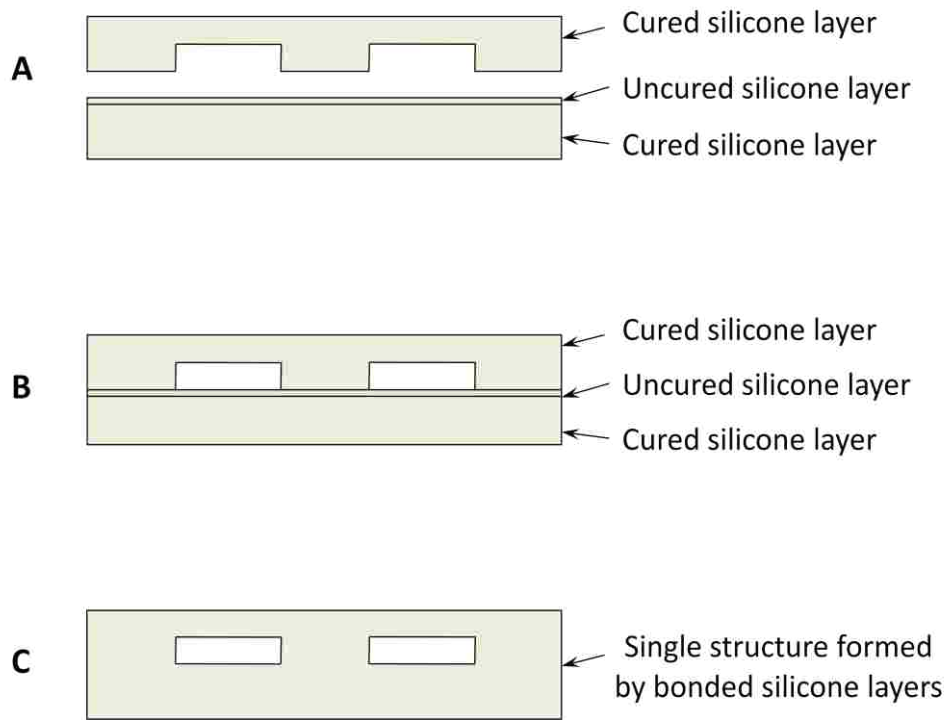

Figure 4.28: Schematic of the bonding of two or more cured silicone layers.

4.2.4. Results

A version of the gastric pacing electrode design, shown in Figure 4.29, was successfully fabricated using the processes detailed in section 4.2.3. The electrode body is a flat circular disc of approximately 24 mm diameter, with a total thickness of approximately 800 µm. The electrode body can be made thinner if required. The total effective electrode area i.e. the surface area of the electrodes exposed to the target tissue is approximately 37 mm^2. Suture threads can be applied at the peripheral through-holes on the silicone body to secure the electrode to the tissue being stimulated. To enhance the anchoring of the device to the tissue, micro-scale porosity is provided in the silicone body where it comes in contact with the target tissue. The

total weight of a typical pacing device is 2.75 g without electrical wiring, and 2.90 g with wiring. The weight increases if PEG is incorporated in the structure.

The developed gastric pacing electrode was subjected to mechanical force tests. A gastric pacing electrode device embedded with PEG was fixed at its edges in a mechanical jig and subjected to a central force (Figure 4.30). The force needed to deflect the center of the device by a certain distance (d_f) was measured. It was ensured that the silicone layers did not sustain tearing or damage during the test process. The PEG was subsequently melted, and the force test was repeated. It was observed that more force was needed to deflect the layer embedded with solid PEG, as compared to the case when PEG was melted in the layer. The tests were repeated for different quantities of PEG in the structure.

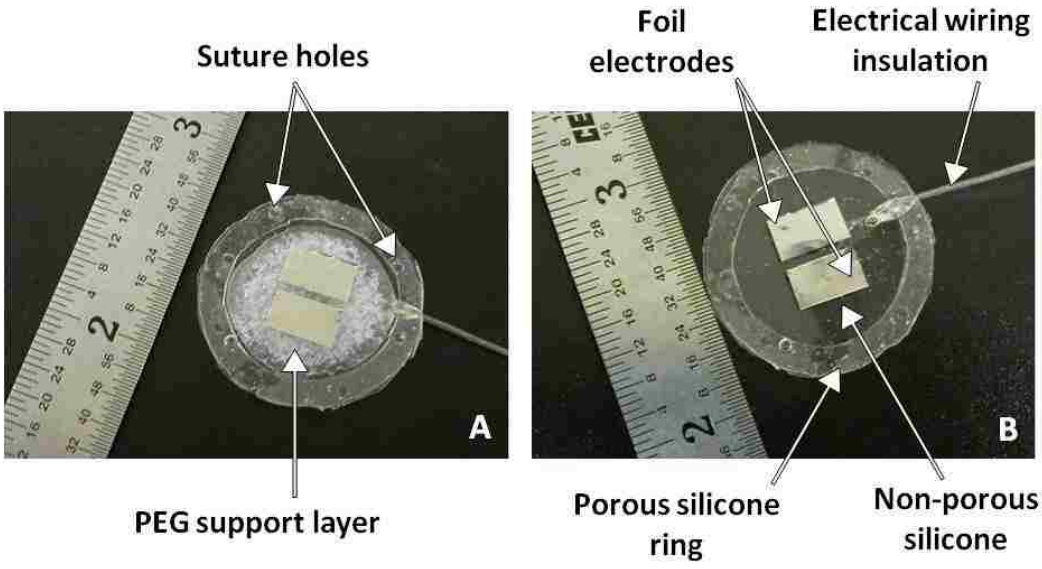

Figure 4.29: Images of a version of the developed gastric pacing electrode, showing (A) a device with a PEG support layer; (B) the device with the PEG layer melted. The scale nearest to the device in both images has 1/64 inch divisions.

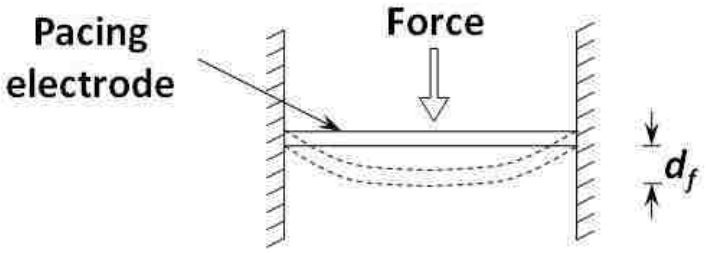

Figure 4.30: Schematic diagrams of force test set-up for the developed gastric pacing electrode structures.

As the amount of PEG was increased in the structure, more force was required to deflect it by the same distance (Figure 4.31). This indicates the feasibility of employing solid PEG (embedded or otherwise) to increase the rigidity of the pacing device structure.

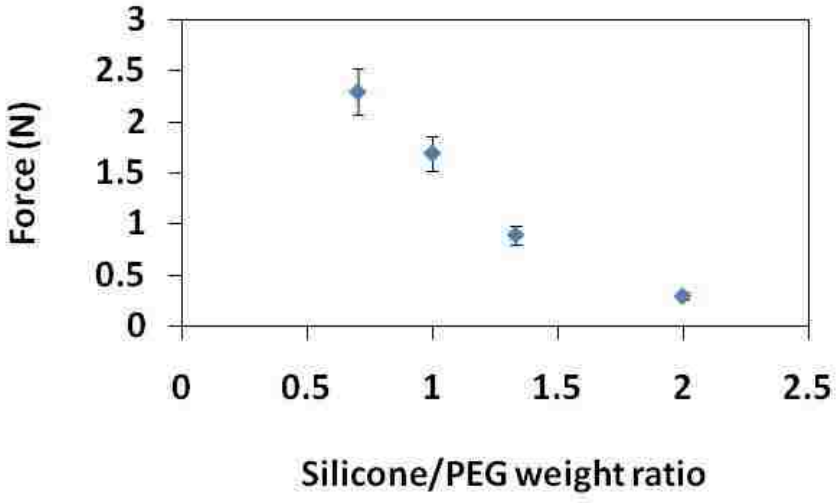

Figure 4.31: Variation of force required to deflect the center of the pacing electrode body embedded with solid PEG by a specific distance d_f = 3 mm. The electrode body diameter was approximately 24 mm.

The use of PEG does not affect the material properties of silicone elastomers like Silastic. Raman spectral analysis of a prototype structure formed by two Silastic layers sandwiching a PEG layer indicated no composite formation between Silastic and PEG (Figure 4.32).

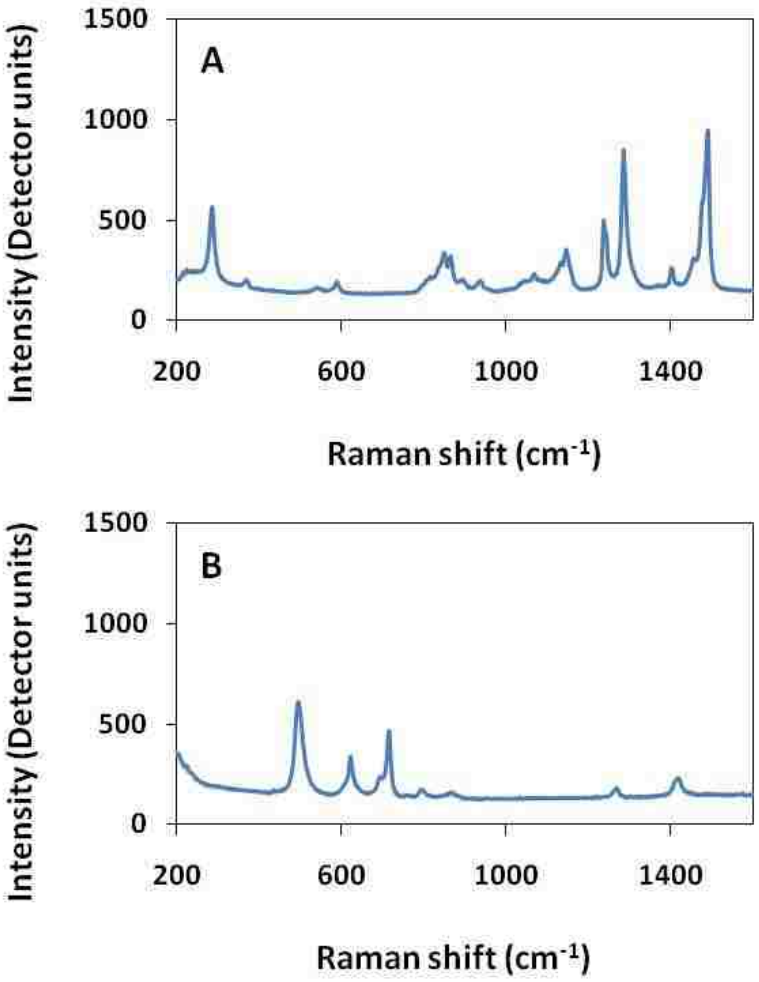

Figure 4.32: Raman spectra of (A) PEG sandwiched between two layers of silicone, showing only PEG-related frequency assignments; (B) the sandwich structure formed by the two silicone layers when the PEG was removed. Only silicone related frequency peaks can be seen.

The frequency assignments for the silicone elastomer and PEG are given in Table 4.6. In conclusion, the choice of PEG to impart thermally regulated structural rigidity in the present device is appropriate.

Table 4.6: Raman spectrum assignments for silicone elastomer and PEG.

Material	Raman shift (cm^{-1})	Assignment
Silicone	~495	Si-O stretch
	~615	Si-CH3 symmetric rocking
	~713	Si-C stretch
PEG	~281	C-O-C bend
	~1234	CH_2 twist
	~1286	Amorphous
	~1486	CH_2 bend

4.2.5. Discussion

The flexible body of the developed gastric pacing electrode is expected to minimize problems pertaining to rigid electrodes, including tissue penetration, device fracture, and displacement. To address the electrode displacement problem further, the flexible body of the pacing electrode is incorporated with suture holes by which the electrode can be secured to the target tissue by applying suture threads. The incorporation of a sealed trough filled with PEG as a 'backing layer' in the developed device is expected to allow for a degree of flexibility modulation, from a less flexible state initially to a flexible state after implantation. The PEG injected in the backing layer is solid at room temperature, but melts at physiological temperatures. Therefore, the device has some rigidity initially, but becomes flexible after implantation. Flexible electrodes can avoid gradual displacement often observed with rigid electrodes during long-term experiments due to continued differential motion in the tissue [274, 275]. This type of displacement occurs when a rigid electrode passes through the interface

between an active muscle and a relatively inactive adjacent muscle [108, 137]. Another advantage of electrode flexibility is the reduced possibility of electrode lead fracture in the implanted environment [108, 137]. Flexibility of the electrode lead is also desired in other applications such as cardiac pacing [137].

The development of muscle stimulation electrodes may follow a path different than for nerve stimulation electrodes. This is primarily due to different dimensions and geometry of muscle tissue. In comparison to nerve stimulation electrodes, stomach pacing electrodes have relatively larger surface areas in contact with the tissue being stimulated, which is typically muscle on the duodenal wall. In general, gastric pacing requires higher stimulus signals compared to nerve stimulation. It is impractical to employ metal wires as stimulation leads. This is a reason for employing flat metal foil electrodes in the developed design. This allows for the maximization of electrode surface area that can be in contact with the tissue. The developed design can be made with a larger or smaller effective electrode area, as required.

Another reason for using commercially available metal foils is the difficulty in patterning metal on flexible polymeric surfaces such as those made of silicone elastomer. Silicone surfaces are not compatible with standard UV photolithographic processes and materials like photoresist developers. Metal layers deposited on layers of silicone elastomers and other polymers by methods like RF/DC sputtering, thermal evaporation and electrodeposition may suffer from problems like cracking due to flexure. This is especially relevant for an application like gastric pacing where flexure of the pacing electrode can occur due to gastric wall motion. The use of commercially available metal foils of the desired thicknesses allows the fabrication of stimulation electrodes while minimizing problems like metal cracking. Alternately, other techniques like screen printing can be used for patterning metal on polymeric surfaces.

The developed design can be made with any lateral dimensions and thickness of the body, as required by the application. The general geometry of the present version of the developed gastric pacing electrode is circular. However, the fabrication processes can be applied to make pacing electrode with other geometries. The choice of silicone elastomer as the body material for the developed device is influenced by factors such as biocompatibility, and structural flexibility. Silicone covered flexible electrode leads have been shown to produce no tissue necrosis or inflammation in animals [276].

Due to the embedding of the spot-welded junction between the electrode foils and the electrical contact wires, the junction is relatively protected from mechanical forces. For a certain degree of additional strain relief, coiled electrical conductor wires can be used to connect the pacing electrode to other implanted or external devices.

CHAPTER 5: EQUIVALENT CIRCUIT MODEL FOR TISSUE-ELECTRODE INTERFACE FOR NERVE STIMULATION

5.1. Introduction

Functional electrical stimulation (FES) of nerves involves creating neuro-electrical and neuro-chemical changes for a desired physiological effect. Therefore, it is useful to have an understanding of the electrical effects at the stimulation electrode-nerve tissue interface. An equivalent model representing such an interface would help in understanding the electrical affects of the stimulus signal on the nerve tissue to ensure that proper electrical stimulus is given to the axons inside the nerve with minimal or no tissue damage.

Several electrode-tissue interfaces have been proposed in the past. In this work, the interface between the stimulating leads of the micro-cuff electrode developed in our laboratory and the target nerve has been modeled by an equivalent circuit involving resistors and capacitors [277]. A detailed examination of the circuit model by circuit analysis software like PSPICE, to our knowledge, has not been previously reported. Such software based analysis is useful in anticipating practical scenarios, and in providing data on the physical parameter values to be used for effective and safe stimulus of the target nerve. The behavior and response results from the equivalent circuit model to different types of stimulus waveforms enables effective and optimal design and use of the stimulating electrodes.

The goal of electrical stimulation of an excitable nerve tissue is the triggering of action potential in an axon[12]. Electric field generated by an electrode will interact with an axon membrane causing a redistribution of charge on the membrane. The extracellular region i.e. the region outside the axon membrane is driven to a more negative potential, which is equivalent to

[12] Axon: a basic component of a neuron or nerve cell. The axon carries signals from the main body of the neuron containing the nucleus to a target.

driving the inside of the axon to a relatively higher positive potential [278]. This sets in motion a cycle of changes in the transmembrane[13] potential that constitutes an action potential[14]. Since electrical stimulation of a nerve tissue mainly deals with the axon, this study focuses on modeling the interactions between an electrode and an axon.

5.2. Methodology and Assumptions

A cuff with two electrode leads is considered in the case study here. This model can be extended to a cuff with more than two electrodes. When a cuff electrode with bipolar stimulating electrode leads is placed on a nerve or a nerve fiber, the two electrode leads are above the nerve element (axon) being stimulated. The stimulating current flows through the tissue between the electrode leads. In the tissue, the current can travel either along the extracellular space, or within the membrane of the nerve cell being stimulated (Figure 5.1). The former current is called the extracellular current and the later current is called the transaxonal current. In the latter case, the current enters the nerve or the axon at a point and exits through another location.

Only the transaxonal current affects the membrane potential and travels through the nerve cell. Therefore, only this component of the applied current produces stimulation i.e. generates an action potential. It is, hence important to determine the transaxonal component of total current for a given magnitude and type of the applied stimulus signal. This is achieved in this work by modeling the electrical properties of the electrode-tissue interface by an equivalent circuit consisting of passive elements, namely resistors and capacitors. An electrode-tissue contact viewed as an electrode-electrolyte interface has been studied by several authors [141, 159, 279].

[13] Transmembrane potential: the potential difference between the inside and just outside an axon's membrane.

[14] Action potential: the cycle of changes in the transmembrane potential, from negative to positive to negative again, that characterizes an excitable tissue. This cycle is also described as the membrane transitioning from a resting state to an excited state, and subsequently returning to the rest state.

When a metal object or electrode is placed in an ionic solution, a space charge layer builds up at the interface. In terms of an electrical circuit equivalent, this space charge layer represents a capacitance, referred to in this study as the interface or interfacial capacitance, C_I.

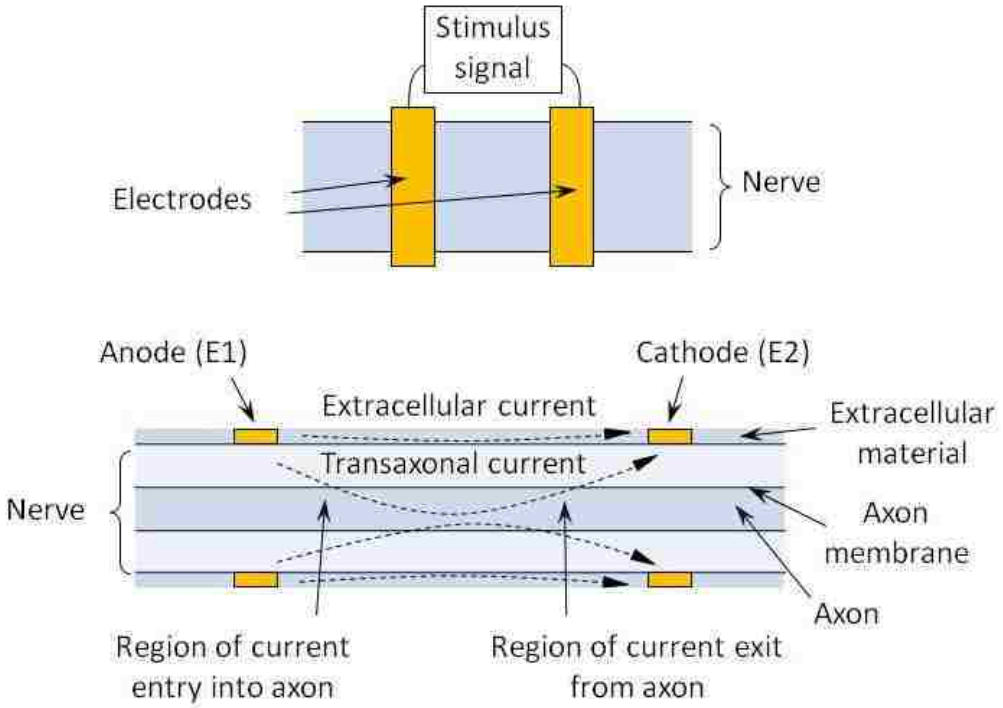

Figure 5.1: Schematic of stimulus current pathways through a nerve subjected to an electrical stimulus by means of two electrodes. Transmembrane potential is measured across the axon membrane.

Some charge manages to leak through the charge layer due to electrochemical reactions taking place at the interface [277]. Such charge leakage experiences a 'charge transfer' resistance, represented by R_{CT} in this study. R_{CT} forms a parallel combination with C_I, as shown in Figure 5.2. The final element to be considered in the circuit model represents the net resistance

R_S encountered by a current spreading out from an electrode into a conductive solution. R_S is in series with the parallel R-C combination [277].

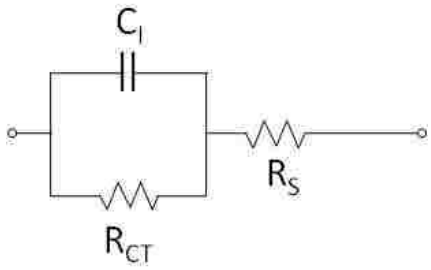

Figure 5.2: Schematic of an equivalent circuit representing an interface between an electrode and an electrolyte.

The second step in the development of the equivalent circuit is to represent the nerve tissue in terms of electrical elements [277]. The impedance for the extracellular current through the extracellular fluid around the axon will be primarily resistive and is represented by R_E in Figure 5.3A. Current can enter and exit an axon at the nodes i.e. the sections of the axon not covered by an insulating myelin sheath[15]. This entry and exit of current, represented by points M1 and M2 in Figure 5.3 encounters impedance associated with the membrane of the axon. The axon membrane can be represented by a capacitance C_M forming a parallel combination with a resistance R_M, shown in Figure 5.3C. The current flow in the axon encounters some resistance inside the axon or intra-axonal resistance R_A.

Following assumptions have been made in the present study [277]:

[15] Myelin sheath: a segmented, white fatty substance covering the axons. Myelin has a high electrical resistance and is considered to be electrically insulating.

1. The general ambient surrounding the cuff electrode device is considered to be a physiological saline medium.
2. For the purpose of simplicity, it is assumed that the cuff device has only two electrode leads.
3. The electrodes are made from platinum and are planar and rectangular with one side exposed to tissue. Though the fabrication of the clip-on micro-cuff device detailed in Chapter 4 describes the incorporation of stainless steel foil electrodes, this was intended for demonstration purposes only. Platinum foil electrodes can be incorporated using the same fabrication processes.
4. Effective surface area of the electrode i.e. the surface area exposed to tissue is 0.5 mm^2. The choice of this value is based on the electrode surface area in one of our clip-on micro-cuff embodiments which incorporated metal foil electrodes.
5. The myelin sheath has an infinitely high resistance i.e. it is a perfect insulator. Typical value for myelin sheath resistivity is 5-8 × 10^{14} Ω.cm [280].

5.3. Results and Discussion

5.3.1. Developed Equivalent Circuit

A version of the equivalent circuit for the electrode-tissue interface is shown in Figure 5.4. The equivalent circuit modules E1 and E2 include elements representing the interface capacitance, charge transfer resistance, and spreading resistance [277]. The modules E1 and E2 are adaptations from theoretical models typically used to represent the electrode-electrolyte interface [164, 281-283]. Our study does not include the Warburg impedance due to diffusion of the chemical reactants in solution. It has been reported that for electrodes based on platinum and platinum alloys, the Warburg impedance does not significantly contribute to the overall impedance in the frequency range 10^{-2} to 10^5 Hz [284].

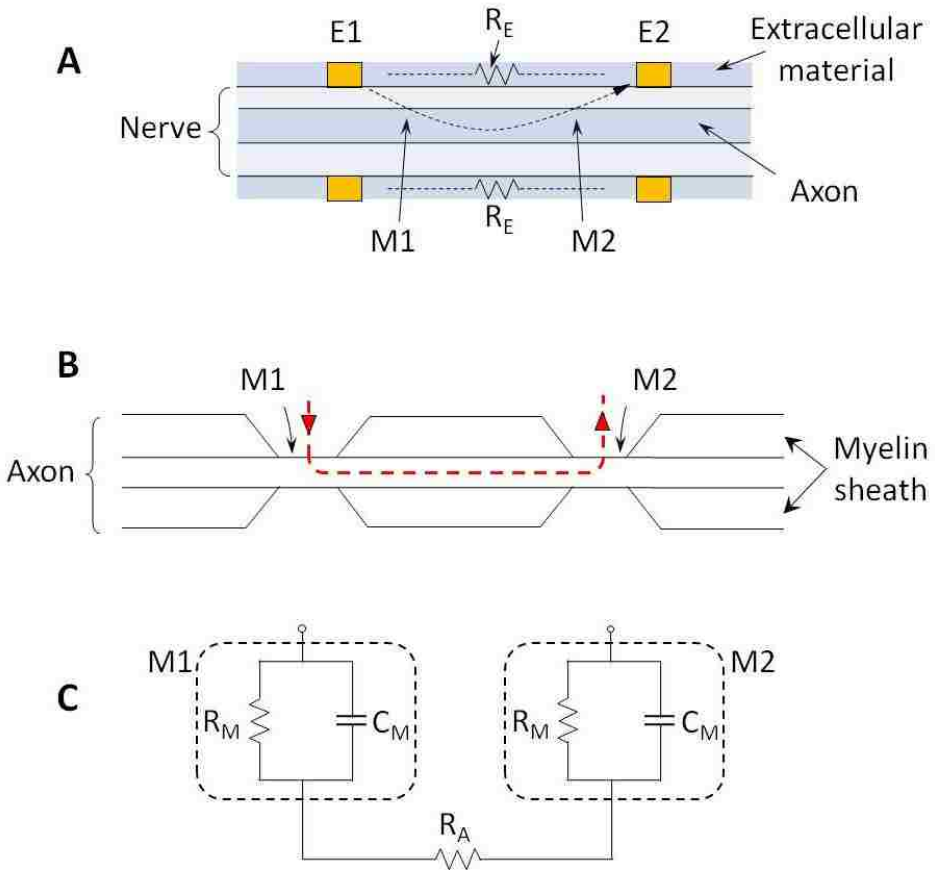

Figure 5.3: Schematic of (A) a nerve under electrical stimulus by means of electrodes E1 and E2; (B) entry and exit of current from an axon through points M1 and M2 at the nodes; (C) equivalent circuit representing the membrane at the two nodes, and the intra-axonal resistance.

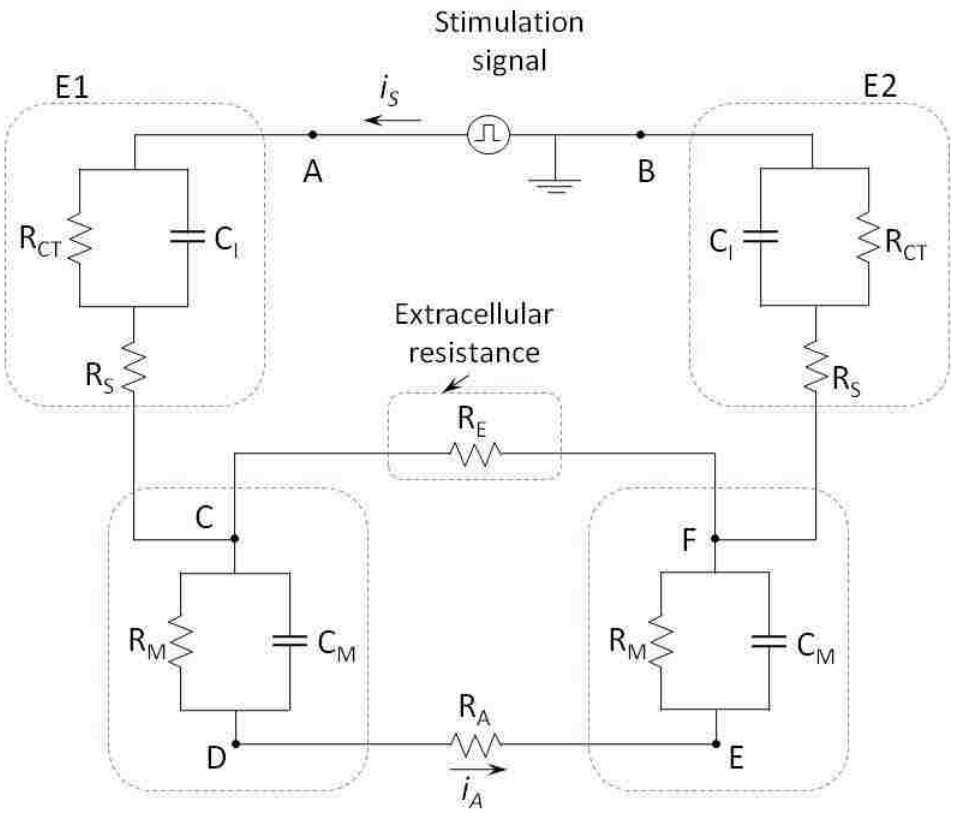

Figure 5.4: Schematic of an equivalent circuit for the electrical stimulus of a nerve by a two-electrode configuration. The circuit contains elements to represent the electrode-tissue interface and the main component axon of the nerve tissue being stimulated.

For the axon model, the distributed impedance for the extracellular current is represented by a resistor represented by R_E. The representation of the impedance for the trans-axonal current is slightly more complex. The membrane impedances at the entry and exit points into and out of the axon are represented by a capacitor C_M and a resistor R_M in parallel [277]. The intra-cellular axial resistance or intra-axonal resistance (i.e. the resistance inside the axon) is represented by resistor R_A. Current flowing in the axon or the axonal current is represented by i_A. The next stage involves the selection of appropriate parameters for the various elements of this equivalent circuit.

5.3.2. Selection of Circuit Element Parameters

Spreading resistance

The spreading resistance R_s (in Ω) for a planar rectangular electrode with one side exposed, is given by [282]:

$$R_S = \frac{\rho}{\pi l} ln\left(\frac{4l}{w}\right), \quad (5.1)$$

where ρ is the resistivity of the solution (in Ω.cm), l and w are the length and width of the rectangle. The solution resistivity ρ is 72 Ω.cm for physiological saline [282]. The values of l and w for the electrode in this study are 1 mm and 0.5 mm respectively and the aspect ratio l/w = 2. Using equation (5.1), we get R_S equal to 476.8 Ω.

Charge transfer resistance:

The charge transfer resistance R_{CT}, is derived from the Butler-Volmer equation, and for small applied signal amplitudes, is given by [285, 286]:

$$R_{CT} = \frac{RT}{AnFJ_0}, \quad (5.2)$$

where J_0 is the exchange current density, n is the number of electrons involved in the electrode reaction, R is the gas constant, T is the temperature (K), F is the Faraday constant. RT/F = 26 mV at 298 K and A is the electrode area. The exchange current density and the number of electrons involved in the reaction depend on the electrode material and the specific reaction occurring at that electrode [277]. In the present study, we assume that the electrode material is platinum. The value of J_0 is 4.5 x 10^{-6} A/cm^2 for a platinum electrode in physiological saline solution [282, 287]. The value of J_0 depends on electrode surface morphology. For the case of Pt electrode, charge transfer arises from the electrolysis of water, given by [288]:

$$2H_2O \leftrightarrow O_2 + 4H^+ + 4e^-. \quad (5.3)$$

From this reaction, n is equal to 4. Substituting for n, J_0, and R_{CT}, from equation (5.2), the value for R_{CT} obtained in this fashion is 289 kΩ for a 0.5 mm^2 Pt electrode in saline solution. A similar methodology can be used to calculate R_{CT} for different electrode materials in a specific solution, when J_0 values are known. Table 5.1 lists the J_0 values for some electrode materials in physiological saline solution.

Table 5.1: Values of exchange current density J_0 reported for some electrode materials operating in physiological saline ambient.

Material	Exchange current density (A/cm^2)	Reference
Bright platinum	8.5×10^{-8}	[284]
Platinum 90%, iridium 10%	6.41×10^{-8}	[283]
Gold	2×10^{-9}	[289]

Interface capacitance, C_I

A theoretical derivation of the interface capacitance is given by the Gouy-Chapman-Stern model [285]. The interface capacitance C_I is considered as a series combination of the Helmholtz capacitance C_H, and the diffuse layer capacitance C_G, and is given by [282]:

$$\frac{1}{C_I} = \frac{1}{C_H} + \frac{1}{C_G} = \frac{d_{OHP}}{\varepsilon_0 \varepsilon_r} + \frac{1}{2.28 cosh(19.5 z V_0) z \sqrt{C^*}}, \qquad (5.4)$$

where d_{OHP} is the thickness of the double-layer, ε_0 is the permittivity of free space, ε_r is the permittivity of the double layer, z is the charge on an ion in solution, V_0 is the applied electrode potential (in volts) with respect to the solution, C^* is the bulk concentration (in moles/liter) of the solution. The values of these variables and constants used in the determination of C_I are listed in Table 5.2.

For the sake of simplicity, the diffuse layer capacitance C_G has been neglected here. The calculated value of C_I from equation (5.4) for a platinum electrode in saline ambient is calculated

to be approximately equal to 1.39 F/m^2. For the electrode surface area (0.5 mm^2) in our study, the C_I capacitors in the equivalent circuit have value of approximately 0.6 μF.

Table 5.2: Values for variables and constants used in evaluating parameter C_I.

Parameter	Value	Note/Reference
d_{OHP}	5.8 Å	For physiological saline, d_{OHP} is 5 Å approximately [282]
ε_0	8.85 x 10^{-12} F/m	
ε_r	78.54	For dilute aqueous solution [282, 285]
z	4	For electrolysis reaction (platinum electrode) [290]
C^*	0.154 mol/liter	For physiological saline [282]

Extracellular resistance

Typical extracellular impedance between two electrode leads is about 2 to 5 kΩ [291]. Therefore, R_E for our study is considered to range between 2 to 5 kΩ.

Membrane capacitance and resistance

For the myelinated fiber, the entry and exit points for current will be at the nodes of Ranvier, as the inter-nodal transmembrane impedance is very high [280, 292]. An average value for the membrane capacitance C_M at a node of Ranvier of a myelinated axon is 0.8 - 1.5 μF/cm^2 [293, 294]. The membrane surface area at a node is given by 2π × (axon radius) × (node length). The axon radius is 5 μm in our model. The node length is assumed to be 4 μm [156]. For the membrane area under consideration, the calculated values of C_M range from 1 - 1.9 pF. The membrane resistance depends on its conductance and its surface area under consideration. The membrane conductance is about 30.3 mS/cm^2 [154]. Therefore, the calculated R_M value is about 26.3 MΩ. In literature, the membrane resistance R_M has been assumed to be 500 MΩ, with no specification on the membrane surface area or geometry [291]. Depending on the dimensions of

the electrodes, it is possible that current may enter the axon over more than one node. In such cases, the circuit considerations will get more involved.

Intra-axonal resistance

The intra-axonal resistance R_A or the resistance faced by the axonal current will depend on how far along inside the axon the current actually flows and the diameter of the axon. R_A can be determined by the following equation:

$$R_A = \frac{\rho l_A}{\pi r^2}, \quad (5.5)$$

where ρ_A is the axoplasmic resistivity, l_A is the length of axon segment, and r is the radius of the axon. The axon diameter is assumed to be 10 μm. This value matches the axon diameter values experimentally observed in frogs and cats [295]. The value of ρ_A is about 90-100 Ω.cm [280, 292]. For the present study, ρ_A is assumed to be 90 Ω.cm. The nodes of an axon are normally 1-2 mm apart, with 1 mm being a widely accepted value [296-298].

If we assume the axonal current flows in and out at immediately adjacent nodes spaced 1 mm apart on an axon, then the resistance to the axonal current will be about 11.46 MΩ. R_A will vary, depending on the length of the axon considered in the model and the spacing between the electrodes. Our micro-cuff electrode has two stimulating electrode leads separated by about 0.5 - 1 mm. Considering an electrode separation of 1 mm, R_A in our model is taken to be 11.46 MΩ. The values and value ranges for various elements in the developed equivalent circuit model are summarized in Table 5.3.

5.3.3. Selection of Stimulus Signal Parameters

Electric current in the electrode wires is carried by electrons, whereas current in the biological tissue is carried by ions. Chemical reactions which occur at the electrode-tissue interface are still

poorly understood. The shape and magnitude of the stimulus waveform used can significantly affect the tissue threshold response, the interface electrochemistry, and any resultant tissue damage [299].

Table 5.3: Values for the equivalent circuit components shown in Figure 5.4 for 0.5 mm^2 electrode area, axon diameter = 10 µm and node length = 4 µm.

Component	Description	Value / value range
R_S	Resistor representing the spreading resistance	477 Ω
R_{CT}	Resistor representing the charge transfer resistance	290 kΩ
C_I	Capacitor representing the interface capacitance	0.6 µF
R_E	Resistor representing the extracellular resistance	2 – 5 kΩ
R_M	Resistor representing the axon membrane resistance	26.3 MΩ
C_M	Capacitor representing the axon membrane capacitance	1 - 1.9 pF
R_A	Resistor representing the resistance inside an axon for 1 mm axon length	11.5 MΩ

The parameters of interest for the stimulus signal are pulse duration, pulse amplitude, signal shape, and frequency. These parameters are linked to the amount of stimulus charge supplied per pulse as they directly influence the amount of current flowing through the axon. These parameters also influence the electrochemical reactions occurring at the electrode surface [300]. The cuff electrode geometry and the details of the stimulus signal need to be optimized for achieving desired specific physiological effect.

For the stimulation of nerves, either current or voltage pulses can be used. Pulse amplitude and width depend on the charge requirement per pulse for the specific application selected. Stimulation of muscles, peripheral nerves or cortical surfaces require charge per pulse on the order of 0.04 – 5 µC [278, 301]. Charge per pulse required for neural stimulation is generally low. For nerves including the splanchnic or celiac ganglia, current signals with

amplitude from μA to mA range have been used [302]. The selection of pulse width parameters for the stimulus waveform is an important part of a FES application. There are some factors to consider including tissue damage by high charge injection, and electrochemical by-products. The selection of the pulse duration primarily depends on the chronaxie of the tissue to be stimulated. Chronaxie is the minimum interval of time necessary to electrically stimulate a muscle or nerve fiber, using twice the minimum current needed to elicit a threshold response. To minimize neuronal damage by the electrodes, the pulse duration should be at the level of the chronaxie of the stimulated tissue or slightly lower [144]. For stimulus durations of less than about one quarter chronaxie, nerve fibers will not be excited [291]. The chronaxie value mainly depends on type of tissue being stimulated. For example, chronaxie for human motor nerve has been reported to be about 0.01 ms, while that for pain receptors is 0.25 ms [303, 304]. The chronaxie for mammalian myocardium is about 2 ms [305]. For small-diameter nerve fibers, the chronaxie is about 1.5 ms [306]. Additionally, the chronaxie also depends on whether the neurons have a myelin sheath or not. The chronaxies for myelinated neurons determined with metal electrodes typically vary from 0.05 to 0.6 ms [307-311]. The chronaxie of unmyelinated neurons can be as high as 4 ms [310].

A review of literature seems to indicate benefits of short stimulus pulses, in general. Short stimulus pulses minimize the threshold charge, which is the amount of charge that must be injected to generate an action potential [145]. Minimizing the injected charge is an important consideration for prevention of electrode corrosion which depends on the charge density on the electrode surface [146]. Short stimulus pulsewidths minimize the time available for irreversible electrochemical reactions to occur on the electrode [148]. Short pulse widths should be used for neural stimulation when maximum selectivity is desired because they improve the ability to activate discrete groups of nerve fibers [150]. Finally, short stimulus pulses may prevent

stimulus induced neural damage [147, 312]. As regards to the frequency of the stimulus signal, frequencies from less than 100 Hz to kHz range have been employed for nerve stimulation [105, 313]. For applications such as electrical stimulation for obesity treatment, frequencies of 100 Hz or lower have been used [302]. Table 5.4 summarizes the typical parameter ranges for current stimulus signals as obtained from literature survey.

Table 5.4: Typical parameter range for current signals employed in the functional electrical stimulation of nerves and nerve fibers, obtained from literature.

Parameter	Value / value range
Pulse amplitude	≤ 3 mA
Pulse width	0.01 – 1.5 ms
Frequency	<100 Hz – <10 kHz
Charge delivered per pulse	0.04 – 5 µC

5.3.4. Results and Discussion

5.3.4.1. PSPICE Simulation Results

The developed equivalent circuit in Figure 5.4 for the electrode-tissue interface is simulated by means of PSPICE software. The values for the circuit elements used in the simulation are listed in Table 5.5. These have been chosen from the value ranges calculated in section 5.3.2.

Table 5.5: Values for the elements in the equivalent circuit shown in Figure 5.4.

Element	Value
R_S	477 Ω
R_{CT}	290 kΩ
C_I	0.6 µF
R_E	2 kΩ
R_M	26.3 MΩ
C_M	1.44 pF
R_A	11.5 MΩ/mm

A monophasic current pulse i_S (Figure 5.5) is applied as the stimulus signal to the circuit. The parameters for the current pulse are I_1 = 0, I_2 = 0.5 mA, and a pulse-width PW of 0.5 ms. The period PER is set at 1 ms. The rise time t_r and fall time t_f are set at 1 ns.

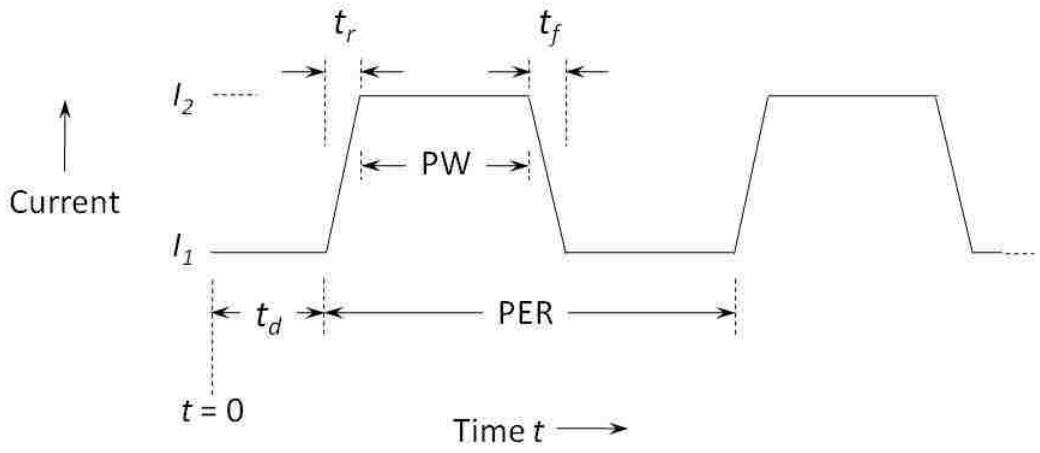

Figure 5.5: Current pulse waveform given as input to the equivalent circuit. The notations are as follows: I_1 = initial current level, I_2 = pulsed peak current level, and t_d is the pulse delay time.

The simulated axon current i_A is shown in Figure 5.6. This is a typical current range inside an axon during a normal action potential [291]. The PSPICE simulation conditions, parameters and an example output file are provided in Appendix E. This simulated current matches the theoretical current (Figure F.1, Appendix F) obtained from equation (F.22), upon excitation by a step pulse of amplitude of 0.5 mA at t = 0. The details are provided in Appendix F. The time constant for the axon current given by equation (F.9) is 6.8 μs resulting in the circuit approaching steady state value in less than 0.05 ms.

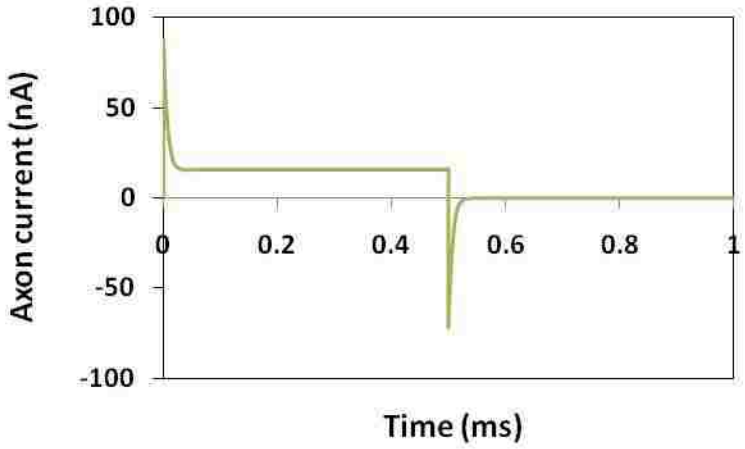

Figure 5.6: The axon current i_A as a function of time, simulated on PSPICE for a pulsed current input signal shown in Figure 5.5. The parameters of the input signal are $I_1 = 0$, $I_2 = 0.5$ mA, $t_d = 0$, $t_r = 1$ ns, $t_f = 1$ ns, $PW = 500$ µs, $PER = 1$ ms.

5.3.4.1.1. Effect of Input Current Signal

The magnitude of the steady-state axon current i_A during the period PW is a function of the amplitude of input current signal i_S (Figure 5.7). For PW and (PER-PW) greater than 5τ (in this case, 34 µs), the magnitude of the steady-state axonal current i_A is not significantly influenced by the values of PW and PER. However, for PW and (PER-PW) within 5τ, the axon current does not approach steady-state values and is influenced by the pulse-width and the period of the input signal.

The axon power changes parabolically with axon current due to relationship between current (i_A) and power ($i_A^2 R_A$) (Figure 5.8). The axon power peaks at the pulse transitions and should reach a steady-state value exponentially with time constant of τ/2 during the pulse period PW. The PSPICE results indicate that steady-state values are not reached for PW less than 5τ, which in the present case is 34 µs.

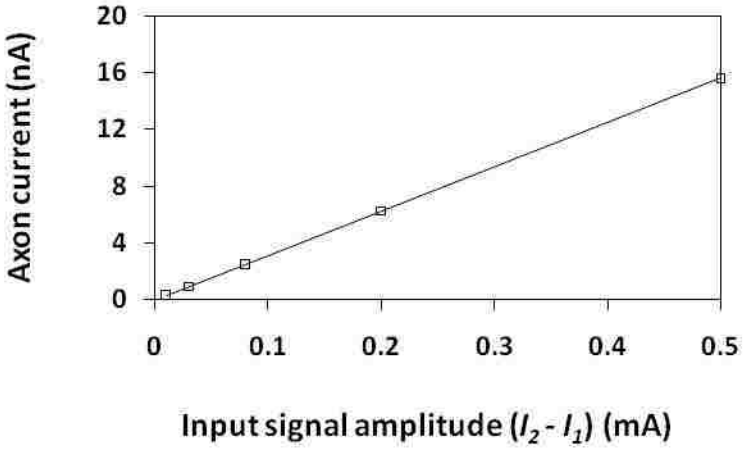

Figure 5.7: Amplitude of steady-state axon current i_A as a function of the steady-state input signal amplitude. I_1 = 0, I_2 = 10, 30, 80, 200, and 500 µA, t_d = 0, t_r = 1 ns, t_f = 1 ns, PW = 500 µs, PER = 1 ms.

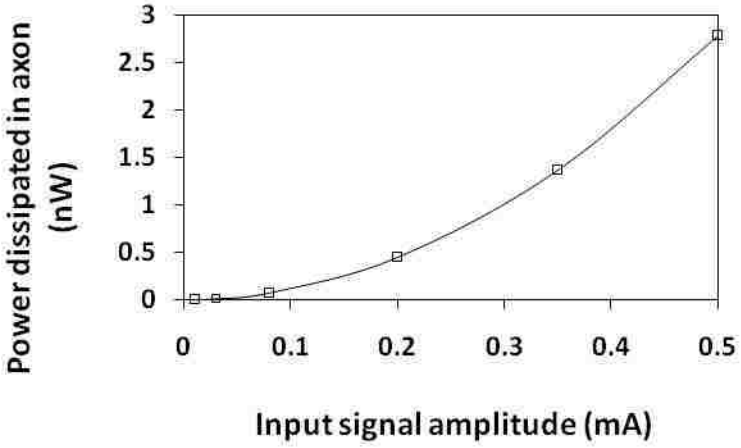

Figure 5.8: Steady-state power dissipated in an axon during the pulse period PW as a function of input signal amplitude. The input signal was a pulsed current signal with I_1 = 0, I_2 = 10, 30, 80, 200, and 500 µA respectively; t_d = 0, t_r = 1 ns, t_f = 1 ns, PW = 500 µs, PER = 1ms.

5.3.4.1.2. Axon Length

Figure 5.9 shows the steady-state membrane voltage during the pulse period PW as a function of distance from the node, or in other words length of the axon. The membrane voltage is the voltage across the membrane, measured at node E with respect to node F in the circuit shown in Figure 5.4. The axon resistance, R_A increases as its length increases. Consequently, the membrane voltage decreases as R_A increases. The decrease in membrane voltage observed in this simulation is similar to that seen in actual measurements of membrane voltage in axons [314].

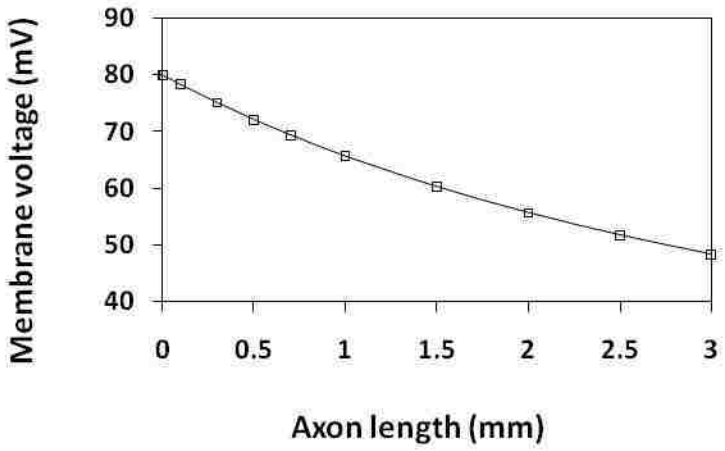

Figure 5.9: The steady-state axon membrane voltage during the pulse period PW as a function of the axon length. The input signal was a pulsed current signal with $I_1 = 0$, $I_2 = 80$ µA; $t_d = 0$, $t_r = 1$ ns, $t_f = 1$ ns, $PW = 500$ µs, $PER = 1$ms.

Figure 5.10 shows the steady-state axon current i_A during the pulse period PW as a function of length of the axon. As can be expected, the steady state axon current decreases with an increase in axon length, and hence increasing R_A. The change in R_A also causes a change in the time constant. These results are supported by equations (F.9) and (F.19) in the theoretical calculations detailed in Appendix F.

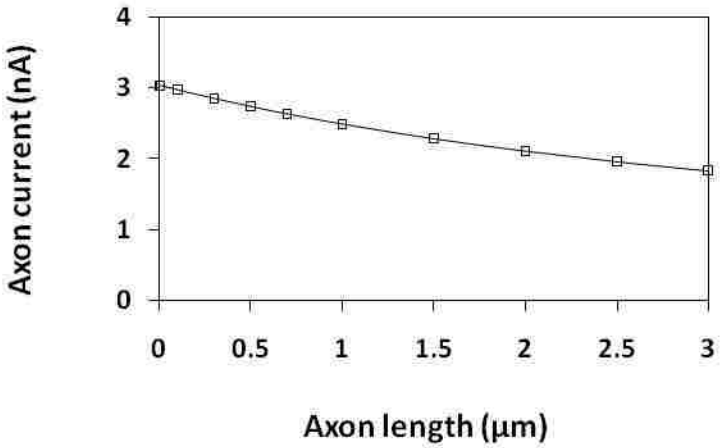

Figure 5.10: The steady-state axon current i_A during the pulse period PW as a function of the axon length. The parameters of the input signal were $I_1 = 0$, $I_2 = 80$ µA; $t_d = 0$, $t_r = 1$ ns, $t_f = 1$ ns, $PW = 500$ µs, $PER = 1$ms.

5.3.4.1.3. Axon Radius

The radius of the axon plays an important role in defining its electrical behavior. Figure 5.11 shows the membrane voltage at node E with respect to node F in Figure 5.4 as a function of the axon radius. As the axon radius increases, its membrane resistance (R_M) decreases and its capacitance (C_M) increases. The axon resistance (R_A) also decreases with an increase in the axon radius. The changes in these component values influence the membrane voltage. A change in axon radius influences the axon current (Figure 5.12). The axon current transients are affected due to change in both the membrane capacitance and the resistance. The magnitude of steady-state axon current i_A during the pulse period PW is affected by a change in the value of resistance only and not by membrane capacitance (Figure 5.12). This is evident from PSPICE simulation data, not shown here.

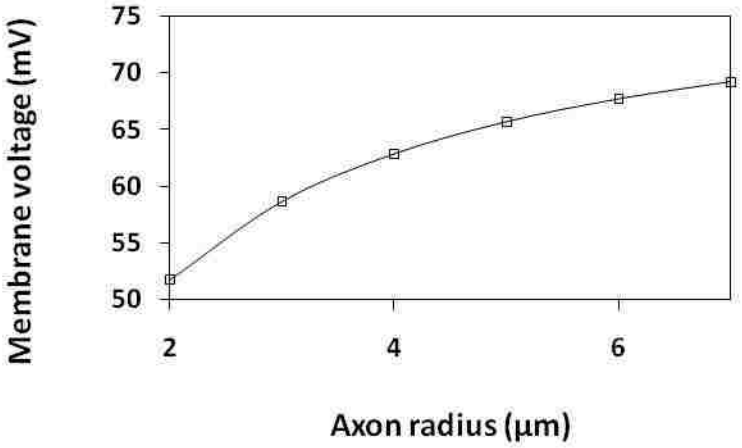

Figure 5.11: Steady-state membrane voltage during the pulse period PW as a function of the axon radius. The parameters of the input signal were I_1 = 0, I_2 = 80 µA; t_d = 0, t_r = 1 ns, t_f = 1 ns, PW = 500 µs, PER = 1ms.

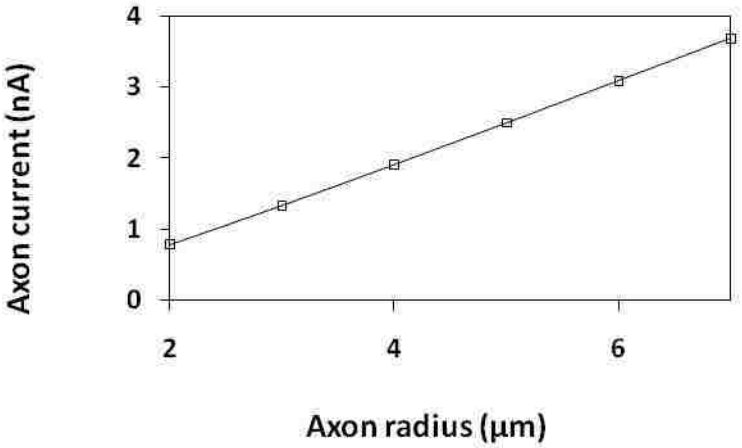

Figure 5.12: The steady-state axon current i_A during the pulse period PW as a function of axon radius. The input signal was a pulsed current signal with I_1 = 0, I_2 = 80 µA; t_d = 0, t_r = 1 ns, t_f = 1 ns, PW = 500 µs, PER = 1ms.

When axon radius is increased, an overall consequence is decrease in time constant for the axon current (Figure 5.13). This is consistent with the reported observation that a larger diameter of axon results in a faster conduction velocity or the rate at which the axon transmits a signal [315].

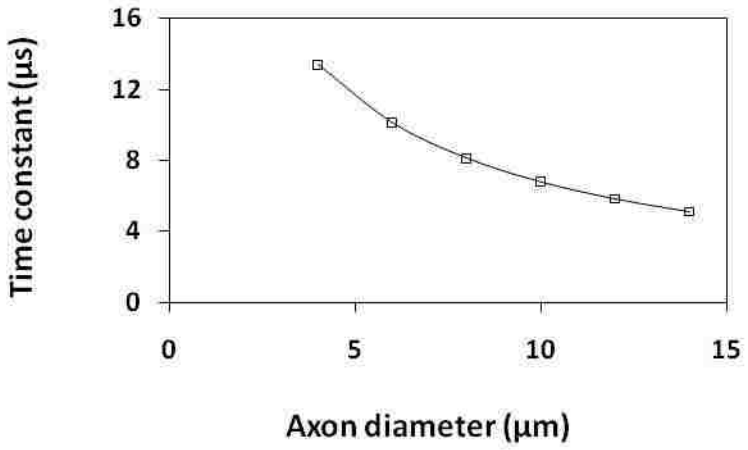

Figure 5.13: Time constant of axon current as a function of its radius, obtained using equation (F.9) in Appendix F.

5.3.4.1.4. Charge per Pulse

For a given set of circuit element values, the charge per pulse injected depends on the amplitude of the input current signal amplitude i_S and the pulse-width (PW) for monophasic signals. The calculation of the charge per pulse is straightforward, given by a product of i_S and PW. The typical values of charge/pulse employed in electrical stimulation of neural tissue for various biomedical applications are wide ranging. Some reports have employed relatively low charge/pulse with neuronal damage being reported at charge values as low as 8 nC/pulse [316]. However, many other reports on neural stimulation have employed larger charge/pulse values.

The charge per pulse can be minimized by employing shorter pulse-widths [274]. To the best of our knowledge, there are no reports on the actual charge flow inside an axon during electrical stimulation.

5.3.4.1.5. Monophasic and Biphasic Current Pulses

The main drawback with monophasic current pulse signals is that voltage level at the electrode (measured at node A with respect to node C in Figure 5.4) builds up by adding on to that of the preceding cycle (Figure 5.14A). This results in voltage levels that can be high enough to induce certain electrochemical reactions at the electrode which may not be desirable in terms of either electrode integrity or for avoiding or minimizing neural damage [317]. Additionally, as voltage levels increase, average power levels over a period also increase at the electrode (Figure 5.14B). The power dissipation is measured between the nodes A and C in Figure 5.4.

The voltage at the electrode in the case of monophasic current pulse increases as the duty cycle is increased to 50%. Electrode voltage data for three different duty cycles of 10%, 33% and 50% is shown in Figure 5.14A. This is due to a large value associated with electrode capacitance C_I. For a monophasic current pulse, it is preferable to employ a low duty cycle by keeping the pulse-widths small.

One way to address the voltage problem is to discharge or depolarize the electrode after every monophasic pulse [318]. This will help maintain voltage levels in a desirable range. PSPICE simulation results suggest a better way to address this by employing biphasic current pulses, where the current goes from a negative to a positive value and returns to the negative value. The electrode voltage magnitude decreases as duty cycle increases to 50% for a biphasic current pulse signal (Figure 5.15A). The average power dissipated during a cycle at the electrode is also low for the 50% duty cycle, compared to 10% and 33% duty cycles (Figure 5.15B).

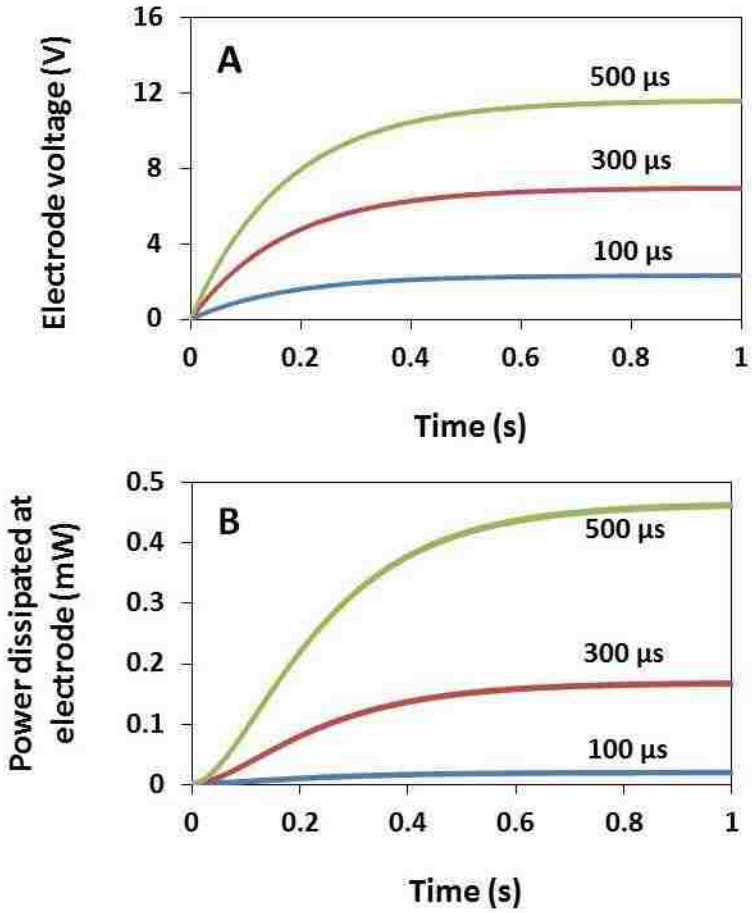

Figure 5.14: (A) Electrode voltage as a function of time for three different PW values of 100 µs, 300 µs, 500 µs respectively, for a monophasic pulsed current input signal. (B) Average power dissipated per cycle at the electrode as a function of time, for the same signal. In both cases, the parameters of the input signal are I_1 = 0, I_2 = 80 µA, t_d = 0, t_r = 1 ns, t_f = 1 ns, *PER* = 1 ms.

For biphasic current pulses, a duty cycle of more than 50% yields increased voltage at the electrode, and therefore increased power dissipation at the electrode. Therefore, it can be inferred that it is appropriate to employ a duty cycle of 50% for biphasic current pulses or a charge balanced current signal. It has been reported by several researchers that charge balanced biphasic current pulses yield good results in terms of reduced neuronal damage [319, 320].

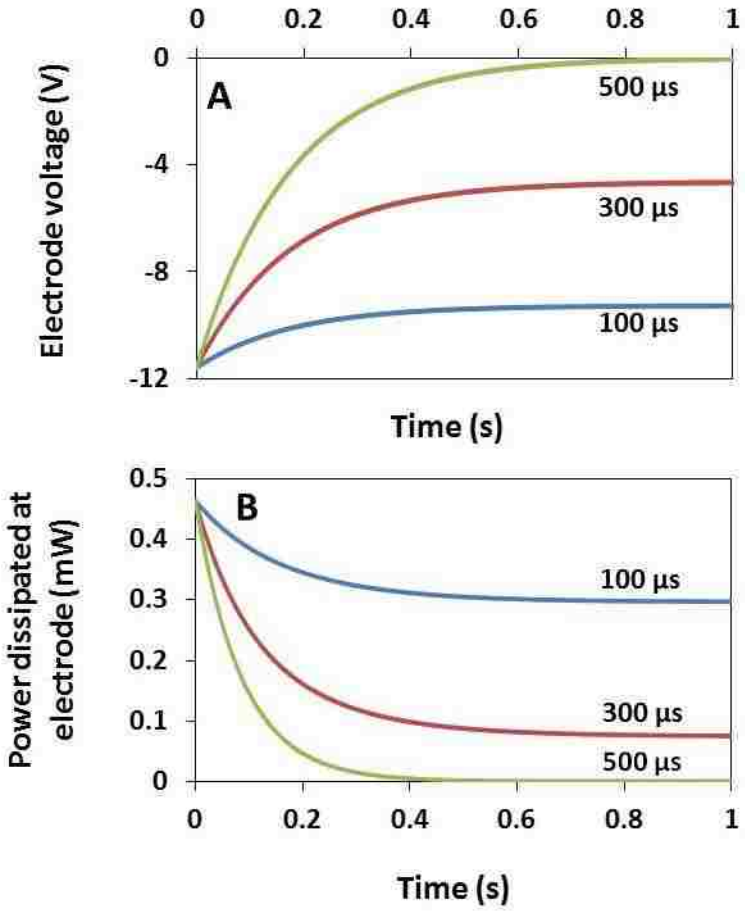

Figure 5.15: (A) Electrode voltage as a function of time for three different pulse-width values of 100 µs, 300 µs, 500 µs respectively, for a biphasic pulsed current input signal. (B) Average power dissipated per pulse at the electrode as a function of time, for the same signal. In both cases, the parameters of the input signal were I_1 = - 40 µA, I_2 = 40 µA, t_d = 0, t_r = 1 ns, t_f = 1 ns, *PER* = 1 ms.

5.3.4.1.6. Pulsed Voltage Signals as Input

PSPICE simulations are presented here for the case of a monophasic pulsed voltage signal as input. The parameter description of this voltage signal is the same as the pulsed current signal described in Figure 5.5, except that units of amperes are replaced with volts. Figure 5.16 shows the input current in the case of a 1V monophasic square pulse signal for two different duty cycles of 10% and 33% respectively. As the pulse-width increases, input current decreases

during the 'ON' time of the input pulse (Figure 5.16A). For long enough voltage pulse-widths (PW > 5 time constants), input current will approach the steady-state value during the 'ON' time (Figure 5.16B). It is desirable to have input current as constant as possible. For this reason, it is preferable to employ a smaller duty cycle or shorter pulse-width for monophasic voltage pulses.

In the case of a voltage pulse input, the problem pertaining to voltage build-up at the electrode and therefore power dissipated at the electrode is decreased, compared to monophasic and biphasic current pulses. This is evident from simulation results showing the average power dissipated at the electrode as a function of time (Figure 5.17), when a 1V square pulse is given to the equivalent circuit. The average power dissipated per pulse from $t = 0$ to $t = 1$s is displayed. This power is measured between nodes A and C in the circuit shown in Figure 5.4. As in the case of monophasic current signals, the average power is lower for a smaller duty cycle. For a 10% duty cycle, the average power is approximately 5 μW. For 33% and 50% duty cycles, the average power is approximately 11 μW, and 14 μW respectively. So, shorter PW is desirable here.

5.3.4.1.7. Tissue Heating

The normal temperature of physiological tissue is 37 ^{0}C. It is a well-established fact that thermal necrosis or damage to cells and biological tissue starts at 42 ^{0}C [321, 322]. For the range of stimulus parameters typically employed in FES, ohmic heating has been excluded as an injury causing mechanism [323, 324]. In their study on heating of tissue in neural stimulation, Ruggeri *et al* reported that for electrodes with surface area greater than 0.0013 mm^2 operated with current densities greater than 10 A/cm^2, the peak temperature rise is less than 1 ^{0}C [324]. They also reported that smaller electrodes or higher current densities will produce greater temperature rise. This implies that tissue heating will not be a factor in our study where the surface area of each

electrode is 0.5 mm^2 and the maximum current density is 2 A/cm^2, assuming a worst-case scenario of a 10 mA pulsed current input signal. Therefore, in the present modeling study, tissue heating aspect has been omitted.

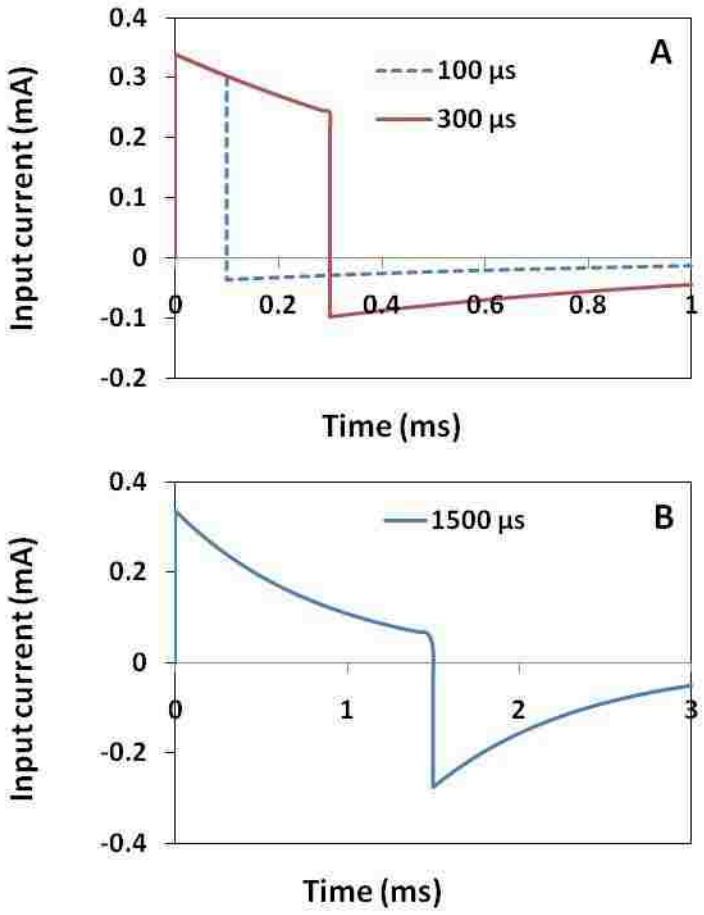

Figure 5.16: (A) Magnitude of input current i_S as a function of time, for a monophasic pulsed voltage input signal v_S with a period of 1 ms, PW of 100 µs, and 300 µs respectively. (B) Input current as a function of time, for the same monophasic pulsed voltage input signal, but with a period of 3 ms and a PW of 1500 µs. In all cases, the parameters of the input signal were V_1 = 0V, V_2 = 1V, t_d = 0, t_r = 1 ns, t_f = 1 ns.

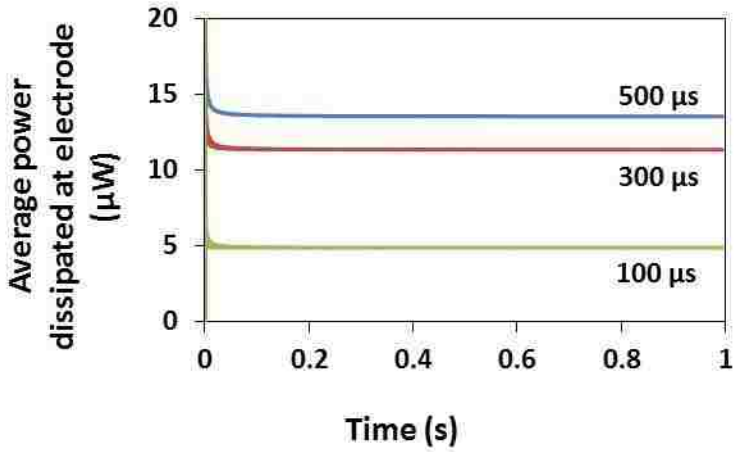

Figure 5.17: Average of power dissipated per pulse at the electrode (between nodes A, C in the circuit) as a function of time, for a monophasic pulsed voltage input signal. The parameters of the input signal were V_1 = 0V, V_2 = 1V, t_d = 0, t_r = 1 ns, t_f = 1 ns, *PER* = 1 ms, PW = 100 µs, 300 µs, and 500 µs.

5.3.5. Summary

An elaborate discrete element equivalent circuit model has been developed to represent an electrode-neural interface. The phenomena occurring in an axon during electrical stimulation define the physiological response incited by the applied electrical stimulus. The equivalent circuit of an axon under electrical stimulation described here can be employed to study the influence of a particular stimulus signal on nerve tissue and to optimize the stimulation protocol. The methodologies described here can be applied to model interfaces formed by electrode surfaces with other types of tissues. The accuracy of the PSPICE simulations, verified by theoretical calculations, shows the feasibility of using this software as a modeling tool in conjunction with such equivalent circuits.

Previous reports have represented the electrode-tissue interface as an electrode immersed in an electrolyte and have neglected any representation of the internal components of the tissue being stimulated [164, 281-283]. Other reports have focused solely on representing the tissue being stimulated in terms of electrical circuit equivalents. To illustrate, some equivalent circuits have been reported to represent nerve tissue and axons in specific [154, 156, 313, 325-327]. However, these models do not include any components or modules to represent the metal surface and the interface formed by it with the tissue. In this context, the present development of an integrated equivalent circuit model with components to address all the aspects of tissue being stimulated by a metal surface is of value.

CHAPTER 6: ROUTING TECHNOLOGY FOR FES APPLICATIONS

6.1. Introduction

In the use of a percutaneous access device (PAD), the interface between the PAD body and the skin tissue has to be preserved for the proper operation of the PAD [328, 329]. A typical PAD has a skin piercing conduit for making connections to the external world. Forces on the skin-piercing PAD conduit create motion, resulting in tearing of the surrounding skin and the loosening of the PAD-tissue anchoring interface at the base [187-189, 209, 228]. This can prevent the PAD from being anchored and provide for pathways for bacterial infection [190, 209]. Therefore, it is essential to minimize the mechanical stresses at the PAD-skin interface, caused by external forces [229, 230].

In a structure subjected to a load, the stress is often assumed to be distributed uniformly over each cross-section. However, there may be conditions that may cause the stress at a point in a structure to be different from the rest of the structure. These conditions including some specific feature or geometrical discontinuity in the structure, may result in stress gradients. Typically, large localized stresses due to stress concentrations are developed only in a small portion of the structure. The nature of stress in the neighborhood of a geometrical discontinuity in a solid can be explained by the theory of lines of force or stress trajectories. The latter, whose paths lie in the material, cluster together when passing around a geometric discontinuity with reduced average spacing between the lines signifying higher local stress [258, 330-332]. The theory of lines of force has been extended to the design of novel PADs developed here [333, 334]. These PAD designs attempt to localize stress in the PAD conduit structure by means of circumferential notches and corrugations with notches in the conduit [333, 334]. The concept of lines of force suggests a redistribution of strain energy from the regions surrounding a notch to a highly

strained region at the tip or the root of the notch. The stress due to applied forces is hence not entirely focused on the base of the PAD conduit due to presence of these high strained regions. The developed PAD designs incorporate a conduit with one or more circular notches or corrugations with notches located circumferentially in the exposed part of the conduit (Figure 6.1).

These designs also incorporate a base with tailor-made pores to allow for device anchoring by connective tissue growth [333]. Ideally, stress is concentrated at the root of a notch on application of an external force, permitting the conduit to bend more easily at the notch rather than at the PAD-skin interface, extending the life of the PAD. This may also reduce or eliminate dermal tear around the conduit, thereby reducing the risk of bacterial infection.

The following sections detail the methodologies to achieve the developed PAD designs. One of the developed designs, the notched conduit PAD structure, has been realized by a molding process using Silastic, a medical grade silicone elastomer. The pores of the PAD base were in-built, i.e. made in the device body material [333, 335].

6.2. Theoretical Modeling

Mechanical modeling of a PAD with a single, circular, circumferential notch on the conduit is considered first to understand the effects of the presence of a notch on the PAD conduit. The study allows selection of optimal parameters for the dimensions of the notch and the PAD base. The following assumptions have been made in the current model:

1. The PAD conduit is assumed to exit the skin at right angles to the plane of the skin. This is a reasonable assumption because most PADs penetrate the skin at right angles to the skin plane [228].

2. In FES applications, a PAD is typically used to route electrical wires from implanted electrodes to externally situated equipment. A small inner diameter of the conduit is sufficient for this purpose since diameter of the insulated electrical wires used is typically small. For example, in nerve cuff devices used in this work, multiple wires from the electrode are enclosed in insulation with a total outer diameter of 300 to 500 µm. Since the inner diameter of the conduit is small compared to its overall diameter (typically about a few mm), the present modeling study considers the PAD conduit as a solid cylindrical shaft.
3. For a typical PAD device, lateral, axial, and torsional forces can be present on the skin piercing conduit [228]. Seldom does a situation exist in which only one of these forces is acting alone. More often, two or perhaps all the three forces act simultaneously. However, for the sake of simplicity, effect of each force is considered separately in the present modeling study.
4. A typical PAD is expected to act as a routing interface for the exit of electrical wires from an implant to outside the body. Wires exiting the body are usually enclosed in cables which may be attached to electronic hardware and instrumentation. The entire cable assembly typically weighs 3.5-13 gm, but this weight is largely supported by relief mechanisms outside the body [336]. Therefore, the actual load experienced by the body is low, with some values reported in the range of ≤0.01 N [55]. The present model assumes forces acting on the PAD to be in the range 0.1-0.2 N.
5. In the simulations, the PAD base is considered as a curved beam with a rectangular cross-section. A cylindrical through-hole is formed at the center of the curved beam. The inner

diameter of the cylindrical through-hole is equal to the outer diameter of the PAD conduit.

6. In a typical PAD, forces acting externally on the PAD conduit are transferred to the PAD base [337]. The present model includes combined forces acting on the base.

The notched conduit of the PAD is modeled as a cylindrical shaft with a notch along the circumference of the shaft (Figure 6.2). The circumferential notch has a circular cross-section. To determine the effect of the notch in the conduit, Neuber's theorem is applied to a cylindrical member with a circumferential notch. Neuber described a dimensionless stress concentration factor to study the influence of cracks, grooves or notches in a member [338, 339]. In the present study, a Neuber-type analysis has been applied to study the effect of a notch on the PAD conduit and the influence of the notch parameters on the concentration of stress at the notch. This kind of analysis has been often employed to study the effect of cracks and related stress concentrations in structures [340, 341].

The calculated stress concentration factor (S_{cc}) is a dimensionless quantity that is indicative of the extent of stress concentration in a structure. For a cylindrical member containing a notch, S_{cc} is given by Neuber as [338, 339]:

$$S_{cc} = 1 + \frac{(S_{cs} - 1)(S_{cd} - 1)}{\sqrt{(S_{cs} - 1)^2 + (S_{cd} - 1)^2}}, \qquad (6.2\text{-}1)$$

where S_{cs} is the calculated stress concentration factor when the notch is shallow, and S_{cd} is the calculated stress concentration factor when the notch is very deep.

$$S_{cs} = 1 + 2\sqrt{\frac{t}{\rho}}, \text{ and} \qquad (6.2\text{-}2)$$

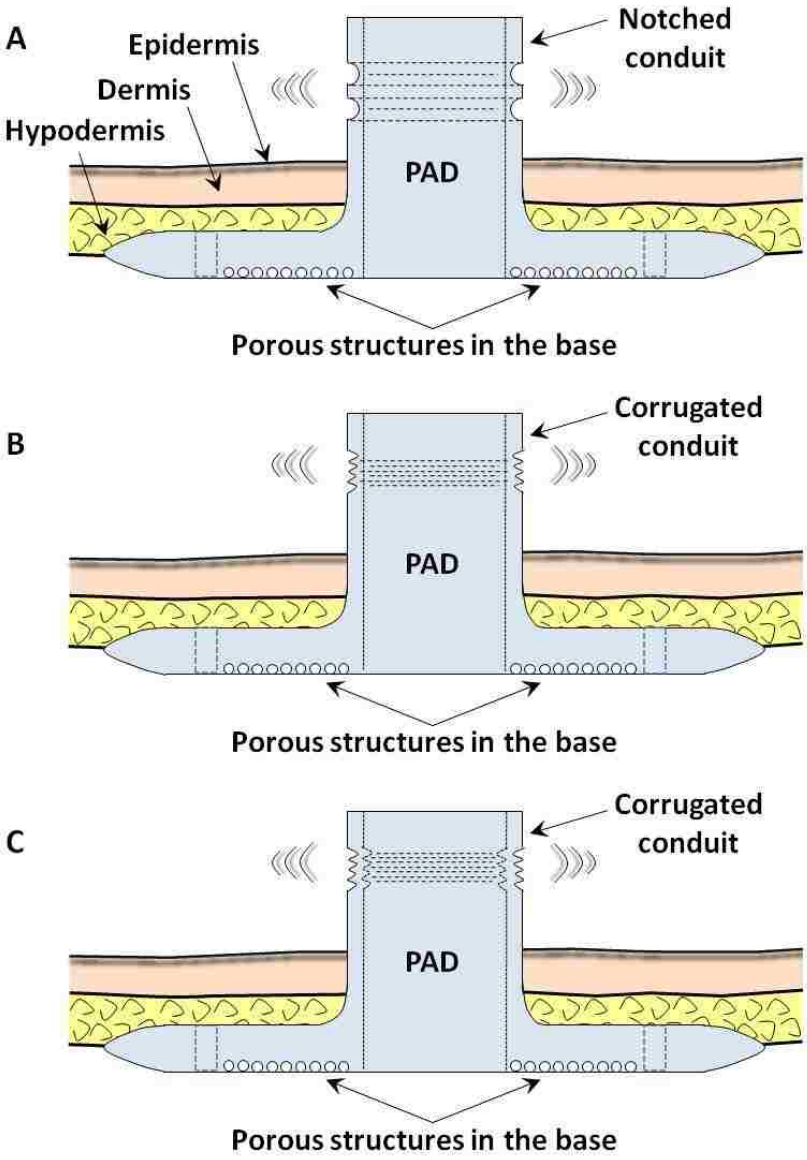

Figure 6.1: Schematic representations of (A) a PAD with circumferential notches on its conduit; (B) a PAD with circumferential corrugations on the outer side of the conduit; (C) a PAD with corrugations on both sides of the conduit. All devices have pores incorporated in the bases. Diagrams are not drawn to scale.

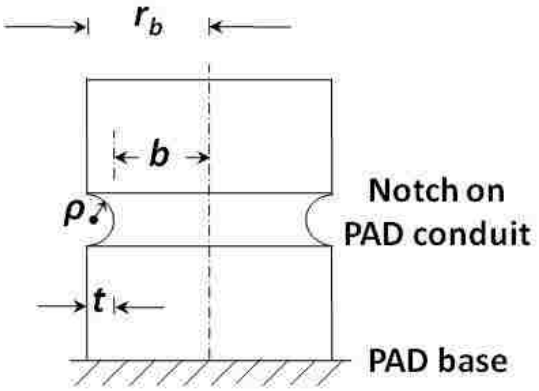

Figure 6.2: Schematic diagram of a cylindrical member with a circumferential notch. The notch has a circular cross-section. The cylindrical member is fixed at one end. The conduit of the developed PAD design is modeled by this structure. Diagram is not to scale.

$$S_{cd} = \frac{2\left(\frac{b}{\rho}+1\right)\sqrt{\frac{b}{\rho}}}{\left(\frac{b}{\rho}+1\right)\left(arctan\sqrt{\frac{b}{\rho}}\right)+\sqrt{\frac{b}{\rho}}}\ , \qquad (6.2\text{-}3)$$

where t is the depth of the notch, ρ is radius of curvature at the root of the notch, $b = r_b - t$ is the cross-section radius at the root of the notch. Using the equations listed above, the influence of the notch dimensions on the stress concentration factor is studied.

Figure 6.3 shows the variation of the stress concentration factor S_{cc} as a function of the depth of the notch. The results show that the presence of a notch is clearly a factor influencing the localization of stress in the cylindrical member. When the value of notch depth is zero, S_{cc} is at its lowest value of 1. As t increases, S_{cc} increases. With increased notch depth, more stress is concentrated at the notch. The increase in S_{cc} is not significant for larger values of ρ at the notch root located at distance b from the center axis. This is apparent from Figures 6.3 and 6.4. The effect of the notch depth on the S_{cc} value is reduced for larger values of radius of curvature at the

notch root. When the value of notch depth is zero, S_{cc} remains constant at its lowest value of 1 indicating that in the absence of a notch, the cylindrical member will not localize the stress in the structure.

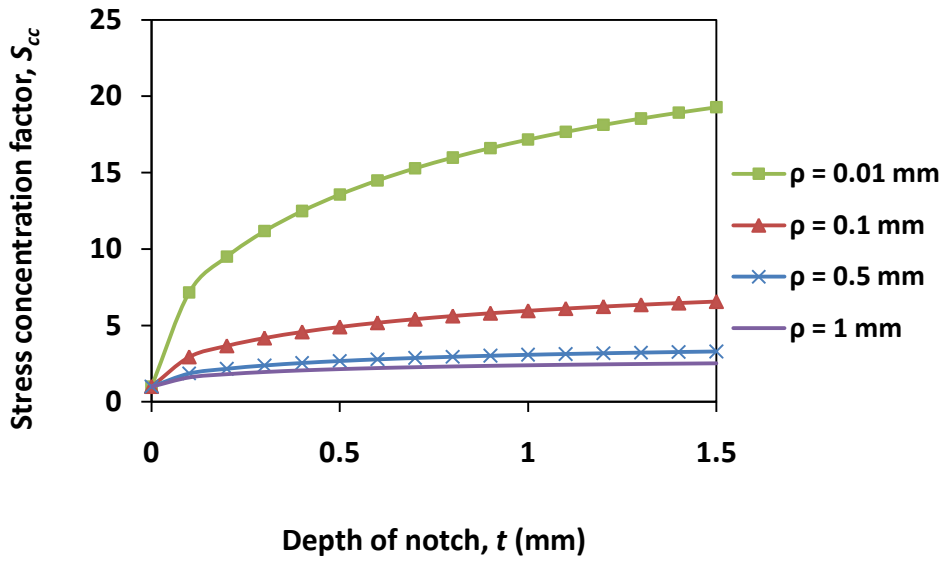

Figure 6.3: Variation of the stress concentration factor S_{cc} as a function of the depth of the notch t. The calculations are repeated for different radii of curvature ρ at the notch root. b = 5 mm. Reprinted with permission from N.S. Korivi, and P.K. Ajmera, "Percutaneous access device with stress relief features," Proceedings of the ASME 2010 5th Frontiers in Biomedical Devices Conference, Paper Number BioMed2010-32022. Copyright 2010 by ASME.

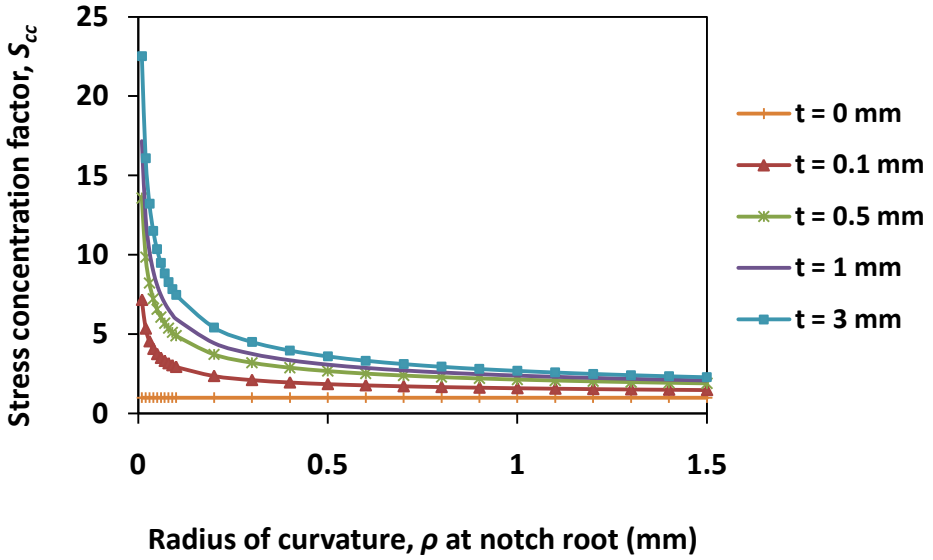

Figure 6.4: Variation of S_{cc} as a function of the radius of curvature ρ at the notch root. The data has been plotted for different values of notch depth t. b = 5 mm. Reprinted with permission from N.S. Korivi, and P.K. Ajmera, "Percutaneous access device with stress relief features," Proceedings of the ASME 2010 5th Frontiers in Biomedical Devices Conference, Paper Number BioMed2010-32022. Copyright 2010 by ASME.

The following equations were employed to calculate the nominal stress produced at the notch root by each type of force [258]:

Stress from axial force $= \frac{P}{\pi b^2}$, (6.2-4)

Stress from shear force $= \frac{1.23V}{\pi b^2}$, (6.2-5)

Stress from bending moment $= \frac{4M}{\pi b^3}$, and (6.2-6)

Stress from twisting moment $= \frac{2T}{\pi b^3}$, (6.2-7)

where P, V, M, T are the axial force, direct shear, bending moment and twisting moment respectively, $b = r_b - t$ is radius of the cylinder cross-section at the root of the notch. The b value is indicative of the physical extent or depth of the notch t for a given overall cylinder radius. As equations (6.2-4) through (6.2-7) give the stress at the notch root and since $t \geq \rho$, the radius of curvature of the notch is not a factor in these equations. The magnitude of a particular incident force was maintained constant and its effect on the induced stress in the cylinder was studied for different values of b.

Figures 6.5 and 6.6 show the variation of nominal stress as a function of the cross-section radius at the notch root when a force or moment is applied. These results may be seen with two different perspectives. In the first case, if the notch depth t is maintained constant and the cross-sectional radius b at the notch root is changed, then the cylinder outer radius r_b or $(b + t)$ changes. Figures 6.5 and 6.6 indicate the expected results that a larger b value will function to reduce the effect of forces or moments applied on the cylinder.

The second case arises when the outer radius of the cylinder $(b + t)$ is kept constant. Then, an increase in b implies a complementary decrease in t. As the b value increases, implying decreasing notch depth, the stress related to a particular incident force or moment is reduced or as the b value decreases, the stress is increased. This is an expected effect of the notch depth influence on stress concentration. For smaller b values, i.e. larger notch depths, there is more effect of the applied force or moment. This can be observed for the four types of forces and moments incident on the cylindrical structure. Regardless of the particular perspective by which these results are observed, the general trends for the results shown here are valid.

For the same magnitude, the direct shear appears to have more influence on the nominal stress than the axial force. Similarly, for the same magnitude, the bending moment appears to

have more influence on the nominal stress than the twisting moment (Figure 6.6). This is clearly evident in the lower *b* region. It should be noted that a value of 0.1 N.mm has been employed to represent each type of moment in these simulations.

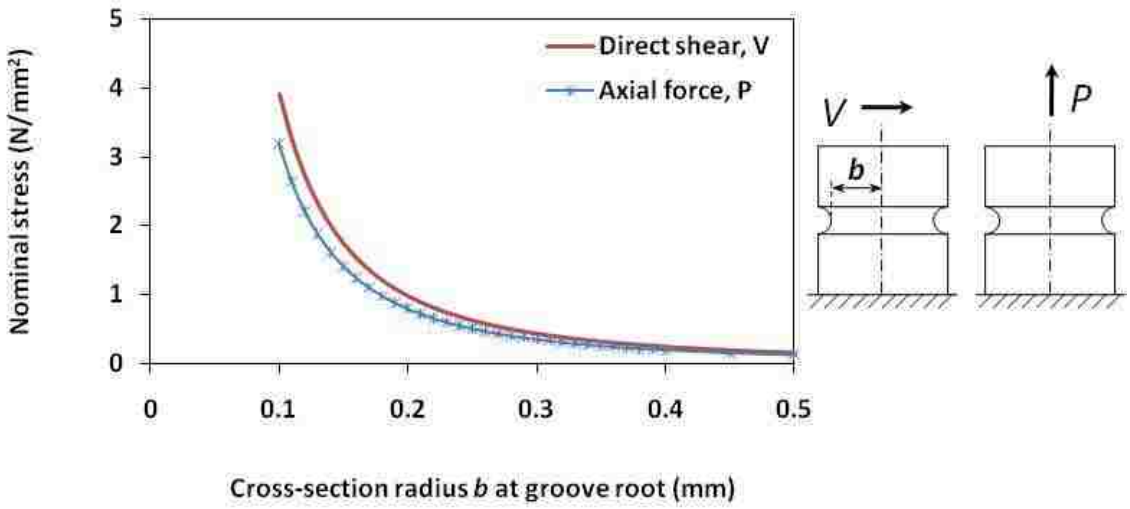

Figure 6.5: Plot showing variation of nominal stress at the notch root due to direct shear *V* and axial forces *P* acting separately on the cylinder as a function of *b*. A value of 0.1 N is used to represent *V* or *P* in this simulation.

In practical cases, the magnitude of different types of forces acting on the cylindrical structure may be different. The magnitude of one type of incident force may be larger than the other type(s). However, these results are valid for any magnitude of incident force, within elastic limit. The yield strength of silicone is about 15 MPa [259]. This corresponds to an elastic limit of 15 N/mm^2.

In practical problems of stress concentration, the state of stress in the neighborhood of a notch is three dimensional in nature. However, due to the complexity of developing three dimensional solutions, the majority of mathematical solutions to stress concentration problems are approximate two-dimensional solutions of plane stress cases [342]. In this light, it is

reasonable to consider the modeling results presented here as approximate two-dimensional computations of stress at the notch root.

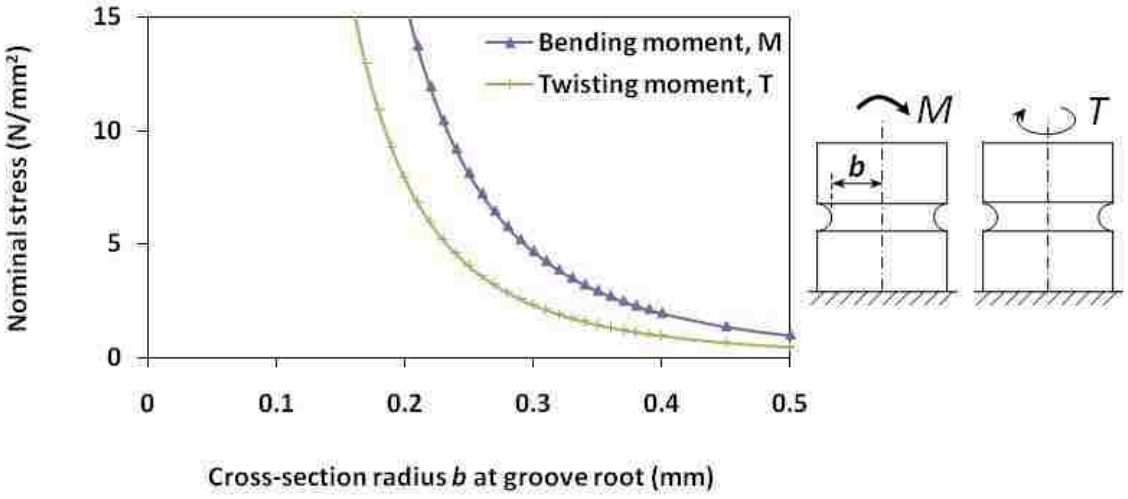

Figure 6.6: Plot showing variation of nominal stress at the notch root due to bending and twisting moments acting separately on the cylinder as a function of *b*. A value of 0.1 N.mm is used to represent the bending and twisting moments respectively in this simulation.

One of the objectives of the developed PAD designs is to reduce the effect of forces acting on the implanted base and to minimize and/or prevent its lateral motion. Therefore, it is necessary to study the influence of the dimensions of the PAD base on the mechanical response of the device. Theoretical simulations were performed to determine a range of dimensional parameters for optimal response of the PAD base vis-à-vis the reduction of circumferential stresses. In the simulations, the PAD base is considered as a curved beam with a rectangular cross-section (Figure 6.7). A cylindrical through-hole is formed at the center of the curved beam. The inner diameter of the cylindrical through-hole is equal to the outer diameter of the PAD conduit. Due to the symmetry of the curved beam, only a segment of the beam is considered for

analysis [343]. Due to action of external forces on the PAD conduit, a combined force is transferred to the PAD base from its conduit. So, the present model assumes a combined force acting centrally on the base. The circumferential stress ($\sigma_{\theta\theta}$) is given by the equation [258]:

$$\sigma_{\theta\theta} = \frac{N}{A} + \frac{M_x(A - rA_m)}{Ar(RA_m - A)}, \quad (6.2\text{-}8)$$

$$R = \frac{a+c}{2}, \quad (6.2\text{-}9)$$

$$A = h(c - a), \text{ and} \quad (6.2\text{-}10)$$

$$A_m = h \ln \frac{c}{a}, \quad (6.2\text{-}11)$$

where N is a force acting centrally at the base, R is the distance between the center of curvature of the curved beam to the centroid of the beam, r is the distance of a point from the center of curvature, a is the outer radius of the conduit or the inner radius of the PAD base, c is the outer radius of the PAD, M_x is a moment acting on the face of the beam cross-section, A is the area of cross-section of the curved beam, A_m has the dimensions of length.

For the purpose of illustration, a force N of 0.2 N has been used in these simulations. The circumferential stress on the base was determined for different thicknesses of the base. Figure 6.8 shows the circumferential stress values calculated for different PAD base thicknesses. The different base thickness values simulated are displayed on the upper right corner of the Figure 6.8. It can be observed that as expected the PAD base thickness influences the circumferential stress. The thicker the base, the lower the values of circumferential stresses produced on the base. A thicker base provides more stability to the device. From a practical perspective, there are limits on the thickness of the PAD base that can be implanted. While a thicker base can be implanted in larger animals and humans, it may pose problems for smaller animals. Also, an increased thickness of the base may pose problems in the percutaneous placement of the base in animals of all sizes.

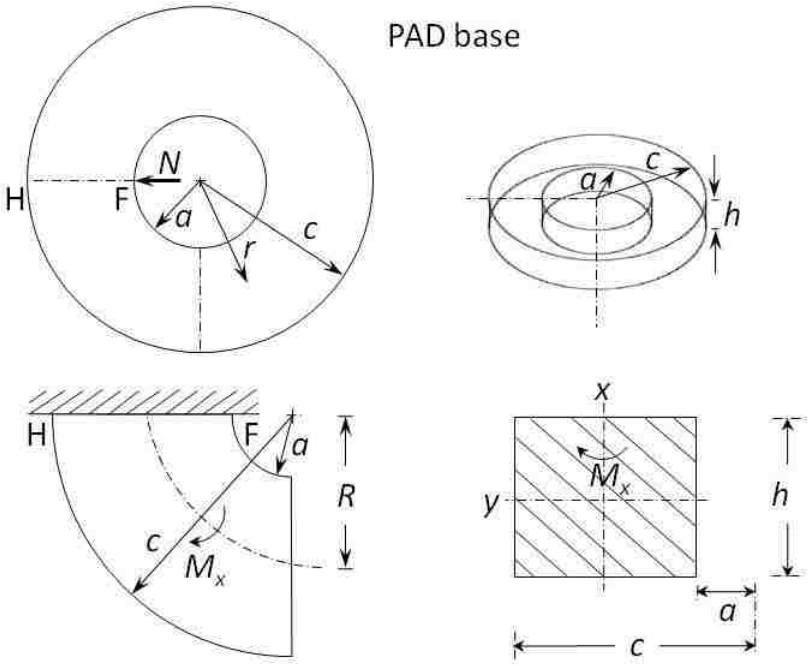

Figure 6.7: Schematic showing the PAD base, modeled as a curved beam with a rectangular cross-section. A force or load *N* is considered to be acting centrally on the base. Diagrams are not drawn to scale.

Figure 6.8 plots the circumferential stress values from inner edge of the PAD base ($r = a$ = 1 mm) to its outer edge ($r = c$ = 5 mm). The maximum circumferential stress is produced at the inner edge of the base. This can be attributed to the fact that the force is applied on the inner edge of the base. The stress produced on the inner edge is tensile and it decreases towards the centroid of the beam, located at $(a+c)/2$ or at 3 mm in the present case. From the centroid onwards, the stress changes from tensile to compressive. Towards the outer edge of the beam, the compressive stress increases. This behavior of induced stress is independent of thickness *h* as the location of the centroid is not influenced by *h*.

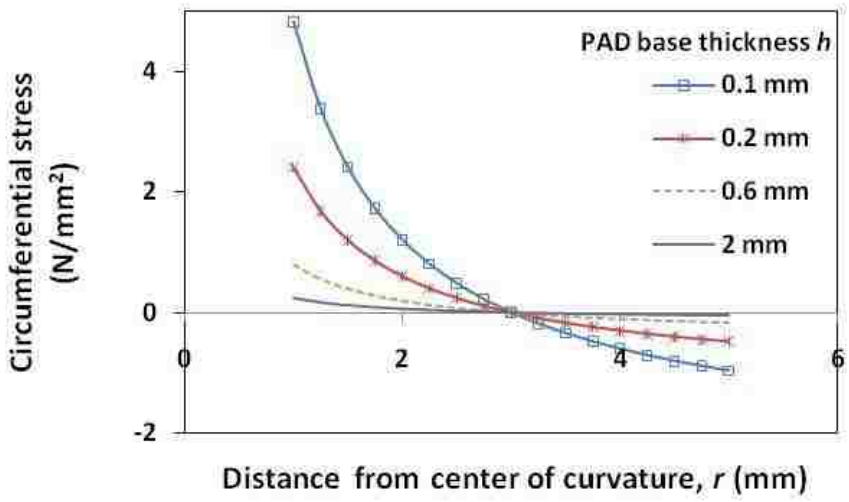

Figure 6.8: Plot of the circumferential stress distribution from the inner edge of the PAD base ($r = a$ = 1 mm) to its outer edge ($r = c$ = 5 mm). A force of 0.2 N is assumed to be acting on the PAD base center. The stress calculations are repeated for different thickness h values of the PAD base.

The tensile stress produced at the inner edge is greater than the compressive stress at the outer edge, typical for this type of section profile. For a more balanced stress distribution in the base, a wider inner section and a thinner outer section will be appropriate. The above results hold true for other values of incident force within elastic limit, though only the simulation data for a 0.2 N force are discussed here.

The maximum tensile stress produced on the base for different values of outer radius c of the PAD base is examined for force N = 0.2 N. The thickness h of the base is maintained constant in these calculations at 1 mm. It can be observed from Figure 6.9 that the stress values are reduced when the outer radius c of the base is increased. The larger the footprint of the base,

the more effective it will function to reduce stress and provide stability to the PAD, consistent with suggestion made by Kantrowitz *et al.* [213]. Additionally, in the developed PAD design, the base is a circular disc to ensure uniform distribution of stress in the base. Other geometries like a square or rectangle-shaped base will result in non-uniform stress distribution.

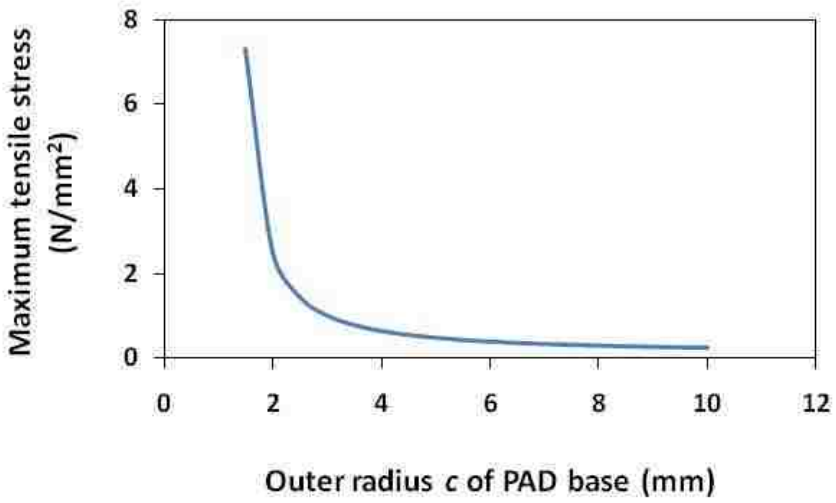

Figure 6.9: Variation of the maximum tensile stress as a function of the outer radius of the PAD base for force N = 0.2 N. The maximum tensile stress is calculated at the inner edge of the PAD base, by substituting $r = a$ = 1 mm in equation (6.2-8). Thickness h is constant at 1 mm.

Another dimension of interest is the inner radius a of the PAD base. While the application at hand largely determines the value of a, its contribution to the stress on the PAD base has to be considered. To study this, the maximum compressive stress has been calculated at the outer radius $r = c$ held constant at 10 mm with varying values of the inner radius a of the PAD base. Figure 6.10 shows that the absolute value of compressive stress increases as the conduit outer radius or the PAD base inner radius is increased. The force N = 0.2 N and thickness

h = 1 mm for data shown in Figure 6.10. The increase in stress is not significant for smaller values of a.

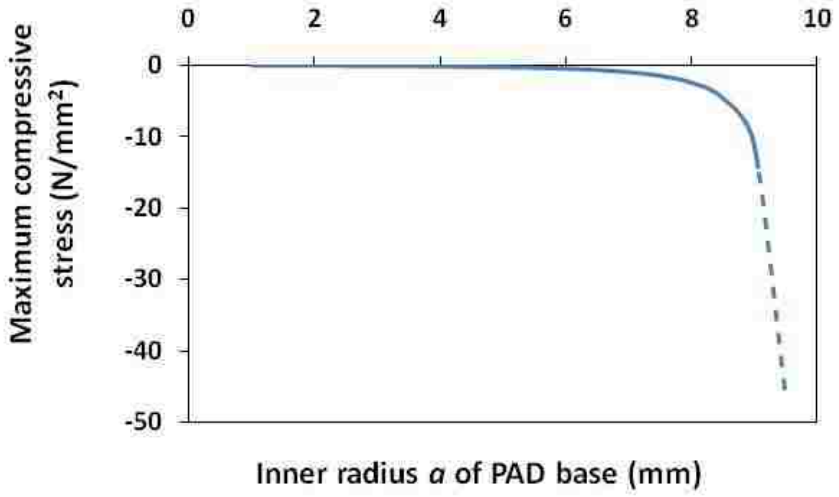

Figure 6.10: Variation of the maximum compressive stress as a function of the inner radius a of the PAD base for force N = 0.2 N. The maximum compressive stress is calculated at the outer edge of the PAD base, by substituting $r = c$ = 10 mm in equation (6.2-8). Thickness h = 1 mm.

In Figure 6.10, the increase in stress in not significant for $(c\text{-}a) \leq 5$ mm. This value is in the typical range of commercially available PAD devices [344]. As the a value approaches that of c i.e. the outer radius of the PAD, the increase in stress is beyond the elastic limit for the PAD material indicated by broken line in the figure. These results imply that the outer radius of the conduit should be small and generally below the lateral width $(c\text{-}a)$ of the base. Based on the results of the mechanical modeling, the following design considerations are arrived at:

1. The notch feature in the conduit is useful to localize stress.
2. For a given diameter of the conduit, a smaller radius of curvature at the notch root on the conduit will focus more stress at the notch root.

3. For a given diameter of the conduit, a larger notch depth will focus more stress.
4. For lower stress, the PAD base should be as thick as practically possible.
5. For lower stress, the lateral dimensions or lateral width of the PAD should be as large as practically possible.
6. The outer radius of the PAD conduit has to be carefully chosen. In terms of forces acting on the base, the outer radius of the conduit should be small.

As an alternative to the grooved conduit approach, the walls of the PAD conduit can be made sufficiently thin, to make it more flexible. However, this can reduce the general robustness of the device. Thin walls may be more susceptible to operational wear and tear. The modeling of the PAD base presented here is applicable to other types of PADs with bases having circular lateral geometry.

In a variation to the notched conduit design, a PAD with a corrugated conduit has also been studied. A mechanical model is given in Appendix G to examine the feasibility of employing corrugations to impart greater flexibility to a PAD conduit and to localize external forces away from the PAD-skin interface.

6.3. Experimental

6.3.1. Pore Formation in Silicone Elastomer

Four different techniques were developed for forming pores in a silicone elastomer [335, 345]. Medical grade silicone elastomer referred to as Silastic from Factor 2 Inc. was employed in this study.

First, in order to realize porosity in Silastic silicone material, layers were formed by doping the silicone with a foreign material and subsequently the layers subjected to selective removal of the dopant (Figure 6.11). Polyvinylidene fluoride (PVDF) powder as a dopant is

dissolved in n-methyl pyrrolidone (NMP), an organic solvent. Liquid Silastic silicone elastomer was mixed with its curing agent in a 10:1 ratio by volume. This mixture is referred to as Silastic pre-polymer in this document. A blend was prepared by mixing Silastic pre-polymer and the PVDF dissolved in NMP. The Silastic to PVDF ratio was 40:1 by weight. After vacuum de-aeration to remove trapped air bubbles, the pre-polymer blend was cured at 60 ^{0}C for 3 h. Alternately, the layer can be cured at room temperature for 24 hrs. Subsequently, the PVDF was removed by soaking the cured Silastic layers in an ultrasonic bath of acetone at room temperature for 1 day. The acetone was replaced after 12 hrs.

Second, a suspension based method was also employed to make pores in the silicone elastomer. This method involved preparing a suspension of Silastic pre-polymer and PVDF powder (7:1 ratio by weight). This suspension was poured into a flat dish or alternately cast on a flat surface and cured at 60 ^{0}C for 3 h to form a solid layer. Alternately, the layer can also be cured at room temperature for 24 hrs. Subsequently, the cured layer was immersed in an ultrasonic bath of acetone or NMP to remove the PVDF for 3 days or more depending on the thickness of the layer. The solvent was replaced every 12 hrs.

Third, for formation of pores in micro-scale dimensions and higher, deionized (DI) water was blended with Silastic pre-polymer to form an immiscible blend, poured into a Petri dish and thermally cured at 100 ^{0}C for 1 h. The curing process crosslinked the Silastic and evaporated the water (Figure 6.12A). The water to Silastic ratio was 1:2 by volume.

In the fourth technique developed here, food grade salt (Morton®) particles (average diameter 150-200 μm) were dispersed over uncured Silastic layers. After the Silastic layers were cured at room temperature, they were placed in an ultrasonic bath of DI water at 35 ^{0}C for 2 days to leach the salt particles (Figure 6.12B).

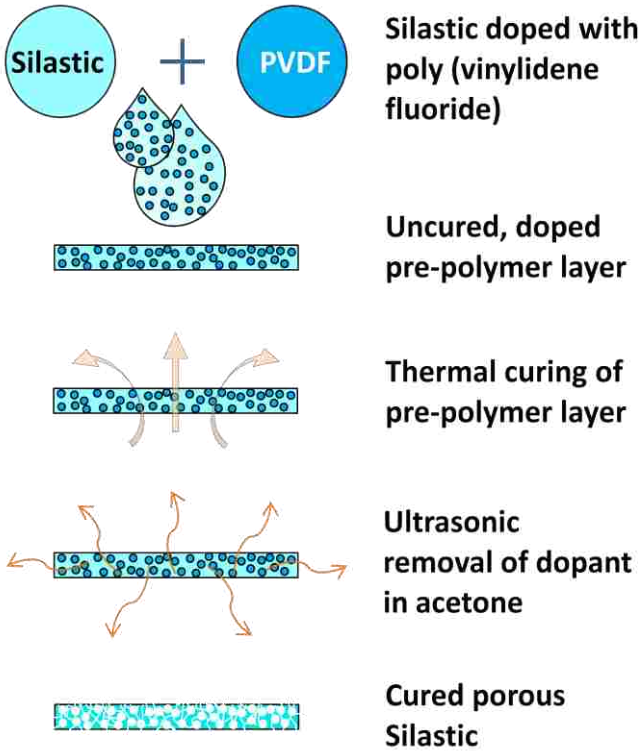

Figure 6.11: Schematic diagram of pore formation in Silastic by doping it with PVDF and subsequently removing the dopant from the cured Silastic. Diagram is not drawn to scale.

6.3.2. PAD Fabrication

The notched conduit PAD developed here was made by molding Silastic silicone elastomer in the desired shape and dimension. The molding involved pouring liquid Silastic pre-polymer into the recesses of a complementary master mold and curing the silicone to solidify the same. The first step involved fabrication of a master mold. From experimentation, it was determined that a master mold consisting of individual modules or parts enabled easy de-molding of cured Silastic silicone structures. Therefore, for the fabrication of the developed

PAD, a master mold was made by assembling four parts, made of plastic with some metal components, and machined to have the desired features.

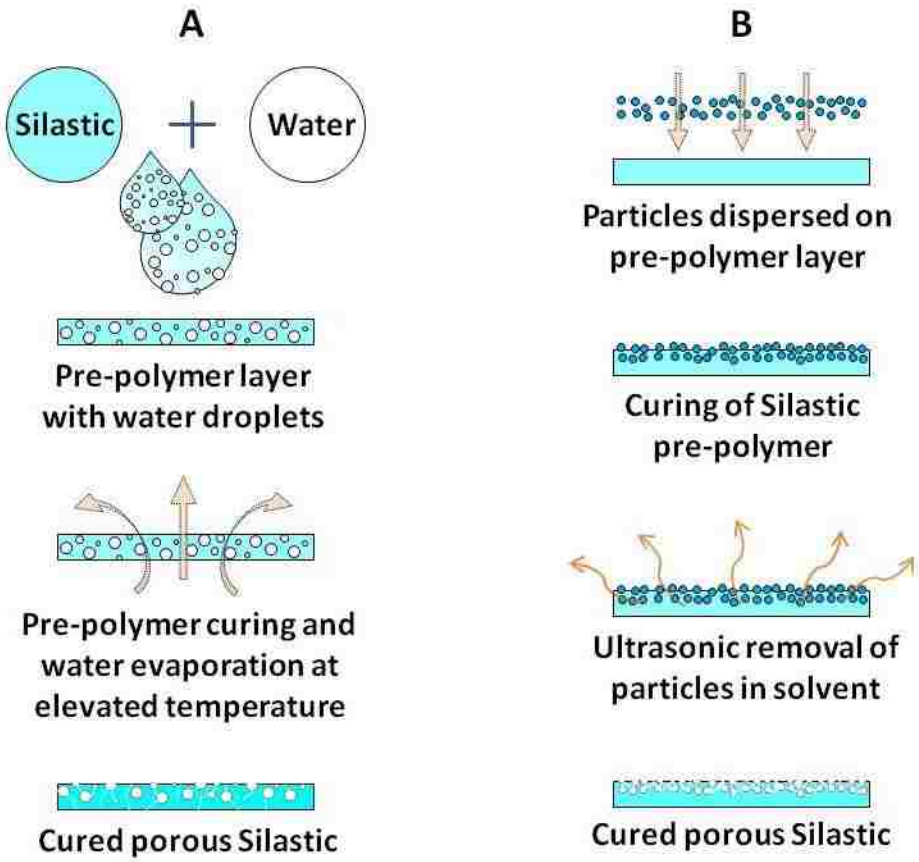

Figure 6.12: Schematic diagrams for pore formation in Silastic by (A) water evaporation, and (B) particulate leaching. Diagrams are not drawn to scale.

Part #1 of the master mold was the bottom layer (made of acrylic) drilled with a hole at its center (Figure 6.13). A modified hypodermic syringe needle was pressure fitted in the hole at the center of part #1. The diameter of the modified hypodermic syringe needle defined the inner diameter of the protruding conduit of the final PAD device. Part #2 was the middle layer that

defined the shape and dimensions of the base of the PAD. Typically, the middle layer was a circular ring whose inner diameter matches the outer diameter of the flat base of the PAD. Alternately, the shape and dimensions of the flat base may be changed by employing an appropriate second layer of the master mold.

Parts #3 and #4 were the upper layers of the master mold that defined the conduit of the final PAD structure. To make these layers, a single flat piece of acrylic was drilled with a through-hole. The diameter of the hole corresponded to the outer diameter of the tubular conduit of the PAD. One end of the through-hole widened into a larger circular recess, created by partial drilling with a larger-diameter drill bit. This recess corresponded to the widened base of the tubular conduit of the interface (Figure 6.13). After making the conduit hole, the single flat piece of acrylic was cut into two halves to form parts #3 and #4. To define the notch, a stainless steel wire of appropriate diameter was attached to the mold parts #3 and #4 by means of thin layer of epoxy. The wire diameter depended on the dimensions of the notch desired on the final PAD conduit. After fabrication, the mold parts were coated with a thin layer of poly vinyl alcohol (PVA), which functioned as a mold release agent. This was done by dip-coating the mold parts in an aqueous solution of PVA (1:8 ratio of PVA to water by weight) for two minutes, and letting the PVA layer solidify at room temperature. The PVA coating was typically a few μm thick.

All parts of the master mold were assembled together by clamping bolts (Figure 6.14A). Silastic silicone elastomer was used as the main material for the PAD body. A specific amount of uncured silicone or silicone pre-polymer was doped with PVDF. Additionally, the doped silicone was blended with salt particles. This blend was subjected to vacuum de-aeration. The doped pre-polymer blend in a measured amount was manually poured into the recess of the master mold

(Figure 6.14B). The doped silicone was thermally cured to form the bottom-most layer of the interface base (Figure 6.14B).

Subsequently, the remaining recess of the mold was filled by un-doped Silastic pre-polymer liquid (Figure 6.14C). The uncured Silastic was allowed to seep into the features of the mold for 10 min. Entrapped air appearing in the form of bubbles was removed by vacuum de-aeration at 25 inches of Hg for 20 min. Following the de-aeration process, the uncured elastomer was placed in a convection oven and thermally cured at 70 ^{0}C for 2 h. Subsequently, the mold was de-assembled by unclamping the mold layers (Figure 6.14D).

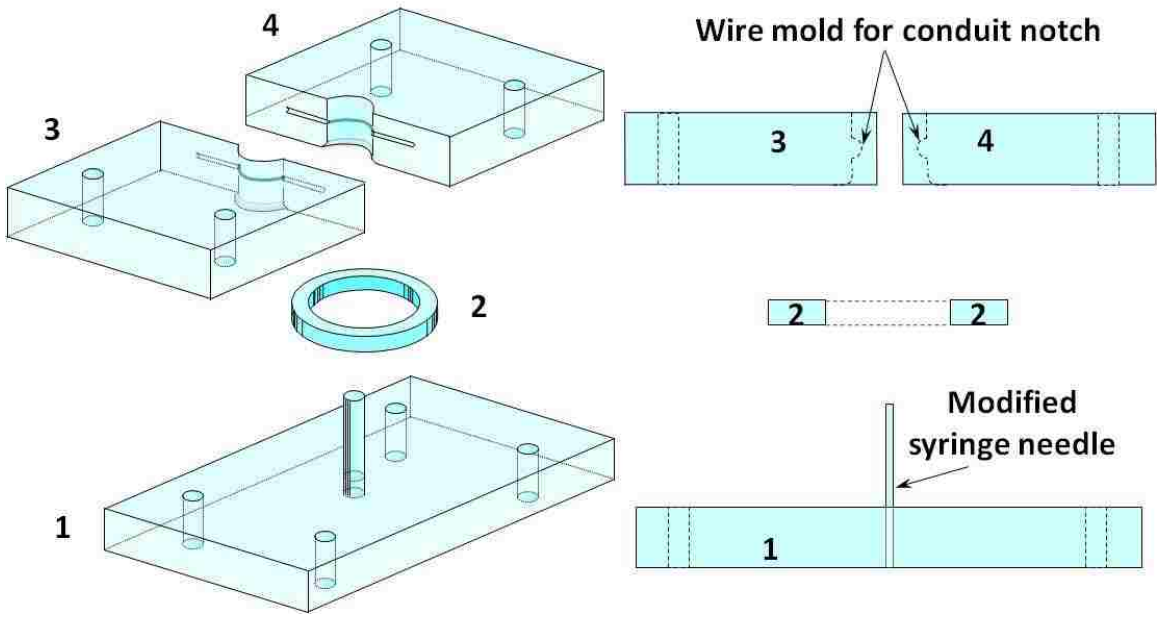

Figure 6.13: Schematic representation of the master mold employed in the fabrication of the developed PAD with notched conduit. Two dimensional representations of the mold parts are also shown. Diagrams are not to scale.

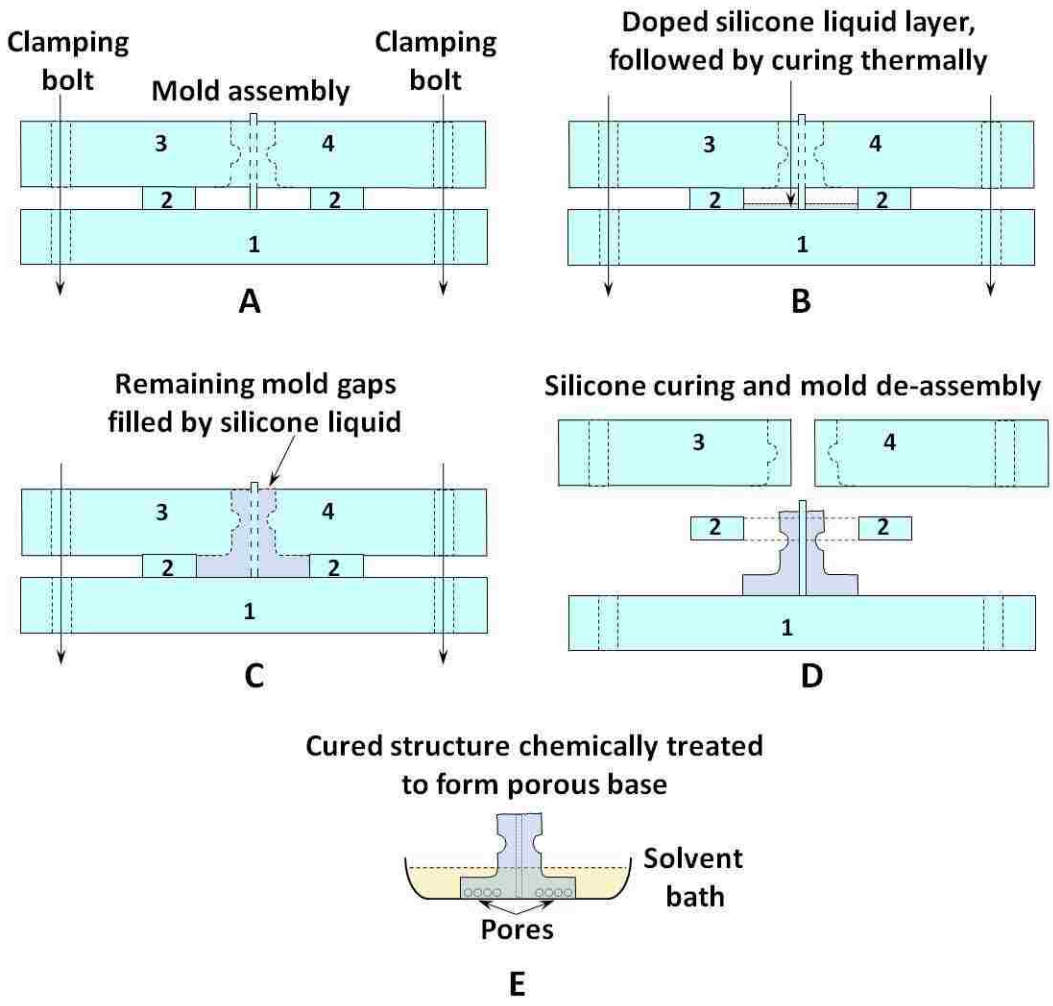

Figure 6.14: Schematic diagram of the fabrication process of the percutaneous access device. Diagrams are not drawn to scale.

The flexible PAD device was released by placing the mold in a water bath to dissolve the intermediate PVA layer. Finally, the free-standing PAD was chemically treated in an ultrasonic bath of acetone to remove the dopant material (PVDF) from the bottom-most layer, yielding pores in the base (Figure 6.14E). The PAD was subsequently placed in an ultrasonic bath of water to leach out the salt particles. Subsequently, suture holes were defined on the PAD base by

coring the base layer with a modified syringe needle. Finally, the PAD was rinsed in DI water and dried in nitrogen.

6.4. Results

6.4.1. Pore Formation in Silicone Elastomer

In order to form micro-scale and submicron pores in Silastic layers, a dopant, PVDF, was incorporated in the Silastic layers by forming a direct blend, as described in section 6.3.1. Subsequently, the PVDF was removed by placing the cured Silastic layer in an ultrasonic bath of acetone. The removal of PVDF created pores in the Silastic layer (Figure 6.15). The acetone did not affect the cured Silastic layer. It was observed that the pore dimensions and characteristics depended on the amount of dopant i.e. PVDF in the Silastic layers.

The Raman spectra of the Silastic with the PVDF dopant and after its removal are shown in Figure 6.15. The spectrum of the doped Silastic sample shows the peaks corresponding to the standard assignments for Silastic and PVDF, as listed in Table 6.1. After removal of PVDF in acetone, Raman spectra showed only the peaks corresponding to Silastic, including its Si-O and Si-C stretch transitions at 495 cm^{-1} and 713 cm^{-1} respectively. No new bonds were observed in the Silastic samples after dopant removal. This implies that there were no new chemical bonds formed in the doping process, indicative of the absence of composite formation.

It is possible that some PVDF dopant may still remain in the inner crevices of the silicone layers after the acetone bath treatment. These layers may require further treatment in acetone. In the dopant removal technique, the pore dimensions and characteristics may depend on the type of dopant and the method used for its removal.

It is relevant to consider the resolution limits of the Raman instrument (LabRAM®, Horiba Jobin-Yvon) used for the analysis. This instrument has a lateral resolution ranging from

0.86-3.1 µm, depending on the objective magnification used. The axial or depth resolution ranges from 1-2 µm, depending on the instrument settings.

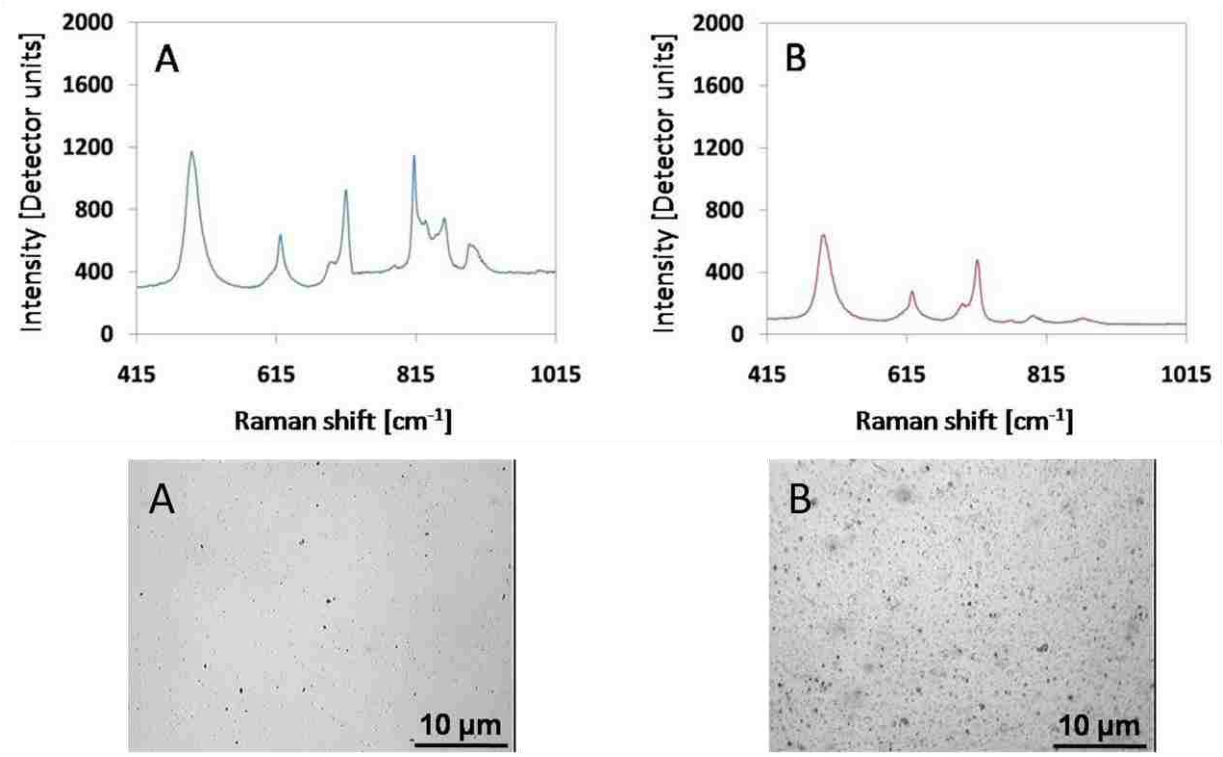

Figure 6.15: Optical microscope images of: (A) Silastic thin film made by doping Silastic pre-polymer with PVDF (40:1 ratio by weight of Silastic to PVDF) prior to dopant removal, and (B) after extraction of PVDF in acetone. Corresponding Raman spectra are also given and show only the peaks corresponding to Silastic after removal of PVDF.

Table 6.1: Raman spectrum assignments for PVDF. Raman spectrum assignments for silicone elastomer are provided in Table 4.6.

Material	Raman shift (cm^{-1})	Assignment
PVDF	~800	CH_2 rocking
	~840	CH_2 rocking CF_2 anti-symmetric stretching

One of the primary requirements for connective tissue growth and for incorporation of cells is the interconnection of pores, or porosity distributed throughout a material or layer. This is achieved by the Silastic-PVDF blend based pore formation technique. Microscopic observation of the cross-section of a porous Silastic layer clearly showed a sponge-like structure, indicative of interconnected porosity throughout the layer. A ratio of 7:1 by weight of Silastic pre-polymer to PVDF was employed to make this layer.

Pores can also be formed in Silastic by a suspension based method where PVDF powder is suspended in Silastic pre-polymer. The pre-polymer-PVDF suspension layer is cured and treated in an ultrasonic bath of a solvent like acetone or NMP. The suspension based method yields pores in the micro-scale dimensions based on the size of PVDF powder, similar to the blend based method. Interconnected porosity throughout a Silastic layer can be obtained by increasing the quantity of the PVDF powder that is suspended in the Silastic pre-polymer solution.

The dopant removal method can be applied to realize porosity in thicker layers. In our experiments, layers of thickness up to 1 mm have been made with interconnected pores distributed throughout the bulk of the material. Figure 6.16 shows a 500 μm thick Silastic layer with pores. The layer was made by a suspension based method (7:1 ratio of pre-polymer to PVDF by weight). Both sides of the layer have pores (Figure 6.16A and 6.16B). An examination of the edge of the layer shows a sponge-like characteristic, indicating interconnected porosity (Figures 6.16C and 6.16D).

In the dopant removal method, the pore characteristics i.e. the pore density and interconnectivity depends on the amount of PVDF in the silicone layer [345-347]. Based on observations, a silicone to PVDF weight ratio of 8:1 or less is generally required to achieve

interconnected porosity. In general, a larger dopant concentration results in more porosity in the silicone layer.

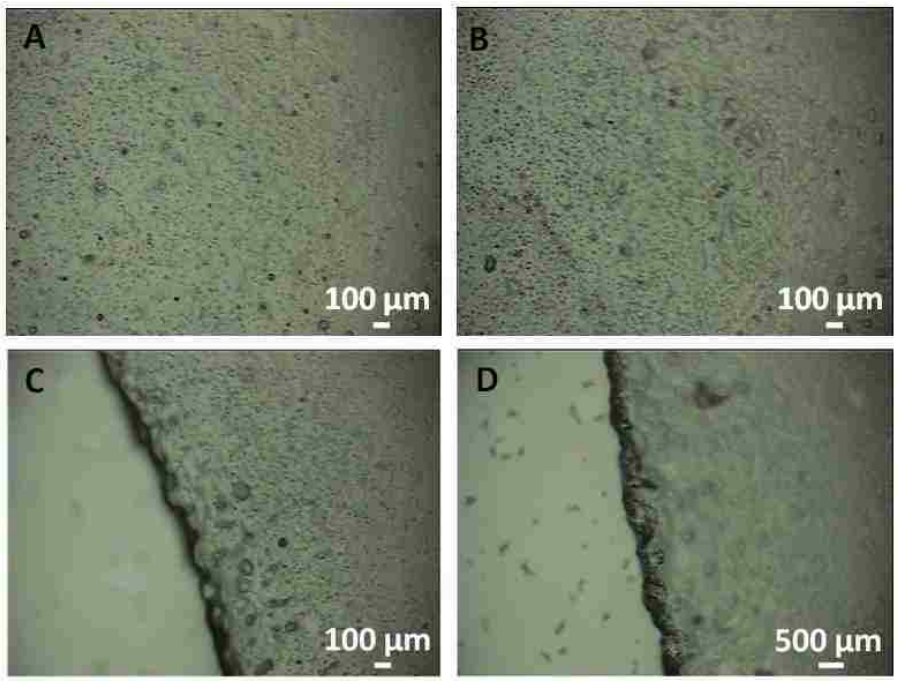

Figure 6.16: Optical microscope images of: (A) Surface of a 500 µm thick porous Silastic layer made by extracting PVDF from a doped Silastic layer; (B) Reverse side of the same 500 µm thick layer; (C) and (D) Sidewalls of 500 µm thick layers, showing sponge-like structure indicative of interconnected porosity. The pores were formed by a Silastic-PVDF suspension method. The size of the PVDF powder ranged from a few µm to < 25 µm.

Another factor to consider is the thickness of the polymer layer. In general, it is more difficult to incorporate porosity in thicker layers of silicone as it is enclosed on one side by the underlying substrate, making it difficult to remove PVDF from that side. For surface coatings and discrete layers, the thickness of the porous silicone layer can be controlled by the viscosity

of the polymer blend and by the coating process employed. The viscosity of the material increases as the silicone:PVDF weight ratio decreases [346, 347]. If required, additional solvents like toluene, ethanol among others, can be used to decrease the viscosity of the silicone/PVDF blend. With a decreased viscosity, thinner layers and coatings can be made.

Among the drawbacks of the dopant removal method is the difficult in precisely controlling the shape of pores in the silicone layer. Second, the overall pore formation process time is relatively long, mainly due to the PVDF removal time. However, this is not seen as a limiting factor in a high throughput application as the process can be carried out inexpensively in a large scale parallel operation. Employing thinner coatings of silicone where permissible allows for faster removal of PVDF because of smaller etchant path [346, 347]. The dopant etching time can be also reduced with choices of a faster dissolving combination of the dopant material and the solvent.

Micro-scale and larger dimension pores are formed in Silastic layers by water evaporation technique. Water and silicone elastomer are immiscible. So, when water and silicone pre-polymer liquid are combined, water remains in the blend in form of droplets and bubbles. These bubbles are removed by evaporation during thermal curing of the silicone elastomer, leaving behind pores (Figure 6.17A). The ratio of water to Silastic pre-polymer influences the porosity. This is especially a factor when the pre-polymer and water blend is subjected to ultrasonic treatment. Figure 6.17B shows a porous Silastic layer formed by curing a manually mixed pre-polymer and water blend (2:1 ratio by volume) at 100 ^{0}C for 1 hr on a hot plate. The pores formed in this layer are relatively sparse with some moisture and vapor embedded in the surface. In contrast, when a Silastic pre-polymer and water blend (2:1 ratio by volume) is prepared by ultrasonic treatment for 1 hr and cured at100 ^{0}C for 1 hr on a hot plate, more pores

are formed with a smaller average size (Figure 6.17C). This is because water is dispersed throughout the pre-polymer in small droplets as a result of the ultrasonic treatment. With manual blending, water is sporadically distributed in larger pockets in the pre-polymer.

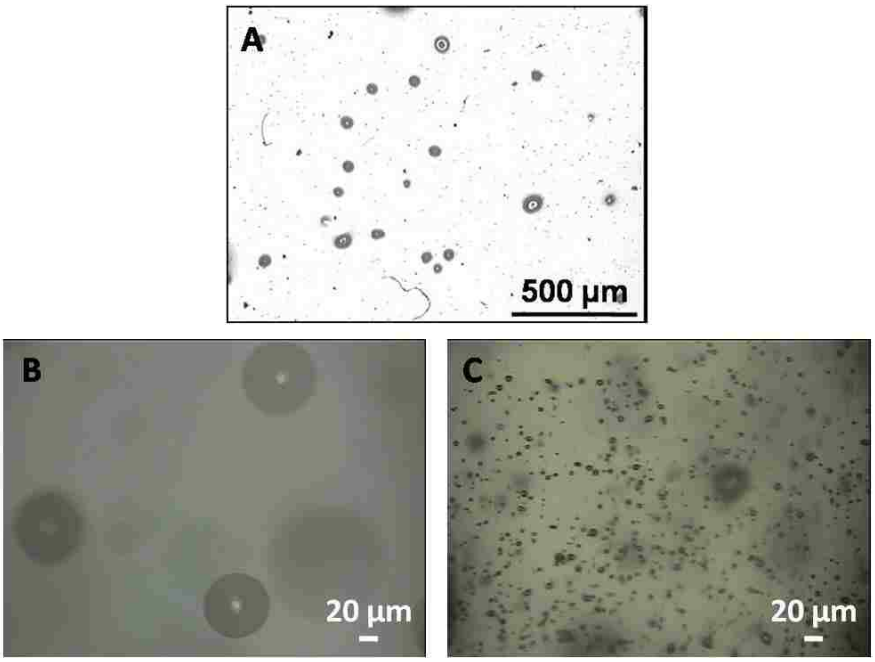

Figure 6.17: Optical microscope images showing Silastic layers with (A) pores formed by water evaporation; (B) embedded vapor and moisture bubbles interspersed with pores, seen in layers made from a manually mixed pre-polymer and water blend; and (C) pores formed by curing a Silastic layer prepared by blending Silastic pre-polymer and water with ultrasonic treatment.

The moisture and vapor embedded in the surface is manifest in the form of bubbles covered by cured Silastic. These embedded bubbles may have a cyst-like appearance. Raman analysis of the surface embedded bubbles shows the suppression of Silastic related frequency assignments, indicating the deficiency of Silastic inside the bubbles (Figure 6.18). These

embedded bubbles are not desirable and need to be minimized. Our experiments indicate that a curing temperature of 100 ^{0}C may not be sufficient to remove embedded bubbles completely, as shown in Figure 6.19. To an extent, higher curing temperatures can be used in this regard. An investigation of the effect of ultrasonic treatment on the pore formation revealed a correlation between the time of ultrasonic treatment and the size and number of pores formed. In silicone layer samples prepared by a longer duration ultrasonic treatment, the average pore size is smaller and number of surface pores is greater, as determined by microscopic observations (Table 6.2). The maximum duration for the ultrasonic treatment was limited to 60 min at room temperature, to avoid the onset of eventual polymerization of the elastomer. Polymerization occurs in samples of silicone pre-polymer containing curing agent, even when they are left at room temperature, albeit at a lower rate than thermally cured samples.

Table 6.2: Effect of room temperature ultrasonic treatment on pore formation by water evaporation in silicone layers.

Time of ultrasonic treatment (min)	**Average number of surface pores / mm^2 of surface**	**Average size range of surface pores (µm)**
0	98±10%	35-85
20	124±10%	30-68
40	207±10%	22-51
60	312±10%	7-35

In general, the porosity achieved by the water evaporation method is influenced by the curing temperature. During curing at a high temperature, the water droplets and bubbles in the bulk of the silicone are transported to the outer surfaces of the layer from where they evaporate. If the temperature is not adequate, then water will not evaporate completely and remain in relatively large quantities within the layer. Typically, curing temperatures of at least 100 ^{0}C or

more have to be used. If the curing temperature is increased drastically, then the vapor exits the layer in a violent manner, leaving behind larger amount of pores.

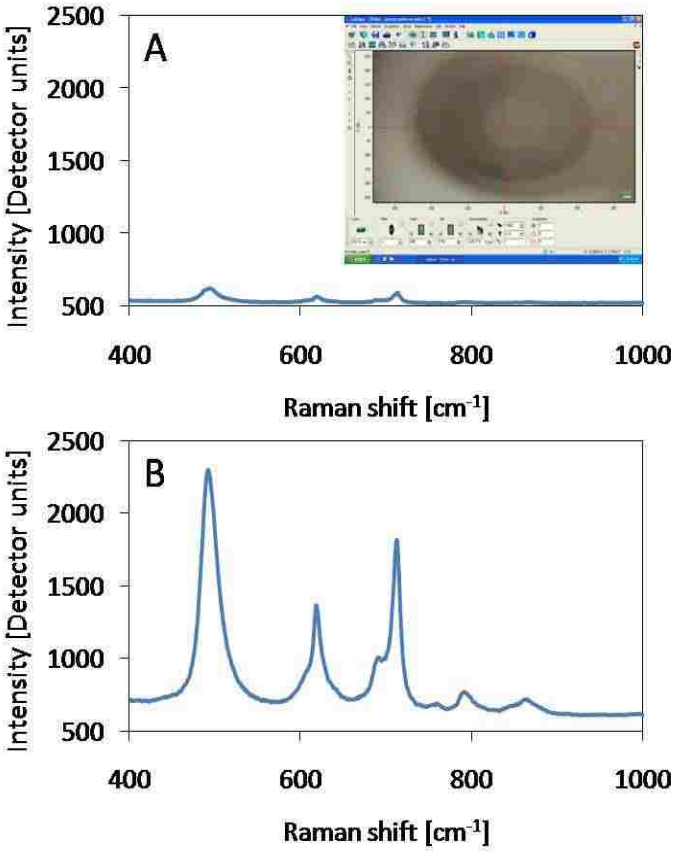

Figure 6.18: Raman spectra of a cured Silastic layer with pores made by water evaporation: (A) Inside a surface embedded bubble; and (B) at a relatively plain region away from surface embedded bubble. The sample was formed by a 2:1 pre-polymer to water ratio, pouring it in a layer in a glass Petri dish and curing at 100 ^{0}C on a hot plate. The inset in (A) shows a screen capture of the Raman software display of the region inside of a surface embedded bubble.

Our experiments indicated a delicate balance between curing temperature and pore size and structure. At higher temperatures, pores are more easily formed due to easier evaporation of

water. However, a higher curing temperature (>100 ^{0}C) can result in water exiting the polymer in a violent manner, leaving behind larger pores with irregular shapes. A bigger problem is posed by the onset of the polymerization process, which is accelerated by thermal treatment. Polymerization prior to the evaporation of water results in the entrapment of water in the polymer. Figure 6.19 shows cross-sectional images of Silastic layers with pores made by water evaporation. Figure 6.19A shows a typical large pore formed by this method. Figure 6.19B shows an arbitrary distribution of pores of varying dimensions. These images show the general isolation of pores i.e. lack of interconnection in the pores in the bulk of the material. Interconnection may exist at a few locations, but is not distributed throughout the layer, and does not match the level of interconnection obtained by the dopant removal method. The water evaporation method is mainly suitable to form shallow pores.

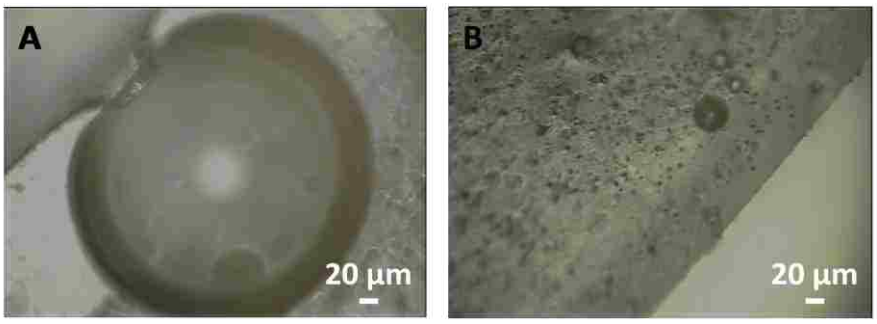

Figure 6.19: Optical microscope images of: (A) Cross-section of a cured Silastic layer showing a large pore; and (B) Cross-section of a cured Silastic layer made from ultrasonic treated pre-polymer-water blend. These Silastic layers were made from a 2:1 ratio (by volume) blend of Silastic pre-polymer to water.

Pores have been formed in Silastic layers by a particulate leaching method (Figure 6.20). The particulate leaching method studied here is suitable to form shallow pores. This is because the particulate matter is dispersed over the surface layer of Silastic pre-polymer, prior to the

curing process. In general, the size of the pores formed by the particulate leaching method depends on the dimensions of the particulates used. However, larger pores can sometimes result if the surface of the Silastic layer is sufficiently packed by particulates prior to leaching. In such cases, some particulates may aggregate and form a larger pore. Pores may also be formed smaller than the particulates due to the partial dissolution of some of the particulates in the Silastic pre-polymer solution. Figure 6.20 shows some pores smaller than the average diameter 150-200 µm size of the particulates used. This situation can be remedied by selecting some other particulate material that does not dissolve in the pre-polymer solution. For particulate matter such as salt particles, dissolution is minimized by curing the Silastic layers at room temperature, as is done in this study.

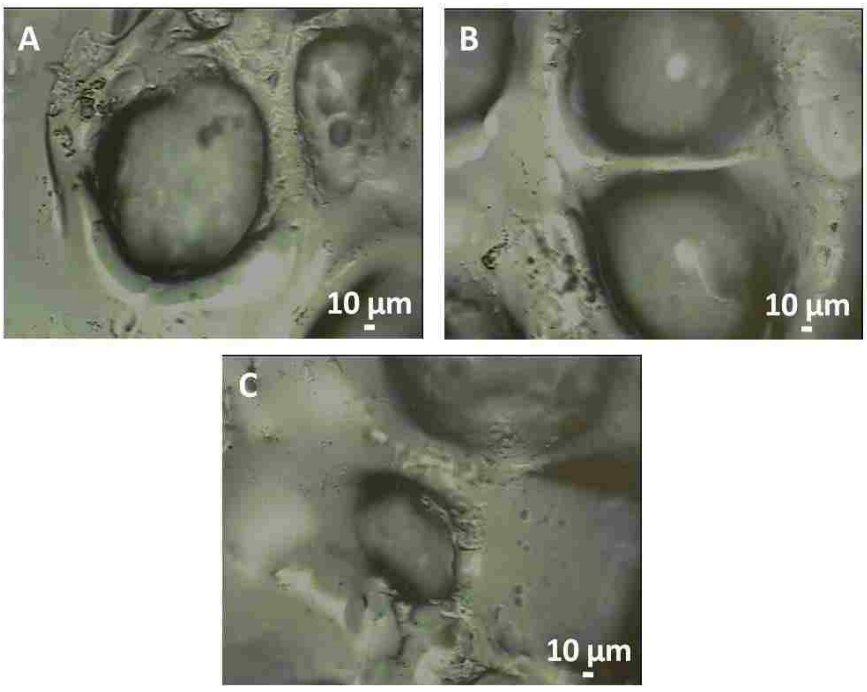

Figure 6.20: Three different optical microscope images showing cured Silastic layers with pores formed by particulate leaching. Food grade salt with average diameter of 150-200 µm was used as the particulate matter.

Previous reports on particulate leaching have described pore formation in materials such as polymers of lactic and glycolic acid, polyurethanes, among others [348, 349]. This method has been suggested for some other types of silicone elastomers [350], but to our knowledge, has not been used for making pores in medical grade silicone such as Silastic and for PAD devices in general. Pore formation methods like water evaporation and particulate leaching can be used to form shallow pores in Silastic silicone layers that allow access to the material enclosed in the inner folds of the Silastic layer. These methods can be employed in conjunction with the dopant removal technique to realize highly porous and fibrous silicone layers. For pore formation by water evaporation and particulate leaching, Raman analysis showed that these processes were benign, i.e. there was no formation of any new composite material.

In comparison to water evaporation and particulate leaching methods, the dopant removal method is more suitable for formation of interconnecting pores. This is due to the fact that PVDF is dissolved on a molecular level before being introduced as a dopant in the elastomer. The pore dimensions achieved by all the three methods are summarized in Table 6.3.

Table 6.3: Summary of pore sizes formed by different methods.

Method	Pore size
Dopant removal	~ 700 nm to 5 µm
Water evaporation	~ 7 µm to 85 µm
Particulate leaching	~65-200 µm (depends on particle size)

The PVDF dopant removal by acetone or NMP is a room temperature process. Additionally, Silastic layers doped with PVDF can be formed at room temperature i.e. by room temperature curing. Water evaporation based pore formation cannot be performed at room temperature. This means that it is not suitable for certain applications, where it is needed to form

pores on structures that may include biological or temperature sensitive material. The particulate leaching method can usually be done at a low temperature, though certain situations may call for heating the sample in a solvent to leach out the particles. In general, both the dopant removal and particulate leaching methods require more time than the water evaporation method.

Previous methods reported for making pores in Silastic have included manual techniques involving the use of a leather punch [210]. Pores have also been made by a mechanical process requiring a rack and pinion tool [172]. Other methods including punching, shear-punching, drilling, piercing and machining have been suggested [172]. The main drawback of these methods is the difficulty in making pores in micro-scale dimensions or smaller. Microfabrication based methods have also been employed to make porous silicone elastomer. Pores were created in silicone (PDMS) sheets by molding PDMS over a master mold template made by electron discharge micromachining [217] or photolithography [218]. This type of technique does not allow for the formation of interconnected pores in a material. For interconnected pores, individual Silastic sheets with pores have to be stacked over each other and carefully offset relative to each other [217]. Among other reports, micro-wave curing has been employed to obtain porous silicone elastomer [351]. A method like this may not be compatible with the molding processes used to make the PAD. Additionally, if there are biological components already incorporated on a silicone structure, this method may not be suitable to make pores on that structure. Other reports include the use of a high intensity narrow beam laser to make pores in a silicone elastomer layer [352]. However, this is a serial process and may not be easy to use to realize highly arbitrary and interconnected pore structure. More recent methods have included the extrusion of a silicone layer over a mold to form pores [353]. The pore formation methods investigated in the work reported here can yield interconnected pores in Silastic with dimensions

appropriate for cell incorporation and growth of connective tissue in percutaneous implants. These methods can also be applied to makes pores in other polymers.

6.4.2. Device Fabrication

One of the developed PAD designs, specifically the notched conduit PAD, was fabricated by molding Silastic, using the multi-part master mold described in section 6.3.2. Figure 6.21 shows some of the fabricated PADs. Notches were incorporated on the PAD conduit by the wire mold method detailed in section 6.3.2. The base of the PAD was incorporated with pores using a combination of dopant removal and particulate leaching. The use of a multi-part master mold facilitates the easy fabrication of the PADs. Since the main body of the developed PAD is made in one piece, the fabrication process is more convenient than those reported by others where individual components were fabricated separately and assembled together to form the PAD [179, 180]. In PADs made by combining components together by adhesive materials such as silicone rubber adhesive, there have been cases of infection caused by failure of the adhesive [199]. The fabrication process negates the necessity for the user to manually assemble components together prior to use, as required by some other reports [181, 354].

The developed PADs were implanted in adult male Sprague-Dawley rats for a maximum period of four weeks. No sign of rejection or infection was observed during and after the implantation period. PAD related problems such as infections due to epidermal migration usually occur within two to three weeks of their implantation [195]. Typical observations periods for PAD related infections span two weeks [200]. Therefore, it is reasonable to conclude that the developed PADs are suitable for chronic implantation applications. The developed fabrication processes can be applied to most biocompatible polymers that can be injection molded. The processes can also be applied to other materials like biocompatible polyimide, polyethylene

among others. Mold-based methods to fabricate PADs using Silastic have been reported on two other instances [355, 356]. However, the previous reports did not mention porosity or rather, in-built porosity (i.e., the pores incorporated in the same material as the device body) as is done here in our devices. The length of a PAD conduit is influenced by the location of its base below the skin and can be changed by employing an appropriate master mold. The actual depth of the PAD base/flange below the skin will depend on the type of animal receiving the implant. For example, in pigs, the flange may be typically positioned between 0.5-0.8 cm below the skin surface in the subcutaneous plane [357].

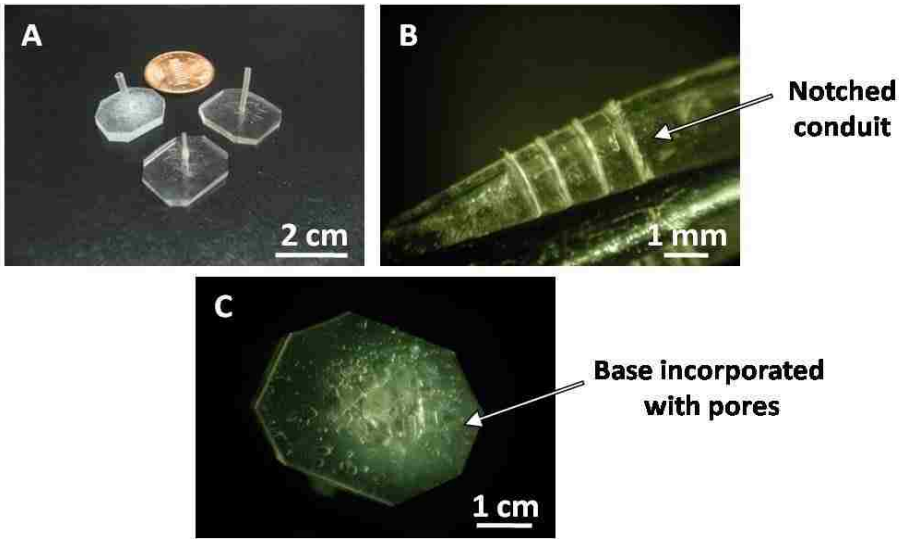

Figure 6.21: Images of: (A) PADs of different dimensions based on the notched conduit design; (B) a PAD conduit with four notches individually spaced by approximately 1 mm. Each notch has a radius of approximately 0.1 mm, and a depth of slightly less than 0.1 mm; (C) a PAD base incorporated with pores. Reprinted with permission from N.S. Korivi, and P.K. Ajmera, "Percutaneous access device with stress relief features," Proceedings of the ASME 2010 5th Frontiers in Biomedical Devices Conference, Paper Number BioMed2010-32022. Copyright 2010 by ASME.

Other considerations in the fabrication process include the removal of air pockets and solvent vapor bubbles that may be trapped in the mold recesses, preventing the flow of pre-polymer into all regions of the mold. Degassing by vacuum may not be sufficient to remove these pockets or bubbles. It is beneficial to incorporate specific outlets in the mold for their removal. In our case, a small-bore outlet provided in mold part 3 was useful (Figure 6.22). A similar small-bore outlet in mold part 1 is more useful in this regard (Figure 6.22), but may result in some leakage of pre-polymer.

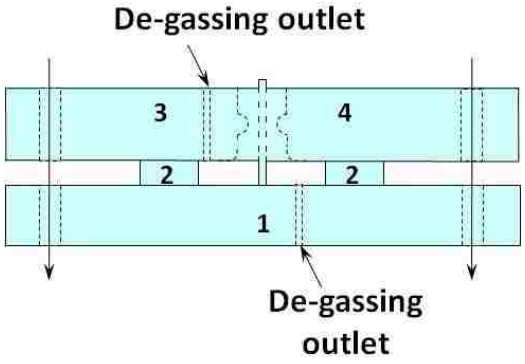

Figure 6.22: Schematic of the mold assembly provided with special outlets for the removal of trapped air pockets and solvent vapor bubbles. The diagram is not to scale.

6.5. Discussion

The developed PAD designs involving conduit with notches or corrugations are designed to concentrate stress caused by applied external forces, at one or more pre-selected points on the PAD conduit. The pre-selected points on the conduit are typically located away from PAD-skin interface. Under the action of external forces, stress is concentrated at the root of a notch on the PAD conduit, away from the crucial PAD-skin interface that needs to be preserved for survival of the PAD. Under the action of external forces, it is expected that the PAD conduit will bend more easily at the notch, rather than at the point of exit from the body. This is expected to relieve

stress on PAD base. It is anticipated that the developed PAD design will attempt to overcome problems indicated in previous reports where forces applied on the conduit could lift the edges of the implanted base of the PAD [337].

For the most part, the PAD-skin interface failure is due to a gross difference between the modulus of elasticity of the skin and the modulus of elasticity of the PAD material. Therefore, the closer the match of the modulus of elasticity of the skin to the PAD material, the lower is the risk of interface failure. Unfortunately, there is no suitable material that exactly meets these elasticity requirements [228]. The skin is non-linear viscoelastic material that in some ways can be compared with an elastomeric material [234]. Therefore, using a material with mechanical properties similar to that of skin will help reduce the possibility of the failure of the PAD-tissue interface. This is the rationale behind using the Silastic silicone elastomer for the PAD body.

Once the PAD is fabricated, it can be sterilized by autoclaving and is ready for implantation. The user does not have to assemble any components, or perform any processes to get the PAD ready for implantation. Due to in-built porosity in the PAD, there is no need for assembling discrete layers containing porous features. In-built porosity in medical grade silicone, to our knowledge has not been reported earlier including its use in conjunction with molding methods to make PAD devices.

Each pore formation technique reported here is capable of producing pores with dimensions in a certain range and with certain characteristics. Tailor-made porosity can be achieved by combining two or more pore formation methods. In conjunction with these pore formation methods, micromolded Silastic structures can be developed to promote growth of connective tissue onto and around the surfaces of biomedical implants, aimed at anchoring implants in-vivo and making them friendlier to the body.

The developed PAD can be readily used for electrical interconnections for functional electrical stimulation (FES) applications. However, the applicability of the developed PAD is not limited to FES applications. PAD technology finds significant usage in wide ranging biomedical applications like chronic measurements/studies on physiological organs and analytes, continuous infusion, chronic measurement of blood pressure and bio-potentials, electrical power and control signal transmission to artificial organs, and plastic surgery, among others [358-362]. The innovations made in this research can be used in their present condition or easily modified to cater to other biomedical applications. The developed PAD can be applied for any biomedical application requiring a physical interconnection between in-vivo and external ambient.

CHAPTER 7: SUMMARY, CONCLUSIONS AND RECOMMENDATIONS FOR FURTHER RESEARCH

7.1. Summary

7.1.1. Clip-on Cuff Electrode

Two embodiments of the clip-on micro-cuff electrode have been successfully fabricated with inner diameters of approximately 300 μm, 400 μm, and 800 μm. The total weight of a typical device including the electrode wires is in the range of 0.2-0.3 gm with total outer surface area in the range 45-60 mm^2. The cuff device can be made with larger cuff inner diameters, in the 1 – 2.5 mm range and higher.

Electrical signals with amplitude as low as 75 μV and frequency in the range 100 Hz – 5 kHz have been successfully read by the micro-cuff device on a laboratory bench. These signals are in the range of typical electroneurogram signals in terms of magnitude and frequency. Electrical impedance measurements in stationary and moving solution ambient indicate little electrical noise from the ambient when the lateral openings of the micro-cuff device are closed. These results are attributed to the more or less fixed enclosed volume inside the cuff when it is under normally closed position, a situation analogous to when the cuff encloses a nerve. Therefore, the developed device can be used for the recording of electrical signals with a high signal to noise ratio from a nerve tissue.

Mechanical force tests indicate the potential of the normally closed cuff to stay secured to a target tissue. The developed micro-cuff device can withstand forces up to 1.9 N before removal from an enclosed pin. This compares favorably to a force of 0.2 N measured for a conventional cylindrical cuff device with outer surface area and total weight similar to those of the micro-cuff device. Force tests also indicate the superior robustness of the interface between cuff wall and

electrode wiring in the micro-cuff, as compared to that of conventional split cylinder cuff. For a typical micro-cuff device having a total outer surface area 45-60 mm^2 and a weight of 0.2-0.3 g, an average force of < 0.8 N is required to open the cuff to its maximum extent. Durability testing of the pinch-hinge feature of the developed cuff electrode indicated that the cuff can withstand more than 50 open-close operations, which is significantly more than needed during a typical lifetime of such a device.

Mechanical modeling indicates the influence of the cuff wall thickness and the cuff material properties on the response of the cuff structure to internal pressure changes. The modeling results should be considered in the context of internal pressure applied on the cuff walls, a case that may occur when a nerve experiences swelling after a cuff is implanted on it. It is preferable to have cuff walls that can expand to accommodate an increase in internal pressure. For larger inner radius, it is beneficial to keep the cuff wall thickness to a smaller value to provide flexibility. Modeling also shows the influence of the cuff material properties such as the elastic modulus. The influence of the Young's modulus is not significant in cuffs with smaller inner radius, but becomes a factor as the cuff inner radius increases.

Mechanical modeling of the pinch-hinge structure demonstrates that factors such as dimensions of the pinch-hinge arm and torsion stiffness of the pinch-hinge influence the force required to open the cuff. For a given set of cuff dimensions, as expected, a larger distance of force application requires a lower force to open the cuff by a certain extent. It is beneficial to apply force at the ends of the pinch-hinge arms, for maximum leverage to open the cuff. The opening force increases with an increase in the torsional stiffness. Torsion stiffness can be decreased by reducing the angle of the pinch-hinge arms, and/or by reducing the distance between the joint of the pinch-hinge arms and the cuff.

7.1.2. Pacing Electrode

A novel electrode for applications in gastric pacing has been successfully fabricated using method based on solution casting of moldable silicone elastomer. The electrode body made of silicone elastomer, is a flat circular disc of approximately 24 mm diameter, with a total thickness of approximately 800 μm. The effective electrode area i.e. the total surface area of the two electrodes exposed to the target tissue is approximately 37 mm^2. Through-holes are provided peripherally on the silicone body. These allow the application of suture thread to secure the electrode to the tissue being stimulated.

A sealed trough is incorporated in the silicone body into which polyethylene glycol (PEG) is introduced as a heated liquid. Upon cooling to below its melting point, the PEG solidifies imparting additional rigidity to the electrode body. The total weight of a typical pacing device without PEG is 2.9 g including the electrical wiring.

Micro-scale porosity is provided in the silicone body where it comes in contact with the tissue. The porosity is expected to encourage the growth of connective tissue into the silicone material, with the objective of enhancing the device anchoring.

Mechanical testing conducted by fixing the device at its edges and deflecting it by a distance of 3 mm at its center shows the influence of PEG on its structural rigidity. More force is needed to deflect the structure embedded with solid PEG, as compared to the case when PEG in the layer is melted. As the amount of PEG is increased in the structure, more force is required for deflection.

Raman spectral analysis on prototype structures of Silastic silicone elastomer layers encompassing PEG reveals lack of any composite formation between PEG and the silicone.

7.1.3. Equivalent Circuit Model

A piece-wise equivalent circuit model has been developed to represent the interface formed by an axon with an electrode. The response of this circuit to an electrical stimulus signal is studied by means of PSPICE software. Simulation results show influence of axon dimensions on its electrical response. An increase in axon length implies an increase in intra-axonal resistance. This results in a decrease in the steady-state current and steady-state membrane voltage during the pulse ON time. Similarly, the radius of the axon plays an important role in defining its electrical behavior. As expected, the steady-state axon current and the steady-state membrane voltage are influenced by the axon radius. As the axon radius changes, the resistance and capacitance associated with its membrane change along with the axon resistance. When axon radius is increased, an overall consequence is the decrease in time constant for axon current. This matches practical observations by others indicating a smaller time constant in larger diameter axons.

The response of the equivalent circuit to different stimulus pulses has been studied. Drawbacks with monophasic current pulse signals are evident in terms of increased voltage levels at the electrode with successive cycles. This results in voltage levels that can be high enough to induce certain electrochemical reactions at the electrode which may not be desirable in terms of electrode integrity and avoiding or minimizing neural damage. Additionally, as voltage levels increase, power levels also increase at the electrode. Another observation with monophasic current pulse is that the electrode voltage increases as the duty cycle is increased from 10% to 33% and then to 50%. It is the opposite case for biphasic current pulses, where the electrode voltage magnitude decreases as duty cycle increases to 50%. The power dissipated at the electrode is also low for the 50% duty cycle, compared to 10% and 33% duty cycles. For

biphasic current pulses, a duty cycle of more than 50% yields increased voltage at the electrode, and therefore increased power dissipation at the electrode. In the case of a voltage pulse input, voltage build-up at the electrode and therefore power dissipated at the electrode are decreased, compared to monophasic and biphasic current pulses. For monophasic voltage pulses, as the pulse-width increases, input current decreases during the 'ON' time of the input pulse.

The PSPICE simulation results are supported by theoretical calculations, indicating that this software can be used in conjunction with equivalent circuits to model the electrical response of tissue to electrical stimulus.

7.1.4. Percutaneous Access Device

Mechanical modeling of the percutaneous access device (PAD) with a notched conduit shows that stress from external forces is concentrated at the root of the notch. This implies that the presence of a notch in the PAD conduit may allow for stress to be focused away from the PAD-skin interface. Modeling of a PAD with corrugated conduit shows that the conduit's torsional and axial stiffness values are influenced by the presence of bellow-like corrugations, more specifically their number and dimensions. As expected, both torsional and axial stiffness are decreased as the number of corrugations increases. A few corrugations can suffice to decrease the stiffness or increase the flexibility of the conduit. For a lower torsional stiffness, it is beneficial to have a smaller ratio of inner and outer radii of the corrugations. For a lower axial stiffness, it is beneficial to keep the inner radius of the corrugations as small as possible and the outer radius as large as possible.

PADs based on these designs are successfully fabricated in Silastic medical grade silicone elastomer by means of a molding process. The PADs are incorporated with pores having micro-scale lateral dimensions, to allow for tissue in-growth for the purpose of anchoring the

implanted part of the PAD. Implantation of the PADs for four weeks in adult male Sprague-Dawley rats did not cause bacterial infections.

7.1.5. Pore Formation

Four different techniques are investigated for forming pores in Silastic silicone elastomer. The dopant removal method allows the formation of interconnected pores, which is one of the primary requirements for connective tissue growth and for incorporation of cells. Pores with sizes in the range 700 nm to 5 μm are possible with this method. The pore characteristics i.e. the pore density and interconnectivity depends on the amount of polyvinylidene fluoride (PVDF) in the silicone layer. A silicone to PVDF weight ratio of 8:1 or less is generally required to achieve interconnected porosity. In general, a larger dopant concentration results in more porosity in the silicone layer.

Micro-scale and larger dimension pores in the size range of 7 μm to 85 μm are formed in Silastic layers by water evaporation technique. This method does not yield the level of interconnection possible by the dopant removal method. In general, the porosity achieved by the water evaporation method is influenced by the curing temperature and ultrasonic treatment of Silastic pre-polymer and water blend.

In the particulate leaching method, the size of pores formed depends on particle size. In the present research, pore sizes in the range 65-200 μm are formed in Silastic layers. This method is suitable to form shallow pores. This is because the particulate matter is dispersed over the surface layer of Silastic pre-polymer, prior to the curing process. In general, both the dopant removal and particulate leaching methods require more time than the water evaporation method. Raman analysis of all the investigated methods shows that the processes are benign, i.e. there is no change in the chemical structure of Silastic silicone. The Raman spectral results also show

that there is no formation of any new composite material.

7.2. Conclusions

For functional electrical stimulation (FES) technology to progress further, it is essential to develop devices and structures that address the challenges with present state-of-art. To this extent, the development of technology detailed in this dissertation is useful in biomedical and medical areas.

The cuff electrode reported here addresses limitations with existing cuff electrodes, namely the aspect of cuff closure after implantation on nerve tissue and a need for cuff devices for micro-scale diameter nerves and nerve fibers. The pinch-hinge feature of the developed cuff device negates the need to close the cuff electrode on the target nerve by suture threads or some other intra-operative procedure. The developed cuff device can be made with any specific internal diameter by means of relatively simple fabrication processes. Due to its superior ease of usage and its applicability for nerves and nerve fibers with wide-ranging effective diameters from sub-mm and greater, the developed cuff device has the potential to be applied in medical devices for neural stimulation and recording.

The results of the mechanical force tests indicate that the naturally closed micro-cuff may stay on a nerve after implantation, and withstand more pulling forces compared to conventional cylindrical cuffs. It offers an alternative to devices that involve securing the electrode directly to the target tissue by means of suture threads, which can be problematic in regions of limited anatomical space. With such devices, there is also the potential hazard of abrasive tissue damage from the relative motion of the cuff. The relatively small force required to open the micro-cuff shows that the self-closing cuff design offers an alternative to other designs requiring application

of a force for cuff closure such as those involving snap and lock mechanisms, and shape memory alloy structures.

In the electrical stimulation of gastric tissues, the main problems encountered are in the use of pacing electrodes. These problems include (a) tissue penetration during and after implantation of the electrodes on the gastric wall, primarily caused by rigidity of electrodes, and; (b) electrode displacement after implantation. The gastric pacing electrode developed in this research shows promise to alleviate these problems. The embedded solid PEG gives some rigidity to the pacing electrode structure, preferable during implantation surgery to facilitate handling. The electrode structure changes to a more flexible state inside the body as the embedded PEG subsequently melts at physiological temperature. Mechanical force tests indicate the feasibility of employing solid PEG (embedded or otherwise) to increase the rigidity of the pacing device structure. The choice of PEG in the device appears appropriate due to its high biocompatibility, coupled with its compatibility with silicone elastomers. Peripheral holes provided in the electrode structure allow for suture thread to be applied, facilitating the securing of the electrode to a target tissue. Porosity in the silicone material in contact with the tissue provides means for connective tissue growth thereby improving anchoring of the electrode. The fabrication processes used to make the device allow for the gastric electrode body to be made thinner if required.

The equivalent circuit of an axon under electrical stimulation described in this dissertation can be employed to study the influence of a particular stimulus signal on nerve tissue and to optimize the stimulation protocol. To illustrate, monophasic and biphasic current pulses influence the circuit differently, as shown by the PSPICE simulations. For monophasic current pulses, it is appropriate to employ a low duty cycle or to keep the pulse-widths small. For

monophasic voltage pulse signals, it is preferable to employ a smaller duty cycle or shorter pulse-widths, in order to have input current as constant as possible. In terms of electrode voltage reduction, it is better to employ biphasic current pulses compared to monophasic current pulses. For biphasic current pulses, it is better to employ a duty cycle close to 50% to minimize the voltage build-up at the electrode, and thereby reduce power dissipated at the electrode. Monophasic voltage pulses are better than monophasic current pulses in terms of reduction of electrode voltage. These results are concurrent with previously reported practical observations. The accuracy of the PSPICE simulations, verified by theoretical calculations, shows the feasibility of using this software as a modeling tool in conjunction with such equivalent circuits. The methodologies described in developing and simulating the circuit can be applied to model interfaces formed by electrode surfaces with other types of tissues.

The silicone elastomer based PAD developed here allows for a physical interconnection between an FES implant and the outer world during chronic animal experiments. The mechanical modeling of the PADs indicates their promise for improved reliability and robustness. The PAD designs developed here have the potential to decrease the stresses acting on the PAD-skin interface, thereby decreasing the possibility of bacterial infection in the PAD. This may extend the life of the PAD and improve its overall reliability. Porous features have been formed on the implantable base of the PAD to encourage the growth of connective tissue. The porous features are inbuilt on the PAD body, which is an improvement over previous approaches. The use of the developed device is not limited to FES applications, and can be extended to other generic application requiring an interconnection between an implant and external devices.

Among the pore formation processes developed to incorporate pores in the micro-scale dimension and above in silicone elastomer layers, the dopant removal method has been

successfully employed to form pores in the gastric pacing electrode and the PAD. In the dopant removal technique, the pore dimensions and characteristics may depend on the type of dopant, its concentration and the method used for its removal. The dopant removal method is more appropriate for making interconnected pores in silicone elastomer layers. Methods such as water evaporation and particulate removal are suitable for making shallow pores. To our knowledge, the pore formation methods investigated in this research have not been employed for making pores in medical grade silicone such as Silastic and for PAD devices in general.

7.3. Recommendations for Further Research

7.3.1. Electrode Development

The continued and growing interest in FES means that the use of devices like cuff electrodes and pacing electrodes will not be limited primarily to research in the future. They will find increasing human implant applications either with humanitarian device exemption or some other approval. The increasing number of FES type devices and systems being commercialized under humanitarian device exemption in the recent years lends credence to this thought. Due to their attributes, the developed clip-on cuff electrode and the pacing electrode have the potential to be candidates for FES medical devices either with humanitarian classification or some other approval. Towards this, it is pertinent to conduct chronic implantation studies in animals to evaluate these devices for FES applications. In the case of the pacing electrodes, histopathology studies are required to determine the functionality of the in-built porosity in tissue anchoring.

7.3.2. Equivalent Circuit Models

In the developed equivalent circuit model representing the interface formed by an axon with an electrode, the axon membrane is represented by a linear *R-C* combination, which may

suffice in most cases. In reality, the behavior of the membrane capacitance and resistance may be non-linear and dependent on how the sodium and potassium channels in the axon membrane respond to applied voltage. Therefore, it may be pertinent to model *R* and *C* components of the membrane by voltage dependent resistance and capacitance components. Additionally, the membrane resting potential may be represented by an independent voltage source situated either in series with the membrane capacitance or its resistance. These modifications to the membrane representation will increase the complexity of the overall circuit model.

7.3.3. PAD Technology

Theoretical and short-term implantation studies on the PAD developed in this research indicate its potential for chronic implantation applications. Further evaluation is necessary to improve our understanding of how this device functions in a practical scenario. In this regard, it is important to conduct further implantation studies including histopathology. This will also allow the evaluation of porous features on the device for connective tissue growth applications. It may also be useful to conduct physical experiments in laboratory environment that allow us to study how the PAD responds to forces acting in a real-life application. The resulting information will complement the theoretical study described in Chapter 6. The challenge here lies in replicating the conditions of an implanted device outside the body in the laboratory.

7.3.4. Pore Formation Methodologies

A part of this dissertation describes new processes to incorporate porosity, micro-pattern and structure medical grade silicone elastomer for connective tissue growth applications. It is pertinent to conduct further characterization of the resulting porous material in terms of pore

dimension, pore volume and surface area, pore distribution by means of techniques such as porometry and bubble-point tests. Though this research was initiated with silicone elastomer, the developed pore formation techniques and micro-patterning methods have been extended to other highly biocompatible materials like polyvinyl alcohol hydrogel, polyethylene oxide, and polyimide. Our results, not described here, have potential applications in biomedical areas such as biomimetics, tissue engineering and in-vitro cell culture growth among others. Further work can focus on the application development aspect for these materials.

REFERENCES

[1] T. Akin, K. Najafi, and R.M. Bradley, "An implantable multichannel digital neural recording system for a micromachined sieve electrode," The 8th International Conference on Solid-State Sensors and Actuators, and Eurosensors IX, Stockholm, Sweden, Vol. 38, pp. 51-54, 1995.

[2] J.A. Von Arx and K. Najafi, "A wireless single-chip telemetry-powered neural stimulation system," Digest of Technical Papers - IEEE International Solid-State Circuits Conference (ISSCC), pp. 214-215, 1999.

[3] J.G. Webster, "The ten most important biomedical engineering devices," IFMBE Proceedings, Vol. 14/2, pp. 664-667, 2008.

[4] M. Nardin, and K. Najafi, "A multichannel neuromuscular microstimulator with bidirectional telemetry," Proceedings of the 8th International Conference on Solid-State Sensors and Actuators, and Eurosensors IX, Stockholm, Sweden, Vol. 1, pp. 59-62, 1995.

[5] M. Wei, J. Mouine, R. Fontaine, and F. Duval, "A dedicated microprocessor for externally powered implantable pain controller," Proceedings of 17th Annual Conference of the IEEE Engineering in Medicine and Biology Society, Vol. 2, pp. 1133-1134, 1995.

[6] J. Mouine, K.A. Ammar, and Z. Chtourou, "A completely programmable and very flexible implantable pain controller," Proceedings of 22nd Annual International Conference of the IEEE Engineering in Medicine and Biology Society, Chicago, USA, pp. 38-43, 2001.

[7] T.S. Lande, J.-T. Marienborg, and Y. Berg, "Neuromorphic cochlea implants," Proceedings of the IEEE International Symposium on Circuits and Systems (ISCAS), Geneva, Switzerland, Vol. 4, pp. 401-404, 2000.

[8] M. Clements, K. Vichienchom, W. Liu, C. Hughes, E. McGucken, C. DeMarco, J. Mueller, M. Humayun, E. De Juan, J. Weiland, and R. Greenberg, "An implantable neuro-stimulator device for a retinal prosthesis," Digest of Technical Papers - IEEE International Solid-State Circuits Conference (ISSCC), pp. 216-217, 1999.

[9] M. Sawan, M.M. Hassouna, J. Li, F. Duval, and M.M. Elhilali, "Stimulator design and subsequent stimulation parameter optimization for controlling micturition and reducing urethral resistance," IEEE Transactions on Rehabilitation Engineering, Vol. 4, No. 1, pp. 39-46, 1996.

[10] C.E. Harrigal, R.A. Walters, and R. Reynolds, "An Implantable device for stimulation of paralyzed vocal chords," Proceedings of the Annual International Conference of the IEEE Engineering in Medicine and Biology Society, pp. 1368-1369, 1992.

[11] B. Smith, Z. Tang, M.W. Johnson, S. Pourmehdi, M.M. Gazdik, J.R. Buckett, and P.H. Peckham, "An externally powered multichannel implantable stimulator telemeter for control of paralyzed muscle," IEEE Transactions on Biomedical Engineering, Vol. 45, pp. 463-475, 1998.

[12] M. Deitel, "Overweight and obesity worldwide now estimated at 1.7 billion people," Obesity Surgery, Vol. 13, pp. 329-330, 2003.

[13] C.L. Ogden, M.D. Carroll, L.R. Curtin, M.A. McDowell, C.J. Tabak, and K.M. Flegal, "Prevalence of overweight and obesity in the United States, 1999-2004," Journal of American Medical Association, Vol. 295, No. 13, pp. 1549-1555, 2006.

[14] R. Sturm, "Increases in morbid obesity in the USA: 2000-2005," Public Health, Vol. 121, pp. 492-496, 2007.

[15] P. Kopelman, "Health risks associated with overweight and obesity," Obesity Reviews, Vol. 8, pp. 13-17, 2007.

[16] N. Barak, E.D. Ehrenpreis, J.R. Harrison, and M.D. Sitrin, "Gastro-oesophageal reflux disease in obesity: pathophysiological and therapeutic considerations," Obesity Reviews, Vol. 3, pp. 9-15, 2002.

[17] S.C. Wearing, E.M. Hennig, N.M. Byrne, J.R. Steele, and A.P. Hills, "Musculoskeletal disorders associated with obesity: a biomechanical perspective," Obesity Reviews, Vol. 7, pp. 239-250, 2006.

[18] H. Bliddal, and R. Christensen, "The management of osteoarthritis in the obese patient: practical considerations and guidelines for therapy," Obesity Reviews, Vol. 7, pp. 323-331, 2006.

[19] R.E. Schmid, "Obesity growing to be top cancer cause," Associated Press, Feb 15 2008.

[20] Y. Linné, "Effects of obesity on women's reproduction and complications during pregnancy," Obesity Reviews, Vol. 5, pp. 137-143, 2004.

[21] K. Elfhag, and S. Rossner, "Who succeeds in maintaining weight loss? A conceptual review of factors associated with weight loss maintenance and weight regain," Obesity Reviews, Vol. 6, pp. 67-85, 2005.

[22] S.C. Wooley, and D.M. Garner, "Obesity treatment: the high cost of false hope," Journal of American Dietetic Association, Vol. 91, pp. 1248-1251, 1991.

[23] R.W. Jeffery, A. Drewnowski, L.H. Epstein, A.J. Stunkard, G.T. Wilson, R.R. Wing, and D.R. Hill, "Long-term maintenance of weight loss: current status," Health Psychology, Vol. 19, pp. 5-16, 2000.

[24] H.J. Sugerman, "Treatment of obesity," Journal of Gastroenterology, Vol. 7, No. 4, pp. 476-477, 2003.

[25] P. Schauer, S. Ikramuddin, W. Gourash, R. Ramanathan, and J. Luketich, "Outcomes after laparoscopic Roux-en-Y gastric bypass for morbid obesity," Annals of Surgery, Vol. 232, pp. 515-529, 2000.

[26] J.B. Dixon, and P. O'Brien, "Health outcomes of severely obese type 2 diabetic subjects 1 year after laparoscopic adjustable silicone gastric banding," Diabetes Care, Vol. 25, pp. 358-363, 2002.

[27] Y. Zhao, and W. Encinosa, "Bariatric surgery utilization and outcomes in 1998 and 2004," Agency for Healthcare Research and Quality (AHRQ), Rockville, MD, Statistical brief #23, January 2007.

[28] K.A. Elder, and B.M. Wolfe, "Bariatric Surgery: A Review of Procedures and Outcomes," Gastroenterology, Vol. 132, Issue 6, pp. 2253-2271, 2007.

[29] V. Cigaina, "Gastric pacing as therapy for morbid obesity: Preliminary results," Obesity Surgery, Vol. 12, pp. 12S-16S, 2002.

[30] F. Greenway, and J. Zheng, "Electrical Stimulation as Treatment for Obesity and Diabetes," Journal of Diabetes Science and Technology, Vol. 1, Issue 2, pp. 251-259, 2007.

[31] V. Cigaina, and A. Hirshberg, "Gastric pacing for morbid obesity: Plasma levels of gastrointestinal peptides and leptin," Obesity Research, Vol. 11, pp. 1456-1462, 2003.

[32] Z. Lin, I. Sarosiek, J. Forster, and R.W. McCallum, "Treatment of diabetic gastroparesis by high-frequency gastric electrical stimulation," Diabetes Care, Vol. 27, pp. 1071-1076, 2004.

[33] G.G. Naples, J.T. Mortimer, and T.G.H. Yuen, "Overview of peripheral nerve electrode design and implantation," Neural prosthesis: Fundamental studies, Edited by W.F. Agnew, D.B. McCreery, Prentice Hall, Englewood Cliffs, NJ, pp. 107-145, 1990.

[34] H. Thoma, W. Girsch, J. Holle, and W. Mayr, "Technology and long-term application of an epineural electrode," Transactions of American Society for Artificial Internal Organs, Vol. 35, pp. 490-494, 1989.

[35] G.W.M. Westby, and H. Wang, "A floating microwire technique for multichannel chronic neural recording and stimulation in the awake freely moving rat," Journal of Neuroscience Methods, Vol. 76, pp. 123-133, 1997.

[36] P.D. Van der Puije, R. Shelley, and G.E. Loeb, "A self-spiraling thin-film nerve cuff electrode," Proceedings of 19th Canadian Medical and Biological Engineering Conference, pp. 186-187, 1993.

[37] T. Stieglitz, H. Beutel, and J.-U. Meyer, "A flexible, light-weight multichannel sieve electrode with integrated cables for interfacing regenerating peripheral nerves," Sensors and Actuators A, Vol. 60, pp. 240-243, 1997.

[38] S.M. Lawrence, G.S. Dhillon, and K.W. Horch, "Fabrication and characteristics of an implantable, polymer-based, intrafascicular electrode," Journal of Neuroscience Methods, Vol. 131, pp. 9-26, 2003.

[39] M. Gruhn, and W. Rathmayer, “An implantable electrode design for both chronic in vivo nerve recording and axon stimulation in freely behaving crayfish,” Journal of Neuroscience Methods, Vol. 118, pp. 33-40, 2002.

[40] P.H. Gorman, and P.H. Peckham, “The effect of stimulus parameters of the recruitment characteristics of direct nerve stimulation,” IEEE Transactions on Biomedical Engineering, Vol. 30, pp. 407-414, 1983.

[41] D.R. McNeal, L.L. Baker, and J.T. Symons, “Recruitment data for nerve cuff electrodes: Implications for design of implantable stimulators,” IEEE Transactions on Biomedical Engineering, Vol. 36, No. 3, pp. 301-308, 1989.

[42] G.E. Loeb, and R.A. Peck, “Cuff electrodes for chronic stimulation and recording of peripheral nerve activity,” Journal of Neuroscience Methods, Vol. 64, pp. 95-103, 1996.

[43] G.L. Warren, C.P. Ingalls, and R.B. Armstrong, “A stimulating nerve cuff for chronic in vivo measurements of torque produced about the ankle in the mouse,” Journal of Applied Physiology, Vol. 84, pp. 2171-2176, 1998.

[44] J-U. Meyer, T. Stieglitz, “Flexible artificial nerve plates,” U.S Patent 5897583, 1999.

[45] F.C. Barone, M.J. Wayner, H.U. Aguilar-Baturoni, and R. Guevara-Aguilar, “A bipolar electrode for peripheral nerve stimulation,” Brain Research Bulletin, Vol. 4, pp. 421-422, 1979.

[46] F.J. Rodriguez, D. Ceballos, M. Schuttler, A. Valero, E. Valderrama, T. Stieglitz, and X. Navarro, “Polyimide cuff electrodes for peripheral nerve stimulation,” Journal of Neuroscience Methods, Vol. 98, pp. 105-118, 2000.

[47] C. Veraart, W.M. Grill, and J.T. Mortimer, “Selective control of muscle activation with a multipolar nerve cuff electrode,” IEEE Transactions on Biomedical Engineering, Vol. 40, pp. 640-653, 1993.

[48] D.R. McNeal, and B.R. Bowman, “Selective activation of muscles using peripheral nerve electrodes,” Medical and Biological Engineering and Computing, Vol. 23, pp. 249-253, 1985.

[49] Z.P. Fang, and J.T. Mortimer, “Selective activation of small motor axons by quasitrapezoidal current pulses,” IEEE Transactions on Biomedical Engineering, Vol. 38, No. 2, pp. 168-174, 1991.

[50] G.S. Brindley, and M.D. Craggs, “A technique for anodally blocking large nerve fibers through chronically implanted electrodes,” Journal of Neurology, Neurosurgery and Psychiatry, Vol. 43, pp. 1083-1090, 1980.

[51] W.M. Grill, and J.T. Mortimer, “Non-invasive measurement of the input-output properties of peripheral nerve stimulating electrodes,” Journal of Neuroscience Methods, Vol. 65, pp. 43-50, 1996.

[52] 'Nerve Cuff Electrodes' product information, Microprobes for Lifesciences Inc, Gaithersburg, MD, USA; http://www.microprobes.com/nerve_cuff.php, [Last retrieved on January 26, 2011].

[53] R.B. Stein, T.R. Nichols, J. Jhamandas, L. Davis, and D. Charles, "Stable long-term recordings from cat peripheral nerves," Brain Research, Vol. 128, pp. 21-38, 1977.

[54] V. Fenik, P. Fenik, and L. Kubin, "A simple cuff electrode for nerve recording and stimulation in acute experiments on small animals," Journal of Neuroscience Methods, Vol. 106, pp. 147-151, 2001.

[55] J.S. Carp, A.M. Tennissen, X.Y. Chen, G. Schalk, and J.R. Wolpaw, "Long-term spinal reflex studies in awake behaving mice," Journal of Neuroscience Methods, Vol. 149, pp. 134-143, 2005.

[56] J.A. Hoffer, G.E. Loeb, W.B. Marks, M.J. O'Donovan, C.A. Pratt, and N. Sugano, "Cat hindlimb motoneurons during locomotion. I. Destination, axonal conduction velocity and recruitment threshold," Journal of Neurophysiology, Vol. 57, pp. 510-529, 1987.

[57] C.A. Pratt, C.M. Chanaud, and G.E. Loeb, "Functionally complex muscles of the cat hindlimb. IV. Intramuscular distribution of movement command signals and cutaneous reflexes in broad, bifunctional thigh muscles," Experimental Brain Research, Vol. 85, pp. 281-299, 1991.

[58] C. Krarup, and G.E. Loeb, "Conduction studies in peripheral cat nerve using implanted electrodes. I. Methods and findings in controls," Muscle Nerve, Vol. 11, pp. 922-932, 1988.

[59] G.E. Loeb, "The distal hindlimb musculature of the cat. I. Interanimal variability of locomotor activity and cutaneous reflexes," Experimental Brain Research, Vol. 96, pp. 125-140, 1993.

[60] T. Jellema, and J.L.J.M. Teepen, "A miniaturized cuff electrode for electrical stimulation of peripheral nerves in the freely moving rat," Brain Research Bulletin, Vol. 37, No. 5, pp. 551-554, 1995.

[61] R.B. Banzett, "Implantable electrode pair for recording from intact small nerves," IEEE Transactions on Biomedical Engineering, Vol. BME-27, pp. 53-54, 1980.

[62] L.L. Hench, and E.C. Ethridge, "Biomaterials: An interfacial approach," Academic Press, New York, N.Y, 1982.

[63] S.I. Schwartz, R.C. Wingrove, and J.A. Anderson, "Implantable electrode for nerve stimulation," U.S Patent 3421511, 1969.

[64] R.L. Testerman, N.R. Hagfors, and S.I. Schwartz, "Design and evaluation of nerve stimulating electrodes," Medical Research Engineering, Vol. 10, pp. 6-11, 1971.

[65] Mr. Martin Bak, CEO, Microprobe Inc, Gaithersburg, MD, USA; direct communication, September 2009.

[66] J.A. Kuzma, T.K. Whitehurst, "Curved paddle electrode for use with a neurostimulator," U.S Patent 7006875 B1, 2006.

[67] Dr. F.L. Greenway, Pennington Biomedical Research Center, Baton Rouge, LA, USA; direct communication, December 2007.

[68] M-A. Crampon, M. Sawan, V. Brailovski, and F. Trochu, "New easy to install nerve cuff electrode using shape memory armature," Artificial Organs, Vol. 23, No. 5, pp. 392-395, 1999.

[69] D.M. Durand, D. Tyler, B. Cottrill, "Nerve cuff for implantable electrode," U.S Patent Application Publication 2008/0046055, 2008.

[70] S.E. Maschino, S.D. Kollatschny, "Circumneural electrode assembly," U.S Patent 6600956, 2003.

[71] C. Dubkin, "A constant-contact stimulating electrode for nerves," Journal of Applied Physiology, Vol. 28, pp. 350, 1970.

[72] L.P. McCarty, "Nerve electrode apparatus," U.S Patent 3157181, 1964.

[73] L.P. McCarty, "A stimulating electrode for nerves," Journal of Applied Physiology, Vol. 20, pp. 542, 1965.

[74] G.G. Naples, J.D. Sweeney, and J.T. Mortimer, "Implantable cuff, method of manufacture, and method of installation," U.S Patent 4602624, 1986.

[75] T. Stieglitz, J-U. Meyer, "Cuff electrode," U.S Patent 5919220, 1999.

[76] J.J. Mrva, J. Coburn, R.B. Strother, G.B. Thrope, "Devices, systems, and methods employing a molded nerve cuff electrode," U.S Patent 2006/0030919 A1, 2006.

[77] Unpublished observations from fluorescence tests on adult male Sprague-Dawley rats, done in collaboration with Dr. Jolene Zheng, Louisiana State University Agricultural Center, Baton Rouge, LA, USA, 2008.

[78] M.D. Tarler, and J.T. Mortimer, "Comparison of joint torque evoked with monopolar and tripolar-cuff electrodes," IEEE Transactions on Neural Systems and Rehabilitation Engineering, Vol. 11, No. 3, pp. 227-235, 2003.

[79] D.J. Tyler, D.M. Durand, "Corrugated inter-fascicular nerve cuff method and apparatus," U.S Patent 5634462, 1997.

[80] R.L. Testerman, R.W. Bierbaum, "Cuff electrode," U.S Patent 5344438, 1994.

[81] M.A. Rossing, S.L. Bolea, D.W. Mayer, A. Hjelle, T. Crowley, E.D. Irwin, "Connection structures for extra-vascular electrode lead body," U.S Patent 2006/0004430, 2006.

[82] J.A. Hoffer, G.E. Loeb, and C.A. Pratt, "Single unit conduction velocities from averaged nerve cuff electrode records in freely moving cats," Journal of Neuroscience Methods, Vol. 4, pp. 211-225, 1981.

[83] J.-F. Sauter, H.-R. Berthoud, and B. Jeanrenaud, "A simple electrode for intact nerve stimulation and/or recording in semi-chronic rats," Pflügers Arch, Vol. 397, pp. 68-69, 1983.

[84] M. Roslin, and M. Kurian, "The use of electrical stimulation of the vagus nerve to treat morbid obesity," Epilepsy Behavior, Vol. 2, pp. S11-S16, 2001.

[85] R.J. Greenstein, "Minimally invasive surgery placement of stimulation leads in mediastinal structures," U.S Patent Application Publication 2005/0027328 A1, 2005.

[86] V. Cigaina, "Treatment of the autonomic nervous system," U.S Patent Application Publication 2006/0058851 A1, 2006.

[87] V. Cigaina, G.P. Pinato, V. Rigo, M. Bevilacqua, F. Ferraro, S. Ischia, and A. Saggioro, "Gastric peristalsis control by mono situ electrical stimulation: a preliminary study," Obesity Surgery, Vol. 5, pp. 247-249, 1996.

[88] M. Flesler, Y. Mika, Z. Belsky, Y.B. Arie, N. Darvish, S. Ben-Haim, "Acute and chronic electrical signal therapy for obesity," U.S Patent 6600953, 2003.

[89] V. Cigaina, "Process for electrostimulation treatment of morbid obesity," U.S Patent 6615084, 2003.

[90] J. Chen, and P.J. Pasricha, "Gastrointestinal electrical stimulation," U.S Patent 6826428, 2004.

[91] M.P. Mintchev, and K.L. Bowes, "Gastro-intestinal electrical pacemaker," U.S Patent 6243607, 2001.

[92] J.D. Chen, R.W. McCallum, R. Williams, R. Ross, Z. Lin, and J. Tillack, "Gastro-intestinal pacemaker having phased multi-point stimulation," U.S Patent 5690691, 1997.

[93] I. Bourgeois, "Method and apparatus for treating irregular gastric rhythms," U.S Patent 6216039, 2001.

[94] J.M. Swoyer, W. Starkebaum, M.T. Gerber, and T. Herbert, "Implantable gastrointestinal lead with active fixation," U.S Patent 6952613, 2005.

[95] Medtronic Enterra™ Therapy 4301 unipolar intramuscular lead for the gastric electrical stimulation system, Technical manual, Medtronic, Inc., Minneapolis, MN, USA, 2000; [www.medtronic.com].

[96] Transcend Implantable Gastric Stimulator pacing electrodes, Medtronic Inc., Minneapolis, MN, USA; [www.medtronic.com].

[97] I. Bourgeois, "Method and apparatus for electrical stimulation of the gastrointestinal tract," U.S Patent 5836994, 1998.

[98] B.O. Familoni, "Method and apparatus for sensing a stimulating gastrointestinal tract on-demand," U.S Patent 5861014, 1999.

[99] R.J. Mason, J. Lipham, G. Eckerling, A. Schwartz, T.R. DeMeester, "Gastric electrical stimulation – An alternative surgical therapy for patients with gastroparesis," Archives of Surgery, Vol. 140, pp. 841-848, 2005.

[100] P.A. Altman, M.E. Bush, D.F. Carson, "Intracardiac lead having a compliant fixation device," U.S Patent 5837007, 1998.

[101] S.T. Foley, "Gastrointestinal stimulation lead," U.S Patent Application Publication 2006/0047323 A1, 2006.

[102] D. Popovic, T. Gordon, V.A. Rafuse, and A. Prochazka, "Properties of implanted electrodes for functional neuromuscular stimulation," Annals of Biomedical Engineering, Vol. 19, pp. 303-316, 1991.

[103] S.A. Shikora, "Implantable gastric stimulation for the treatment of severe obesity," Obesity Surgery, Vol. 14, pp. 545-548, 2004.

[104] A. Bohdjalian, G. Prager, R. Aviv, S. Policker, K. Schindler, S. Kretschmer, R. Riener, J. Zacherl, and B. Ludvik, "One-year experience with Tantalus™: a new surgical approach to treat morbid obesity," Obesity Surgery, Vol. 16, pp. 627-634, 2006.

[105] F. Favretti, M. De Luca, G. Segato, L. Busetto, A. Ceoloni, A. Magon, and G. Enzi, "Treatment of morbid obesity with the Transcend implantable gastric stimulator (IGS): A prospective survey," Obesity Surgery, Vol. 14, pp. 666-670, 2004.

[106] J. Yin, H. Ouyang, and J.D.Z. Chen, "Potential of intestinal electrical stimulation for obesity: A preliminary canine study," Obesity, Vol. 15, No. 5, pp. 1133- 1138, 2007.

[107] Y. Handa, N. Hoshimiya, Y. Iguchi, and T. Oda, "Development of percutaneous intramuscular electrode for multichannel FES system," IEEE Transactions on Biomedical Engineering, Vol. 36, No. 7, pp. 705-710, 1989.

[108] C.W. Caldwell, and J.B. Reswick, "A percutaneous wire electrode for chronic research use," IEEE Transactions on Biomedical Engineering, Vol. BME-22, No. 5, pp. 429-432, 1975.

[109] W.D. Memberg, P.H. Peckham, and M.W. Keith, "A surgically-implanted intramuscular electrode for an implantable neuromuscular stimulation system," IEEE Transactions on Rehabilitation Engineering, Vol. 2, No. 2, pp. 80-91, 1994.

[110] V. Cigaina, V. Rigo, and R.J. Greenstein, "Gastric myo-electrical pacing as therapy for morbid obesity: preliminary results," Obesity Surgery, Vol. 9, pp. 333-334, 1999.

[111] E.B. Marsolais, and R. Kobetic, "Implantation techniques and experiences with percutaneous intramuscular electrodes in the lower extremities," Journal of Rehabilitation Research and Development, Vol. 23, No. 3, pp. 1-8, 1986.

[112] A. Scheiner, J.T. Mortimer, and T. Kicher, "A study of the fatigue properties of small diameter wires used in intramuscular electrodes," Journal of Biomedical Materials Research, Vol. 25, pp. 589-608, 1991.

[113] A&E Medical Corporation, Farmingdale, NJ, USA; [www.aemedical.com].

[114] S.A. Shikora, "What are the Yanks doing? The U.S experience with implantable gastric stimulation (IGS) for the treatment of obesity – update on the ongoing clinical trials," Obesity Surgery, Vol. 14, pp. S40-S48, 2004.

[115] Tantalus^{TM} implantable system electrodes, Metacure (USA) Inc., Orangeburg, NY, USA; [www.metacure.com].

[116] L.R. Bolduc, "Body tissue electrode and device for screwing the electrode into body tissue," U.S Patent 3737579, 1973.

[117] E.G. O'Neill, "Device for screwing body tissue electrode into body tissue," U.S Patent 4207903, 1980.

[118] D.N. Hess, N.M. Lokhoff, M.A. Ruff, R.D. Sandstrom, T.G. Laske, "Medical lead fixation," U.S Patent 7251532, 2007.

[119] T.M. Williams, J.L. Jula, J.E. Upton, S.J. Ryden, P.D. Blankenau, "Implantable lead system," U.S Patent 5246014, 1993.

[120] J.J. Daly, K. Kollar, A.A. Debogorski, B. Strasshofer, E.B. Marsolais, A. Scheiner, S. Snyder, R.L. Ruff, "Performance of an intramuscular electrode during functional neuromuscular stimulation for gait training post stroke," Journal of Rehabilitation Research and Development, Vol. 38, No. 5, pp. 513-526, 2001.

[121] D.A. Jenkins, "Gastric stimulator apparatus and method for installing," U.S Patent 6606523, 2003.

[122] D.N. Hess, S.D. Myrum, and M.J. Ebert, "Multi-component lead body for medical electrical leads," U.S Patent 5968087, 1999.

[123] R.H. Rockland, and D.H. Gobeli, "Bipolar body tissue electrode," U.S Patent 4010758, 1977.

[124] R.G. Dutcher, and E.G.O'Neill, "Epicardial pacing lead with stylet controlled helical fixation screw," U.S Patent 4357946, 1982.

[125] J.M. Ocel, G.A. Boser, T.W. Holleman, "Retraction stop for helical medical lead electrode," U.S Patent 5837006, 1998.

[126] V. Cigaina, and D. Jenkins, "Medical stimulation," U.S Patent 6041258, 2000.

[127] A. Scheiner, G. Polando, and E.B. Marsolais, "Design and clinical application of a double helix electrode for functional electrical stimulation," IEEE Transactions on Biomedical Engineering, Vol. 41, No. 5, pp. 425-431, 1994.

[128] J.M. Swoyer, W. Starkebaum, M.T. Gerber, and T. Herbert, "Implantable bifurcated gastrointestinal lead with active fixation," U.S Patent 6876885, 2005.

[129] V. Cigaina, "Process and device for treating obesity and syndromes related to motor disorders of the stomach of a patient," U.S Patent 5423872, 1995.

[130] J.M. Swoyer, and W. Starkebaum, "Implantable medical device affixed internally within the gastrointestinal tract," U.S Patent Application Publication 2002/0103424 A1, 2002.

[131] O. Colliou, K. Nason, H. Tenhoff, M.A. Imran, T. Layman, "Gastric device and suction assisted method for implanting a device on a stomach wall," U.S Patent 7020531, 2006.

[132] M.A. Imran, O.K. Colliou, T.W. Layman, D.R. Gandhi, S.L. Lake, "Gastric anchor and method," U.S Patent 7016735, 2006.

[133] M.A. Imran, O.K. Colliou, T.W. Layman, D.R. Gandhi, S.L. Lake, "Method and device for securing a functional device to a stomach," U.S Patent 7120498, 2006.

[134] B. Griffin, M. Dann, and G. Fluet, "Methods and devices for gastrointestinal stimulation," U.S Patent Application Publication 2008/0058887 A1, 2008.

[135] C.A. Tronnes, K. Carlton, M.T. Gerber, D.J. Stetson, and J.M. Swoyer, "Adjustable implantable captivation fixation anchor-stop," U.S Patent Application Publication 2003/0220678 A1, 2003.

[136] S. Ben-Haim, N. Darvish, Y. Mika, M. Fenster, B. Felzen, I. Shemer, "Method of increasing the motility of a GI tract," U.S Patent 6571127, 2003.

[137] J.R. Davis, Handbook of Materials for Medical Devices, ASM International, Materials Park, Ohio, 2003.

[138] K.B. Stokes, "Myocardial sutureless lead," U.S Patent 4313448, 1982.

[139] T.G.H. Yuen, W.F. Agnew, L.A. Bullara, D. Jacques, and D.B. McCreery, "Histological evaluation of neural damage from electrical stimulation: Considerations for the selection of parameters for clinical applications," Neurosurgery, Vol. 9, pp. 292-299, 1981.

[140] W.J. Brown, T.L. Babb, H.V. Soper, J.P. Lieb, C.A. Ottino, and P.H. Crandall, "Tissue reactions to long-term electrical stimulation of the cerebellum in monkeys," Journal of Neurosurgery, Vol. 47, pp. 366-379, 1977.

[141] L.A. Geddes, K.S. Foster, J. Reilly, W.D. Voorhees, J.D. Bourland, T. Ragheb, and N.E. Fearnot, "The rectification properties of an electrode-electrolyte interface operated at high sinusoidal current density," IEEE Transactions on Biomedical Engineering, Vol. 34, No. 9, pp. 669-672, 1987.

[142] W.F. Agnew, D.B. McCreery, T.G.H. Yuen, and L.A. Bullara, "Histologic and physiologic evaluation of electrically stimulated peripheral nerve: Considerations for the selection of parameters," Annals of Biomedical Engineering, Vol. 17, pp. 39-60, 1989.

[143] D.B. McCreery, W.F. Agnew, T.G.H. Yuen, and L. Bullara, "Charge density and charge per phase as cofactors in neural injury induced by electrical stimulation," IEEE Transactions on Biomedical Engineering, Vol. 37, No. 10, pp. 996-1001, 1990.

[144] E.J. Tehovnik, "Electrical stimulation of neural tissue to evoke behavioral responses," Journal of Neuroscience Methods, Vol. 65, pp. 1-17, 1996.

[145] P.E. Crago, P.H. Peckham, J.T. Mortimer, and J.P. Van Der Meulen, "The choice of pulse duration for chronic electrical stimulation via surface, nerve, and intramuscular electrodes," Annals of Biomedical Engineering, Vol. 2, pp. 252-264, 1974.

[146] L.S. Robblee, and T.L. Rose, "Electrochemical guidelines for selection of protocols and electrode materials for neural stimulation," in Neural Prosthesis: Fundamental Studies, W.F. Agnew, D.B. McCreery, Eds., Englewood Cliffs, NJ, Prentice-Hall, pp. 25-66, 1990.

[147] D.B. McCreery, W.F. Agnew, T.G.H. Yuen, and L.A. Bullara, "Damage in peripheral nerve from continuous electrical stimulation: comparison of two stimulus waveforms," Medical and Biological Engineering and Computing, Vol. 3, pp. 109-114, 1992.

[148] M.D. Bonner, M. Daroux, T. Crish, and J.T. Mortimer, "The pulse-clamp method for analyzing the electrochemistry of neural stimulating electrodes," Journal of Electrochemical Society, Vol. 140, pp. 2740-2744, 1993.

[149] S.L. Morton, M. Daroux, and J.T. Mortimer, "The role of oxygen reduction in electrical stimulation of neural tissue," Journal of Electrochemical Society, Vol. 141, pp.122-130, 1994.

[150] W.M. Grill, and J.T. Mortimer, "The effect of stimulus pulse duration on selectivity of neural stimulation," IEEE Transactions on Biomedical Engineering, Vol. 43, No. 2, pp. 161-166, 1996.

[151] The Biomedical Engineering Handbook, J.D. Bronzino, Ed, 2nd edition, Vol. 1, CRC Press, Boca Raton, FL, 2000.

[152] http://www.vancouver.wsu.edu/fac/morgan/lecture/ions.html, [Last retrieved on October 17, 2009].

[153] J.D. Sweeney, K. Deng, E. Warman, and J.T. Mortimer, "Modeling of electric field effects on the excitability of myelinated motor nerve," Proceedings of 11th Annual International Conference of the IEEE Engineering in Medicine and Biology Society, pp. 1281-1282, 1989.

[154] D.R. McNeal, "Analysis of a model for excitation of myelinated nerve," IEEE Transactions on Biomedical Engineering, Vol. BME-23, pp. 329-337, 1976.

[155] B. Frankenhaeuser, and A.F. Huxley, "The action potential in the myelinated nerve fiber of Xenopus Laevis as computed on the basis of voltage clamp data," Journal of Physiology, Vol. 171, pp. 302-315, 1964.

[156] N. Ganapathy, and J.W. Clark, "Extracellular currents and potentials of the active myelinated nerve fiber," Biophysical Journal, Vol. 52, pp. 749-761, 1987.

[157] F. Rattay, "The basic mechanism for the electrical stimulation of the nervous system," Neuroscience, Vol. 89, No. 2, pp. 335-346, 1999.

[158] K.J. Vetter, Electrochemical Kinetics, Academic Press, New York, 1967.

[159] A.M. Dymond, "Characteristics of the metal-tissue interface of stimulation electrodes," ," IEEE Transactions on Biomedical Engineering, Vol. 23, No. 4, pp. 274-280, 1976.

[160] L.A. Geddes, "Historical evolution of circuit models for the electrode-electrolyte interface," Annals of Biomedical Engineering, Vol. 25, pp. 1-14, 1997.

[161] H. Helmholtz, "Studien uber electrische Grenzschichten," Annals of Physical Chemistry, Vol. 7, pp. 337-382, 1879.

[162] L.A. Geddes, and L.E. Baker, Principles of Applied Biomedical Instrumentation, 1st edition, John Wiley & Sons, New York, 1968.

[163] M. Sluyters-Rehbach, and J.H. Sluyters, "Sine wave methods in the study of electrode processes," Electroanalytical Chemistry, Vol. 4, pp. 1-121, 1970.

[164] E.T. McAdams, A. Lackermeier, J.A. McLaughlin, D. Macken, and J. Jossinet, "The linear and non-linear electrical properties of the electrode-electrolyte interface," Biosensors and Bioelectronics, Vol. 10, pp. 67-74, 1995.

[165] V. Cigaina, A. Saggioro, V. Rigo, G. Pinato, and S. Ischai, "Long-term effects of gastric pacing to reduce feed intake in swine," Obesity Surgery, Vol. 6, pp. 250-253, 1996.

[166] W.D. Memberg, P.H. Peckham, G.B. Thrope, M.W. Keith, and T.P. Kicher, "An analysis of the reliability of percutaneous intramuscular electrodes in upper extremity FNS

applications," IEEE Transactions on Rehabilitation Engineering, Vol. 1, No. 2, pp. 126-132, 1993.

[167] P.J. Nelson, "Silastic skin button for chronic exteriorization of tubing in dogs," Journal of Applied Physiology, Vol. 27, No. 5, pp. 763-764, 1969.

[168] Y. Handa, T. Oda, S. Ito, Y. Iguchi, and N. Hoshimiya, "Studies on ultrafine intramuscular electrode and skin button for FES," Proceedings of 10th Annual International Conference of the IEEE Engineering in Medicine and Biology Society, pp. 1686-1687, 1988.

[169] V. Mooney, D.B. Hartman, and D. McNeal, "The use of pure carbon for permanent percutaneous electrical connector systems," Archives of Surgery, Vol. 108, pp. 148-153, 1974.

[170] L. Vodovnik, T. Bajd, A. Kralj, F. Gracanin, and P. Strojnk, "Functional electrical stimulation for control of locomotor systems," CRC Critical Reviews in Bioengineering, pp. 63-131, 1981.

[171] K. Akazawa, M. Makikawa, J. Kawamura, and H. Aoki, "Functional neuromuscular stimulation system using an implantable hydroxyapatite connector and a microprocessor-based portable stimulator," IEEE Transactions on Biomedical Engineering, Vol. 36, No. 7, pp. 746-753, 1989.

[172] H.L. Lee, G.W. Culp, and D.E. Ocumpaugh, "Bacteria-resistant percutaneous conduit device," U.S Patent 3663965, May 1972.

[173] T. Tsuji, T. Togawa, H. Aoki, and Y. Shin, "Development of percutaneous device made of sintered hydroxyapatite for clinical use," Proceedings of 9th Annual International Conference of the IEEE Engineering in Medicine and Biology Society, pp. 1467-1468, 1987.

[174] A. Kojima, K. Yamazaki, T. Mori, S. Kobayashi, and O. Tagusari, "Skin button," U.S Patent 5971962, October 1999.

[175] L.C. Cosentino, F.J. Martinez, "Percutaneous implant," U.S Patent 4417888, 1983.

[176] E. Klein, R.L. Wathen, R.A. Ward, L.C. Cosentino, L.E. Fuller, and F.J. Martinez, "Percutaneous implant for peritoneal dialysis," U.S Patent 4488877, December 1984.

[177] D.A. Raible, "Implant device," U.S Patent 4534761, 1985.

[178] T. Shimotoso, A. Terui, H. Kitano, "Living body-supporting member and preparation process thereof," U.S Patent 6010336, 2000.

[179] C.E. Zimmerman, "Percutaneous vascular access portal and catheter," U.S Patent 4318401, 1982.

[180] L.C. Cosentino, "Percutaneous implant," U.S Patent 4496349, 1985.

[181] A. Kantrowitz, P.S. Freed, F.L. Vaughan, I.A. Bernstein, and R.H. Gray, "Percutaneous access device and method for implanting same," U.S Patent 4634422, January 1987.

[182] K.A. Dasse, "Infection of percutaneous devices: Prevention, monitoring, and treatment," Journal of Biomedical Materials Research, Vol. 18, pp. 403-411, 1984.

[183] T. Furuzono, S. Yasuda, T. Kimura, S. Kyotani, J. Tanaka, and A. Kishida, "Nano-scaled hydroxyapatite/polymer composite IV. Fabrication and cell adhesion properties of a three-dimensional scaffold made of composite material with a silk fibroin substrate to develop a percutaneous device," Journal of Artificial Organs, Vol. 7, pp. 137-144, 2004.

[184] M.R. Hales, W.E. Bloomer, and W.D. Widmann, "A polyethylene needle guide for percutaneous access to the portal vein of the dog," Journal of Applied Physiology, Vol. 21, No. 5, pp. 1649-1652, 1966.

[185] K.D. Murray, S. Hughes, D. Bearnson, and D.B. Olsen, "Infection in total artificial heart recipients," ASAIO Transactions, Vol. 29, pp. 539-544, 1983.

[186] D.L. Holmberg, P. Dew, C. Crump, G. Burns, Y. Taenaka, and D.B. Olsen, "Percutaneous access devices in calves receiving an artificial heart," ASAIO Transactions, Vol. 12, No. 1, pp. 34-39, 1988.

[187] K.D. Murray, T. Abbott, W.C. DeVries, R. Gaykowski, and D.B. Olsen, "The microscopic evaluation of skin buttons used in a long-term human total artificial heart," ASAIO Transactions, Vol. 32, pp. 42-45, 1986.

[188] K.D. Murray, T.M. Abbott, and D. Olsen, "Correlation of gross and microscopic appearance of skin buttons in total artificial heart animals," ASAIO Transactions, Vol. 36, No. 4, pp. 825-829, 1990.

[189] P.A. Topaz, S.R. Topaz, and W.J. Kolff, "Molded double lumen silicone skin button for drivelines to an artificial heart," ASAIO Transactions, Vol. 37, No. 3, pp. M222-M223, 1991.

[190] J.A. Jansen, J.P.C.M. van der Waerden, and K. de Groot, "Development of a new percutaneous access device for implantation in soft tissues," Journal of Biomedical Materials Research, Vol. 25, pp. 1535-1545, 1991.

[191] Y.G.C.J. Paquay, J.E. de Ruijter, J.P.C.M. van der Waerden, and J.A. Jansen, "Titanium fiber mesh anchorage for percutaneous devices applicable for peritoneal dialysis," Journal of Biomedical Materials Research, Vol. 28, pp. 1321-1328, 1994.

[192] A.F. von Recum, "Applications and failure modes of percutaneous devices: A review," Journal of Biomedical Materials Research, Vol. 18, pp. 323-336, 1984.

[193] K. Merritt, J.W. Shafer, and S.A. Brown, "Implant site infection rates with porous and dense materials," Journal of Biomedical Materials Research, Vol. 13, pp. 103-108, 1979.

[194] S.F. Kiechel, G.T. Rodeheaver, J.J. Klawitter, M.T. Edgerton, and R.E. Edlich, "The role of implant porosity on the development of infection," Surgery, Gynecology and Obstetrics, Vol. 144, pp. 58-62, 1977.

[195] B. Chehroudi, T.R.L. Gould, and D.M. Brunette, "The role of connective tissue in inhabiting epithelial downgrowth on titanium-coated percutaneous implants," Journal of Biomedical Materials Research, Vol. 26, pp. 493-515, 1992.

[196] G.D. Winter, "Transcutaneous Implants: Reactions of the skin-implant interface," Journal of Biomedical Materials Research Symposium, Vol. 5, No. 1, pp. 99-113, 1974.

[197] B. Chehroudi, T.R.L. Gould, and D.M. Brunette, "A light and electron microscopic study of the effects of surface topography on the behavior of cells attached to titanium-coated percutaneous implants," Journal of Biomedical Materials Research, Vol. 25, pp. 387-405, 1991.

[198] S.F. Hulbert, F.W. Cooke, J.J. Klawitter, R.B. Leonard, B.W. Sauer, and D.D. Moyle, "Attachment of prosthesis to the musculo-skeletal system by tissue ingrowth and mechanical locking," Journal of Biomedical Materials Research Symposium, Vol. 4, pp. 1-23, 1973.

[199] J. Miller, C.E. Brooks, "Problems related to the maintenance of chronic percutaneous electronic leads," Journal of Biomedical Materials Research Symposium, Vol. 2, pp. 251-267, 1971.

[200] S.F. Hulbert, S.J. Morrison, J.J. Klawitter, "Tissue reaction to three ceramics of porous and non-porous structures," Journal of Biomedical Materials Research, Vol. 6, pp. 347-374, 1972.

[201] H.J. Cestero, K.E. Salyer, I.R. Toranto, "Bone growth into porous carbon, polyethylene, and polypropylene prostheses," Journal of Biomedical Materials Research, Vol. 9, pp. 1-7, 1975.

[202] A.J. Arem, J.W. Madden, "Soft tissue response to blood-impregnated Proplast," Plastic Reconstructive Surgery, Vol. 58, pp. 580-586, 1976.

[203] R.A. White, F.M. Hirose, R.W. Sproat, R.S. Lawrence, R.J. Nelson, "Histopathologic observations after short-term implantation of two porous elastomers in dogs," Biomaterials, Vol. 2, pp. 171-176, 1981.

[204] D. Lundgren, J.P. Hakansson, and P. Bodo, "Morphometric analysis of tissue components adjacent to percutaneous implants," in Tissue Integration in Oral and Maxillo-Facial Reconstruction, Excerpta Medica, Elsevier Science Publishers B.V., Amsterdam, pp. 173-180, 1986.

[205] J.H. Brauker, R.C. Johnson, L.A. Martinson, R.S. Hill, "Close vascularization implant material," U.S Patent 5741330, 1998.

[206] J.E. Sanders, S.E. Lamont, S.B. Mitchell, S.G. Malcolm, "Small fiber diameter fibro-porous meshes: Tissue response sensitivity to fiber spacing," Journal of Biomedical Materials Research, Vol. 72A, pp. 335-342, 2005.

[207] C.A. Squier, and P. Collins, "The relationship between soft tissue attachment, epithelial downgrowth and surface porosity," Journal of Periodontal Research, Vol. 16, pp. 434-440, 1981.

[208] J.H. Brauker, V.E. Carr-Brendel, L.A. Martinson, J. Crudele, W.D. Johnston, R.C. Johnson, "Neovascularization of synthetic membranes directed by membrane microarchitecture," Journal of Biomedical Materials Research, Vol. 29, pp. 1517-1524, 1995.

[209] A. Kantrowitz, P.S. Freed, A.A. Ciarkowski, I. Hayashi, F.L. Vaughan, J.I. VeShancey, R.H. Gray, R.K. Brabec, I.A. Bernstein, "Development of a percutaneous access device," ASAIO Transactions, Vol. 26, pp. 444-449, 1980.

[210] R.W. Bessette, T. Cowper, J. Natiella, M. Meenaghan, S. Shatkin, and N. Schaaf, "Histological evaluation of pore size and shape in silicone implants in rhesus monkeys," Annals of Plastic Surgery, Vol. 7, No. 6, pp. 447-452, 1981.

[211] C.E. Campbell, and A.F. von Recum, "Microtopography and soft tissue response," Journal of Investigative Surgery, Vol. 2, pp. 51-74, 1989.

[212] V.L Poirier, W.C. Clay, B.D.T. Daly, "Percutaneous access device," U.S Patent 4897081, 1990.

[213] A. Kantrowitz, and P.S. Freed, "Percutaneous access device," U.S Patent 5242415, 1993.

[214] N.T. Aubin, "Method and surgically implantable apparatus for providing fluid communication with the interior of the body," U.S Patent 4344435, August 1982.

[215] J.H. Brauker, R.S. Hill, L.A. Martinson, D.R. Boggs, R.C. Johnson, "Tissue implant systems and methods for sustaining viable high cell densities within a host," U.S patent 5593440, 1997.

[216] J.D. Raulerson, "Subcutaneous catheter stabilizing devices," U.S Patent 5599311, 1997.

[217] E.W. White, "Mesh sheet with microscopic projections and holes," U.S Patent 5348788, September 1994.

[218] A.F. von Recum, C.E. Campbell, "Soft tissue implant with micron-scale surface texture to optimize anchorage," U.S Patent 5219361, 1993.

[219] I.A. Brown, G.J.J. Cremore, P.J. Gibson, "Skeletal implants," U.S Patent 4863474, 1989.

[220] D.M. Brunette, "The effect of surface topography on cell migration and adhesion," Progress in Biomedical Engineering, Vol. 6, B.D. Ratner (ed.), Elsevier, New York, pp. 203-217, 1988.

[221] B. Chehroudi, T.R.L. Gould, and D.M. Brunette, "Titanium-coated micromachined grooves of different dimensions affect epithelial and connective-tissue cells differently in vivo," Journal of Biomedical Materials Research, Vol. 24, pp. 1203-1219, 1990.

[222] B. Chehroudi, T.R. Gould, and D.M. Brunette, "Effects of a grooved epoxy substratum on epithelial cell behavior in vitro and in vivo," Journal of Biomedical Materials Research, Vol. 22, pp. 459-473, 1988.

[223] B. Chehroudi, E. Soorany, N. Black, L. Weston, and D.M. Brunette, "Computer-assisted three-dimensional reconstruction of epithelial cells attached to percutaneous implants," Journal of Biomedical Materials Research, Vol. 29, pp. 371-379, 1995.

[224] A. Rich, and A.K. Harris, "Anomalous preferences of cultured macrophages for hydrophobic and roughened substrata," Journal of Cell Science, Vol. 5, pp. 1-7, 1981.

[225] T.N. Salthouse, "Some aspects of macrophage behavior at the implant interface," Journal of Biomedical Materials Research, Vol. 18, pp. 395-401, 1984.

[226] J.M. Anderson, "Inflammatory response to implants," ASAIO Transactions, Vol. 34, No. 2, pp. 101-107, 1988.

[227] L.A. Martinson, J.H. Brauker, R.C. Johnson, T. Loudovaris, "Methods for enhancing vascularization of implant devices," U.S Patent 5569462, 1996.

[228] C.W. Hall, P.A. Cox, S.R. McFarland, and J.J. Ghidoni, "Some factors that influence prolonged interfacial continuity," Journal of Biomedical Materials Research, Vol. 18, pp. 383-393, 1984.

[229] J.A. Jansen, J.P.C.M. van der Waerden, and K. de Groot, "Wound-healing phenomena around percutaneous devices implanted in rabbits," Journal of Materials Science: Materials in Medicine, Vol. 1, pp. 192-197, 1990.

[230] J.A. Jansen, and K. de Groot, "Guinea pig and rabbit model for the histological evaluation of permanent percutaneous implants," Biomaterials, Vol. 9, pp. 268-272, 1988.

[231] J.A. Svensson, R. Axelsson, "Percutaneous access device," U.S Patent 5098397, 1992.

[232] C. Grosse-Siestrup, W. Krautzberger, and E.S. Bucherl, "Arterio-venous shunt with percutaneous leads in calves for long-term in vivo testing of blood contact materials," Journal of Biomedical Materials Research, Vol. 13, pp. 15-22, 1979.

[233] W.L. Hastings, J.L. Aaron, J. Deneris, T.R. Kessler, A.B. Pons, K.J. Razzeca, D.B. Olsen, and W.J. Kolff, "A retrospective study of nine calves surviving five months on the pneumatic total artificial heart," Transactions of American Society of Artificial Internal Organs, Vol. 27, pp. 71-76, 1981.

[234] A.F. von Recum, and J.B. Park, "Permanent percutaneous devices," CRC Critical Reviews in Bioengineering, Vol. 5, No. 1, pp. 37-77, 1981.

[235] J.A. Jansen, J.P.C.M. van der Waerden, H.B.M. van der Lubbe, and K. de Groot, "Tissue response to percutaneous implants in rabbits," Journal of Biomedical Materials Research, Vol. 24, pp. 295-307, 1990.

[236] A. Tjellstrom, "Percutaneous implants in clinical practice," CRC Critical Reviews on Biocompatibility, Vol. 1, pp. 205-208, 1985.

[237] D.L. Powers, M.L. Hendriks, and A.F. von Recum, "Percutaneous healing of clinical tympanic membrane implants," Journal of Biomedical Materials Research, Vol. 20, pp. 143-151, 1986.

[238] C. Grosse-Siestrup, and K. Affeld, "Design criteria for percutaneous devices," Journal of Biomedical Materials Research, Vol. 18, pp. 357-382, 1984.

[239] J.A. Jansen, Y.G.C.J. Paquay, and J.P.C.M. van der Waerden, "Tissue reaction to soft-tissue anchored percutaneous implants in rabbits," Journal of Biomedical Materials Research, Vol. 28, pp. 1047-1054, 1994.

[240] D.C. MacGregor, "Strain relief for percutaneous lead," U.S Patent 4579120, 1986.

[241] H. Becker, R. Schurig, G. Gahl, M. Kessel, and K. Affeld, "Clinical and technical experiences in peritoneal dialysis: Technique, complications and new technical devices," in Peritoneal Dialysis, S. Fenton, M. Kaye, and J. Price, Eds., Princeton Junction, NJ, 1982.

[242] N.S. Korivi, P.K. Ajmera, "Implantable Clip-On Micro-Cuff Electrode for Functional Electrical Stimulation and Bio-potential Recording," US Patent Application 12/653,476, 15 December 2009.

[243] N.S. Korivi, and P.K. Ajmera, "Clip-on cuff electrode for neural stimulation and recording," Journal of Medical and Biomedical Engineering, in press, 2011.

[244] A.C. Spiers, and R. Blocksma, "New implantable silicone rubbers," Plastic Reconstructive Surgery, Vol. 31, pp. 166-175, 1963.

[245] S.A. Braley, "The use of silicones in plastic surgery. A retrospective view," Plastic Reconstructive Surgery, Vol. 51, pp. 280-288, 1973.

[246] J.A. Lilla, and L.M. Vistnes, "Long-term study of reactions to various silicone implants in rabbits," Plastic Reconstructive Surgery, Vol. 57, pp. 637-649, 1976.

[247] Leptos Biomedical, San Mateo, CA, USA, e-mail correspondence, 16 June 2008.

[248] C. Donfack, M. Sawan, and Y. Savaria, "Implantable measurement technique dedicated to the monitoring of electrode-nerve contact in bladder stimulators," Medical and Biological Engineering and Computing, Vol. 38, pp. 465-468, 2000.

[249] K.W. Altman, and R. Plonsey, "Analysis of the longitudinal and radial resistivity measurements of the nerve trunk," Annals of Biomedical Engineering, Vol. 17, pp. 313-324, 1989.

[250] M.S. Ju, H.C. Chien, G.S. Chen, C.-C.K. Lin, C.-H. Chang, "Design and fabrication of multi-microelectrode array for neural prosthesis," Journal of Medical and Biological Engineering, 22: 33-40, 2002.

[251] N. Bhadra, and J.T. Mortimer, "Extraction forces and tissue changes during explants of CWRU-type intramuscular electrodes from rat gastrocnemius," Annals of Biomedical Engineering, Vol. 25, pp. 1017-1025, 1997.

[252] N. Bhadra, and J.T. Mortimer, "Extraction force and tissue change during removal of a tined intramuscular electrode from rat gastrocnemius," Annals of Biomedical Engineering, Vol. 34, pp. 1042-1050, 2006.

[253] M. Mascini, M.A. Mateescu, and R. Pilloton, "Polyvinylalcohol-collagen membranes for enzyme immobilization," Bioelectrochemistry and Bioenergetics, vol. 16, pp. 149-157, 1986.

[254] Martin Bak, CEO, Microprobes for Lifescience, Inc., Gaithersburg, MD, USA, telephone conversation, 25 January 2010.

[255] Martin Bak, CEO, Microprobes for Lifescience, Inc., Gaithersburg, MD, USA, E-mail correspondence, 24 November 2009.

[256] B. Rydevik, G. Lundborg, and U. Bagge, "Effects of graded compression on intraneural blood flow – An in vivo study on rabbit tibial nerve," Journal of Hand Surgery, Vol. 6, pp. 3-12, 1981.

[257] D. Tyler, and D.M. Durand, "Flat interface nerve electrode and a method for use," US Patent 6456866, 2002.

[258] A.P. Boresi, and O.M. Sidebottom, Advanced Mechanics of Materials, 4th Edition, New York; Wiley, 1985.

[259] Silastic fluorosilicone rubbers, product data sheet, Dow Corning, New York, USA.

[260] J.L. Tan, J. Tien, D.M. Pirone, D.S. Gray, K. Bhadriraju, and C.S. Chen, "Cells lying on a bed of microneedles: An approach to isolate mechanical force," Proceedings of National Academy of Science, Vol. 100, No. 4, pp. 1484-1489, 2003.

[261] K. Rau, R. Singh, and E. Goldberg, "Nanoindentation and nanoscratch measurements on silicone thin films synthesized by pulsed laser ablation deposition (PLAD)," Materials Research Innovations, Vol. 5, pp. 151-161, 2002.

[262] J.N. Lee, X. Jiang, D. Ryan, and G.M. Whitesides, "Compatibility of mammalian cells on surfaces of poly(dimethylsiloxane)," Langmuir, Vol. 20, pp. 11684-11691, 2004.

[263] A. Mata, A.J. Fleischman, and S. Roy, "Characterization of polydimethylsiloxane (PDMS) properties for biomedical micro/nanosystems," Biomedical Microdevices, Vol. 7, No. 4, pp. 281-293, 2005.

[264] J.C. Lotters, W. Olthuis, P.H. Veltink, and P. Bergveld, "The mechanical properties of the rubber elastic polymer polydimethylsiloxane for sensor applications," Journal of Micromechanics and Microengineering, Vol. 7, pp. 145-147, 1997.

[265] L.B. Tang, Y.H. Chen, and X.J. He, "Multi-material compliant mechanism design and haptic evaluation," Virtual and Physical Prototyping, Vol. 2, pp. 155-160, 2007.

[266] Y. Tian, B. Shirinzadeh, and D. Zhang, "Closed-form compliance equations of filleted V-shaped flexure hinges for compliant mechanism design," Precision Engineering, Vol. 34, pp. 408-418, 2010.

[267] T.B. Ducker, and G.J. Hayes, "Experimental improvements in the use of Silastic cuff for peripheral nerve repair," Journal of Neurosurgery, Vol. 28, pp. 582-587, 1968.

[268] N.S. Korivi, and P.K. Ajmera, "Bio-implantable Pacing Electrode with Thermally Regulated Structural Flexibility," LSU Office of Intellectual Property disclosure #1030, March 2010.

[269] N.S. Korivi, C. Halliburton, and P.K. Ajmera, "Thermally responsive structures for gastric pacing and other applications," Proceedings of ASME 5th Frontiers in Biomedical Devices Conference & Exhibition, Newport Beach, California, September 20-21, 2010.

[270] A. Kishida, K. Mishima, E. Corretge, H. Konishi, and Y. Ikada, "Interactions of poly(ethylene glycol)-grafted cellulose membranes with proteins and platelets," Biomaterials, Vol. 13, pp. 113-118, 1992.

[271] M. Malmsten, K. Emoto, and J.M. Van Alstine, "Effect of chain density on inhibition of protein adsorption by poly(ethylene glycol) based coatings, Journal of Colloid Interface Science, Vol. 202, pp. 507-517, 1998.

[272] D.W. Branch, B.C. Wheeler, G.J. Brewer, and D.E. Leckband, "Long-term stability of grafted polyethylene glycol surfaces for use with microstamped substrates in neuronal cell culture," Biomaterials, Vol. 22, pp. 1035-1047, 2001.

[273] S. Sharma, R.W. Johnson, and T.A. Desai, "Ultrathin poly(ethylene glycol) films for silicone-based microdevices," Applied Surface Science, Vol. 206, pp. 218-229, 2003.

[274] E.V. Goodall, T.M. Lefurge, and K.W. Horch, "Information contained in sensory nerve recordings made with intrafascicular electrodes," IEEE Transactions on Biomedical Engineering, Vol. 38, pp. 846-850, 1991.

[275] T. Lefurge, E. Goodall, K. Horch, L. Stensaas, and A. Schoenberg, "Chronically implanted intrafascicular recording electrodes," Annals of Biomedical Engineering, Vol. 19, pp. 197-207, 1991.

[276] J.M. Norton, and P.W. Rand, "Chronically implanted tissue oxygen electrodes in rabbits," Journal of Applied Physiology, Vol. 36, No. 1, pp. 118-122, 1974.

[277] N.S. Korivi, and P.K. Ajmera, "Equivalent circuit model for a neural interface," International Journal of Recent Trends in Engineering and Technology, Vol. 4, No. 3, pp. 160-163, 2010.

[278] D.R. Merrill, M. Bikson, J.G.R. Jefferys, "Electrical stimulation of excitable tissue – design of efficacious and safe protocols," Journal of Neuroscience Methods, Vol. 141, pp. 171-198, 2005.

[279] S.R. Taylor, and E. Gileadi, "Physical interpretation of the Warburg impedance," Corrosion Science, Vol. 51, pp. 664-671, 1994.

[280] W.B. Marks, and G.E. Loeb, "Action currents, internodal potentials, and extracellular records of myelinated mammalian nerve fibers derived from node potentials," Biophysical Journal, Vol. 16, pp. 655-668, 1976.

[281] D.C. Grahame, "Mathematical theory of the faradaic admittance," Journal of Electrochemical Society, Vol. 99, pp. 370C-385C, 1952.

[282] G.T.A. Kovacs, "Introduction to the theory, design, and modeling of thin-film microelectrodes for neural networks," in Enabling Technologies for Cultured Neural Networks, D.A. Stenger and T.M. McKenna, Eds., Academic Press, London, U.K, pp. 121-165, 1994.

[283] E.T. McAdams, and J. Jossinet, "Physical interpretation of Schwan's limit voltage of linearity," Med. Biol. Eng. Comp., Vol. 32, pp. 126-130, 1994.

[284] W. Franks, I. Schenker, P. Schmutz, and A. Hierlemann, "Impedance characterization and modeling of electrodes for biomedical applications," IEEE Transactions on Biomedical Engineering, Vol. 52, No. 7, pp. 1295-1302, 2005.

[285] A.J. Bard, and L.R. Faulkner, Electrochemical Methods, J. Wiley & Sons, New York, 2001.

[286] Application Note, Gamry Instruments, PA, USA; [www.gamry.com].

[287] P.W. Davies, "The oxygen cathode," in Physical Techniques in Biological Research, W.L. Nastuk, Ed., Academic Press, London, U.K, Vol. IV, pp. 137-179, 1962.

[288] E. Yeager, "Electrocatalysts for O_2 reduction," Electrochimica Acta, Vol. 29, pp. 1527-1537, 1984.

[289] K. Najafi, and K.D. Wise, "An implantable multielectrode array with on-chip signal processing," IEEE Journal of Solid-State Circuits, Vol. 21, No. 6, pp. 1035-1044, 1986.

[290] D.A. Borkholder, "Cell based biosensors using microelectrodes," Ph.D. thesis, Stanford University, Stanford, CA, USA, 1998.

[291] J. Millar, and T.G. Barnett, "Zeta pulse - a new stimulus waveform for use in electrical stimulation of the nervous system," Journal of Neuroscience Methods, Vol. 77, pp. 1-8, 1997.

[292] K.S. Cole, "Membranes, Ions and Impulses," University of California Press, Los Angeles, CA, 1968.

[293] A.L. Hodgkin, and A.F. Huxley, "A quantitative description of membrane current and its application to conduction and excitation in nerve," Journal of Physiology, Vol. 117, pp. 500-544, 1952.

[294] A.L. Hodgkin, The conduction of the nervous impulse, Thomas, Springfield, IL, 1964.

[295] P.L. Williams, and C.P. Wendell-Smith, "Some additional parametric variations between peripheral nerve fiber populations," Journal of Anatomy, Vol. 109, pp. 505, 1971.

[296] S.G. Waxman, Physiology and Pathobiology of Axons, Raven Press, New York, 1978.

[297] A. Hess, J.Z. Young, "The nodes of Ranvier," Proceedings of Royal Society London B Biological Sciences, Vol. B140, pp. 301-319, 1952.

[298] J. Cronin, Mathematical aspects of Hodgkin-Huxley neural theory, Cambridge University Press, New York, USA, 1987.

[299] S.B. Brummer, L.S. Robblee, and F.T. Hambrecht, "Criteria for selecting electrodes for electrical stimulation: theoretical and practical considerations," Annals of the New York Academy of Sciences, Vol. 405, pp. 159-171, 1983.

[300] G.E. Loeb, M.W. White, and W.M. Jenkins, "Biophysical considerations in electrical stimulation of the auditory nervous system," Annals of the New York Academy of Sciences, Vol. 405, pp. 123-136, 1983.

[301] M. Gerhardt, and A. Stett, "Subretinal stimulation with hyperpolarising and depolarising voltage steps," Proceedings of 6th International Meeting on Substrate-Integrated Microelectrodes, pp. 144-147, 2008.

[302] Leptos Biomedical, San Mateo, CA, USA, e-mail correspondence, 17 December 2007.

[303] A. Ritchie, "The electrical diagnosis of peripheral nerve injury," Brain, Vol. 67, pp. 314-330, 1944.

[304] E.D. Adrian, "The response of human sensory nerves to currents of short duration," Journal of Physiology, Vol. 53, pp. 70-85, 1919.

[305] J.A. Pearce, J.D. Bourland, W. Neilson, L.A. Geddes, and M. Voelz, "Myocardial stimulation with ultrashort duration current pulses," PACE, Vol. 5, pp. 52-58, 1982.

[306] C.-L. Li, and A. Bak, "Excitability characteristics of A and C fibers," Experimental Neurology, Vol. 50, pp. 67-79, 1976.

[307] S.D. Stoney, W.D. Thompson, and H. Asanuma, "Excitation of pyramidal tract cells by intracortical microstimulation: effective extent of stimulating current," Journal of Neurophysiology, Vol. 31, pp. 659-669, 1968.

[308] J.B. Ranck, "Which elements are excited in electrical stimulation of mammalian central nervous system: a review," Brain Research, Vol. 98, pp. 417-440, 1975.

[309] H. Asanuma, A. Arnold, and P. Zarzecki, "Further study on the excitation of pyramidal tract cells by intracortical microstimulation," Experimental Brain Research, Vol. 26, pp. 443-461, 1976.

[310] D.C. West and J.H. Wolstencroft, "Strength-duration characteristics of myelinated and non-myelinated bulbospinal axons in the cat spinal cord," Journal of Physiology, Vol. 337, pp. 37-50, 1983.

[311] I.D. Hentall, G. Zorman, S. Kansky, and H.L. Fields, "An estimate of minimum number of brainstem neurons required for inhibition of a flexion reflex," Journal of Neurophysiology, Vol. 51, pp. 978-985, 1984.

[312] D.B. McCreery, and W.F. Agnew, "Neuronal and axonal injury during functional electrical stimulation; a review of the possible mechanisms," Proceedings of the 12th Annual Conference of the IEEE Engineering in Medicine and Biology Society, Vol. 12, No. 4, pp. 1488-1489, 1990.

[313] C. van der Honert, and J.T. Mortimer, "Generation of unidirectionally propagated action potentials in a peripheral nerve by brief stimuli," Science, Vol. 206, pp. 1311-1312, 1979.

[314] J.H. Byrne, Propagation of the action potential, Neuroscience Online: An electronic textbook for the neurosciences, The University of Texas Health Science Center at Houston, The University of Texas Medical School at Houston; http://neuroscience.uth.tmc.edu/s1/i3-1.html, [Last retrieved on March 1, 2011].

[315] A.G. Brown, Nerve Cells and Nervous Systems: An Introduction to Neuroscience, 2nd edition, Springer-Verlag London, 2001.

[316] H. Asanuma, and A.P. Arnold, "Noxious effects of excessive currents used for intracortical microstimulation," Brain Research, Vol. 96, pp. 103-107, 1975.

[317] E.J. Tehovnik, "Electrical stimulation of neural tissue to evoke behavioral responses," Journal of Neuroscience Methods, Vol. 65, pp. 1-17, 1996.

[318] E.J. Tehovnik, and J.S. Yeomans, "Two converging brainstem pathways mediating circling behavior," Brain Research, Vol. 385, pp. 329-342, 1986.

[319] J. Schlag, and M. Schlag-Rey, "Evidence for a supplementary eye field," Journal of Neurophysiology, Vol. 57, pp. 179-200, 1987.

[320] E.J. Tehovnik, and K.-M. Lee, "The dorsomedial frontal cortex of the rhesus monkey: topographic representation of saccades evoked by electrical stimulation," Experimental Brain Research, Vol. 96, pp. 430-442, 1993.

[321] R.V. Davalos, B. Rubinsky, and L.M. Mir, "Theoretical analysis of the thermal effects during in vivo tissue electroporation," Bioelectrochemistry, Vol. 61, pp. 99-107, 2003.

[322] N. Dafny, Pain Principles, Neuroscience Online: An electronic textbook for the neurosciences, The University of Texas Health Science Center at Houston, The University of Texas Medical School at Houston; http://neuroscience.uth.tmc.edu/s2/ii6-2.html, [Last retrieved on March 1, 2011].

[323] D.B. McCreery, and W.F. Agnew, "Neuronal and axonal injury during functional electrical stimulation; a review of the possible mechanisms," Proceedings of the IEEE Engineering in Medicine and Biology Society, Vol. 12, pp. 1488-1489, 1990.

[324] R.T. Ruggeri, and T.R. Beck, "Calculations of temperature rise produced in body tissue by a spherical electrode," Annals of Biomedical Engineering, Vol. 13, pp. 177-194, 1985.

[325] L. Goldman, and J.S. Albus, "Computation of impulse conduction in myelinated fibers: theoretical basis of the velocity-diameter relation," Biophysical Journal, Vol. 8, pp. 596-607, 1968.

[326] C. Abzug, M. Maeda, B.W. Peterson, and V.J. Wilson, "Cervical branching of lumbar vestibulospinal axons," Journal of Physiology, Vol. 243, pp. 499-522, 1974.

[327] D.A. Teicher, and D.R. McNeal, "Comparison of a dynamic and steady-state model for determining nerve fiber threshold," IEEE Transactions on Biomedical Engineering, Vol. BME-25, pp. 105-107, 1978.

[328] C.W. Hall, L.M. Adams, and J.J. Ghidoni, "Development of skin interfacing cannula," Transactions of American Society for Artificial Internal Organs, Vol. 21, pp. 281-284, 1975.

[329] P. Didisheim, and J.T. Watson, "Cardiovascular Applications," Biomaterials Science: An Introduction to Materials in Medicine, Editors: B.D. Ratner, A.S. Hoffman, F.J. Schoen, J.E. Lemons, Academic Press, San Diego, USA, 1996.

[330] M.A. Sadowsky, and E. Sternberg, "Stress concentration around a tri-axial ellipsoidal cavity," Journal of Applied Mechanics, Vol. 71, pp. 149, 1949.

[331] C.S Yen, and T.J. Dolan, "A critical review of the criteria for notch-sensitivity in fatigue of metals," University of Illinois Bulletin, Vol. 49, No. 53, 1952.

[332] R.E. Peterson, Stress Concentration Factors for Design, Wiley, New York, 1974.

[333] N.S. Korivi, P.K. Ajmera, "Percutaneous Interface for Implant-to-External World Interconnections," LSU Office of Intellectual Property disclosure #0846, June 2008.

[334] N.S. Korivi, and P.K. Ajmera, "Percutaneous access device with stress relief features," Proceedings of ASME 5th Frontiers in Biomedical Devices Conference & Exhibition, Newport Beach, California, September 20-21, 2010.

[335] N.S. Korivi, P.K. Ajmera, "Method for Incorporating Selective and At-Large Porosity in Elastomeric Layers and Microfluidic Structures," US Patent Provisional Application #61/266,765, 4 December 2009.

[336] Vascular infusion cables and swivels, product data sheet, Instech Labs, Plymouth Meeting, PA, USA.

[337] R. Nyman, H. Eklof, L-G. Eriksson, B-M. Karlsson, I. Rasmussen, D. Lundgren, P. Thomsen, "Soft-tissue-anchored transcutaneous port for long-term percutaneous transhepatic biliary drainage," Cardiovascular and Interventional Radiology, Vol. 28, pp. 53-59, 2005.

[338] H. Neuber, Kerbspannungslehre, 2nd Edition, Springer-Verlag, Berlin, 1958.

[339] H. Neuber, "Theory of stress concentration for shear strained prismatic bodies with nonlinear stress-strain law," Journal of Applied Mechanics, Vol. 28, No. 4, pp. 544-550, 1961.

[340] H. Neuber, "Research on distribution of tension in notched construction parts," Wright Air Development Division (WADD) Technical Report 60-906, 1961.

[341] V.M. Kornev, "Modified Neuber-Novozhilov criterion of rupture for v-shaped cuts (antiplane problem)," Journal of Applied Mechanics and Technical Physics, Vol. 43, No. 1, pp. 128-132, 2002.

[342] G.A. Savin, Stress Concentration around Holes, Pergamon Press, New York, 1961.

[343] S. Timoshenko, and J. Goodier, Theory of Elasticity, 3rd Edition, McGraw-Hill, 1970.

[344] Connectors for precision perivascular flowprobes, Transonic System Inc., Ithaca, NY, USA; [www.transonic.com].

[345] N.S. Korivi and P.K. Ajmera, "Micropatterning of Biocompatible Materials," International Conference on MEMS (ICMEMS 2009), Chennai, India, January 2009.

[346] N.S. Korivi, and P.K. Ajmera, "Incorporation of micro- and nano-scale porosity on silicon surfaces," Proceedings of the 54th International Conference on Electron, Ion & Photon Beam Technology and Nanofabrication, Anchorage, AK, June 1-4, 2010.

[347] N.S. Korivi, J. Hoffpauir, and P.K. Ajmera, "Texturing of silicon using a microporous polymer etch mask," Journal of Vacuum Science and Technology B: Microelectronics and Nanometer Structures, Vol. 28, Issue 6, pp. C6K8, 2010.

[348] D.J. Mooney, C. Breuer, K. McNamara, J.P. Vacanti, and R. Langer, "Fabricating tubular devices from polymers of lactic and glycolic acid for tissue engineering," Tissue Engineering, Vol. 1, No. 2, pp. 107-118, 1995.

[349] D.L. Boutle, "Production of porous materials," US Patent 4242464, 1980.

[350] E.E. Frisch, "Methods for forming hollow, porous-surfaced elastomeric bodies," US Patent 4892544, 1990.

[351] C-I. Lee, S. Spells, "Microwave cured silicone elastomeric foam," US Patent 4460713, 1984.

[352] D. Knight, "Stretchable tear resistant porous elastomeric film elements and processes," US Patent 5336554, 1994.

[353] J.D. Morse, K.A. Rose, M. Maghribi, W. Benett, P. Krulevitch, J. Hamilton, R.T. Graff, A. Jankowski, "Microfluidic systems with embedded materials and structures and method thereof," US Patent 7186352, 2007.

[354] K.L. Goetz, and F.F. Hanis, "A convenient skin button connector for withdrawal of blood samples," Journal of Applied Physiology, Vol. 22, No. 6, pp. 1165-1166, 1967.

[355] O.Z. Roy, "A Silastic interface," Medical and Biological Engineering and Computing, Vol. 6, pp. 443-445, 1968.

[356] C. Fritzsch, "A skin button to anchor and lead out catheters or cable links from the skin," Zeitschrift fűr experimentelle Chirurgie, Transplantation, und kűnstliche Organe, Vol. 23, No. 1, pp. 51-52, 1990.

[357] B.D. Daly, M. Worthington, and R.J. Cleveland, "Percutaneous energy transmission systems (PETS)," Transactions of American Society of Artificial Internal Organs, Vol. 27, pp. 147-150, 1981.

[358] M. Lipsky, M. Brown, H. Harrower, and W.R. Thayer, "An intermittent pyloric occluder for obtaining complete gastric contents in dogs," Journal of Applied Physiology, Vol. 27, No. 5, pp. 737-739, 1969.

[359] J.E. Levasseur, K.C. Corley, R.M. Butler, C.R. Fields, and F.T. Grove, "Long-term measurement of pulsatile blood pressure and ECG in the squirrel monkey," Journal of Applied Physiology, Vol. 32, No. 2, pp. 271-275, 1972.

[360] A.J. Snyder, "An electrically powered total artificial heart. Over 1 year survival in the calf," ASAIO Journal, Vol. 38, No. 3, pp. M707-M712, 1992.

[361] D.L. Johnson, J.M. Findlay, D. Higgs, W.E. McMorran, and M.W. Jacobs, "Apparatus for intraosseous infusion or aspiration," US Patent 5817052, 1998.

[362] G.G. Bosquet, G.L. Cote, A. Gowda, R. McNichols, S. Rastegar, “Method and apparatus for analyte detection using intradermally implanted skin port,” US Patent 6438397, 2002.

APPENDIX A: GLOSSARY OF TERMS

[1] Action potential – the cycle of changes in the transmembrane potential, negative to positive to negative again, that characterizes excitable tissue. This cycle is also described as resting to excited and returning to rest.

[2] Axon – a basic component of a neuron or nerve cell. The axon carries signals from the main body of the neuron containing the nucleus to a target.

[3] Chronaxie – the minimum interval of time necessary to electrically stimulate a muscle or nerve fiber using twice the minimum current needed to elicit a threshold response.

[4] Depolarization – a process that is said to occur whenever the transmembrane potential becomes more positive than a resting potential.

[5] Extracellular – outside a cell.

[6] Intracellular – inside a cell.

[7] Myelin - a segmented, white fatty substance forming a sheath on the axons.

[8] Myelinated – a term used to describe parts of the axon that are covered by a myelin sheath.

[9] Repolarization – a process that usually follows depolarization and causes the transmembrane potential to return to its polarized state.

[10] Transmembrane potential – the potential inside a cell membrane measured with respect to the potential just outside the membrane.

[11] Unmyelinated - a term used to describe parts of the axon that are not covered by a myelin sheath. There are unmyelinated regions between the myelin covered segments on the axon, known as nodes of Ranvier.

APPENDIX B: DETERMINATION OF TARGET NERVE DIMENSIONS

Fluorescence Tests

Some of the cuff electrodes developed in this research were intended for a pilot project undertaken by the Pennington Biomedical Research Center to evaluate functional neural stimulation for obesity treatment in rodents. Prior to designing the electrodes, it was necessary to accurately determine the dimensions of the nerve tissue targeted for electrical stimulation. This was done by means of fluorescence tests conducted by Dr. Jolene Zheng of the Louisiana State University Agricultural Center, under an approval from the Institutional Animal Care and Use Committee (IACUC). Three test rats (Adult male, Sprague-Dawley) were individually injected with Fluoro-Gold^{TM} (3mg/ml) in 0.9% saline. Fluoro-Gold^{TM} (Fluorochrome LLC, Denver CO) is a fluorescent retrograde marker typically used for neuronal labeling and neuroanatomical tracing [1].

After a waiting period of three to five days, the rats were dissected and the inner tissues were observed under a dissection microscope. Under ultra-violet light, the Fluoro-Gold^{TM} injected nervous tissue was clearly observed. The celiac ganglion hub was found to be about 2-2.5 mm in diameter and 5 mm in length. The left and right celiac branches were observed to be approximately 250-300 μm in diameter with a length of 3-4 mm (Figure B.1). The branch dimensions were significant because it was intended to electrically stimulate the celiac branches for obesity control.

References

[1] L.A. Catapano, S.S. Magavi, and J.D Macklis, "Neuroanatomical Tracing of Neuronal Projections with Fluoro-Gold," Neural Stem Cells: Methods and Protocols, Methods in Molecular Biology, Vol. 438, pp. 353-359, 2008.

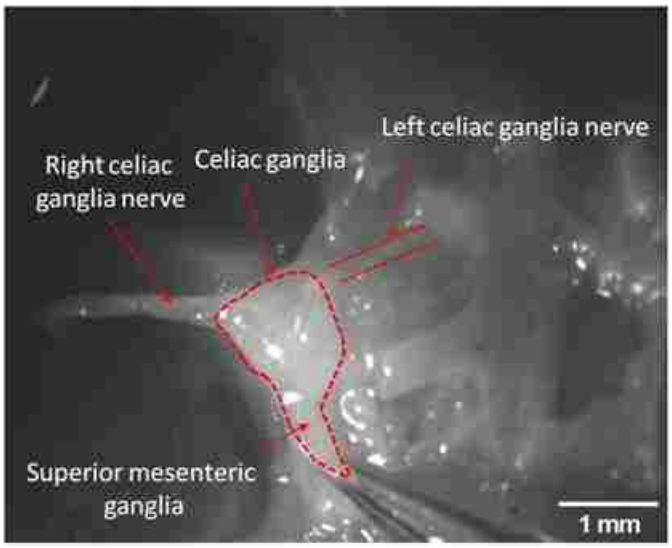

Figure B.1: Microscope image of celiac ganglia anatomy in adult male Sprague-Dawley rodents. [Courtesy of Dr. Jolene Zheng, Louisiana State University]

APPENDIX C: FABRICATION OF CLIP-ON MICRO-CUFF ELECTRODE BY MOLDING

Fabrication by Molding

A molding process was investigated for its feasibility in fabricating the clip-on micro-cuff electrode. The process consisting of a single molding step employs a master mold comprising of two or more individual parts. The fabricated version of the clip-on micro-cuff electrode is shown in Figure C.1.

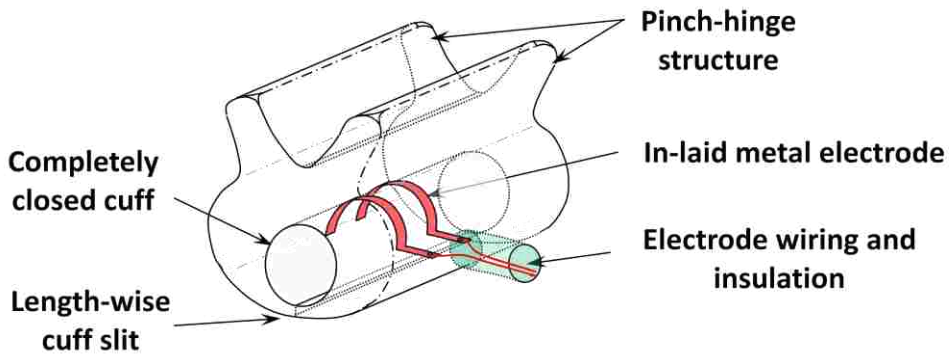

Figure C.1: Schematic of a version of the clip-on micro-cuff electrode to be realized by a molding process.

The master mold parts are made by machining individual pieces of plastic, and then assembled together. Figure C.2 shows a master mold made of plastic with two main parts. One part of the master mold consists of a half cylinder, with a pin attached at its bottom (Figure C.2A). The pin is attached by means of adhesive epoxy. A semi-circular groove is provided on one side of this mold part, extending from the centrally located pin to the outer edge of one side of the mold part. This groove serves to hold electrode wires. Another part of the master mold consists of a half cylinder, with two grooves at its bottom (Figure C.2B). Similar to the first part

of the mold, a semi-circular groove is provided on the second mold part, extending from the center to the outer edge of one side of the mold part. This groove serves to hold electrode wires. The two parts of the master mold are coated with a mold release chemical, polyvinyl alcohol (PVA), by a dip-coating process. The PVA coating is allowed to cure at room temperature.

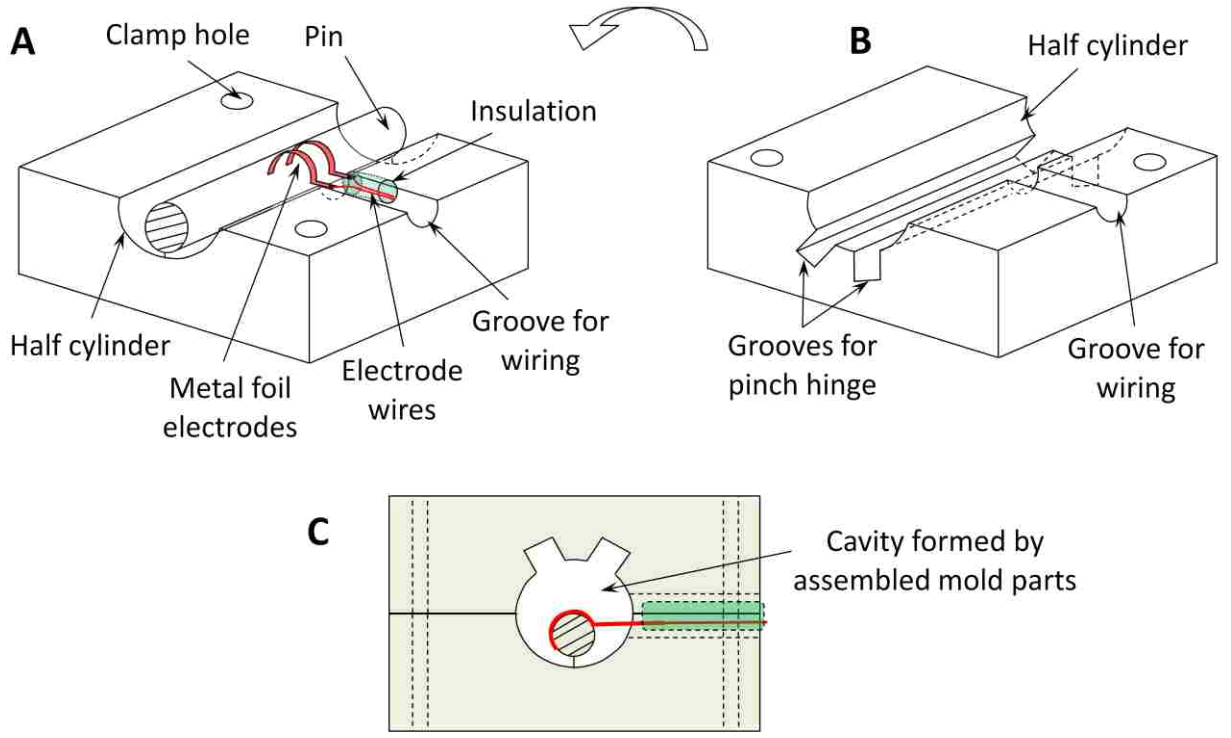

Figure C.2: Schematic diagram of molding-based fabrication of the clip-on micro-cuff electrode. A single molding step is employed with a master mold consisting of two individual parts.

Metal foil electrodes (two are shown in Figure C.2A) are placed in contact with approximately half the circumference of the pin in the first mold part. The number of metal foil electrodes depends on the application. The metal foil electrodes are previously cut to size from commercial available stainless steel foil (25 µm thick) and spot-welded to wires made of

stainless steel. These wires serve as interconnecting wires from the implanted electrodes to other electronic equipment. The stainless steel wires are coated with insulation and additionally, surrounded by silicone tubing. The wires with the insulation are placed in the mold groove leading away from the foil electrodes placed on the pin. The two parts of the master mold are secured together by means of the holes provided for clamping (Figure C.2C). Optionally, more holes, threaded or plain, can be employed to hold the parts of the mold together.

After the mold parts are clamped together, the master mold is placed vertically on a glass surface such as a Pyrex dish and Silastic silicone elastomer pre-polymer liquid is poured into the enclosed cavity of the mold. The silicone is cured thermally at 60 ^{0}C for 3 hrs. Following the curing process, the master mold assembly is unclamped and the two mold parts are detached. Dissolving the mold release layer in an ultrasonic bath of water aids the detachment of the parts. The removal of the mold release layer also causes the cured silicone structure to be released from the mold. Subsequently, the cured silicone structure is optionally trimmed to obtain the clip-on micro-cuff with the desired cuff length. A typical master mold for the molding process is shown in Figure C.3.

Some problems were encountered in the molding of thicker layers of Silastic silicone i.e. layers with thickness in the order of a few mm or more. To study this problem, molds made of materials such as aluminum, stainless steel, acrylic, polypropylene, polyethylene, and polyvinyl chloride were investigated. Silastic pre-polymer did not cure completely when poured over mold parts or into cavities made by assembling mold parts together. More specifically, it was observed that Silastic silicone was being cured in areas away from the mold walls, but not in the immediate vicinity of the mold walls. The curing parameters like temperature and time were changed. Temperatures ranging from room temperature to 100 ^{0}C and curing periods ranging

from 2 hours to 7 days were investigated. Modulating these parameters did not appear to have an appreciable impact on the curing of the Silastic silicone adjacent to the mold surfaces.

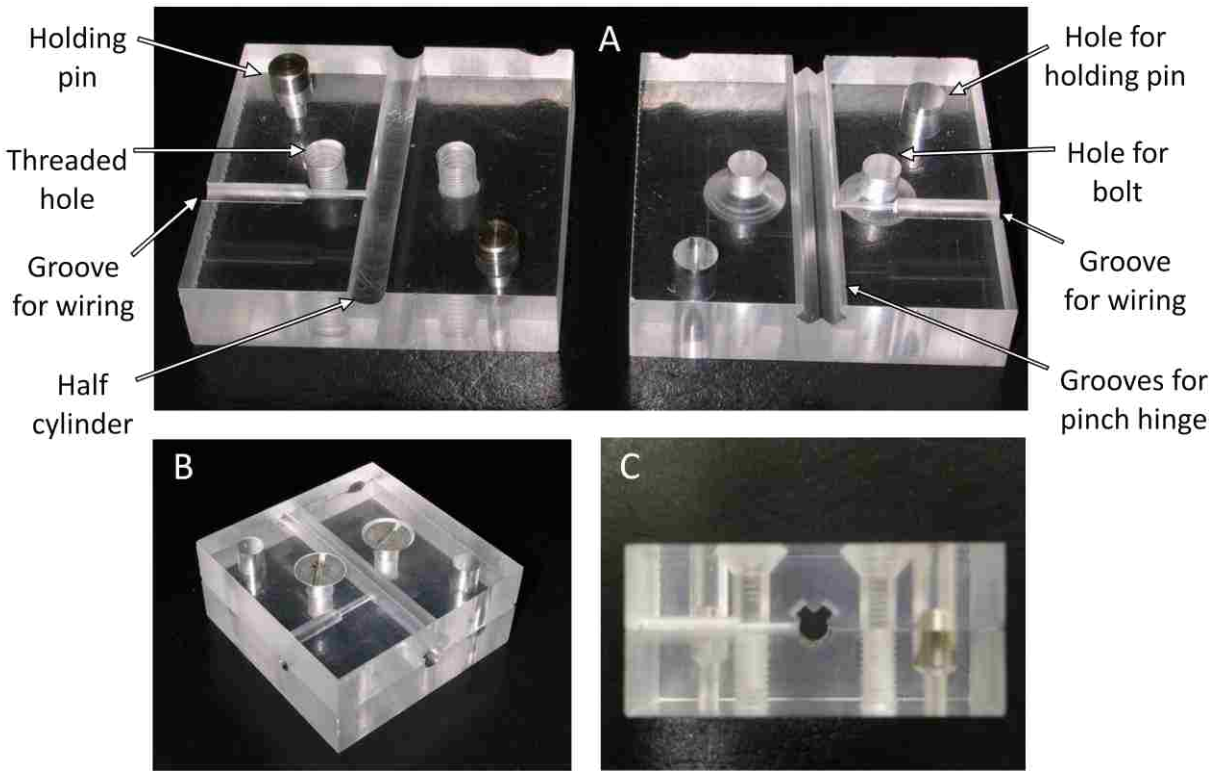

Figure C.3: Photographic images of (A) the two parts of the master mold for fabrication of the clip-on micro-cuff electrode; (B) the two parts of the mold clamped together; (C) cross-sectional view of the mold parts clamped together. In addition to the originally envisioned clamp hole-holding pin scheme, a threaded bolt arrangement has been included for enhanced clamping in the most recent embodiment of the master mold. The master mold with both parts clamped together has dimensions of 18 mm (height) x 40 mm (length) x 40 mm (width).

The effect of the curing ambient was also investigated by curing some samples in vacuum at a specific temperature. The incomplete curing persisted in the vacuum cured samples. Decreasing the ratio of the Silastic pre-polymer to curing agent from a manufacturer recommended 10:1 to 8:1 and even 7:1 enhanced the curing to an extent, but did not adequately

solve the curing problem. This applied for all the plastic and metal mold materials tested. A drawback of increasing the amount of curing agent was the increased rigidity in the resulting cured Silastic structures. This was not desirable because of the need for flexibility in the cuff body.

In subsequent experiments, the mold parts were subjected to oxygen plasma treatment (100W, 50 mTorr) for 15 min, prior to the molding process. It was found that the curing of Silastic was enhanced with all the different mold materials. Silicone elastomers are generally hydrophobic [1-3]. An oxygen plasma treatment of the mold parts enhances their hydrophilic nature. This allows for the naturally hydrophobic Silastic pre-polymer to make a more intimate contact with the mold walls. Subsequently, the extent of curing in the immediate vicinity of the mold walls is improved.

In further experimentation, it was observed that better curing results were obtained by heating the Silastic pre-polymer solution, before introducing it onto the mold cavities. Heating the Silastic pre-polymer accelerates its cross-linking process. When the heated pre-polymer is poured onto the mold cavities, it is easier to cure further, since the curing process i.e. the cross-linking has already started. When silicone pre-polymer is heated, its viscosity increases [4]. Therefore, the pre-heating of the Silastic pre-polymer has to be moderated, to ensure that the viscosity does not increase to the extent that its flow and coverage characteristics are considerably altered. Our experiments showed that Silastic samples cured at higher temperatures (90-100 ^{0}C) for extended periods of time (3-4 hours) resulted in more flexible structures in general. This observation is corroborated by a recent report that heat treatment of cured polydimethylsiloxane (PDMS) layers results in enhanced flexibility due to reduced mechanical strength of the material [5]. In summary, our experimental observations indicate the feasibility of

realizing the clip-on micro-cuff device by molding process. As an alternate to silicone elastomer, any biocompatible, injection moldable polymer can be used for the molding based fabrication process described here.

References

[1] D.C. Duffy, J.C. McDonald, O.J.A. Schueller, and G.M. Whitesides, "Rapid prototyping of microfluidic systems in poly(dimethylsiloxane)," Analytical Chemistry, vol. 70, no. 23, pp. 4974-4984, 1998.

[2] B. Schnyder, T. Lippert, R. Kotz, A. Wokaun, V-M. Graubner, and O. Nuyken, "UV-radiation induced modification of PDMS films investigated by XPS and spectroscopic ellipsometry," Surface Science, Vol. 532-535, pp. 1067-1071, 2003.

[3] S. Thorslund, O. Klett, F. Nikolajeff, K. Markides, and J. Bergquist, "A hybrid poly(dimethylsiloxane) microsystem for on-chip whole blood filtration optimized for steroid screening," Biomedical Microdevices, Vol. 8, pp. 73-79, 2006.

[4] F. Schneider, J. Draheim, R. Kamberger, and U. Wallrabe, "Process and material properties of polydimethylsiloxane (PDMS) for optical MEMS," Sensors and Actuators A: Physical, Vol. 151, pp. 95-99, 2009.

[5] M. Liu, J. Sun, and Q. Chen, "Influences of heating temperature on mechanical properties of polydimethylsiloxane," Sensors and Actuators A: Physical, Vol. 151, pp. 42-45, 2009.

APPENDIX D: MATLAB CODE EXAMPLE FOR CALCULATION OF TORSIONAL STIFFNESS

```
% Torsion stiffness of cuff
clear all; close all; clc;

% Equation driving parameters
wc = 4E-3;
tc = 1E-3;
NumPoints = 50;
AlphaDeg = linspace(0.0001,90,NumPoints)';
Alpha = AlphaDeg*pi/180;
E = 2.5E6;
Eta1 = [0.2 0.4 0.6 0.8 1.0];
lc = 5E-4;
fc = 4E-3;
Eta2 = tc/(2*fc);
[m n] = size(Eta1);
Stiff = zeros(NumPoints,n);
for i = 1:n
%  Compute the most used terms
sT = sin(Alpha);
cT = cos(Alpha);
B = Eta1(i);
Bsq = B.^2;
B2 = 2*B;

% Compute constants, numerators and denominators
C1 = 3./(2*E*wc*lc.^2);
C2 = 1./(B2+Bsq);
N1 = (1+B).*sT;
D1 = (1+B-cT).^2;
N2 = (3+B2+Bsq).*sT;
D2 = (B2+Bsq).*(1+B-cT);
N3 = 6*(1+B).*atan(sqrt((2+B)./B).*tan(Alpha/2));
D3 = (B2+Bsq).^1.5;
N4 = Eta2^2.*cot(Alpha);
D4 = Bsq.*((1+Eta2).^2);
N5 = cot(Alpha);
D5 = (1+B-cT).^2;

% Compute equation
K = C1.*(C2.*(N1./D1 + N2./D2 + N3./D3) - N4./D4 + N5./D5);
Stiff(:,i) = 1./K;
end
```

```
plot(ThetaDeg,Stiff(:,1),'*b-'); hold on;
plot(ThetaDeg,Stiff(:,2),'vg-'); hold on;
plot(ThetaDeg,Stiff(:,3),'or-'); hold on;
plot(ThetaDeg,Stiff(:,4),'^k-'); hold on;
plot(ThetaDeg,Stiff(:,5),'sm-'); title('Stiffness of hinge'); grid on;
legend('Eta1 = 0.2','Eta1 = 0.4','Eta1 = 0.6','Eta1 = 0.8','Eta1 = 1.0','Location','NorthWest');
xlabel('Alpha---->');ylabel('Stiffness---->');

% Export values
xlswrite('varyalpha.xlsx', [AlphaDeg Stiff],'stiff');
```

APPENDIX E: PSPICE SIMULATIONS

E.1. PSPICE Schematic

An example circuit used to simulate the electrode-tissue interface developed in this study is shown in Figure E.1. The corresponding simulations results are described in Chapter 5, section 5.3.4. The output file generated by the PSPICE software for this circuit is given below in section E.2.

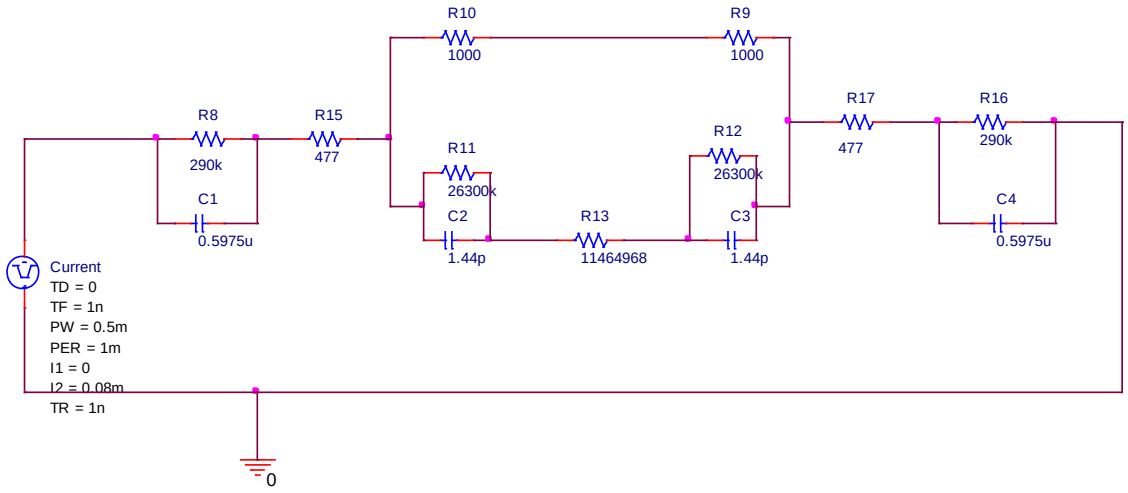

Figure E.1: PSPICE schematic representation of the developed equivalent circuit for the electrode-tissue interface.

E.2. Output File for Schematic

The output file generated by the PSPICE software for the above circuit is given below.

**** 04/20/11 18:37:10 ******* PSpice 16.2.0 (Oct 2008) ******* ID# 0 ********
** Profile: "SCHEMATIC1-bias" [C:\Users\Naga\fns 8oct2010-pspicefiles\schematic1\bias.sim]
**** CIRCUIT DESCRIPTION
****
** Creating circuit file "bias.cir"
** WARNING: THIS AUTOMATICALLY GENERATED FILE MAY BE OVERWRITTEN BY SUBSEQUENT SIMULATIONS
*Libraries:
* Profile Libraries :
* Local Libraries :

```
* From [PSPICE NETLIST] section of C:\OrCAD\OrCAD_16.2\tools\PSpice\PSpice.ini file:
.lib "nom.lib"
*Analysis directives:
.TRAN  0 3ms 0
.PROBE V(alias(*)) I(alias(*)) W(alias(*)) D(alias(*)) NOISE(alias(*))
.INC "..\SCHEMATIC1.net"
**** INCLUDING SCHEMATIC1.net ****
* source FNS 8OCT2010
C_C2         N46397 N46369  1.44p  TC=0,0
R_R16        N46085 0  290k TC=0,0
R_R12        N46379 N46077  26300k TC=0,0
R_R17        N46077 N46085  477 TC=0,0
R_R13        N46369 N46379  11464968 TC=0,0
C_C3         N46379 N46077  1.44p  TC=0,0
C_C4         N46085 0  0.5975u  TC=0,0
I_Current        0 N46115 DC 0Adc AC 0Aac
+PULSE 0 0.08m 0 1n 1n 0.5m 1m
R_R8         N46115 N46487  290k TC=0,0
C_C1         N46115 N46487  0.5975u  TC=0,0
R_R9         N71573 N46077  1000 TC=0,0
R_R10        N46397 N71573  1000 TC=0,0
R_R11        N46397 N46369  26300k TC=0,0
R_R15        N46487 N46397  477 TC=0,0
**** RESUMING bias.cir ****
.END
**** 04/20/11 18:37:10 ******* PSpice 16.2.0 (Oct 2008) ******* ID# 0 ********
 ** Profile: "SCHEMATIC1-bias"  [ C:\Users\Naga\fns 8oct2010-
pspicefiles\schematic1\bias.sim ]
 ****     INITIAL TRANSIENT SOLUTION       TEMPERATURE =   27.000 DEG C
********************************************************************************
 NODE   VOLTAGE     NODE   VOLTAGE     NODE   VOLTAGE     NODE   VOLTAGE
(N46077)    0.0000 (N46085)    0.0000 (N46115)    0.0000 (N46369)    0.0000
(N46379)    0.0000 (N46397)    0.0000 (N46487)    0.0000 (N71573)    0.0000
   VOLTAGE SOURCE CURRENTS
   NAME         CURRENT
   TOTAL POWER DISSIPATION   0.00E+00  WATTS
        JOB CONCLUDED
**** 04/20/11 18:37:10 ******* PSpice 16.2.0 (Oct 2008) ******* ID# 0 ********
 ** Profile: "SCHEMATIC1-bias"  [ C:\Users\Naga\fns 8oct2010-
pspicefiles\schematic1\bias.sim ]
 ****     JOB STATISTICS SUMMARY
********************************************************************************
  Total job time (using Solver 1)   =         .05
```

APPENDIX F: THEORETICAL RESPONSE OF EQUIVALENT CIRCUIT TO A STEP FUNCTION

F.1. Theoretical Derivation for Axon Current

An expression for the theoretical magnitude of axon current is derived when a current pulse (similar to that shown in Figure 5.5) is applied as the stimulus signal to the equivalent circuit shown in Figure 5.4. The values for the circuit elements used here are listed in Table 5.5. These have been chosen from the value ranges calculated in section 5.3.2. The impedance Z_M associated with the axon membrane is considered since it is associated with the entry and exit points for the axon. This impedance is given by:

$$Z_M = R_M \,||\, (1/sC_M), \tag{F.1}$$

where s is a complex frequency. The derivation of the axon current will involve a study of the transient characteristics of the equivalent circuit. The total impedance Z_A associated with the axon is given by:

$$Z_A = 2Z_M + R_A. \tag{F.2}$$

$$Z_A = \frac{2R_M}{1+sR_MC_M} + R_A\,, \tag{F.3}$$

$$Z_A = \frac{(2R_M + R_A) + sR_AR_MC_M}{1+sR_MC_M}\,. \tag{F.4}$$

By current division,

$$\frac{I_A}{I_S} = \frac{R_E}{Z_A + R_E}\,. \tag{F.5}$$

Substituting the expression for Z_A from equation (F.4) in equation (F.5),

$$\frac{I_A}{I_S} = \frac{R_E\,(1+sR_MC_M)}{(2R_M + R_E + R_A) + s(R_A + R_E)R_MC_M}\,. \tag{F.6}$$

The equation (F.6) is of the form,

$$\frac{I_A}{I_S} = K\frac{s+s_1}{s+s_2}\,, \tag{F.7}$$

where s_1, s_2 and K are given by:

$$s_1 = \frac{1}{R_M C_M}, \tag{F.8}$$

$$s_2 = \frac{2R_M + R_E + R_A}{(R_A + R_E)R_M C_M}, \tag{F.9}$$

$$K = \frac{R_E}{R_A + R_E}, \tag{F.10}$$

First, the input response of the equivalent circuit is determined for a step function defined by $f(t) = \begin{cases} 0, & t < 0 \\ A, & t > 0 \end{cases}$.

For the step function, the Laplace transform is given by:

$$\mathscr{L}[f(t)] = \frac{A}{s}. \tag{F.11}$$

Therefore, $I_S = \frac{A}{s}$. (F.12)

Equation (F.7) becomes:

$$I_A = KA\frac{s + s_1}{s + s_2}.\frac{1}{s}, \tag{F.13}$$

$$I_A = KA\left[\frac{1}{(s + s_2)} + \frac{s_1}{s(s + s_2)}\right]. \tag{F.14}$$

The inverse Laplace transform of $1/(s+s_2)$ is given by [1]:

$$\mathscr{L}^{-1}\left[\frac{1}{s + s_2}\right] = e^{-s_2 t}. \tag{F.15}$$

The inverse Laplace transform of $1/(s+a)(s+b)$ is given by [1]:

$$\mathscr{L}^{-1}\left[\frac{1}{(s + a)(s + b)}\right] = \frac{1}{b-a}(e^{-at} - e^{-bt}) \quad . \tag{F.16}$$

In the present case ($a = 0$, $b = s_2$):

$$\mathscr{L}^{-1}\left[\frac{1}{s(s + s_2)}\right] = \frac{1}{s_2}(1 - e^{-s_2 t}) \quad . \tag{F.17}$$

Therefore, equation (F.14) becomes,

$$i_A(t) = KA\left[e^{-s_2 t} + \frac{s_1}{s_2}(1 - e^{-s_2 t})\right], \tag{F.18}$$

$$i_A(t) = \frac{KAs_1}{s_2} + KA\left[1 - \frac{s_1}{s_2}\right]e^{-s_2 t}. \quad \text{(F.19)}$$

The time constant is given by $1/s_2$ and from equation (F.9) is equal to 6.8 μs.

The equation (F.19) is the input response for $t > 0$. $i_A(t)$ can also be represented by:

$$i_A(t) = \left\{\frac{KAs_1}{s_2} + KA\left[1 - \frac{s_1}{s_2}\right]e^{-s_2 t}\right\}u(t), \quad \text{(F.20)}$$

where *u(t)* is a unit step function, defined by $u(t) = \begin{cases} 0, & t < 0 \\ 1, & t > 0 \end{cases}$.

The circuit response is studied for a pulse function, defined by $i_{S1}(t) = \begin{cases} A, & 0 < t < t_0 \\ 0, & t < 0,\ t > t_0 \end{cases}$.

This pulse function of width t_0 can also be represented by $i_{S1}(t) = f(t) - f(t - t_0)$.

Since the system is a linear time invariant system, the axon current is given by:

$$i_{A1}(t) = i_A(t) - i_A(t - t_0), \quad \text{(F.21)}$$

$$i_{A1}(t) = \left\{\frac{KAs_1}{s_2} + KA\left[1 - \frac{s_1}{s_2}\right]e^{-s_2 t}\right\}u(t) - \left\{\frac{KAs_1}{s_2} + KA\left[1 - \frac{s_1}{s_2}\right]e^{-s_2 (t-t_0)}\right\}u(t - t_0). \quad \text{(F.22)}$$

Based on the values of components given in Table 5.5, the values of K, s_1 and s_2 are calculated and substituted in equation (F.22) to plot the response of the circuit to a pulse input with A = 0.5 mA, t_0 = pulse-width (PW) = 0.5 ms. This theoretical response shown in Figure F.1 matches the PSPICE simulated response to a current pulse with the same amplitude and PW.

References

[1] K. Ogata, Modern Control Engineering, Prentice Hall, Englewood Cliffs, NJ, USA, 1970.

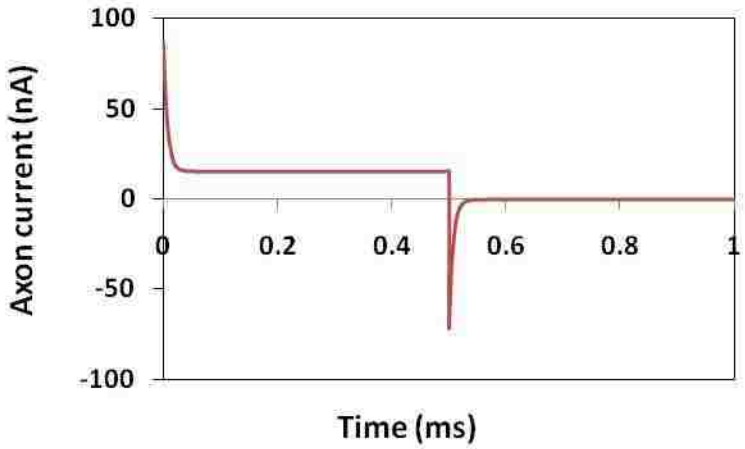

Figure F.1: The axon current as a function of time, calculated theoretically using equation (F.22). This is the input response for a pulse signal of amplitude 0.5 mA, and pulse-width 0.5 ms.

APPENDIX G: MECHANICAL MODELING OF A PAD WITH CORRUGATED CONDUIT

In a variation to the notched conduit design, a PAD with corrugations in its conduit is modeled here as a thin-walled cylindrical member with circular bellows, located axially along part of its length (Figure G.1). The bellows have rectangular geometry. The equations developed in bellow theory are applied here [1-3]. A more accurate representation of the PAD corrugations is a U-shaped bellows. However, analysis of this particular geometry of bellows is rather complex, with wide-ranging deviations reported between theoretical and experimental data [4-6]. When a bellows is modeled using equations for thin shells, calculations such as those for torsional stiffness vary less than 10% over the complete range of bellow geometries [7]. Therefore, modeling the corrugations of the PAD as a rectangular geometry bellows is a reasonable approach for bellows with thin shells.

A PAD conduit is considered to have circumferential corrugations of total length for 'n' corrugations equal to L_c, wall thickness of t_1, inner radius of R_{in}, and outer radius of R_{out}. The total length L_c of the corrugations is given by:

$$L_c = 4na_1, \tag{G-1}$$

where $4a_1$ is the pitch of each corrugation as shown in Figure G.1. The average radius of the corrugations is given by:

$$R_{av} = \frac{R_{in}+R_{out}}{2}. \tag{G-2}$$

The average cross-sectional area of the corrugations is:

$$A_c = 2\pi R_{av} t_1. \tag{G-3}$$

The torsional stiffness of the member due to the corrugations is given by [7]:

$$K_{\theta_x M_x} = \frac{G\pi {R_{av}}^3 t_1}{4na_1}, \tag{G-4}$$

where G is the modulus of rigidity, given by [8-9]:

$$G = \frac{E}{2(1+\nu)}, \tag{G-5}$$

where E is the Young's modulus and ν is the Poisson's ratio of the PAD conduit material. For Silastic silicone, E = 2.5 N/mm^2 and ν = 0.5.

The ratio of the inner and outer radii ζ is given by:

$$\zeta = \frac{R_{in}}{R_{out}}. \tag{G-6}$$

Therefore, the average radius can be expressed as:

$$R_{av}{}^3 = \frac{[R_{out}]^3}{8}[\zeta^3 + 3\zeta^2 + 3\zeta + 1]. \tag{G-7}$$

Substituting the expression for R_{av} in equation G-4, the torsional stiffness equation becomes:

$$K_{\theta_x M_x} = \frac{G\pi R_{out}{}^3 t_1[\zeta^3+3\zeta^2+3\zeta+1]}{32na_1}. \tag{G-8}$$

The axial stiffness of the member is given by [7]:

$$K_{\Delta x M_x} = \frac{E'2\pi R_{av} t_1}{4na_1}, \tag{G-9}$$

where E' is a modified Young's modulus given by:

$$E' = \frac{4E t_1{}^2(1-\lambda^2)(a_1/R_{av}{}^2)\eta}{3R_{av}(1-\nu^2)\left(1+\frac{b_1}{R_{av}}\right)^2[(1-\lambda^2)^2-(2\lambda\ln\lambda)^2]}, \tag{G-10}$$

in which

$$b_1 = \frac{R_{out}-R_{in}}{2}, \tag{G-11}$$

$$\lambda = \frac{1-b_1/R_{av}}{1+b_1/R_{av}}, \tag{G-12}$$

$$\eta = 1 + \frac{2(a_1/R_{av})}{1+b_1/R_{av}}\left[\frac{D_1}{S} + \frac{D_2}{S}\right], \tag{G-13}$$

$$D_1 = \xi_1(1 - \lambda^2 + 2\lambda^2\ln\lambda)^2, \tag{G-14}$$

$$D_2 = \xi_2\lambda(1 - \lambda^2 + 2\ln\lambda)^2, \tag{G-15}$$

$$S = (1 - \lambda^2)[(1 - \lambda^2)^2 - (2\lambda \ln \lambda)^2] \,, \tag{G-16}$$

$$\xi_1 = \frac{sinh2\phi_1 + sin2\phi_1}{2\phi_1(cosh2\phi_1 + cos2\phi_1)} \,, \tag{G-17}$$

$$\xi_2 = \frac{sinh2\phi_2 + sin2\phi_2}{2\phi_2(cosh2\phi_2 + cos2\phi_2)} \,, \tag{G-18}$$

$$\phi_1 = \frac{(3-3\nu^2)^{1/4}}{[\psi(1+ b_1/R_{av})]^{1/2}} \,, \tag{G-19}$$

$$\phi_2 = \frac{(3-3\nu^2)^{1/4}}{[\psi(1- b_1/R_{av})]^{1/2}} \,, \quad \text{and} \tag{G-20}$$

$$\psi = \frac{R_{av}t_1}{{a_1}^2} \tag{G-21}$$

The use of the modified Young's modulus *E'* in the place of a traditional Young's modulus value allows one to employ a beam bending treatment towards modeling bellows [10]. Using equations G-8 and G-9, the torsional and axial stiffness of the corrugated PAD conduit can be determined.

The presence of the corrugations has an effect on the flexure characteristics of the conduit. This is evident from Figure G.2 which shows the torsional stiffness $K_{\theta xMx}$ as a function of the number of corrugations, obtained by equation G-8. The stiffness decreases as the number of corrugations or bellows increases. This is expected because the corrugations impart some degree of flexibility to the PAD conduit. The decrease in stiffness becomes minor as the number of corrugations increases.

For the dimensions of the corrugated conduit modeled here, the decrease in stiffness is considerably small for more than 5 corrugations. This implies that a few corrugations can suffice to decrease the stiffness or increase the flexibility of the conduit.

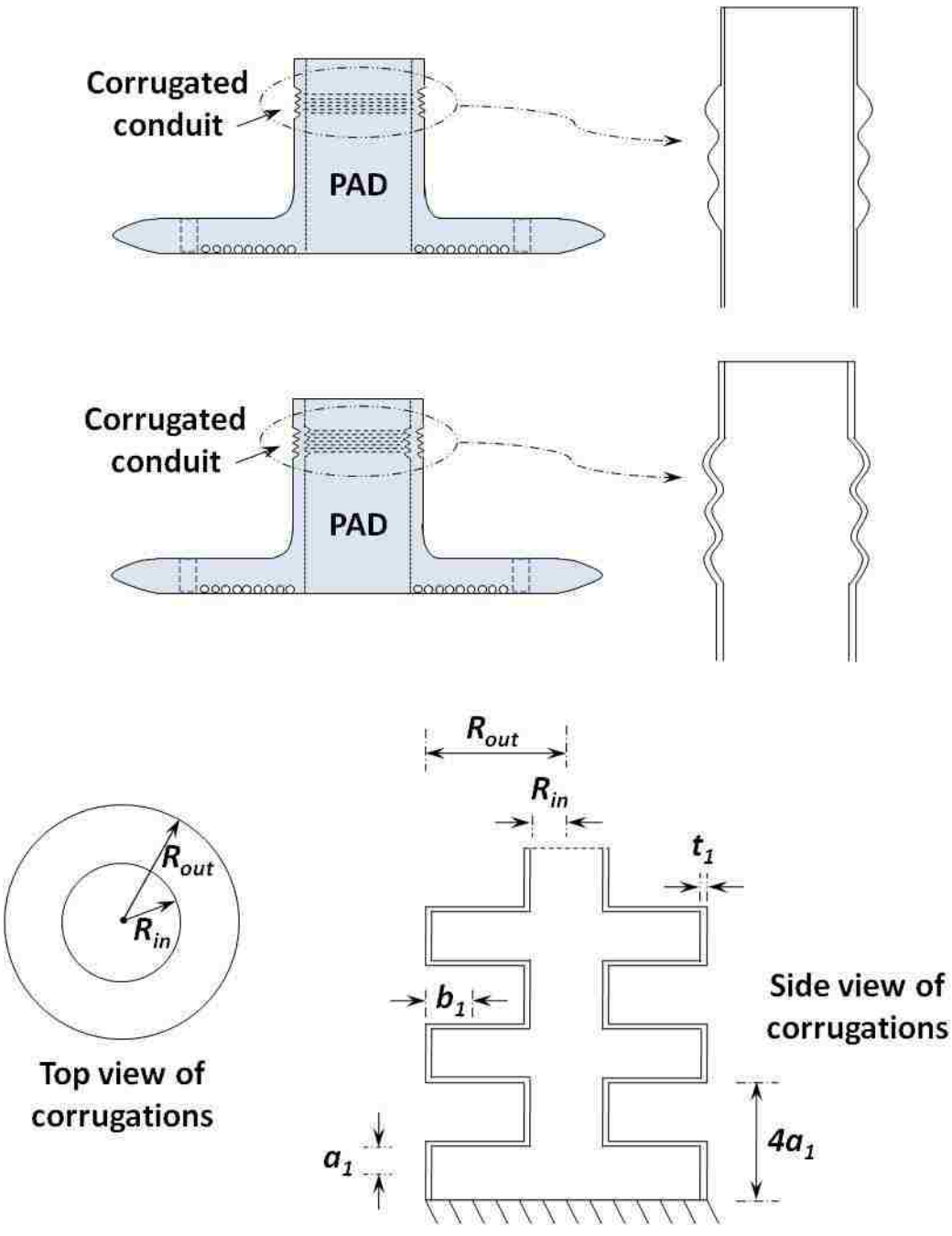

Figure G.1: A rectangular geometry bellow configuration showing modeling parameters used. Diagrams are not to scale.

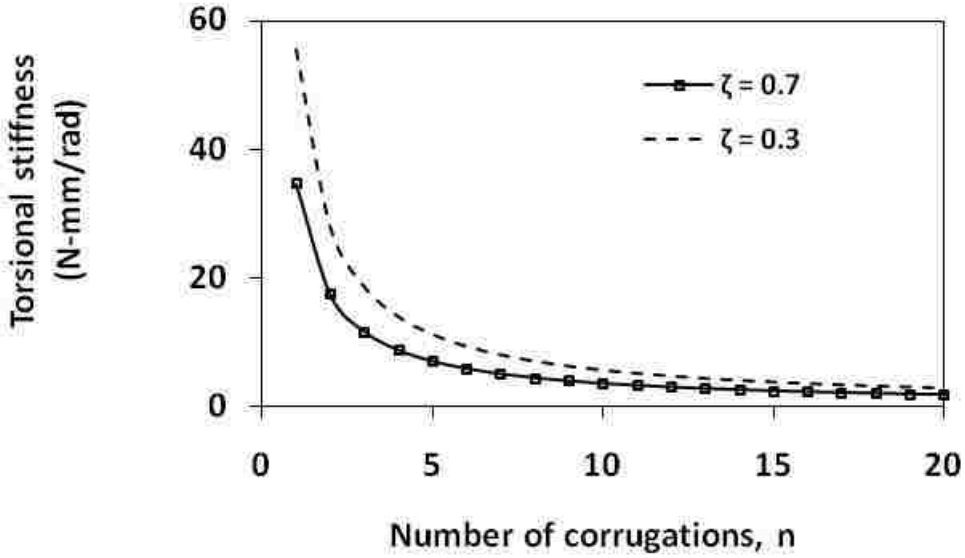

Figure G.2: Variation of the torsional stiffness $K_{\theta xMx}$ of a Silastic silicone PAD conduit as a function of the number of corrugations n on the conduit, calculated using eq. G-8 for t_1 = 0.5 mm, a_1 = 1.5 mm, R_{out} = 2.5 mm, and $\zeta = R_{in}/R_{out}$ = 0.3 and 0.7.

The torsional stiffness is also influenced by the inner and outer radii of the corrugations. This is apparent from Figure G.3 which plots the torsional stiffness as a function of the ratio of inner and outer radii (R_{in}/R_{out}) of the corrugations. Two cases are shown here, for 1 corrugation and for 3 corrugations respectively. However, the result holds true for other number of corrugations. It is beneficial to have a smaller value for the ratio of inner to outer radii ζ for a lower value for torsional stiffness. As inner and outer radii of the corrugations become comparable, the torsional stiffness increases. In Figure F.4, ζ = 1 corresponds to a straight hollow tube with no bellows.

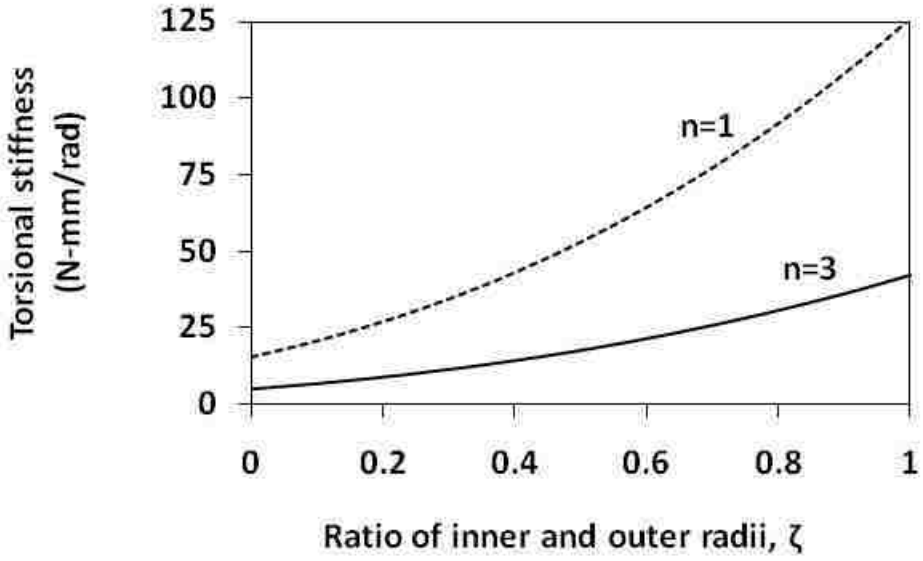

Figure G.3: Variation of the torsional stiffness $K_{\theta xMx}$ of a Silastic silicone PAD conduit as a function of the ratio ζ of inner and outer radii of the corrugations, calculated using eq. G-8 for t_1 = 0.5 mm, a_1 = 1.5 mm, R_{out} = 2.5 mm, and n = 1 and 3.

The axial stiffness $K_{\Delta xMx}$ of the PAD conduit is influenced by the dimensions and the number of corrugations (Figure G.4). As in the case of the torsional stiffness, the axial stiffness decreases as the number of corrugations on the PAD conduit increase (Figure G.4). Again, this decrease in stiffness is not significant for higher number of corrugations. Similar to the torsional stiffness, the axial stiffness is influenced by the dimensions of the corrugations. This can be seen in Figure G.5, which plots axial stiffness as a function of the ratio b_1 which is an aspect of the lateral dimension of the corrugations. In general, a smaller value of b_1 yields larger axial stiffness. Note that b_1=0 corresponds to no corrugations.

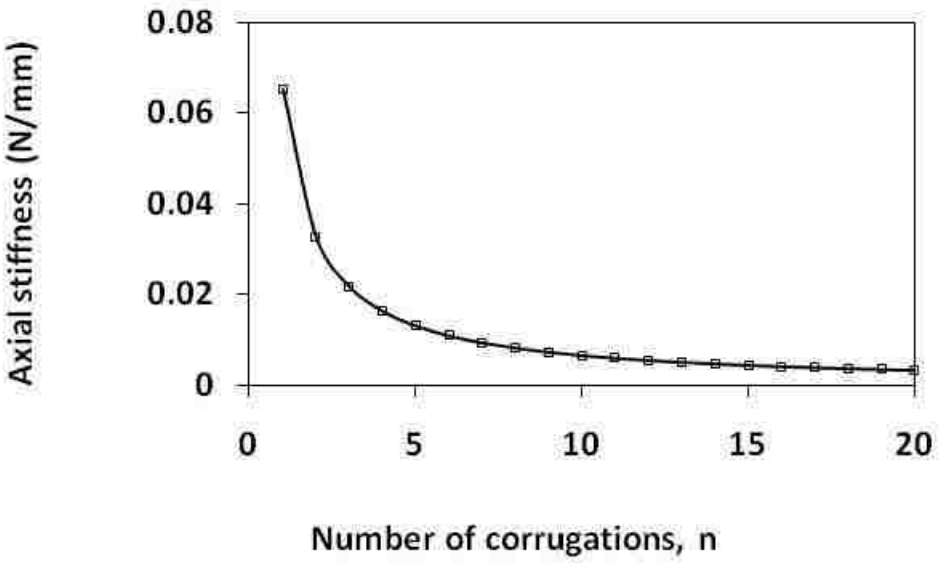

Figure G.4: Variation of the axial stiffness $K_{\Delta xMx}$ of a Silastic silicone PAD conduit as a function of the number of corrugations n on the conduit, calculated using eq. G-9 for t_1 = 0.5 mm, a_1 = 1.5 mm, R_{in} = 2.5 mm, and ζ = 0.3.

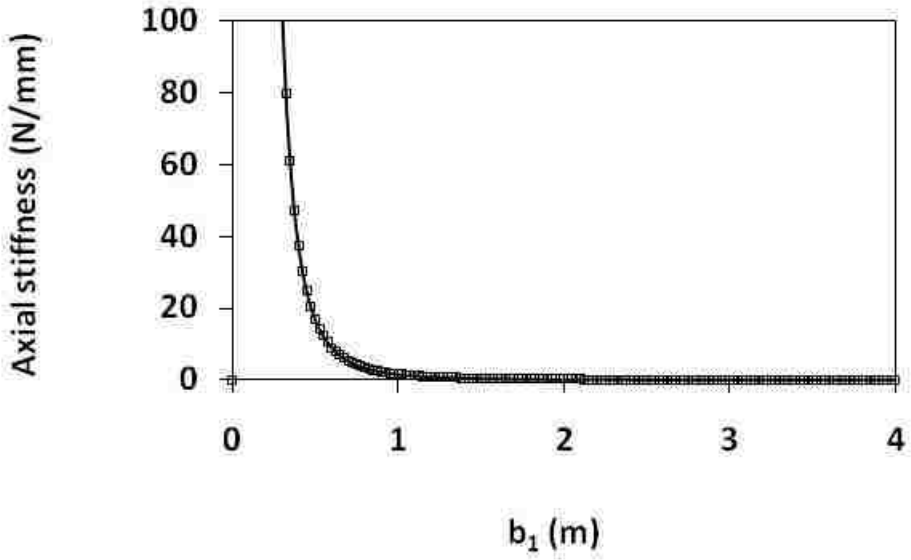

Figure G.5: Variation of the axial stiffness $K_{\Delta xMx}$ of a Silastic silicone PAD conduit as a function of b_1, calculated using eq. G-9 for t_1 = 0.5 mm, a_1 = 1.5 mm, R_{in} = 2.5 mm, and b_1 dependent on R_{out} which was varied from 2.5 mm (b_1 = 0) to 10.5 mm (b_1 = 4).

In summary, the following conclusions can be drawn from the mechanical modeling of the PAD with a corrugated conduit:

1. The presence of the corrugations has an effect on the torsional and axial stiffness characteristics of the conduit.
2. The torsional stiffness is influenced by the inner and outer radii of the corrugations. It is beneficial to have a smaller ratio of inner to outer radii for a lower torsional stiffness. As the inner and outer radii of the corrugations become comparable, the torsional stiffness increases.
3. The dimensions and number of corrugations influence the axial stiffness of the member. The axial stiffness decreases as the number of corrugations on the PAD conduit increase. The incremental decrease in stiffness with corrugation number is not significant for higher number of corrugations.

References

[1] J.F. Wilson, "Mechanics of bellows: a critical survey," International Journal of Mechanical Sciences, Vol. 26, No. 11/12, pp. 593-605, 1984.

[2] C. Brecht IV, "Predicting bellows response by numerical and theoretical methods," Transactions of ASME: Journal of Pressure Vessel Technology, Vol. 108, pp. 334-341, 1986.

[3] M. Hamada, and T. Tsuda, "On design formulas of U-shaped bellows," Transactions of ASME: Journal of Pressure Vessel Technology, Vol. 119, pp. 127-131, 1997.

[4] M. Hamada et al, "Design diagrams and formulae for U-shaped bellows," International Journal of Pressure Vessel Technology, Vol. 4, pp. 315, 1976.

[5] Y.I. Berliner, and Y.L. Vikhman, "The axial rigidity of flexible elements of compensators with U- and Ω-shaped profiles of waves," Chemistry and Petroleum Engineering, Vol. 12, pp. 31, 1976.

[6] J.A. Haringx, "Instability of bellows subjected to internal pressure," Phillips Research Reports, Vol. 7, pp. 189-196, 1952.

[7] S.T. Smith, Flexures: Elements of Elastic Mechanisms, ISBN: 90-5699-261-9, 2000, Gordon and Breach Science Publishers.

[8] S.P. Timoshenko, and S. Woinowski-Kreiger, Theory of plates and shells, McGraw-Hill Book Company, NY, 1959.

[9] S.P. Timoshenko, Strength of Materials: Pt. II Advanced Theory and Problems, 2nd ed., D. Van Nostrand, Inc., NY, chapter II, 1941.

[10] L.H. Donnell, "The flexibility of corrugated pipes under longitudinal forces and bending," ASME Transactions: Journal of Applied Mechanics, Vol. APM-54-7, pp. 69, 1932.

APPENDIX H: LETTER OF PERMISSION TO REPRINT FROM J. MED. BIOL. ENG.

Dear Korivi,

Yes, as long as cite properly, the authors can include the submission in their thesis works. In addition, the DOI number of your article (JMBE 819, "Self-closing Cuff Electrode for Functional Neural Stimulation and Recording") is "10.5405/jmbe.819".

You can cite this article by using this DOI. The article in press version is attached in this letter.
For more articles in press, you can visit our website.
http://jmbe.bme.ncku.edu.tw/index.php/bme/about/aboutThisPublishingSystem

Thanks for your support to JMBE.

Yu-Jing Marcell Lin
Editorial assistant, JMBE (SCIE & EI)
ADD: Biosignal Lab, Institute of Biomedical Engineering, National Cheng Kung University, Tainan
TEL: +886-6-2757575 ext. 63406-133
FAX: +886-6-2343270
E-mail: jmbe@jason.bme.ncku.edu.tw; z9808152@email.ncku.edu.tw
JMBE Website: http://jmbe.bme.ncku.edu.tw

APPENDIX I: LETTER OF PERMISSION TO REPRINT FROM ASME

Dear Mr. Korivi:
It is our pleasure to grant you permission to use the following ASME materials:

- Figures 1, 2, 3 from "Percutaneous Access Device With Stress Relief Features," by Naga S. Korivi, Pratul K. Ajmera, Proceedings of the ASME 2010 5th Frontiers in Biomedical Devices Conference, Paper Number BioMed2010-32022,

- Figures 1, 2, 3 from "Thermally Responsive Structures for Gastric Pacing and Other Applications, by Naga S. Korivi, Charles Halliburton, Pratul K. Ajmera, Proceedings of the ASME 2010 5th Frontiers in Biomedical Devices Conference, Paper Number BioMed2010-32074

cited in your letter for inclusion in a Doctoral Thesis entitled Bio-Implantable Microdevices and Structures for Functional Electrical Stimulation Applications to be published by Louisiana State University.

As is customary, we ask that you ensure full acknowledgment of this material, the author(s), source and ASME as original publisher on all printed copies being distributed.

Many thanks for your interest in ASME publications.

Sincerely,
Beth Darchi
Permissions & Copyrights
ASME, 3 Park Avenue
New York, NY 10016
T: 212-591-7700
F: 212-591-7841
E: darchib@asme.org

APPENDIX J: LETTER OF PERMISSION TO REPRINT FROM J. VAC. SCI. TECHNOL., AVS

Dear Dr. Korivi:

Thank you for requesting permission to reproduce material from American Vacuum Society publications.
Permission is granted – subject to the conditions outlined below – for the following:

N.S. Korivi, J. Hoffpauir, and P.K. Ajmera, "Texturing of silicon using a microporous polymer etch mask," J. Vac. Sci. Technol. B, 28(6), Nov/Dec 2010, pp. C6K8-C6K12.
To be used in the following manner:

Reproduced as part of your Ph.D. dissertation for submission to Louisiana State University.

1. The American Vacuum Society grants you the right to reproduce the material indicated above on a one-time, non-exclusive basis, solely for the purpose described. Permission must be requested separately for any future or additional use.
2. This permission pertains only to print use and its electronic equivalent, including CD-ROM or DVD.
3. The following copyright notice must appear with the material (please fill in the information indicated by capital letters): "Reprinted with permission from [FULL CITATION]. Copyright [PUBLICATION YEAR], American Vacuum Society."
Full citation format is as follows: Author names, journal title, Vol. #, Page #, (Year of publication). For an article, the copyright notice must be printed on the first page of the article or book chapter. For figures, photographs, covers, or tables, the notice may appear with the material, in a footnote, or in the reference list.
4. This permission does not apply to any materials credited to sources other than the copyright holder.

Please let us know if you have any questions.
Sincerely,
Susann Brailey
~~~~~~~~~~~
Office of the Publisher, Journals and Technical Publications
Rights & Permissions
American Institute of Physics
Suite 1NO1
2 Huntington Quadrangle
Melville, NY 11747-4502
516-576-2268 TEL
516-576-2450 FAX
rights@aip.org
~~~~~~~~~~~

VITA

Naga S. Korivi graduated from the University of Madras, Chennai, India, in 1998 with a bachelor's degree in electronics and communication engineering. He obtained a master's degree in electrical engineering from Louisiana Tech University, Ruston, Louisiana, in 2002. He has been enrolled at Louisiana State University since 2003 in the doctoral program in the Department of Electrical and Computer Engineering. His research interests lie in the development of devices for biomedical and medical applications, micro- and nano-scale engineering, and tailoring of materials for energy applications, among others.